Modeling and simulation of vacancy-assisted charge transport in innovative semiconductor devices

Dissertation

zur Erlangung des Grades eines
Doktors der Naturwissenschaften
(Dr. rer. nat.)

am Fachbereich Mathematik und Informatik
der Freien Universität Berlin

vorgelegt von
Dilara Abdel

Berlin 2024

Erstgutachter:	PD Dr. Patricio Farrell *Freie Universität Berlin und Weierstraß-Institut für Angewandte Analysis und Stochastik, Berlin*
Zweitgutachterin:	Prof. Dr. Nella Rotundo *Università degli Studi di Firenze, Florenz*

Tag der Disputation: 15. Februar 2024

Abstract

In response to the climate crisis, there is a need for technological innovations to reduce the escalating CO_2 emissions. Two promising semiconductor technologies in this regard, perovskite-based solar cells and memristive devices based on two-dimensional layered transition metal dichalcogenide (TMDC), can potentially contribute to the expansion of renewable energy sources and the development of energy-efficient computing hardware. Within perovskite and TMDC materials, ions dislocate from their ideal position in the semiconductor crystal and leave void spaces. So far, the precise influence of these vacancies and their dynamics on device performance remain underexplored. Therefore, this thesis is dedicated to comprehensively examining the impact of vacancy-assisted charge transport in innovative semiconductor devices through a theoretical approach by modeling and simulating systems of partial differential equations. We start by deriving drift-diffusion equations using thermodynamic principles, including Maxwell-Stefan diffusion and the grand canonical ensemble of an ideal lattice gas. Particular attention is directed towards accurately limiting vacancy accumulation. Furthermore, we formulate drift-diffusion models to describe charge transport in perovskite solar cells and TMDC memristors. We discretize the transport equations via the finite volume method and establish the existence of discrete solutions using the entropy method. Our study concludes with simulations conducted with `ChargeTransport.jl`, an open source software tool developed in the programming language Julia. These simulations investigate the large time behavior of discrete solutions for both transport models. Additionally, we explore the influence of volume exclusion effects on charge transport in perovskite solar cells and compare our simulation results with experimental measurements found in literature for TMDC-based memristive devices.

Contents

List of publications

The following presents a complete list of my publications. Furthermore, all the required scripts to generate and visualize the simulation data are available here:

[DA1] D. Abdel. *`VacancyAssistedChargeTransport.jl` – Simulating vacancy-assisted charge transport in semiconductors*. DOI: 10.5281/zenodo.8396870 (cit. on pp. 96, 144).

Dissertation related publications

Peer-reviewed articles

[DA2] D. Abdel, C. Chainais-Hillairet, P. Farrell, and M. Herda. "Numerical analysis of a finite volume scheme for charge transport in perovskite solar cells". *IMA Journal of Numerical Analysis* (2023), pp. 1–40. DOI: 10.1093/imanum/drad034 (cit. on pp. ix, 8, 10, 33, 35, 64, 65, 96, 98–102).

[DA3] D. Abdel, N. E. Courtier, and P. Farrell. "Volume exclusion effects in perovskite charge transport modeling". *Optical and Quantum Electronics* 55.884 (2023). DOI: 10.1007/s11082-023-05125-9 (cit. on pp. ix, 8, 10, 21, 24, 96, 110–114, 116).

[DA4] D. Abdel, P. Vágner, J. Fuhrmann, and P. Farrell. "Modelling charge transport in perovskite solar cells: Potential-based and limiting ion depletion". *Electrochimica Acta* (2021), p. 138696. DOI: 10.1016/j.electacta.2021.138696 (cit. on pp. 2, 8, 10, 16, 27, 33, 34, 64).

[DA5] B. Spetzler, D. Abdel, F. Schwierz, M. Ziegler, and P. Farrell. "The Role of Vacancy Dynamics in Two-Dimensional Memristive Devices". *Advanced Electronic Materials* 10.1 (2024), p. 2470002. DOI: 10.1002/aelm.202470002 (cit. on pp. 4, 8, 10, 33, 43, 44, 46, 96, 119–125).

Conference papers

[DA6] D. Abdel, N. Courtier, and P. Farrell. "Volume exclusion effects in perovskite charge transport modeling". *2022 International Conference on Numerical Simulation of Optoelectronic Devices (NUSOD)*. 2022. DOI: 10.1109/NUSOD54938.2022.9894826 (cit. on pp. 72, 110).

Software

[DA7] D. Abdel, P. Farrell, and J. Fuhrmann. ***ChargeTransport.jl*** – *Simulating charge transport in semiconductors*. DOI: 10.5281/zenodo.6257906 (cit. on pp. 95, 110, 127).

[DA8] J. Fuhrmann, D. Abdel, J. Weidner, A. Seiler, P. Farrell, and M. Liero. ***VoronoiFVM.jl*** *- Finite volume solver for coupled nonlinear partial differential equations*. DOI: 10.5281/zenodo.3529808 (cit. on pp. 95, 96).

Further publications

Peer-reviewed articles

[DA9] D. Abdel, P. Farrell, and J. Fuhrmann. "Assessing the quality of the excess chemical potential flux scheme for degenerate semiconductor device simulation". *Optical and Quantum Electronics* 53.163 (2021). DOI: 10.1007/s11082-021-02803-4 (cit. on pp. 6, 72).

Conference papers

[DA10] D. Abdel, J. Fuhrmann, and P. Farrell. "Comparison of Scharfetter-Gummel Schemes for (Non-)Degenerate Semiconductor Device Simulation". *2020 International Conference on Numerical Simulation of Optoelectronic Devices (NUSOD)*. 2020. DOI: 10.1109/NUSOD49422.2020.9217691.

List of abbreviations

Abbreviation	Description
2D	Two-dimensional
3D	Three-dimensional
2H	Two-hexagonal
AI	Artificial intelligence
CMOS	Complementary metal-oxide-semiconductor
DFT	Density functional theory
ETL	Electron transport layer
FDM	Finite difference method
FEM	Finite element method
FVM	Finite volume method
HRS	High-resistive state
HTL	Hole transport layer
IC	Initial condition
I-V	Current-voltage
IT	Information technology
LED	Light-emitting diode
LRS	Low-resistive state
MAPI	Methylammonium lead iodide
PDE	Partial differential equation
PCE	Power conversion efficiency
PSC	Perovskite solar cell
SBL	Schottky barrier lowering
SRH	Shockley-Read-Hall
TMDC	Transition metal dichalcogenide
TPFA	Two-point flux approximation

List of notations and physical constants

Symbol	Description	SI (derived) unit
α_g	Absorption coefficient	m^{-1}
C_p	Acceptor density	m^{-3}
$B_\mathrm{n}, B_\mathrm{p}$	Auger rate coefficient	m^6/s
C_{V_α}	Average vacancy density	m^{-3}
$\mathscr{E}_\alpha$	Band-edge	J
E_g	Band gap	J
n_α	Carrier density	m^{-3}
$\tau_\mathrm{n}, \tau_\mathrm{p}$	Carrier lifetimes	s
z_α	Charge number	–
χ_α	Chemical potential	V
$DOS_\mathrm{n}, DOS_\mathrm{p}$	Density of states	$1/(\mathrm{Jm}^3)$
ε_s	Dielectric permittivity	$\mathrm{C}/(\mathrm{Vm})$
D_α	Diffusion coefficient	m^2/s
g_α	Diffusion enhancement	–
η_α	Dimensionless chemical potential	–
$\mathbf{\Gamma}^D$	Dirichlet boundary	–
C_n	Donor density	m^{-3}
C	Doping density	m^{-3}
$\mathbf{F}_\alpha$	Driving force (mass transfer)	N
$N_\mathrm{n}, N_\mathrm{p}$	Effective density of states	m^{-3}
$m_\mathrm{n}^*, m_\mathrm{p}^*$	Effective mass	m_0
$\mathbf{j}_\alpha$	Electric current density	$\mathrm{C}/(\mathrm{m}^2\mathrm{s})$
ψ	Electric potential	V
ϕ	Electric potential energy	J
$z_\alpha q \varphi_\alpha$	Electrochemical potential	J
ψ	Electrostatic potential	V
$\mathbb{E}_f$	Free energy	J
$\zeta_{\alpha\beta}$	Friction coefficient	Ns/m

Symbol	Description	SI (derived) unit
ε_i	Image-force permittivity	C/(Vm)
F_{ph}	Incident photon flux	$1/(\mathrm{m}^2\mathrm{s})$
E_α	Intrinsic band-edge energy	J
N_{intr}	Intrinsic carrier density	m^{-3}
$\boldsymbol{\Omega}_{\mathrm{intr}} \subseteq \boldsymbol{\Omega}$	Intrinsic domain	–
ϕ_0	Intrinsic Schottky barrier	J
μ_α	Mobility	$\mathrm{m}^2/(\mathrm{Vs})$
$\boldsymbol{\Gamma}^N$	Neumann boundary	–
$\mathbf{J}_\alpha$	Particle current density	$1/(\mathrm{m}^2\mathrm{s})$
G	Photogeneration rate	$1/(\mathrm{m}^3\mathrm{s})$
φ_α	Quasi Fermi potential	V
$r_{0,\mathrm{rad}}$	Radiative rate coefficient	m^3/s
R	Recombination rate	$1/(\mathrm{m}^3\mathrm{s})$
$v_{\mathrm{n}}, v_{\mathrm{p}}$	Recombination velocity	m/s
$n_{\mathrm{n},\tau}, n_{\mathrm{p},\tau}$	Reference carrier density	m^{-3}
ε_r	Relative permittivity	–
$\boldsymbol{\Gamma}^S$	Schottky boundary	–
$\boldsymbol{\Omega} \subset \mathbb{R}^d$	Spatial domain	–
$\mathcal{F}_\alpha$	Statistics function	–
T	Temperature	K
U_T	Thermal voltage	V
N_{V_α}	Vacancy saturation limit	m^{-3}

Symbol	Description	Value	SI (derived) unit
k_B	Boltzmann constant	$1.380\,649 \times 10^{-12}$	J/K
m_0	Electron rest mass	$9.109\,383\,701\,5 \times 10^{-31}$	kg
q	Elementary charge	$1.602\,176\,634 \times 10^{-19}$	C
h	Planck constant	$6.626\,070\,15 \times 10^{-34}$	J/Hz
$\hbar = h/2\pi$	Reduced Planck constant	$\approx 1.054\,571\,817 \times 10^{-34}$	J s
ε_0	Vacuum permittivity	$\approx 8.854\,187\,812\,8 \times 10^{-12}$	C/(Vm)

List of figures

List of tables

1. Introduction

Semiconductor technology ranks among the leading sectors in today's industrial landscape. We face technology based on semiconductors several times a day, from the touchscreen displays of smartphones (thin film transistors) to the illumination provided by LEDs (light-emitting diodes) [101]. Developing new semiconductor devices and materials drives innovation in established technologies while potentially positively contributing to environmental sustainability. These innovations influence areas such as next-generation solar cells, and brain-inspired computing hardware [166, 168]. While some of these technologies are already on the path to commercialization, others remain in their early developmental stages, working toward readiness for mass production.

The design of new technologies and devices offers an interdisciplinary interface between science, technology, engineering, and mathematics. Modeling and simulating charge transport phenomena in these devices can assist in making predictions and optimizing their performance, addressing challenges that are often difficult and costly to overcome solely through experimental approaches [71]. In Section 1.1, we motivate the necessity to advance theoretical research for two concrete innovative applications. Then, in Section 1.2, we categorize the models and numerical schemes used in this thesis within the existing literature. Finally, in Section 1.3, we outline how this thesis aims to analyze these devices theoretically.

1.1. Motivation

According to the World Meteorological Organization, there is a 66 % probability that the world will surpass the critical 1.5 °C temperature threshold for the first time within the next four years [247]. This threshold, denoting the rise in the global average temperature above the pre-industrial baseline (1850 – 1900), was established in 2016 in response to the escalating global warming crisis and enshrined in the Paris Agreement [56]. Due to this alarming trend, the urgency of stabilizing the global climate has never been more pronounced. The Intergovernmental Panel on Climate Change has recommended achieving net-zero greenhouse gas emissions by 2050 to ensure sustainable climate stabilization [114]. As a result, rapid and transformative changes in the coming decades are needed. In this thesis, we pay particular attention to the charge transport

in two semiconductor technologies that can be part of the solution for CO_2 reduction. Specifically, we introduce perovskite-based solar cells for advancing renewable energy production and transition metal dichalcogenide (TMDC)-based memristors designed to enhance energy-efficient data storage and processing in future electronic devices.

1.1.1. Perovskite solar cells

In recent years, perovskite solar cells (PSCs) have emerged as a rapidly advancing technology within the field of photovoltaics [178, 188]. PSCs have demonstrated remarkable power conversion efficiency (PCE) rates, defined as the proportion of incident light power converted into electrical power, exceeding 30 % [16, 40, 162]. These PCE rates surpass the efficiency of widely used silicon solar cells under laboratory conditions. Furthermore, specific PSC architectures can significantly reduce production costs compared to conventional silicon solar cells. Due to their high efficiency and low-cost manufacturing, PSCs can potentially revolutionize renewable energy production, which is crucial for reducing greenhouse gas emissions. However, the commercialization of PSCs is still in its early stages, and several substantial challenges must be addressed, including issues related to stability, limited lifespan, and toxicity concerns [213].

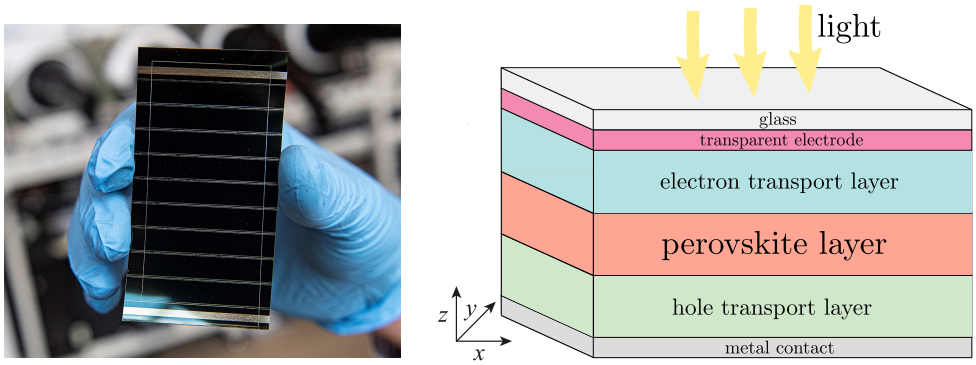

Figure 1.1.: A fabricated thin-film perovskite solar cell (left) and an illustration of a planar perovskite-based solar cell architecture (right). (Left image from [214] and the right image from [DA4] with modifications.)

In a PSC configuration, a perovskite layer is sandwiched between an electron transport (ETL), a hole transport layer (HTL), and additional contact layers, as illustrated in Figure 1.1 (right). A planar cell is among the common architectures where incident light enters through the ETL. Perovskites do not describe one concrete material but belong to a class of crystalline semiconductors with the formula unit ABX_3, composed of two cations, A and B, and an anion, X. In reality, these ions are not rigidly fixed

within the crystalline lattice. Dynamic crystal defects occur, forming void spaces known as vacancies within the crystal lattice. Ions can occupy these vacancies. The continually changing crystalline structure, caused by ionic migration occurring on a timescale about ten orders of magnitude slower than that of electron and hole motion, significantly impacts the overall device charge behavior and cannot be neglected. In perovskites, the movement of numerous negatively charged anions plays a substantial role in charge transport. Several experimental observations and simulations indicate the occurrence of ionic accumulation near the perovskite interface [29, 141, 224].

Furthermore, the phenomenon of current-voltage (I-V) hysteresis, where different output currents are observed for varying voltage scanning directions, is directly linked to vacancy migration [213, 225]. Despite notable advancements in characterizing vacancy-assisted migration in perovskites, it is still necessary to comprehensively understand its impact on device performance. As a result, it is crucial to gain a deeper understanding of charge transport within perovskite materials through advanced modeling and simulation techniques.

1.1.2. Memristive devices

Energy consumption and, consequently, carbon emissions present a substantial challenge across all sectors of modern IT (information technology) [123]. This challenge extends to traditional computing, from personal computers to supercomputers, managing and analyzing large and complex datasets, and the emerging field of artificial intelligence (AI). Most of today's IT systems rely on digital CMOS (complementary metal-oxide-semiconductor) logic and the von Neumann architecture [199]. Regrettably, the energy efficiency of this type of hardware is insufficient to meet the increasing demands. In particular, the increasing popularity of AI in recent times [60, 198, 238] raises significant concerns about the energy consumption of AI and its damaging impact on the environment [8, 55, 154].

An alternative, more energy-efficient, and sustainable approach to address many AI challenges is using hardware that processes information similarly to biological brains. This approach is known as neuromorphic computing [87, 254]. This innovative hardware architecture can be implemented using memristive devices, often called memristors, as their fundamental building blocks. The term "memristor", a portmanteau of "memory" and "resistor", was initially conceptualized by Chua in 1971 [42]. It took nearly four decades to realize the first prototype in 2008 [228]. Memristors elegantly enable the emulation of synapses and neurons, the fundamental components of biological brains. Their electrical behavior is characterized by hysteresis in the current-voltage characteristics [43]. More precisely, memristors are known for

exhibiting pinched hysteresis loops, as depicted in Figure 1.2 (middle).

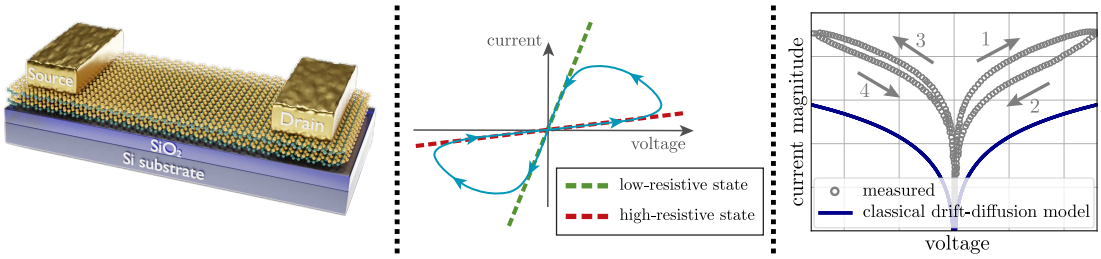

Figure 1.2.: Example of a lateral memristive device architecture comprising two electrodes (source and drain) on top of a two-dimensional memristive material (left), illustration of a pinched I-V hysteresis loop of a memristive device (middle), and comparison of a measured current-voltage characteristics from [150] with simulations based on the classical van Roosbroeck model [204] (right). (Left figure from [DA5] with modifications.)

Memristors based on two-dimensional (2D) layered materials have recently attracted considerable attention [109, 137]. Transition metal dichalcogenides (TMDCs) represent a promising class of layered memristive materials [57, 146, 207, 252]. These materials are characterized by the formula unit AX_2, where A is a transition metal atom and X belongs to the family of chalcogen atoms. In Figure 1.2 (right), a measured curve from [150] shows the classical memristive hysteresis behavior. In contrast, simulation results from the standard drift-diffusion model [204], without additional physical effects, fail to exhibit any hysteresis and underestimate the current-voltage characteristics of the measured curve. Indeed, the origin of experimental hysteresis in these devices and, thus, the physics of TMDC memristors is incompletely understood and continues to be subjects of active debate.

Experimental findings have provided evidence of the accumulation and migration of chalcogen vacancies within TMDC-based memristive devices [177, 206, 258]. Specifically, studies have shown a correlation between the dynamics of charged chalcogen point defects and the observed hysteresis in the current-voltage characteristics [150, 206]. Unlike perovskites, the mechanisms leading to the formation of defects within TMDC crystals and the stable charge states still need to be fully understood. Consequently, there is a lack of physically meaningful charge transport models and simulation tools to investigate the potential vacancy-assisted migration in TMDC memristors adequately.

1.2. Semiconductor modeling and simulation

In summary, perovskite solar cells and TMDC-based memristive devices represent promising semiconductor technologies characterized by hysteresis behavior closely

linked to the migration of vacancies. However, these devices also exhibit other physical effects, such as charged trap states [64, 110, 147, 231], which can impact the overall device charge and, thus, the current-voltage characteristics. Distinguishing between various physical phenomena solely through experimental approaches can be challenging. Moreover, the production of semiconductor devices itself contributes significantly to greenhouse gas emissions [96, 172]. Consequently, the primary objective of this thesis is to provide a comprehensive, physics-based theoretical exploration of vacancy-assisted charge transport in these two devices.

1.2.1. Model hierarchy

Semiconductor device transport modeling aims to understand and predict the behavior of charge carriers within semiconductor materials and devices. When we treat charge carriers as discrete quantities that distribute within a medium, microscopic semi-classical kinetic equations like the Boltzmann transport equation can describe their behavior. The Boltzmann equation is a partial differential equation (PDE) formulated for an individual quantity dependent on a three-dimensional spatial vector and a three-dimensional wave vector (both dependent on time). As the number of quantities we consider grows (e.g., $N = 10^4$ electrons), the number of dimensions $6N$ to solve this coupled set of equations linearly increases. Consequently, kinetic models come with high computational costs in numerical simulations.

However, we often only need specific physical information for certain devices, and simpler models are preferred for computational efficiency. In light of this, macroscopic semi-classical *drift-diffusion models* have been developed to effectively represent the device behavior while accurately preserving the fundamental physics. Indeed, more detailed semi-classical macroscopic models, such as general hydrodynamic models (which account for smaller timescales and temperature dependencies) or energy-transport models (which consider temperature-dependent behavior), also exist, see, e.g., [1, 99, 116, 164, 169]. Since our primary objective is to investigate the influence of vacancy-assisted charge transport, we, consequently, assume negligible temperature variations and timescales that do not need more general models in favor of computational costs.

Thus, this thesis focuses on semi-classical drift-diffusion models, which balance accuracy and computational efficiency. Additionally, the semiconductor structures investigated in this thesis have dimensions where quantum effects can be neglected. When dealing with much smaller device scales, more comprehensive quantum mechanical models (microscopic or macroscopic) instead of semi-classical models must be considered. For further mathematically-focused details on the presented and other model types, we refer to [128].

1.2.2. Overview of existing numerical methods

Drift-diffusion models, being nonlinear PDE systems, often allow for analytical solutions only under simplified conditions. Consequently, extensive literature has been dedicated to the numerical solution of these models. These numerical methods include discretization schemes based on both the finite difference method (FDM) and the finite element method (FEM), see, e.g., [10, 24, 174, 216, 242]. Another alternative, which is as flexible as FEM with respect to the device geometry, but still correctly reflects physical phenomena, is the finite volume method (FVM). These physical phenomena include, for instance, the local conservativity of fluxes and consistency with thermodynamic laws [70, 72]. Therefore, in the context of this thesis, we introduce FVM-based schemes.

Adequately decomposing a multi-dimensional computational domain and correctly discretizing charge carrier current densities is essential to formulate effective FVM schemes. Admissible meshes [70], which meet certain orthogonality constraints, form the basis for large classes of finite volume schemes based on two-point flux approximations (TPFA). For instance, central finite difference flux (suitable for problems governed by diffusion) and upwind flux discretizations (suitable for problems governed by drift) have been thoroughly analyzed, e.g., [19, 37, 38]. Moreover, exponential fitting flux approximations, which have been recently investigated and/or developed (see, e.g., [19, 32, 72, 85, 140, 190]), have been successfully employed in commercial software [46, 223, 233]. Exponential fitting schemes are characterized by numerical stability, thermodynamic consistency, and applicability to general charge carrier statistics [71].

Therefore, this thesis relies on admissible meshes and the excess chemical potential flux scheme as an exponential fitting TPFA. The earliest reference we could find for this discretization scheme is [255] which was later numerically analyzed in [30, 92] and compared in [DA9, 132]. We note that in cases where charge transport models exhibit anisotropies, such as those related to a magnetic field [88], multi-point flux approximations formulated on more general, not necessarily admissible, meshes have been developed and analyzed [63, 69, 84, 191]. Specifically, in [35, 173], hybrid finite volume schemes for drift-diffusion models have been explored mathematically.

1.3. Outline

This thesis is organized as follows.

In **Chapter 2**, we derive general semi-classical macroscopic drift-diffusion equations from Maxwell-Stefan diffusion and electrostatic drift for charge transport in crystalline

semiconductors. Instead of carrier densities, we use quasi Fermi potentials as primary variables, which allows us to easily include nonlinear diffusion for electrons and holes as well as limit the vacancy accumulation. The latter is motivated by a grand canonical formalism for ideal lattice gas. We also examine crystal lattice diffusion processes for perovskites and TMDCs. Lastly, we discuss selected thermodynamic properties such as thermodynamic equilibrium, electroneutrality, as well as the free energy.

In **Chapter 3**, we apply the derived charge transport equations to two physically and societally relevant applications: perovskite solar cells and TMDC-based memristive devices. In order to formulate well-posed initial boundary value problems for these applications, we employ suitable initial and boundary conditions. Additionally, we discuss photogeneration, recombination, and image-charge-induced Schottky barrier lowering. After the non-dimensionalization of both charge transport models, we introduce the concept of entropy methods. This theoretical framework allows us to establish an entropy-dissipation inequality, a tool to study the well-posedness of the equations and the asymptotic behavior of their solution.

Chapter 4 deals with the formulation of numerical schemes for the non-dimensionalized models and their numerical analysis. We introduce the notion of admissible meshes and develop implicit-in-time two-point flux finite volume schemes tailored to vacancy-assisted charge transport in PSCs and TMDC memristors. For both discretizations, we show an entropy-dissipation inequality within the discrete framework. This inequality helps us to prove the existence of a discrete solution of the nonlinear discrete systems with the help of a corollary of Brouwer's fixed point theorem and the minimization of a convex functional.

Chapter 5 complements our theoretical results with numerical experiments. We perform the simulations with `ChargeTransport.jl`, an open source software tool in the programming language Julia, designed explicitly for solving charge transport problems in semiconductors via the Voronoi finite volume method. We validate the finite volume schemes by examining properties, including relative entropy decay, large time behavior, and spatial convergence rate. In addition, we discuss the influence of volume exclusion effects on perovskite charge transport modeling. To achieve this, we compare two different ionic current density descriptions, treating either the mobility or the diffusion coefficient as density-dependent while the other quantity remains constant. Finally, we focus on the phenomenon of hysteresis in TMDC-based memristive devices. We analyze the hysteresis' origin through simulations and compare the results with experimental measurements found in literature.

Chapter 6 summarizes the findings of this thesis and suggests reasonable continuations for future research.

The main parts of the derivation in Chapter 2 are based on [DA4]. Other parts of this chapter can be found in [DA2], [DA3], and [DA5]. In Chapter 3, the work is partially from [DA2], [DA4], and [DA5]. Furthermore, the main results in Chapter 4 are published in [DA2], whereas minor parts are published in [DA4]. Lastly, Chapter 5 is based on [DA2, DA3, DA5]. Detailed information on which sections are published in which reference will be given in the introduction of each chapter.

2. Derivation of vacancy-assisted charge transport equations

Defects in semiconductor crystals can significantly affect the performance and reliability of electronic devices. Although impressive advancements have been made in characterizing defects and their impact on electrical properties [101, 196], this characterization highly depends on the specific semiconductor material. When dealing with novel semiconductors, understanding the impact of vacancies on structural properties, such as the electronic behavior, and, consequently, on the device performance needs to be understood. As previously discussed, emerging materials like perovskites and TMDCs are attractive for future electronic devices. However, accurately predicting and controlling the behavior of devices based on these materials poses a major challenge due to the additional vacancy migration. Therefore, a physically meaningful characterization of such crystal defects and their dynamics is crucial to advance semiconductor technology.

To capture the charge carrier transport in semiconductor devices, semi-classical macroscopic drift-diffusion models are commonly used. This model class provides a computationally efficient approach to describe the average motion of particles, focusing on the overall electronic device behavior, where the interactions at the microscale are not of primary interest. Arguably, this is the most convenient approach with respect to the computational cost while still yielding an interpretable output of the device physics. This output can be compared to experimental measurements, such as I-V characteristics. For this reason, we will exclusively deal with *macroscopic semi-classical drift-diffusion models*. We refer to [116, 128] for further information on different types of models, such as kinetic models, like the Boltzmann equation, or quantum models, such as density functional theory (DFT) models.

On the one hand, there is a well-established mathematical literature concerning drift-diffusion models to describe charge transport in (in)organic semiconductors and similar physical systems, where *electrons and holes* migrate through a device (see for instance [89, 90, 163, 164, 174, 204]). Usually, these models are called *semiconductor device equations* or *van Roosbroeck system* [71]. On the other hand, there is well-established mathematical literature concerning drift-diffusion mathematical models to describe the charge transport in electrolytes, batteries, and ion channels, where *ionic particles*

migrate through a medium, e.g., [25, 62, 85, 133, 143], which are referred to as *(modified) Poisson-Nernst-Planck* equations [180, 192, 193].

Indeed, literature addresses the migration of electrons, holes, and additional ionic carriers in specific oxides. For example, studies are conducted on metal oxide cells (e.g., [3, 160, 161]). Moreover, some investigations have centered around iron oxide and its impact on nuclear waste canisters' corrosion [12, 13, 31], as well as solid oxide cells employing YSZ as the electrolyte material [170, 240]. Nevertheless, these models are primarily tailored to specific applications and may not readily apply to other crystalline semiconductors that support vacancy migration. Thus, this chapter aims to develop suitable drift-diffusion equations describing vacancy-assisted charge transport in novel semiconductor materials, such as perovskites and TMDCs.

We start in Section 2.1 with an introduction and review of the initial and the final equations. In Section 2.2, we derive suitable electric current density descriptions. Then, we formulate carrier concentration and current density descriptions for electrons and holes (Section 2.3) and ionic defect carriers (Section 2.4). To complete the charge transport equations for a crystalline semiconductor layer supporting vacancy migration, we state in Section 2.5 suitable volumetric space charge densities for concrete ionic defect migration scenarios. This chapter ends with Section 2.6, where selected thermodynamic properties are introduced, such as thermodynamic equilibrium and thermodynamic free energy.

This chapter is based in large parts on [DA4]. Parts of the discussion of statistics functions (Section 2.3) were published in [DA2], and parts of the discussion on the limitation of vacancy accumulation and the resulting current density descriptions (Section 2.4) in [DA3]. Minor parts of Section 2.4.1.2 are based on [DA5].

2.1. Starting point and review

This chapter aims to construct charge transport equations incorporating the influence of vacancy dynamics by starting from a general system of nonlinear partial differential equations. This system consists of the Poisson equation for the electrostatic potential as well as the balance equations for the particle densities in an isothermal electrostatic setting. The development of these vacancy-assisted charge transport equations lays the foundation for Chapter 3, where we formulate drift-diffusion models tailored to two real-world applications, providing the necessary initial and boundary conditions.

In the following, we focus solely on an intrinsic subdomain $\mathbf{\Omega}_{\mathrm{intr}}$, as highlighted in Figure 2.1. This subdomain describes the spatial region of a crystalline semiconductor

material within the device where vacancy-assisted migration phenomena occur. For example, in the context of PSCs, we can think of the perovskite layer, while in the context of TMDC memristive devices, $\mathbf{\Omega}_{\text{intr}}$ corresponds to the TMDC layer. The domain $\mathbf{\Omega}_{\text{intr}}$ is a subset of the overall spatial domain $\mathbf{\Omega}$ representing the entire device geometry, i.e., the total solar cell (see Figure 1.1) or the total memristive device (see Figure 1.2, left). In simpler terms, $\mathbf{\Omega}_{\text{intr}} \subseteq \mathbf{\Omega}$, where $\mathbf{\Omega}_{\text{intr}}, \mathbf{\Omega} \subset \mathbb{R}^d$, $d \in \{1, 2, 3\}$.

To derive now suitable bulk equations for vacancy-assisted charge transport in $\mathbf{\Omega}_{\text{intr}}$, we further assume that $\mathbf{\Omega}_{\text{intr}}$ contains charged species α, labeled by a finite index set $\mathbb{A}$. The quantity $n_\alpha(\mathbf{x}, t)$ denotes the particle density associated with the species $\alpha \in \mathbb{A}$ at the location $\mathbf{x} \in \mathbf{\Omega}_{\text{intr}}$ for a time $t \geq 0$. Furthermore, the charge density carried by the species α is given by $z_\alpha q n_\alpha$, where q denotes the positive elementary charge and $z_\alpha \in \mathbb{Z}$ the charge number of the species α.

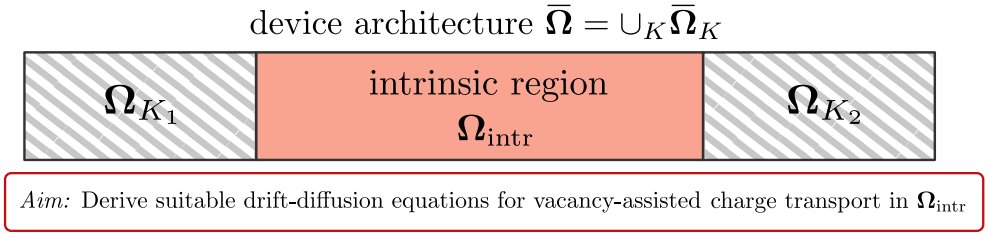

Figure 2.1.: An example illustration of a model device geometry $\mathbf{\Omega}$ with indicated material layer $\mathbf{\Omega}_{\text{intr}}$ supporting vacancy-assisted migration on which we focus in this chapter.

The Poisson equation describes the distribution of electric charge within the material layer $\mathbf{\Omega}_{\text{intr}}$ by relating the electric potential ψ to the overall volumetric space charge density given as the sum of charge densities

$$-\nabla \cdot \Big(\varepsilon_s \nabla \psi(\mathbf{x}, t)\Big) = q\Big(\sum_{\alpha \in \mathbb{A}} z_\alpha n_\alpha(\mathbf{x}, t) + z_{\text{C}} n_{\text{C}}(\mathbf{x})\Big), \quad \mathbf{x} \in \mathbf{\Omega}_{\text{intr}},\ t \geq 0. \tag{2.1a}$$

Here, n_{C} denotes the density of a fixed background charge uniform in time with charge number $z_{\text{C}} \in \mathbb{Z}$. We define $\varepsilon_s = \varepsilon_0 \varepsilon_r$ as the (absolute) dielectric permittivity given as a product of the vacuum permittivity ε_0 and the relative material permittivity ε_r. Additionally, mass balance equations for the particle densities, which are self-consistently coupled to the Poisson equation, are taken into account

$$\partial_t n_\alpha(\mathbf{x}, t) + \nabla \cdot \mathbf{J}_\alpha(\mathbf{x}, t) = r_\alpha(\mathbf{x}, t), \quad \mathbf{x} \in \mathbf{\Omega}_{\text{intr}},\ t \geq 0, \quad \text{for } \alpha \in \mathbb{A}. \tag{2.1b}$$

The particle fluxes are given by $\mathbf{J}_\alpha$ and the density production/reduction rates of species α are denoted by r_α. As a matter of readability, we do not highlight the spatial and temporal dependence of quantities in the following.

In this chapter, we will systematically derive from (2.1) suitable equations describing the charge transport in $\mathbf{\Omega}_{\text{intr}}$. These equations will apply to all mobile carriers $\alpha \in \mathbb{M}$, where $\mathbb{M} \subset \mathbb{A}$ denotes the respective index set. For example, $\mathbb{M}$ may contain the indices of electrons, holes, and vacancies. To provide greater clarity, we will outline the principal findings of the following sections.

- Section 2.2 will show that the *electric currents* $\mathbf{j}_\alpha$ are defined as

$$\mathbf{j}_\alpha = -z_\alpha^2 q \mu_\alpha n_\alpha \nabla \varphi_\alpha, \qquad \alpha \in \mathbb{M}, \tag{2.2}$$

  with the negative gradient of *quasi Fermi potentials* φ_α being the driving force of motion.

- In Section 2.3.1 and Section 2.4.2 we will find out that we can link the carrier densities n_α to the respective quasi Fermi potentials φ_α and the electric potential ψ via the *state equations*

$$n_\alpha = N_\alpha \mathcal{F}_\alpha\Big(\eta_\alpha(\varphi_\alpha, \psi)\Big), \quad \eta_\alpha(\varphi_\alpha, \psi) = z_\alpha \frac{q(\varphi_\alpha - \psi) + E_\alpha}{k_B T}, \quad \alpha \in \mathbb{M}, \tag{2.3}$$

  with $\mathcal{F}_\alpha$ being the underlying *statistics function*.

- In Section 2.3.2 and Section 2.4.3, we will see that the moving carriers satisfy a *generalized Einstein relation* which links the diffusion coefficient D_α and the mobility μ_α

$$D_\alpha = \mu_\alpha U_T g_\alpha\left(\frac{n_\alpha}{N_\alpha}\right), \qquad g_\alpha\left(\frac{n_\alpha}{N_\alpha}\right) = \frac{n_\alpha}{N_\alpha}\left(\mathcal{F}_\alpha^{-1}\right)'\left(\frac{n_\alpha}{N_\alpha}\right), \qquad \alpha \in \mathbb{M}. \tag{2.4}$$

  Here, g_α denotes the *nonlinear diffusion enhancement*. This relation will eventually help to rewrite the electric currents $\mathbf{j}_\alpha$ into a drift-diffusion form.

- Lastly, for each concrete index set $\mathbb{M}$, we must adapt the right-hand side of the Poisson equation (2.1a), which will be done in Section 2.5.

We refer to 'List of notations and physical constants' on page xiii for additional information on the SI (derived) units of each quantity.

2.2. Maxwell-Stefan diffusion and electrostatic drift

We start with adapting (2.1b) and deriving the electric current (2.2). First, we can relate the motion of a species to the friction with another species with the help of

Maxwell-Stefan diffusion and electrostatic drift via

$$\mathbf{F}_\alpha = \sum_{\substack{\beta\in\mathbb{A},\\ \beta\neq\alpha}} \zeta_{\alpha\beta}\left(\frac{\mathbf{J}_\alpha}{n_\alpha} - \frac{\mathbf{J}_\beta}{n_\beta}\right), \qquad \alpha\in\mathbb{A}, \tag{2.5}$$

where $\mathbf{F}_\alpha$ is the main driving force acting on mass transfer and motion of species $\alpha\in\mathbb{A}$ and $\zeta_{\alpha\beta}=\zeta_{\beta\alpha}$ is the symmetric binary friction coefficient between two species α and β, see, e.g., [142, 165, 227, 246]. We call $\mathbf{J}_\alpha/n_\alpha$ the velocities of species α.

Let us assume that one of the species within the semiconductor material layer $\mathbf{\Omega}_{\text{intr}}$ represents the crystalline lattice with index $\alpha=\mathrm{L}$ and charge number $z_\mathrm{L}=0$. Moreover, we assume that the friction is solely observed as an interaction between the lattice and the other species,

$$\zeta_{\alpha\beta}=0 \quad \text{and} \quad \zeta_{\alpha\mathrm{L}}\geq 0\,, \quad \alpha,\beta\in\mathbb{A}\setminus\{\mathrm{L}\}.$$

We describe the transport of a species $\alpha\in\mathbb{A}\setminus\{\mathrm{L}\}$ from the viewpoint of the lattice. In other words, we assume no movement and no production/reduction of lattice species, i.e., $\mathbf{J}_\mathrm{L}=\mathbf{0}$, $r_\mathrm{L}=0$. This implies by (2.1b) that $\partial_t n_\mathrm{L}=0$. Furthermore, we assume that the friction does not cause a deformation of the lattice. Moreover, due to $z_\mathrm{L}=0$ the lattice species density does not contribute to the overall charge density (2.1a).

With this, we can simplify (2.5) and model the particle fluxes by

$$\mathbf{J}_\alpha = \frac{1}{\zeta_{\alpha\mathrm{L}}} n_\alpha \mathbf{F}_\alpha, \quad \alpha\in\mathbb{A}\setminus\{\mathrm{L}\}. \tag{2.6}$$

Next, we discuss the choices of the friction coefficient $\zeta_{\alpha\mathrm{L}}$ and the driving force $\mathbf{F}_\alpha$, entering the particle flux $\mathbf{J}_\alpha$. In analogy to classical semiconductor theory, we define the following relation between the *quasi Fermi potential* φ_α, the chemical χ_α and the electrostatic potential ψ (see e.g. [11, 15])

$$\varphi_\alpha = \frac{\chi_\alpha}{z_\alpha q} + \psi - \frac{E_\alpha}{q}, \qquad \alpha\in\mathbb{A}\setminus\{\mathrm{L}\}, \tag{2.7}$$

where we introduced a species-dependent intrinsic energy level E_α with $\nabla E_\alpha=\mathbf{0}$. We assume that the force $\mathbf{F}_\alpha$ depends on the negative gradient of the chemical potential χ_α (per particle) as well as on the electrical field $-\nabla\psi$ for $\alpha\in\mathbb{A}\setminus\{\mathrm{L}\}$

$$\mathbf{F}_\alpha = -\nabla\chi_\alpha - z_\alpha q\nabla\psi = -\nabla\left(\chi_\alpha + z_\alpha q\psi - z_\alpha E_\alpha\right) = -z_\alpha q\nabla\varphi_\alpha, \tag{2.8}$$

where we inserted (2.7). In electrochemistry, $z_\alpha q\varphi_\alpha$ is frequently called electrochemical potential [11, 15], and, in solid state physics, the quantity $z_\alpha q\varphi_\alpha$ is often called (total)

chemical potential. Contrarily, χ_α is sometimes referred to as (internal) chemical potential [136, 189]. In this thesis, we use the terminology quasi Fermi potential for φ_α and electrochemical potential for $z_\alpha q\varphi_\alpha$. Furthermore, we set the friction coefficient to

$$\zeta_{\alpha\mathrm{L}} = \frac{q}{\mu_\alpha}, \quad \alpha \in \mathbb{A} \setminus \{\mathrm{L}\}, \tag{2.9}$$

where μ_α describes the mobility of species α. Substituting now (2.8) and (2.9) into (2.6) shows that the negative gradient of the electrochemical potential is the driving force of the particle current density

$$\mathbf{J}_\alpha = -z_\alpha \mu_\alpha n_\alpha \nabla\varphi_\alpha, \quad \alpha \in \mathbb{A} \setminus \{\mathrm{L}\}. \tag{2.10}$$

Remark 2.1. (Friction coefficient in the literature) The friction coefficient can be related to the inverse of the (Maxwell-Stefan) diffusion coefficient $Đ_{\alpha\mathrm{L}}$ (see e.g. [142, 201, 246])

$$\zeta_{\alpha\mathrm{L}} = \frac{k_B T}{Đ_{\alpha\mathrm{L}}}, \tag{2.11}$$

where k_B is the Boltzmann constant and T the temperature. It is worth noting that with the definition of the friction coefficient (2.9) and the relation (2.11) we recover the classical Einstein relation $Đ_{\alpha\mathrm{L}} = \frac{k_B T}{q}\mu_\alpha$ between diffusion coefficient and mobility of a species α. In the following of this work, we use the notation $D_\alpha := Đ_{\alpha\mathrm{L}}$ and refer to D_α as diffusion coefficient.

The *electric current density* (sometimes also referred to as *electric flux*) $\mathbf{j}_\alpha$ observed due to the transport of species α is related to the particle flux $\mathbf{J}_\alpha$ by

$$\mathbf{j}_\alpha = z_\alpha q \mathbf{J}_\alpha, \quad \alpha \in \mathbb{A} \setminus \{\mathrm{L}\}. \tag{2.12}$$

Using the description of the particle flux (2.10) yields

$$\mathbf{j}_\alpha = -z_\alpha^2 q \mu_\alpha n_\alpha \nabla\varphi_\alpha, \quad \alpha \in \mathbb{A} \setminus \{\mathrm{L}\}. \tag{2.13}$$

Thus, we have successfully established the desired electric current density description (2.2) for $\alpha \in \mathbb{M} = \mathbb{A} \setminus \{\mathrm{L}\}$. For such an electric flux the drift-diffusion equation now finally reads

$$z_\alpha q \partial_t n_\alpha + \nabla \cdot \mathbf{j}_\alpha = z_\alpha q r_\alpha \ , \quad \alpha \in \mathbb{A} \setminus \{\mathrm{L}\}, \tag{2.14}$$

where we multiplied (2.1b) by $z_\alpha q$. We emphasize that the carrier density n_α entering (2.13) and (2.14) can be rewritten in terms of the quasi Fermi potential φ_α and the electrostatic potential ψ as indicated in the state equation (2.3), which will be addressed in the next two sections.

2.3. Electron and hole concentration and current density

Following [101, 216, 235], we relate the carrier density n_α to the electrostatic potential ψ and the respective quasi Fermi potential φ_α for electrons $\alpha = \mathrm{n}$ and holes $\alpha = \mathrm{p}$ as species $\alpha \in \mathbb{A}$ in accordance with the state equation (2.3). Additionally, we discuss the implications of different choices for the *statistics function* $\mathcal{F}_\alpha$ entering the state equation, and we equivalently reformulate the current density (2.13) in drift-diffusion form. The charge numbers for electrons and holes are $z_\mathrm{n} = -1$ and $z_\mathrm{p} = 1$, respectively.

2.3.1. Carrier concentration

The carrier densities of electrons and holes can be defined as a convolution integral of the densities of (electronic) states $DOS_\mathrm{n}, DOS_\mathrm{p}$ in the conduction and valence band and the particle occupation probabilities of an orbital $f_\mathrm{n}, f_\mathrm{p}$ over the energy space

$$n_\mathrm{n} = \int_{E_\mathrm{n}}^{\infty} DOS_\mathrm{n}(E) f_\mathrm{n}\left(\frac{E - z_\mathrm{n} q(\varphi_\mathrm{n} - \psi)}{k_B T}\right) \mathrm{d}E, \tag{2.15a}$$

$$n_\mathrm{p} = \int_{-\infty}^{E_\mathrm{p}} DOS_\mathrm{p}(E) f_\mathrm{p}\left(\frac{E + z_\mathrm{p} q(\varphi_\mathrm{p} - \psi)}{k_B T}\right) \mathrm{d}E. \tag{2.15b}$$

We call $E_\mathrm{n}, E_\mathrm{p}$ the intrinsic conduction and valence band-edge energies. For non-interacting, identical fermions with half-integer spin (ideal Fermi gas model [58, 78, 136]), we can choose the Fermi-Dirac distribution

$$f_\mathrm{n}(x) = \frac{1}{\exp(x) + 1}, \quad f_\mathrm{p}(x) = 1 - f_\mathrm{n}(x) = \frac{1}{\exp(-x) + 1}, \quad x \in \mathbb{R}. \tag{2.16}$$

This choice of occupation probability is fundamental in the modeling and simulation of inorganic three-dimensional semiconductors [71, 216, 235]. The densities of states $DOS_\mathrm{n}, DOS_\mathrm{p}$ in (2.15) can be calculated explicitly for different dimensions and assumptions on the electronic band structure. In case of a parabolic band approximation [209], the three-dimensional densities of states read

$$DOS_\mathrm{n}(E) = \frac{1}{2\pi^2}\left(\frac{2m_\mathrm{n}^*}{\hbar^2}\right)^{3/2} \Theta(E - E_\mathrm{n})\sqrt{E - E_\mathrm{n}}, \tag{2.17a}$$

$$DOS_\mathrm{p}(E) = \frac{1}{2\pi^2}\left(\frac{2m_\mathrm{p}^*}{\hbar^2}\right)^{3/2} \Theta(E_\mathrm{p} - E)\sqrt{E_\mathrm{p} - E}, \tag{2.17b}$$

with the effective masses m_n^* and m_p^* of electrons and holes, the reduced Planck constant $\hbar$ and the Heaviside step function $\Theta(x) = \mathbf{1}_{\{x \geq 0\}}$.

Substituting (2.16) and (2.17) into (2.15) and setting $\xi = E/(k_BT)$ shows

$$n_\mathrm{n} = N_\mathrm{n} F_{1/2}(\eta_\mathrm{n}), \quad \eta_\mathrm{n} = z_\mathrm{n} \frac{q(\varphi_\mathrm{n} - \psi) + E_\mathrm{n}}{k_BT}, \tag{2.18a}$$

$$n_\mathrm{p} = N_\mathrm{p} F_{1/2}(\eta_\mathrm{p}), \quad \eta_\mathrm{p} = z_\mathrm{p} \frac{q(\varphi_\mathrm{p} - \psi) + E_\mathrm{p}}{k_BT}, \tag{2.18b}$$

where $N_\mathrm{n}, N_\mathrm{p}$ are the effective densities of states

$$N_\mathrm{n} = 2 \cdot \left(\frac{m_\mathrm{n}^* k_BT}{2\pi\hbar^2} \right)^{3/2} \quad \text{and} \quad N_\mathrm{p} = 2 \cdot \left(\frac{m_\mathrm{p}^* k_BT}{2\pi\hbar^2} \right)^{3/2}. \tag{2.19}$$

Since $\chi_\alpha = z_\alpha q(\varphi_\alpha - \psi) + z_\alpha E_\alpha = k_BT\eta_\alpha$, we call the argument of the statistics function η_α *dimensionless chemical potential*. Moreover,

$$F_{1/2}(\eta) = \frac{2}{\sqrt{\pi}} \int_0^\infty \frac{\xi^{1/2}}{\exp(\xi - \eta) + 1} \, \mathrm{d}\xi, \quad \eta \in \mathbb{R}, \tag{2.20}$$

is the Fermi-Dirac integral of order $1/2$. The function $F_{1/2}$ behaves like $\eta^{3/2}$ when the dimensionless chemical potential η tends to $+\infty$, namely, in the large density limit (also called degenerate limit). In the low density limit (non-degenerate limit), when the dimensionless chemical potential η tends to $-\infty$, it behaves like

$$F(\eta) = \exp(\eta), \quad \eta \in \mathbb{R}, \tag{2.21}$$

which is called (Maxwell-)Boltzmann statistics. Choosing the Boltzmann distribution $f_\mathrm{n}(x) = 1/\exp(x)$, $x \in \mathbb{R}$, in (2.15) instead of the Fermi-Dirac distribution (2.16), yields (2.18) with the Boltzmann statistics (2.21). This is equivalent to the assumption of a (classical) ideal gas model [189].

Another useful approximation of (2.20) for a certain region of parameters in the non-degenerate limit is the Blakemore approximation [22, 71]

$$F_{B,\gamma}(\eta) = \frac{1}{\exp(-\eta) + \gamma}, \quad \eta \in \mathbb{R}, \quad \gamma \in \mathbb{R}, \tag{2.22}$$

with $\gamma = 0.27$. Due to [DA4, Remark 1.7.1.] we point out that the Blakemore approximation for $\gamma = 1$ coincides with the Fermi-Dirac integral of order -1, i.e., $F_{-1} = F_{B,1}$. For this reason, we refer to

$$F_{-1}(\eta) = \frac{1}{\exp(-\eta) + 1}, \quad \eta \in \mathbb{R}, \tag{2.23}$$

as Fermi-Dirac integral of order -1, which will play an important role. All the functions stated are visualized in Figure 2.2 (left).

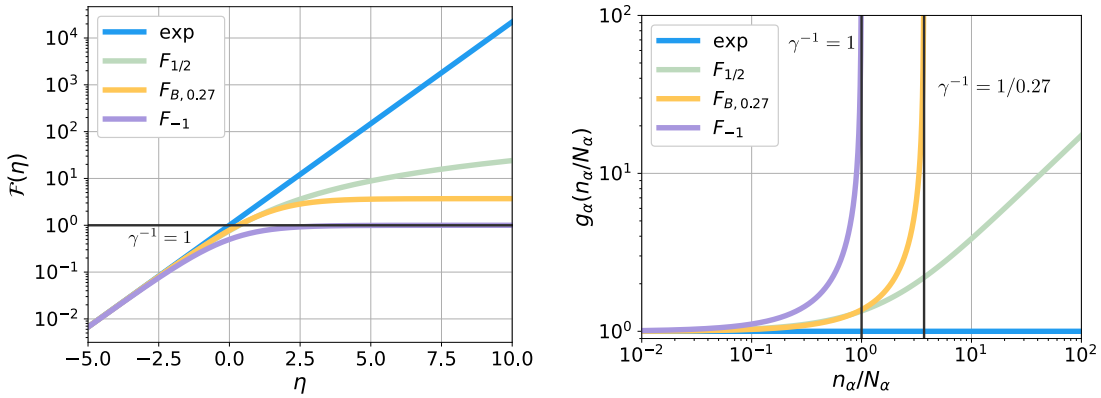

Figure 2.2.: Semi-logarithmic plot of the introduced statistics functions $\mathcal{F}_\alpha$ for $-5 \leq \eta \leq 10$ (left) and logarithmic plot of the diffusion enhancement g_α for the statistics functions in the left figure, where we used (2.27) (right). The carrier density (2.24) can be limited by the Fermi-Dirac integral of order -1 which agrees with the Blakemore function ($\gamma = 1$).

In the following of this thesis, we generalize the state equations (2.18) to

$$n_\alpha = N_\alpha \mathcal{F}_\alpha\Big(\eta_\alpha(\varphi_\alpha, \psi)\Big), \quad \eta_\alpha(\varphi_\alpha, \psi) = z_\alpha \frac{q(\varphi_\alpha - \psi) + E_\alpha}{k_B T}, \quad \alpha = \mathrm{n}, \mathrm{p}, \tag{2.24}$$

where $\mathcal{F}_\mathrm{n}, \mathcal{F}_\mathrm{p}$ are now general statistics functions, which satisfy the hypothesis

$$\begin{cases} \mathcal{F}_\mathrm{n}, \mathcal{F}_\mathrm{p} : \mathbb{R} \to (0, \infty) \text{ are } C^1\text{- diffeomorphisms;} \\ 0 < \mathcal{F}'_\alpha(\eta) \leq \mathcal{F}_\alpha(\eta) \leq \exp(\eta), \quad \eta \in \mathbb{R},\ \alpha \in \{\mathrm{n}, \mathrm{p}\}, \end{cases} \tag{H1}$$

if not mentioned otherwise. With (2.24), we have successfully attained our objective of establishing a generalized relation between the carrier density and the potentials (2.3) for electrons and holes.

The positivity of the statistics functions due to (H1) reflects the positivity of the densities n_α. The Fermi-Dirac integral of order $1/2$ in (2.20) and the Boltzmann approximation (2.21) satisfy the hypothesis (H1). In case of $\mathrm{im}(F_{B,\gamma}) = (0, \gamma^{-1})$, the Blakemore approximation (2.22) also satisfies (H1). The proofs can be found in Appendix A.1. In case of organic semiconductors, the state equation (2.24) also holds true resulting in a statistics function $\mathcal{F}_\alpha$ which is referred to as Gauss-Fermi integral [186] and with different effective densities of states $N_\mathrm{n}, N_\mathrm{p}$. For further information, we refer to [72] and the references therein.

Remark 2.2. Since various definitions of band-edge energies can be found in literature, we give an overview of how the different terminologies are related. We refer, for example,

to [101, 216, 235] for additional information. In case of not necessarily well-defined band structures (e.g., organic semiconductors) the lowest unoccupied (LUMO) E_{LUMO} and the highest occupied molecular orbital (HOMO) edge level E_{HOMO} are used, respectively, instead of the intrinsic conduction and valence band-edge energies [45, 82]. Some references also introduce the electron affinity ϕ_{ea} and the ionization potential ϕ_{ip}, e.g., [82, 181, 249]. However, mathematically all these energies play identical roles. Thus, we assume in this thesis $E_{\mathrm{n}} = E_{\mathrm{LUMO}} = -\phi_{\mathrm{ea}}$ and $E_{\mathrm{p}} = E_{\mathrm{HOMO}} = -\phi_{\mathrm{ip}}$. Lastly, sometimes the state equation (2.24) is formulated with respect to the band-edge (energy) of electrons and holes which is defined as the sum of the intrinsic band-edge energy E_α and the electric potential energy ϕ

$$\mathscr{E}_\alpha = E_\alpha + \phi, \quad \phi = -q\psi, \quad \alpha \in \{\mathrm{n}, \mathrm{p}\}. \tag{2.25}$$

2.3.2. Drift-diffusion current density

In the literature, carrier densities are usually used as primary unknowns. To see the connection to the literature, we express the electric fluxes in gradient structure form (2.13) mathematically equivalent in terms of densities. For this, we introduce the *nonlinear diffusion enhancement* [167] for electrons and holes given by

$$g_\alpha(\eta_\alpha) = \frac{\mathcal{F}_\alpha(\eta_\alpha)}{\mathcal{F}_\alpha{}'(\eta_\alpha)}, \quad \eta \in \mathbb{R}, \quad \alpha \in \{\mathrm{n}, \mathrm{p}\}. \tag{2.26}$$

For the choice of Boltzmann statistics (2.21), the diffusion enhancement reduces to $g_\alpha = 1$ and in the case of Blakemore approximation (2.22), we have $g_\alpha(\eta) = 1+\gamma\exp(\eta)$. Generally, due to (H1), it holds that $g_\alpha \geq 1$. Thus, the diffusion enhancement can be seen as a measure of how far a model is from the non-degenerate case [72]. We stress that the diffusion enhancement g_α in (2.26) can be equivalently formulated in terms of densities as shown in (2.27). For different statistics functions $\mathcal{F}_\alpha$ the expression for g_α in (2.27) is portrayed in Figure 2.2 (right). With the help of the diffusion enhancement we can formulate now a generalized Einstein relation [101] (see the outline in (2.4))

$$D_\alpha = \mu_\alpha U_T g_\alpha\left(\frac{n_\alpha}{N_\alpha}\right), \quad g_\alpha\left(\frac{n_\alpha}{N_\alpha}\right) = \frac{n_\alpha}{N_\alpha}\left(\mathcal{F}_\alpha^{-1}\right)'\left(\frac{n_\alpha}{N_\alpha}\right), \quad \alpha \in \{\mathrm{n}, \mathrm{p}\}, \tag{2.27}$$

which relates the carriers' mobility introduced in (2.9) to the respective diffusion coefficient D_α. Here, $U_T = k_B T/q$ is the thermal voltage. Finally, it is now possible to express the electric currents (2.13) in drift-diffusion form due to the relation (2.27) and the state equation (2.24)

$$\mathbf{j}_\alpha = -z_\alpha q\Big(D_\alpha\left(\frac{n_\alpha}{N_\alpha}\right)\nabla n_\alpha + z_\alpha \mu_\alpha n_\alpha \nabla\psi\Big), \quad \alpha \in \{\mathrm{n}, \mathrm{p}\}. \tag{2.28}$$

From (2.28), it becomes evident that the motion exhibits a drift-diffusion character. The first term corresponds to diffusion, which arises due to variations in the carrier density. Contrarily, the second term corresponds to the drift caused by the presence of the electric field $-\nabla\psi$. For electrons and holes, mathematically, choosing the Boltzmann approximation (2.21) as statistics functions yields linear diffusion. Statistics functions deviating from the Boltzmann approximation lead to nonlinear diffusion which grows for larger densities or dimensionless chemical potentials as can be seen from (2.26) and (2.27) or visually in Figure 2.2 (right). This means, we can interpret the generalized Einstein relation for electrons and holes (2.27) as a nonlinear, density-dependent diffusion [72, 101].

2.4. Vacancy carrier concentration and current density

As mentioned in the introduction, all materials contain structural defects that affect their electronic properties [101, 196]. Particularly in the case of perovskite-based solar cells (e.g., [29, 202, 213, 225]) and TMDC-based memristive devices (e.g., [150, 206]) the hysteretic behavior is linked to vacancy migration on the crystal lattice. We begin by reviewing the literature on perovskites and transition metal dichalcogenides and making some basic assumptions about defects occurring in their crystal structures. This will allow us to derive a description for the ionic defect carrier concentrations from a grand canonical formalism for ideal lattice gas, correctly reflecting the limitation of vacancy accumulation. Finally, we can formulate suitable defect current densities.

In the following, $\mathbb{P}$ is the index set of all unit particles (atomic or ionic) for a given crystalline semiconductor, whereas $\mathbb{P}_\mathrm{V}$ denotes the index set of respective vacancies/defects.

2.4.1. Examples of crystal structures

2.4.1.1. Perovskites

Perovskites have the formula unit ABX_3, where in the context of perovskite solar cells A and B denote positively charged cations and X denotes a negatively charged anion. Several choices for the anions and cations are possible [213]:

- the cation A is chosen to be an organic ion such as methylammonium (MA^+) or formamidinium (FA^+),
- the other cation B is a metal, frequently B = Pb^{2+} (lead) or B = Sn^{2+} (tin),

- the halide anion X is commonly chosen to be either I^- (iodine), Br^- (bromine), or Cl^- (chlorine).

The most commonly used combination is methylammonium ($A = (CH_3NH_3)^+ = MA^+$), lead ($B = Pb^{2+}$), and iodine ($X = I^-$), resulting into methylammonium lead (tri-)iodide (MAPI). As perovskites have a highly ordered crystal structure, a variety of A, B, and X site compositions are possible. In fact, mixing different ions for the anion and cation sites seems to be the most promising method for developing efficient solar cells based on perovskites [5, 213].

Not all perovskite structures exhibit the same degree of ionic movement. However, ion migration is most likely caused by Schottky defects [65, 244], which can be described by the Kröger-Vink notation, namely,

$$\underbrace{\mathrm{nil}}_{\text{ideal unit cell}} \longrightarrow \underbrace{\underbrace{\mathrm{V_A^{'}} + \mathrm{V_B^{''}} + 3\,\mathrm{V_X^{\bullet}}}_{\text{vacancies}} + \underbrace{\mathrm{ABX_3}}_{\substack{\text{perturbed/realistic}\\ \text{unit cell}}}}_{\text{Schottky defect}} \tag{2.29}$$

Here, nil denotes the ideal perovskite crystalline unit cell. However, in reality, the ions dislocate from their ideal positions, forming vacancies V_α in the ideal lattice, where $\alpha \in \mathbb{P} = \{A, B, X\}$. The superscript $'$ denotes a negative charge and the superscript $^\bullet$ denotes a positive charge. We make some assumptions for these dynamically appearing and reappearing crystal defects which leave void spaces within the crystal:

1. Each Schottky defect creates oppositely charged vacancies $V_A^{'}$, $V_B^{''}$ and $3V_X^{\bullet}$.
2. Each vacancy V_α can be only occupied by an ionic species $\alpha \in \mathbb{P} = \{A, B, X\}$.

Changes in the crystalline structure affect the electronic properties of the underlying device. Figure 2.3 visualizes the crystal configuration for an ideal unit cell and in the case of present vacancies. The quantity β_α in Figure 2.3 denotes an *ideal lattice weight*. The parameter β_α can be determined by counting the number of α-sites in each ideal unit cell, respecting shared faces and edges with neighboring unit cells. Generally, we assume $\beta_{V_\alpha} = \beta_\alpha$.

There are a number of modeling approaches [28, 77, 182, 200], where mobile A and X ions are taken into account. In [65], it was reported that the hopping of $X = I^-$ appears to have the lowest energy barrier for $ABX_3 = (CH_3NH_3)^+Pb^{2+}I_3^-$. Therefore, it is reasonable to assume that both cations A and B are immobile on short timescales [49]. Additionally, simulations on MAPI indicate that assuming either only mobile anions or mobile anions and mobile cations produces the same results [182]. Hence, in some applications, it is convenient to consider a charge transport model, in which only the

anion species X is considered to be mobile. This is done, e.g., in [29, 48]. Furthermore, there is a discrepancy in the literature on whether to formulate the equations for mobile ions (e.g., [28, 77, 182, 200]) or mobile ion vacancies (e.g., [44, 48]). Both ways are equivalent. Nonetheless, Section 2.4.2 will demonstrate why it is more appropriate to formulate the charge transport based on vacancy-assisted migration.

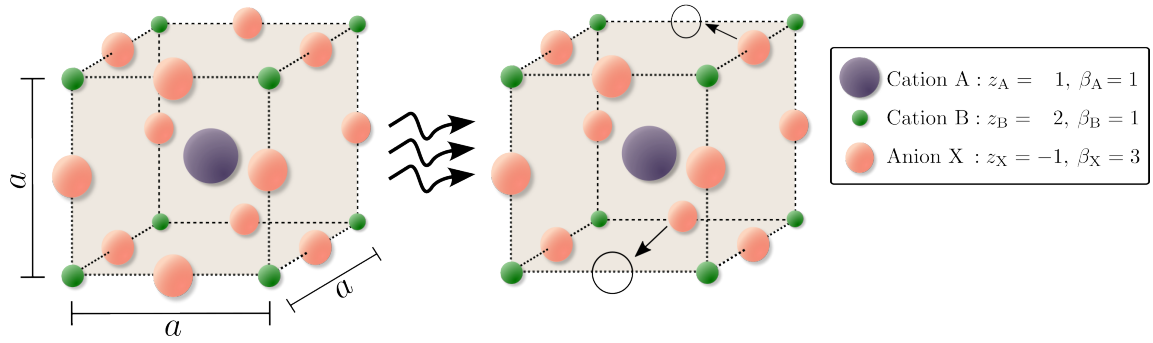

Figure 2.3.: A cubic perovskite unit cell under idealized conditions (left) and with realistic crystal defects (right) with the corresponding charge numbers z_α and the ideal dimensionless lattice weights β_α, for $\alpha \in \mathbb{P}$. The lattice constant a is also shown. (From [DA3] with modifications.)

2.4.1.2. Transition metal dichalcogenides

Transition metal dichalcogenides represent a promising class of layered materials. Usually, in the context of memristive devices, they have thicknesses of only a few nanometers. In such devices, the length and width are typically on the order of a few micrometers and, thus, much larger than the thickness, see e.g., [39, 41, 112, 121, 134, 152]. Therefore, these atomic-layered crystal structures are often referred to as two-dimensional materials. The formula unit is AX_2 given by an A-atom layer sandwiched between two X-atom layers, where the following choices are possible [109]:

- A is a transition metal atom such as molybdenum (Mo) or tungsten (W),
- X belongs to the family of chalcogen atoms such as sulfur (S) or selenium (Se).

Molybdenum disulfide ($AX_2 = MoS_2$) along with its electronic properties is among the most extensively researched TMDC materials [260]. Figure 2.4 illustrates different idealized schematics of a two-hexagonal (2H) MoS_2 monolayers. For TMDCs, the lattice weights β_α depend on the number of monolayers within one unit cell and the type of crystal structure. In case of 2H MoS_2, as depicted in Figure 2.4, we have $\beta_A = 2$ and $\beta_X = 4$.

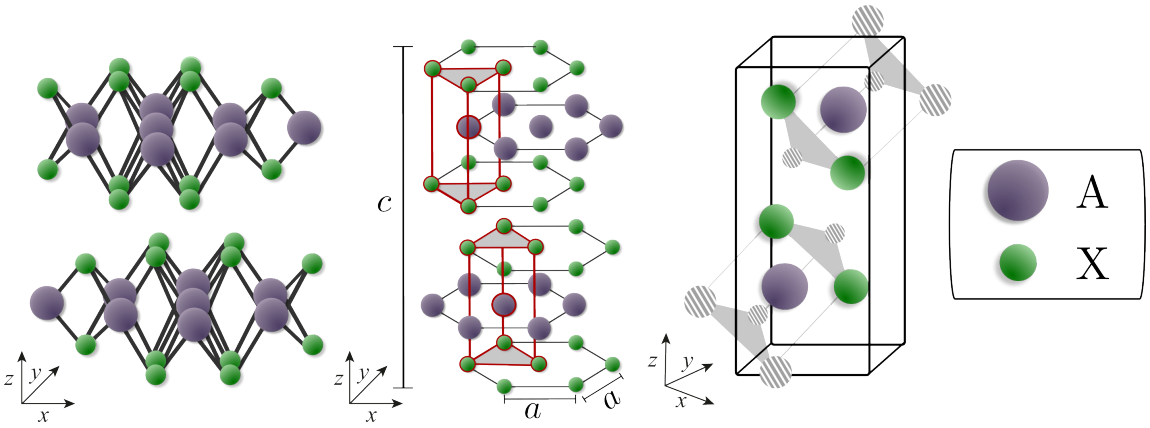

Figure 2.4.: Different idealized representations of two MoS_2 monolayers arranged in a hexagonal lattice structure [120, 215]. The figure includes a three-dimensional representation of the two monolayers (left), a schematic of the hexagonal lattice structure with indicated trigonal prismatic covalent bond (middle), and a view of a single unit cell (right). The lattice constants a and c are likewise indicated.

Experimental work suggests that sulfur vacancies in MoS_2 can migrate [177, 206, 258]. Specifically, studies have shown a correlation between the drift of charged sulfur point defects and the observed hysteresis in the current-voltage characteristics [150, 206]. In contrast to perovskites, the mechanisms that lead to the formation of defects within TMDC crystals and their stable charge states are not fully understood yet. However, it is expected that when present in high concentrations, such defects V_X will act as n-type dopants [212, 219, 253], i.e., $z_{V_X} \in \mathbb{N}$. As before, we formulate the following general assumptions on defects in TMDC for the unit particle index set $\mathbb{P} = \{A, X\}$:

1. Each defect V_α has a charge number $z_{V_\alpha} \in \mathbb{Z}$, where $\alpha \in \mathbb{P} = \{A, X\}$.
2. Each defect V_α can be only occupied by a unit particle $\alpha \in \mathbb{P}$.

2.4.2. Limiting vacancy accumulation

In order to understand now why and under which assumptions the physical meaningful statistical relationship (2.3) holds for vacancies, we need to discuss how to limit vacancy accumulation. Accumulating too many vacancies is physically unrealistic as it can destroy the crystal structure and lead to unrealistically high vacancy concentrations.

In the fields of electrolytes and battery modeling (e.g., [15, 23, 85, 144, 230]) or cell and molecular biology (e.g., [25, 26, 108, 187, 248]), the need to limit ionic (defect) concentrations is already well known. Depending on the literature this phenomenon is either called *volume exclusion effects*, *excluded-volume effects*, *steric effects*, *volume*

filling or *limitation of overcrowding*. Within our framework this means that the finite number of available lattice sites within a crystalline semiconductor needs to be incorporated into the charge transport model. This can be achieved by either limiting the vacancy accumulation of V_α or the depletion of a unit particle $\alpha \in \mathbb{P}$. To be more precise, assuming imperfections in the unit cell, we can relate the (realistic) unit particle density n_α and the corresponding (ionic) vacancy density n_{V_α} via

$$n_\alpha = \overline{n}_\alpha - n_{\mathrm{V}_\alpha}, \quad \alpha \in \mathbb{P}, \tag{2.30}$$

where $\overline{n}_\alpha$ is the ideal unit particle density which can be linked to the ideal lattice density $\overline{n}_\mathrm{L}$

$$\beta_\alpha \overline{n}_\mathrm{L} = \overline{n}_\alpha, \quad \alpha \in \mathbb{P}, \tag{2.31}$$

with the lattice weights β_α discussed in Section 2.4.1. The relationship (2.31) becomes apparent, when considering that

$$\overline{n}_L = \frac{\#(\text{unit cells})}{\text{volume of material}} = \frac{1}{\text{volume of unit cell}},$$

since the ideal lattice density $\overline{n}_\mathrm{L}$ is constant and, thus, $\overline{n}_\alpha = \text{const}$. This means, the equality (2.30) reveals the equivalence between either limiting the unit particle depletion or limiting the vacancy accumulation in a unit cell. We focus on the latter and model thermodynamically consistently the limitation of vacancy accumulation. We note that, if the vacancy concentration becomes zero, i.e., $n_{\mathrm{V}_\alpha} = 0\ \mathrm{m}^{-3}$, then (2.30) yields $n_\alpha = \overline{n}_\alpha$ for $\alpha \in \mathbb{P}$ and all vacancies in a unit cell are occupied. Hence, in the following, we exclusively discuss the more interesting case, the presence of defects in the crystal structure, i.e., $n_{\mathrm{V}_\alpha} > 0\ \mathrm{m}^{-3}$.

We assume the existence of a non-zero and uniform average vacancy concentration C_{V_α} and a temperature-dependent, upper saturation density for the vacancy concentration denoted with $N_{\mathrm{V}_\alpha} = N_{\mathrm{V}_\alpha}(T)$. The latter indicates that we cannot arbitrarily create new vacancies. We have $0\ \mathrm{m}^{-3} < n_{\mathrm{V}_\alpha} < N_{\mathrm{V}_\alpha}$. For the saturation density N_{V_α} we have the following bounds:

1. As a lower bound for the saturation density, we have $C_{\mathrm{V}_\alpha} \leq N_{\mathrm{V}_\alpha}$. In the case of equality, vacancy movement is suppressed.
2. As an upper bound, we have $N_{\mathrm{V}_\alpha} \leq \beta_\alpha \overline{n}_\mathrm{L} = \overline{n}_\alpha$ which means that the ideal unit particle density bounds the saturation limit.

As an example, in case of MAPI as perovskite material, we have an average vacancy concentration C_{V_α} in the range of $1.0 \times 10^{23} - 1.6 \times 10^{25}\ \mathrm{m}^{-3}$, see [202]. Furthermore,

DFT calculations [65] provide the lattice constant of 6.28 Å$= 6.28 \times 10^{-10}$ m, leading to an ideal halide density of $\overline{n}_{\mathrm{X}} = 1.21 \times 10^{28}$ m^{-3}. As a result, approximately one vacancy can be found in every 1.0×10^3 to 1.0×10^5 unit cell. Figure 2.5 visualizes the vacancy density n_{V_α} for different choices of the saturation limit N_{V_α}, including the two special cases of suppressing vacancy movement (left) or choosing the saturation limit equal to the ideal unit particle density (right). Experimentally observed accumulation of vacancies may be reproduced for a saturation limit N_{V_α} between these two saturation limit bounds. Hence, we can identify N_{V_α} as a model parameter limiting the vacancy accumulation.

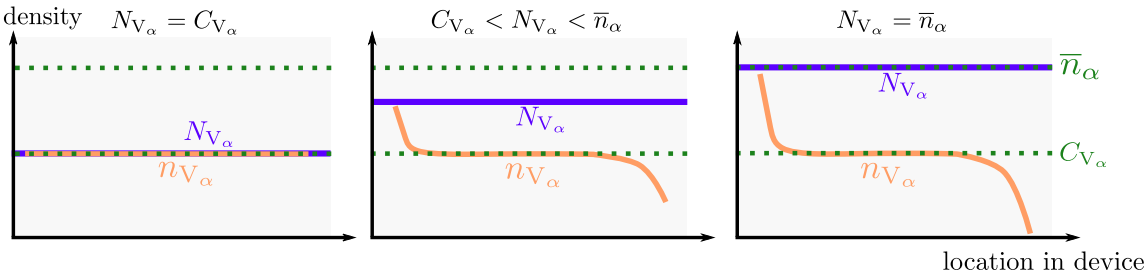

Figure 2.5.: Three possible vacancy density configurations depending on the choice of the saturation limit N_{V_α}. The left and right figures visualize the case, where N_{V_α} agrees with its lower or upper bound, respectively. The value of the maximum vacancy density N_{V_α} can be chosen to ensure that, e.g., experimentally observed accumulation is correctly limited (middle). (From [DA3] with modifications.)

Not limiting the vacancy density can lead to non-physical behavior, such as all ion sites becoming vacant. Especially in out-of-equilibrium calculations, a model needs to indicate a limit for saturation to reflect experimental observations of ionic accumulation near the interface. Indeed, in the context of solid oxide cells with YSZ as electrolyte material, a similar model was formulated for mobile ionic carriers, where a saturation limit $N_{\mathrm{V}_\alpha} < \overline{n}_\alpha$ was successfully fitted to measurements [170]. In the numerical simulations in Chapter 5, we will analyze how varying N_{V_α} influences the behavior of charge transport within perovskite solar cells.

In the following, we will include volume exclusion effects in a thermodynamically consistent manner while accounting for the limitation of vacancy accumulation. These features shall be reflected by a suitable statistical relationship between the vacancy density n_{V_α} and the quasi Fermi and electric potential $\varphi_{\mathrm{V}_\alpha}$, ψ, respectively, for a unit particle $\alpha \in \mathbb{P}$. The derived state equation for vacancies will mirror the one previously established for electrons and holes in (2.24), and its derivation is based on a grand canonical formalism.

Grand canonical formalism for ideal lattice gas. We use the grand canonical ensemble to analyze the behavior of interacting particle systems [6]. In the following, we let $\alpha \in \mathbb{P}_\mathrm{V}$, i.e., the index α refers to the vacancies and, e.g., n_α to the vacancy density. Our specific ensemble, called Ξ, includes the electrochemical potential $z_\alpha q\varphi_\alpha$, a volume of the semiconductor material $\mathbf{\Omega}_\mathrm{vol} \subset \mathbf{\Omega}_\mathrm{intr}$ and a temperature T, i.e., $\Xi = (z_\alpha q\varphi_\alpha, \mathbf{\Omega}_\mathrm{vol}, T)$. We assume that $n_\alpha|\mathbf{\Omega}_\mathrm{vol}|$ vacancies exist in $\mathbf{\Omega}_\mathrm{vol}$. For the sake of simplicity, we further assume no interaction with any of the other species vacancy $\beta \in \mathbb{P}_\mathrm{V} \setminus \{\alpha\}$. The upper bound for the number of the vacancies in the volume $\mathbf{\Omega}_\mathrm{vol}$ is $N_\alpha|\mathbf{\Omega}_\mathrm{vol}|$. Generally, the *grand (canonical) partition function* [14, 189, 232] is given as a sum over all microstates of the ensemble

$$\mathcal{Z}(\Xi, \mathscr{E}_\alpha) = \sum_{(n_\alpha|\mathbf{\Omega}_\mathrm{vol}|)=0}^{(N_\alpha|\mathbf{\Omega}_\mathrm{vol}|)} Z(n_\alpha, N_\alpha, T, \mathscr{E}_\alpha) \exp\left(n_\alpha|\mathbf{\Omega}_\mathrm{vol}|\frac{z_\alpha q\varphi_\alpha}{k_B T}\right), \quad \alpha \in \mathbb{P}_\mathrm{V}, \tag{2.32}$$

where the function Z corresponds to the *(canonical) partition function* which is dependent on the number of vacancies and an energy level $\mathscr{E}_\alpha$. To derive a suitable expression for the partition function Z, we make use of an ideal lattice gas (or mean field lattice gas) model for the description of the occupying behavior of particles on a fixed number of sites on a lattice [14, 83]. There exist

$$W(n_\alpha, N_\alpha) = \frac{(N_\alpha|\mathbf{\Omega}_\mathrm{vol}|)!}{(n_\alpha|\mathbf{\Omega}_\mathrm{vol}|)!(N_\alpha|\mathbf{\Omega}_\mathrm{vol}| - n_\alpha|\mathbf{\Omega}_\mathrm{vol}|)!}, \quad \alpha \in \mathbb{P}_\mathrm{V},$$

distinguishable configurations of the vacancies in the volume $\mathbf{\Omega}_\mathrm{vol}$ since the species and the species vacancies are indistinguishable. We note that the defect configurations are distinguishable, but we assume that their location on the lattice is fixed. Otherwise, we may distribute the vacancies among all possible $\beta_\alpha \overline{n}_\mathrm{L}|\mathbf{\Omega}_\mathrm{vol}|$ sites. Additionally, every vacancy brings an energy of $\mathscr{E}_\alpha = z_\alpha q\psi - z_\alpha E_\alpha$ to its microstate, where the first term corresponds to the electrostatic potential energy and E_α to an intrinsic defect energy level. With this, the partition function Z entering (2.32) reads

$$Z(n_\alpha, N_\alpha, T, \mathscr{E}_\alpha) = W(n_\alpha, N_\alpha) \exp\left(-n_\alpha|\mathbf{\Omega}_\mathrm{vol}|\frac{z_\alpha q\psi - z_\alpha E_\alpha}{k_B T}\right), \quad \alpha \in \mathbb{P}_\mathrm{V},$$

and we can reformulate the grand partition function $\mathcal{Z}$ in (2.32) due to the binomial formula to

$$\mathcal{Z}(\Xi, \mathscr{E}_\alpha) = \left[1 + \exp\left(\frac{z_\alpha q\varphi_\alpha - z_\alpha q\psi + z_\alpha E_\alpha}{k_B T}\right)\right]^{N_\alpha|\mathbf{\Omega}_\mathrm{vol}|}, \quad \alpha \in \mathbb{P}_\mathrm{V}.$$

Furthermore, the following relation holds between the so-called *grand potential* $\mathcal{U}$ and the grand partition function $\mathcal{Z}$ (see [232])

$$\mathcal{U} = -k_B T \log \mathcal{Z} \; = -k_B T N_\alpha|\mathbf{\Omega}_\mathrm{vol}| \log\left[1 + \exp\left(z_\alpha \frac{q(\varphi_\alpha - \psi) + E_\alpha}{k_B T}\right)\right], \quad \alpha \in \mathbb{P}_\mathrm{V}.$$

The partial derivative of the negative grand potential $\mathcal{U}$ with respect to the vacancy electrochemical potential $z_\alpha q\varphi_\alpha$ equals the number of the vacancies $n_\alpha|\mathbf{\Omega}_{\mathrm{vol}}|$ in the volume (see [232])

$$n_\alpha|\mathbf{\Omega}_{\mathrm{vol}}| = -\frac{\partial}{\partial(z_\alpha q\varphi_\alpha)}\mathcal{U} = N_\alpha|\mathbf{\Omega}_{\mathrm{vol}}|\frac{\exp\left(z_\alpha\frac{q(\varphi_\alpha-\psi)+E_\alpha}{k_BT}\right)}{1+\exp\left(z_\alpha\frac{q(\varphi_\alpha-\psi)+E_\alpha}{k_BT}\right)}, \qquad \alpha\in\mathbb{P}_{\mathrm{V}}. \tag{2.33}$$

Thus, in analogy to the state of equation for electrons and holes (2.24) we can formulate

$$n_\alpha = N_\alpha F_{-1}\Big(\eta_\alpha(\varphi_\alpha,\psi)\Big), \quad \eta_\alpha(\varphi_\alpha,\psi) = z_\alpha\frac{q(\varphi_\alpha-\psi)+E_\alpha}{k_BT}, \quad \alpha\in\mathbb{P}_{\mathrm{V}}, \tag{2.34}$$

where F_{-1} is the Fermi-Dirac integral of order -1 in (2.23). With (2.34), we have established a statistical relation for ionic charge carriers. From Figure 2.2 (right), one can clearly see that the vacancy density can never become larger than N_α, meaning that this choice of statistics function reflects correctly the limitation of defect density by a saturation limit N_α. In some prior works, such as [23], the relation (2.34) was derived for electrolyte solutions from a phenomenological free energy framework. This derivation was based on the assumption that a vacancy site V_α, initially associated with a unit particle α, can be occupied by a different unit particle β. In our current derivation, we do not consider such a scenario. By employing the grand canonical formalism for an ideal Fermi gas, we can similarly derive the descriptions of the electron and hole concentrations in (2.18), see, e.g., [131].

As before, we formulate a generalized (mathematical) hypothesis which needs to be satisfied by the statistics function of vacancies

$$\begin{cases} \mathcal{F}_\alpha : \mathbb{R}\to(0,1) \text{ is a } C^1\text{- diffeomorphism;} \\ 0<\mathcal{F}_\alpha'(\eta)\le\mathcal{F}_\alpha(\eta)\le\exp(\eta), \quad \eta\in\mathbb{R}, \end{cases} \qquad \text{for } \alpha\in\mathbb{P}_{\mathrm{V}}, \tag{H2}$$

if not mentioned otherwise. Contrarily to the hypothesis on the electron and hole statistics functions (H1), the image of the vacancy statistics is bounded. The boundedness of the image of $\mathcal{F}_\alpha$ reflects the boundedness of the vacancy density, which can be likewise observed in Figure 2.2 (left). We refer to Appendix A.1 for the proof that the Fermi-Dirac integral of order -1 indeed satisfies (H2).

2.4.3. Drift-diffusion current density

Similarly to electrons and holes, we can introduce the nonlinear diffusion enhancement g_α for vacancy carriers which is sometimes called *activity coefficient* [15]. In the specific

case of the Fermi-Dirac integral of order -1 as statistics function we have

$$g_\alpha\left(\frac{n_\alpha}{N_\alpha}\right) = \frac{n_\alpha}{N_\alpha}\left(\mathcal{F}_\alpha^{-1}\right)'\left(\frac{n_\alpha}{N_\alpha}\right) = \frac{1}{1-\frac{n_\alpha}{N_\alpha}}, \qquad \alpha \in \mathbb{P}_{\mathrm{V}}. \tag{2.35}$$

The generalized Einstein relation between the diffusion coefficient and the mobility of vacancies for diffusion processes on a lattice [15] also holds

$$D_\alpha = \mu_\alpha U_T g_\alpha\left(\frac{n_\alpha}{N_\alpha}\right), \qquad \alpha \in \mathbb{P}_{\mathrm{V}}. \tag{2.36}$$

While it is a common practice for electrons and holes that the nonlinearity of the diffusion enhancement is directly incorporated into the diffusion coefficient of the current density, see, e.g., [46, 71, 223], the situation appears to be more inconclusive in the literature concerning ionic vacancy carriers, see, e.g., [25, 31, 85, 240]. Whether we assume now a constant mobility or a constant diffusion coefficient results into two different drift-diffusion current densities, when reformulating the gradient form description of the current density $\mathbf{j}_\alpha = -z_\alpha^2 q\mu_\alpha n_\alpha \nabla\varphi_\alpha$ in (2.13). We call these two resulting descriptions *nonlinear diffusion* and *modified drift* current density.

Nonlinear diffusion. On the one hand, to be consistent with the electron and hole current density expressions we can assume a constant mobility $\overline{\mu}_\alpha = \mu_\alpha$ in (2.13), apply the generalized Einstein relation (2.36), and make use of the state equation (2.34) with a general statistics function satisfying (H2). We receive a current density with nonlinear diffusion [DA4, 28]

$$\mathbf{j}_{\alpha,\mathrm{ND}} = -z_\alpha q\overline{\mu}_\alpha U_T\left(g_\alpha\left(\frac{n_\alpha}{N_\alpha}\right)\nabla n_\alpha + \frac{z_\alpha}{U_T} n_\alpha \nabla\psi\right), \qquad \alpha \in \mathbb{P}_{\mathrm{V}}. \tag{2.37}$$

Modified drift. On the other hand, a constant diffusion coefficient $\overline{D}_\alpha = D_\alpha$ allows us to express the mobility in terms of the diffusion enhancement g_α. Reformulating (2.13) similarly as before leads to a current density with linear diffusion but with a modified drift term [15, 44, 51]

$$\mathbf{j}_{\alpha,\mathrm{MD}} = -z_\alpha q\overline{D}_\alpha\left(\nabla n_\alpha + \frac{z_\alpha}{U_T g_\alpha\left(\frac{n_\alpha}{N_\alpha}\right)} n_\alpha \nabla\psi\right), \qquad \alpha \in \mathbb{P}_{\mathrm{V}}. \tag{2.38}$$

It is worth noting that both current densities, (2.37) and (2.38), lead to two *different* charge transport models. Assuming that the constant prefactors in both current density descriptions are proportional, i.e., $\overline{\mu}_\alpha U_T \sim \overline{D}_\alpha$, leads to

$$\mathbf{j}_{\alpha,\mathrm{ND}} \sim g_\alpha\left(\frac{n_\alpha}{N_\alpha}\right)\mathbf{j}_{\alpha,\mathrm{MD}}, \qquad \alpha \in \mathbb{P}_{\mathrm{V}}. \tag{2.39}$$

Hence, if $\overline{\mu}_\alpha U_T \sim \overline{D}_\alpha$, then the main difference between the nonlinear diffusion and the modified drift current density is the additional diffusion enhancement as prefactor. In this thesis, we assume a constant mobility, implying that we implicitly employ the nonlinear diffusion description (2.37) for the vacancy current density. This choice may not be immediately apparent when considering the quasi Fermi potential description of the fluxes (2.13). In Chapter 4, we will prove the existence of discrete solutions for an appropriate discretization of the nonlinear diffusion current density. Additionally, in Section 5.2, we thoroughly investigate the impact of both current density descriptions on the electric potential, the vacancy carrier density and the current-voltage characteristics of a PSC configuration.

Remark 2.3. (Special cases of vacancy current densities) We note that the current densities introduced in (2.37) and (2.38) align when the Boltzmann statistics is applied. Furthermore, under suitable conditions, they recover Fick's law of diffusion.

1. **Boltzmann statistics.** We assume $\mathcal{F}_\alpha = \exp$ for $\alpha \in \mathbb{P}_\mathrm{V}$. Then, the diffusion enhancement reduces to $g_\alpha = 1$. Both current densities in (2.37) and (2.38) coincide:

$$\mathbf{j}_\alpha = -z_\alpha q \left(\overline{D}_\alpha \nabla n_\alpha + z_\alpha \overline{\mu}_\alpha n_\alpha \nabla \psi \right), \qquad \alpha \in \mathbb{P}_\mathrm{V}.$$

   The model assumption $\mathcal{F}_\alpha = \exp$ is, for example, used in [29, 48, 77, 182, 200, 229]. However, as discussed in the current section, this assumption is non-physical.

2. **Fick's law of diffusion.** Again, we assume a statistical Boltzmann relation in (2.3). Furthermore, the driving force acting on motion in (2.8) shall be solely given by the negative gradient of the chemical potential, which is $\mathbf{F}_\alpha = -\nabla \chi_\alpha = -k_B T \nabla \eta_\alpha = -k_B T \nabla \log \frac{n_\alpha}{N_\alpha} = -\frac{k_B T}{n_\alpha} \nabla n_\alpha$ With (2.6) and (2.9) we receive a particle flux of the form

$$\mathbf{J}_\alpha = -\mu_\alpha \frac{k_B T}{q} \nabla n_\alpha = -D_\alpha \nabla n_\alpha, \qquad \alpha \in \mathbb{P}_\mathrm{V},$$

   where we used the Einstein relation (2.4) with $g_\alpha = 1$. We immediately see that we recover Fick's first law of diffusion [79, 142].

2.5. Volumetric space charge density

Up to this point, we discussed the electric current density descriptions, the state equations, and the generalized Einstein relation applicable to electrons, holes, and vacancies. Lastly, we must adapt the right-hand side of the general Poisson equation

(2.1a) to suit concrete cases of present carriers. For this, the index set of all species $\mathbb{A}$ shall be given by $\mathbb{A} = \mathbb{P}_{\mathrm{V}} \cup \{\mathrm{n}, \mathrm{p}\} \cup \{\mathrm{L}\}$, where we recall that $\alpha = \mathrm{L}$ denotes the crystalline lattice with $z_{\mathrm{L}} = 0$. Additionally, $\alpha = \mathrm{C}$ in (2.1a) denotes the index of stationary charges. For example, in case of singly ionized acceptor atoms with a density C_{p}, we have $z_{\mathrm{C}} n_{\mathrm{C}} = -C_{\mathrm{p}}$. Analogously, we have for an effective donor background charge $z_{\mathrm{C}} n_{\mathrm{C}} = C_{\mathrm{n}}$, where C_{n} is the density of singly ionized donor atoms.

In the following, we discuss three concrete choices of the index set of moving carriers $\mathbb{M}$, initially introduced in Section 2.1.

Case 1. We do not allow any vacancy migration. In this case, we have as index set of moving carriers $\mathbb{M} = \{\mathrm{n}, \mathrm{p}\}$, and we recover the classical Poisson equation [204]

$$-\nabla \cdot (\varepsilon_s \nabla \psi) = q\Big(z_{\mathrm{n}} n_{\mathrm{n}} + z_{\mathrm{p}} n_{\mathrm{p}} + z_{\mathrm{C}} n_{\mathrm{C}}\Big). \tag{2.40}$$

Case 2. All vacancies $\alpha \in \mathbb{P}_{\mathrm{V}}$ are able to move, i.e., $\mathbb{M} = \{\mathrm{n}, \mathrm{p}\} \cup \mathbb{P}_{\mathrm{V}}$ and

$$-\nabla \cdot (\varepsilon_s \nabla \psi) = q\Big(z_{\mathrm{n}} n_{\mathrm{n}} + z_{\mathrm{p}} n_{\mathrm{p}} + \sum_{\alpha \in \mathbb{P}_{\mathrm{V}}} z_\alpha n_\alpha + z_{\mathrm{C}} n_{\mathrm{C}}\Big). \tag{2.41}$$

Case 3. We have only one migrating vacancy $\alpha = \mathrm{V_X}$, where for the sake of readability we define $\mathrm{a} := \mathrm{V_X}$. For example, in Section 2.4.1 we introduced two materials, perovskites and TMDCs, where it is reasonable to assume the migration of only the halide or the chalcogen vacancies, respectively. Hence, the moving carriers are given by $\mathbb{M} = \{\mathrm{n}, \mathrm{p}, \mathrm{a}\}$. In that case, we can formulate the underlying Poisson equation

$$-\nabla \cdot (\varepsilon_s \nabla \psi) = q\Big(z_{\mathrm{n}} n_{\mathrm{n}} + z_{\mathrm{p}} n_{\mathrm{p}} + z_{\mathrm{a}} n_{\mathrm{a}} + C\Big), \tag{2.42}$$

where C is the sum of the background charge density and the uniform immobile vacancy densities

$$C := \sum_{\alpha \in \mathbb{P}_{\mathrm{V}} \setminus \{\mathrm{a}\}} z_\alpha n_\alpha + z_{\mathrm{C}} n_{\mathrm{C}}. \tag{2.43}$$

Before ending this chapter and applying the gained knowledge to two real device applications, we briefly discuss selected thermodynamic properties that hold significance within the context of this thesis.

2.6. Selected thermodynamic properties

Generally, (non-equilibrium) thermodynamics studies the relationship between energy and matter and how they interact and transform in physical systems. For example,

the negative gradients of quasi Fermi potentials are the driving forces of motion. Due to that, the quasi Fermi potentials have a natural appearance in the thermodynamic description of a drift-diffusion model [9, 71]. Also, consistency with fundamental laws of non-equilibrium thermodynamics is needed when extending the charge transport model such that optical and thermal effects are considered [9, 131]. Without going into further details of thermodynamics, we present two thermodynamically meaningful concepts in this section: thermodynamic equilibrium and free energy. While discretization schemes preserving thermodynamic equilibrium on a discrete level properly avoid non-physical state dissipation [18, 71, 73, 140], the free energy is not only a well-known tool in physics and chemistry but also mathematics to analyze PDE systems and underlying discretization schemes [36, 129].

For the sake of readability, $\mathbb{M} = \{\mathrm{n}, \mathrm{p}, \mathrm{a}\}$ gives the index set of moving charge carriers denoting electrons, holes and vacancies, i.e., we are in the Case 3 of Section 2.5.

2.6.1. Thermodynamic equilibrium and local electroneutrality

Thermodynamic equilibrium describes a physical state, where vanishing currents imply constant quasi Fermi potentials, i.e.,

$$\mathbf{j}_\alpha = \mathbf{0} \quad \text{implying} \quad \varphi_{\alpha,0} := \varphi_\alpha = \text{const.}, \quad \text{for all} \quad \alpha \in \mathbb{M}. \tag{2.44}$$

Without any loss of generality, we assume that both $\varphi_{\mathrm{n},0}$ and $\varphi_{\mathrm{p},0}$ equal the same value φ_0. This indicates that there is only one Fermi level in thermodynamic equilibrium, and the electron and hole quasi Fermi potentials have the same value in this case.

The gradient structure of the current densities (2.2) guarantees that thermodynamic equilibrium is satisfied. Assuming additionally to thermodynamic equilibrium a vanishing left-hand side of the Poisson equation (2.42), we can compute a locally electroneutral solution ψ_0. In case of present vacancies, we have

$$0 = z_\mathrm{n} n_\mathrm{n}\Big(\eta_\mathrm{n}(\psi_0, \varphi_0)\Big) + z_\mathrm{p} n_\mathrm{p}\Big(\eta_\mathrm{p}(\psi_0, \varphi_0)\Big) + z_\mathrm{a} n_\mathrm{a}\Big(\eta_\mathrm{a}(\psi_0, \varphi_{\mathrm{a},0})\Big) + C. \tag{2.45}$$

Usually, this equation cannot be solved directly. However, suppose we assume linear diffusion of the electron and hole current density, i.e., modeling the charge carrier statistics $\mathcal{F}_\mathrm{n}$, $\mathcal{F}_\mathrm{p}$ with a Boltzmann approximation (2.21), and assume that no vacancies are present. In that case, we can solve (2.45) analytically, yielding

$$\psi_0 = \varphi_0 + \frac{E_\mathrm{n} + E_\mathrm{p}}{2q} - \frac{1}{2} U_T \log \frac{N_\mathrm{n}}{N_\mathrm{p}} + U_T \operatorname{arcsinh}\left(\frac{C}{2N_\mathrm{intr}}\right), \tag{2.46}$$

where the intrinsic carrier density N_intr is defined by

$$N_\mathrm{intr}^2 = N_\mathrm{n} N_\mathrm{p} \exp\left(-\frac{E_\mathrm{n} - E_\mathrm{p}}{k_B T}\right). \tag{2.47}$$

The solution ψ_0 of the equation (2.45) will be precisely the function we evaluate at the boundaries in (3.7), when modeling ohmic contacts.

2.6.2. Thermodynamic free energy

The sum of different energy contributions gives the thermodynamic free energy in $\mathbf{\Omega}_{\text{intr}}$. Following [1, 157], on the one hand, the contribution of electrons and holes can be derived from an ideal Fermi gas. On the other hand, the electrostatic field energy gives the electric potential contribution to the total energy. Lastly, assuming an ideal lattice gas as in Section 2.4.2, we can also derive a consistent energy contribution of vacancies, which extends the electric free energy formulation in [157]. In total, the free energy functional reads

$$\begin{aligned}\mathbb{E}_f(t) =& \frac{1}{2}\int_{\mathbf{\Omega}_{\text{intr}}} \varepsilon_s |\nabla\psi|^2 \, d\mathbf{x} \; + \sum_{\alpha\in\{\text{n,p}\}} \int_{\mathbf{\Omega}_{\text{intr}}} \left[k_B T N_\alpha \Phi_\alpha\left(\frac{n_\alpha}{N_\alpha}\right) - z_\alpha E_\alpha n_\alpha \right] d\mathbf{x} \\ &+ \int_{\mathbf{\Omega}_{\text{intr}}} \left[k_B T N_{\text{a}} \Phi_{\text{a}}\left(\frac{n_{\text{a}}}{N_{\text{a}}}\right) - z_{\text{a}} E_{\text{a}} n_{\text{a}} \right] d\mathbf{x},\end{aligned} \tag{2.48}$$

where Φ_α is an antiderivative of $\mathcal{F}_\alpha^{-1}$ for $\alpha \in \mathbb{M}$. Following [1], we neglected the external interaction effects of the electric potential. Thus, for non-degenerate semiconductors, i.e., for $\mathcal{F}_{\text{n}} = \mathcal{F}_{\text{p}} = \exp$ and $\mathcal{F}_{\text{a}}$ chosen as Fermi-Dirac integral of order -1, the free energy simplifies to

$$\begin{aligned}\mathbb{E}_f(t) =& \frac{1}{2}\int_{\mathbf{\Omega}_{\text{intr}}} \varepsilon_s |\nabla\psi|^2 \, d\mathbf{x} \; + \sum_{\alpha\in\{\text{n,p}\}} \int_{\mathbf{\Omega}_{\text{intr}}} \left[k_B T n_\alpha \left(\log\left(\frac{n_\alpha}{N_\alpha}\right) - 1 \right) - z_\alpha E_\alpha n_\alpha \right] d\mathbf{x} \\ &+ \int_{\mathbf{\Omega}_{\text{intr}}} \left[k_B T \left(n_{\text{a}} \log\left(\frac{n_{\text{a}}}{N_{\text{a}}}\right) + (N_{\text{a}} - n_{\text{a}}) \log\left(1 - \frac{n_{\text{a}}}{N_{\text{a}}}\right)\right) - z_{\text{a}} E_{\text{a}} n_{\text{a}} \right] d\mathbf{x},\end{aligned} \tag{2.49}$$

where $\Phi_{\text{n}}(x) = \Phi_{\text{p}} = x\log(x) - x$ and $\Phi_{\text{a}}(x) = x\log(x) + (1-x)\log(1-x)$. A variation of the energy functional (2.48) will help us in Chapter 4 to prove the existence of a discrete solution for an implicit-in-time finite volume scheme.

3. Charge transport models for two real device applications

In Chapter 2, we derived vacancy-assisted charge transport equations in a crystalline semiconductor layer $\mathbf{\Omega}_{\mathrm{intr}}$. Next, we apply these equations to two practical device applications and formulate well-defined initial boundary value problems. Section 3.1 introduces a drift-diffusion model that describes the charge transport in perovskite solar cells, including photogeneration and recombination. Section 3.2 presents a consistent charge transport model for TMDC-based memristive devices and a comprehensive description of an image-charge-induced Schottky barrier lowering boundary model. After non-dimensionalizing both models in Section 3.1.4 and Section 3.2.3, we discuss *entropy methods* in Section 3.3, a mathematical tool to analyze PDE systems. We conclude this chapter by proving a continuous entropy-dissipation inequality.

Within the intrinsic domain $\mathbf{\Omega}_{\mathrm{intr}}$, we assume the transport of three carriers: Electrons ($\alpha = \mathrm{n}$), holes ($\alpha = \mathrm{p}$), and vacancies ($\alpha = \mathrm{a}$). In case of perovskites, we can think of the carrier $\alpha = \mathrm{a}$ as the halide anion vacancies and, in case of TMDCs, as the chalcogen defects. We have the standard charge numbers $z_{\mathrm{n}} = -1$, $z_{\mathrm{p}} = 1$ for electrons and holes. For the ionic defect carriers, we allow $z_{\mathrm{a}} \in \mathbb{Z}$ for the mathematical modeling, noting that we discussed previously that in perovskites (Section 2.4.1.1) and TMDCs (Section 2.4.1.2), negative charge numbers may have limited physical relevance.

The set of unknowns is given by $(\varphi_{\mathrm{n}}, \varphi_{\mathrm{p}}, \varphi_{\mathrm{a}}, \psi)$, i.e., we consider the quasi Fermi potentials instead of the carrier densities n_α as unknowns. Using quasi Fermi potentials instead of densities as unknowns has several practical advantages: First, they are on the same order of magnitude as the electrostatic potential and do not vary over more than twenty orders of magnitude as densities may do, simplifying numerical computations. Second, unlike densities, quasi Fermi potentials are usually assumed to be continuous across heterojunctions, meaning no additional discontinuity-preserving internal boundary conditions are needed. Third, current densities proportional to gradients of potentials are easier to interpret physically and mathematically, e.g., as gradient flows [61, 95, 169].

Parts of Section 3.1 are based on [DA2, DA4]. Furthermore, parts of Section 3.2 can be found in [DA5], whereas Section 3.3 was partially published in [DA2].

3.1. Perovskite solar cells

Already in the 80ies, the diffusion of ionic halide vacancies in perovskites was studied [171]. However, only in 2014 did ion migration in perovskite devices become of practical interest when experiments suggested that the mobility of ionic defects is one possible reason for current-voltage hysteresis in perovskite solar cells [225]. Since then, few materials within photovoltaics have gained such interest as perovskites in the last years [135, 188, 237]. These materials show promise for use in applications, including lasers, memristors, LEDs, and solar cells. Notably, perovskite-silicon tandem cells have recently surpassed the efficiency of high-performing single junction silicon solar cells [16, 40, 162, 178], achieving world record efficiencies exceeding 30 % where further efficiency gains are likely. Even though specific architectures have significantly lower production costs than conventional solar cells, a couple of challenges must be overcome for the mass production of PSCs, especially the fast device degradation. For this reason, it is paramount to understand the charge transport in perovskites better via improved modeling and simulation.

A substantial difference between drift-diffusion charge transport models for (in)organic semiconductors and those for perovskites lies in the fundamental role played by ion migration within the perovskite material. In PSCs, the various charge carrier species live in different parts of the domain, evolve on different timescales, and obey different diffusion laws. Moreover, we need to consider the photogeneration rate due to sun illumination. These differences and new features compared to classical semiconductors require additional mathematical and numerical modeling and comprehensive analysis of these devices, which include all relevant physical effects, to predict the behavior of such complex physical devices. Initial drift-diffusion models incorporating ionic movement such as [29, 50, 77, 182, 217, 237] did not impose constraints on the vacancy density, meaning the presented models did not bound the number of available lattice sites within a perovskite crystal. Later, models were introduced to address this limitation [DA4, 28, 44, 51]. Note that other ways exist to model the charge transport in PSCs. For example, we can find approaches based on atomistic density functional theory [65, 236] and equivalent circuit models [175, 224]. However, a comprehensive discussion of such models goes beyond the scope of this thesis.

3.1.1. Bulk equations

In a perovskite solar cell, the perovskite layer $\mathbf{\Omega}_{\text{intr}}$ is sandwiched between a doped electron transport layer (ETL) and a doped hole transport layer (HTL), denoted by $\mathbf{\Omega}_{\text{ETL}}$ and $\mathbf{\Omega}_{\text{HTL}}$, respectively. TiO_2, PCBM, and ZnO are typically chosen as ETL

materials, whereas spiro-OMeTAD, PTAA, and PEDOT:PSS are common materials for the hole transport layer [213]. More precisely, the device geometry $\mathbf{\Omega} \subset \mathbb{R}^d$, $d \in \{1, 2, 3\}$, is separated into three pairwise disjoint, polygonal (or polyhedral), open subdomains such that $\overline{\mathbf{\Omega}} = \cup_k \overline{\mathbf{\Omega}}_k$, $k \in \{\mathrm{ETL}, \mathrm{intr}, \mathrm{HTL}\}$. We assume that $\mathbf{\Omega}$ is an open, connected, and bounded spatial domain, and we denote the interface between the transport layers and the perovskite layer by $\mathbf{\Sigma}_{\mathrm{ETL}} = \partial\mathbf{\Omega}_{\mathrm{ETL}} \cap \partial\mathbf{\Omega}_{\mathrm{intr}}$ and $\mathbf{\Sigma}_{\mathrm{HTL}} = \partial\mathbf{\Omega}_{\mathrm{HTL}} \cap \partial\mathbf{\Omega}_{\mathrm{intr}}$. The electron and hole transport layer boundaries do not intersect, i.e., $\partial\mathbf{\Omega}_{\mathrm{ETL}} \cap \partial\mathbf{\Omega}_{\mathrm{HTL}} = \emptyset$. We refer to Figure 3.1 for a possible visual representation of the device geometry.

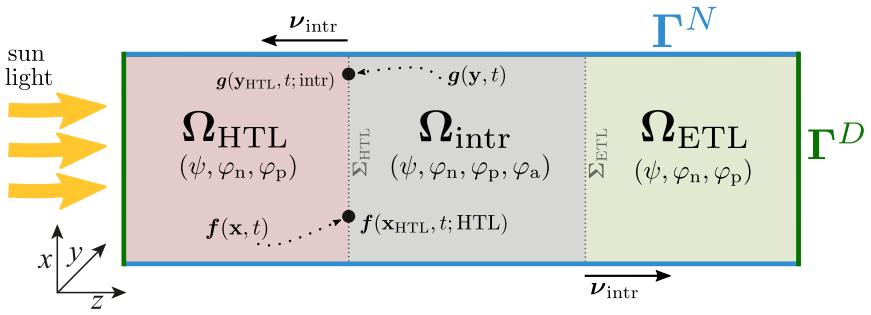

Figure 3.1.: A two-dimensional three-layer perovskite solar cell device geometry with the relevant potentials stated per subdomain and a visualization of the notation used for the definition of the interfacial conditions in Section 3.1.3.2. (From [DA2] with modifications.)

Unlike quasi Fermi potentials for electrons and holes $\varphi_{\mathrm{n}}, \varphi_{\mathrm{p}}$ and the electric potential ψ, which are defined on all of $\mathbf{\Omega}$, the quasi Fermi potential of halide vacancies φ_{a} is defined only in the intrinsic domain $\mathbf{\Omega}_{\mathrm{intr}}$. The continuity equations are given by

$$z_{\mathrm{n}} q \partial_t n_{\mathrm{n}} + \nabla \cdot \mathbf{j}_{\mathrm{n}} = z_{\mathrm{n}} q \Big(G(\mathbf{x}) - R(n_{\mathrm{n}}, n_{\mathrm{p}}) \Big), \qquad \mathbf{x} \in \mathbf{\Omega},\ t \geq 0, \tag{3.1a}$$

$$z_{\mathrm{p}} q \partial_t n_{\mathrm{p}} + \nabla \cdot \mathbf{j}_{\mathrm{p}} = z_{\mathrm{p}} q \Big(G(\mathbf{x}) - R(n_{\mathrm{n}}, n_{\mathrm{p}}) \Big), \qquad \mathbf{x} \in \mathbf{\Omega},\ t \geq 0, \tag{3.1b}$$

$$z_{\mathrm{a}} q \partial_t n_{\mathrm{a}} + \nabla \cdot \mathbf{j}_{\mathrm{a}} = 0, \qquad \mathbf{x} \in \mathbf{\Omega}_{\mathrm{intr}},\ t \geq 0, \tag{3.1c}$$

which are self-consistently coupled to the nonlinear and region-wise defined Poisson equation for $t \geq 0$

$$-\nabla \cdot (\varepsilon_s \nabla \psi) = \begin{cases} q\Big(z_{\mathrm{n}} n_{\mathrm{n}} + z_{\mathrm{p}} n_{\mathrm{p}} + C(\mathbf{x}) \Big), & \mathbf{x} \in \mathbf{\Omega}_{\mathrm{HTL}} \cup \mathbf{\Omega}_{\mathrm{ETL}}, \\ q\Big(z_{\mathrm{n}} n_{\mathrm{n}} + z_{\mathrm{p}} n_{\mathrm{p}} + z_{\mathrm{a}} n_{\mathrm{a}} + C(\mathbf{x}) \Big), & \mathbf{x} \in \mathbf{\Omega}_{\mathrm{intr}}. \end{cases} \tag{3.1d}$$

Moreover, the electric current densities of electrons, holes, and vacancies are defined as before (see (2.2))

$$\mathbf{j}_\alpha = -z_\alpha^2 q \mu_\alpha n_\alpha \nabla \varphi_\alpha, \qquad \mathbf{x} \in \mathbf{\Omega},\ t \geq 0, \qquad \text{for } \alpha \in \{\mathrm{n}, \mathrm{p}, \mathrm{a}\}. \tag{3.1e}$$

Concerning the right-hand side of the continuity equations (3.1a), (3.1b) and the Poisson equation (3.1d) we assume that the doping profile C is bounded, i.e., $C \in L^\infty(\mathbf{\Omega})$ and that the photogeneration rate satisfies $0 \leq G \in L^\infty(\mathbf{\Omega})$. In other words, the carrier-dependent doping profile and the photogeneration rate are constant in time and bounded in space. In practice, the doping C is equal to a singly ionized donor density $C_\mathrm{n} \geq 0$ in the ETL and a singly ionized acceptor density $C_\mathrm{p} \geq 0$ in the HTL, i.e., $C(\mathbf{x}) = C_\mathrm{n}(\mathbf{x})$ for $\mathbf{x} \in \mathbf{\Omega}_\mathrm{ETL}$ and $C(\mathbf{x}) = -C_\mathrm{p}(\mathbf{x})$ for $\mathbf{x} \in \mathbf{\Omega}_\mathrm{HTL}$. The doping C in the intrinsic region $\mathbf{\Omega}_\mathrm{intr}$ corresponds to the uniform density of cation vacancies in accordance with (2.43). For global charge neutrality, C is set to the negative average anion vacancy density $-C_\mathrm{a}$ in the intrinsic region, multiplied by the respective charge number, i.e., $C = -z_\mathrm{a} C_\mathrm{a}$, see [29, 50].

3.1.2. Photogeneration and recombination rates

3.1.2.1. Photogeneration

The photogeneration, i.e., the process of generating charge carriers through light absorption, is a fundamental feature of photovoltaic devices. We assume that light enters through one of the transport layers (z direction in Figure 3.1). In the general case, photogeneration is linked to the electromagnetic field distribution within the solar cell device, which can be described by Maxwell's equations [7]. Solving these equations requires advanced numerical techniques such as the finite element method [194] or the transfer-matrix method [208]. However, in the context of this thesis, which primarily focuses on the electric properties of perovskite solar cells, we can rely on a more straightforward approach. We describe the photogeneration rate using an analytical formula, following the Beer-Lambert law of light absorption [179], as

$$G(\mathbf{x}) = F_\mathrm{ph} \alpha_g \exp(-\alpha_g z), \quad \mathbf{x} = (x, y, z)^T. \tag{3.2}$$

Here, F_ph denotes the incident photon flux and α_g the material absorption coefficient which depends on the light wave length. Thus, the photogeneration rate can be described as an exponential decay in z direction. For further insights into numerical studies regarding the optical optimization of perovskite solar cells using advanced optical models, we refer to, e.g., [119, 239].

3.1.2.2. Recombination rates

Within the device, electrons and holes may recombine. The recombination rate R on the right-hand side of the electron and hole mass balance equations (3.1a), (3.1b) is given by the sum of the most common recombination processes: Schockley-Read-Hall

(SRH), radiative, and Auger [71] with $r \in \{\mathrm{SRH}, \mathrm{rad}, \mathrm{Auger}\}$

$$R(n_\mathrm{n}, n_\mathrm{p}) = \sum_r R_r(n_\mathrm{n}, n_\mathrm{p}),$$

where all recombination processes can be modeled by the following formula

$$R_r(n_\mathrm{n}, n_\mathrm{p}) = r_r(n_\mathrm{n}, n_\mathrm{p}) n_\mathrm{n} n_\mathrm{p} \left(1 - \exp\left(\frac{q\varphi_\mathrm{n} - q\varphi_\mathrm{p}}{k_B T}\right)\right). \tag{3.3}$$

The process-dependent non-negative rate r_r will be defined in the following paragraphs. It is worth noting that the recombination processes stated in the literature for the simulation of PSCs such as [28, 44, 77, 182] assume a Boltzmann relation between the carrier densities and the quasi Fermi potentials, yielding an expression

$$R_r(n_\mathrm{n}, n_\mathrm{p}) = r_r(n_\mathrm{n}, n_\mathrm{p}) \left(n_\mathrm{n} n_\mathrm{p} - N_\mathrm{intr}^2\right), \tag{3.4}$$

where the intrinsic carrier density N_intr is defined by (2.47). Using (3.4) and assuming a nonlinear diffusion for electrons and holes via the generalized Einstein relation (2.4) violates consistency with thermodynamic equilibrium in the sense of Section 2.6.1.

One of the most common recombination processes is the *Shockley-Read-Hall* recombination, which models trapping of electrons. In general, this process can be described by a trap continuity equation [97], which implies different recombination rates for electrons and holes. However, a simplified version of this physical process can be given in a closed form when we assume the system to be stationary, namely,

$$r_\mathrm{SRH}(n_\mathrm{n}, n_\mathrm{p}) = \frac{1}{\tau_\mathrm{p}(n_\mathrm{n} + n_{\mathrm{n},\tau}) + \tau_\mathrm{n}(n_\mathrm{p} + n_{\mathrm{p},\tau})}, \tag{3.5}$$

where $\tau_\mathrm{n}, \tau_\mathrm{p}$ are the carrier lifetimes and $n_{\mathrm{n},\tau}, n_{\mathrm{p},\tau}$ some reference carrier densities. For the constant reference carrier densities different expressions can be assumed [28, 46, 223, 233]. In the case of a trap energy level close to the equilibrium Fermi level we may even assume $n_{\mathrm{n},\tau} \approx n_{\mathrm{p},\tau} \approx N_\mathrm{intr}$, see, e.g., [48, 259]. Choosing the simplified version (3.5) is applicable when assuming that the trapping and detrapping processes are faster than the timescale of measurements [27]. Otherwise, this way of defining the SRH recombination needs to be extended as in, e.g., in the context of PSCs [77, 182].

The *radiative recombination* (frequently called *bimolecular* or *band-to-band* recombination) is given by

$$r_\mathrm{rad}(n_\mathrm{n}, n_\mathrm{p}) = r_{0,\mathrm{rad}} \tag{3.6}$$

for a constant rate coefficient $r_{0,\mathrm{rad}}$.

For the *Auger recombination* we have

$$r_{\text{Auger}}(n_{\text{n}}, n_{\text{p}}) = B_{\text{n}} n_{\text{n}} + B_{\text{p}} n_{\text{p}}$$

with rate constants B_{n} and B_{p}. This type of recombination becomes likely for high carrier densities or in semiconductors with small band gaps [101]. For example, for MAPI, it was shown that including Auger recombination has a minor influence on the resulting current-voltage characteristics [245].

3.1.3. Initial and boundary conditions

We supply the system (3.1) with initial conditions for $t = 0$

$$\varphi_{\text{n}}(\mathbf{x}, 0) = \varphi_{\text{n}}^0(\mathbf{x}), \qquad \varphi_{\text{p}}(\mathbf{x}, 0) = \varphi_{\text{p}}^0(\mathbf{x}), \qquad \text{for } \mathbf{x} \in \boldsymbol{\Omega}, \tag{PICa}$$

$$\varphi_{\text{a}}(\mathbf{x}, 0) = \varphi_{\text{a}}^0(\mathbf{x}), \qquad \text{for } \mathbf{x} \in \boldsymbol{\Omega}_{\text{intr}}, \tag{PICb}$$

where we assume $\varphi_{\text{n}}^0, \varphi_{\text{p}}^0 \in L^\infty(\boldsymbol{\Omega})$ and $\varphi_{\text{a}}^0 \in L^\infty(\boldsymbol{\Omega}_{\text{intr}})$. Correspondingly, we define the initial densities $n_\alpha^0(\mathbf{x}) = N_\alpha \mathcal{F}_\alpha(\eta_\alpha(\varphi_\alpha^0, \psi(\mathbf{x}, 0)))$ for $\alpha \in \{\text{n}, \text{p}, \text{a}\}$.

3.1.3.1. External boundary conditions

The outer boundary of $\boldsymbol{\Omega}$ is decomposed into two ohmic contacts at the metal interfaces modeled by Dirichlet conditions $\boldsymbol{\Gamma}^D$ and isolated interfaces $\boldsymbol{\Gamma}^N$, where we impose no flux Neumann boundary conditions. We assume that $\boldsymbol{\Gamma}^D$ and $\boldsymbol{\Gamma}^N$ are closed subsets of $\partial\boldsymbol{\Omega}$ with $\partial\boldsymbol{\Omega} = \boldsymbol{\Gamma}^D \cup \boldsymbol{\Gamma}^N$. In particular, the ohmic contacts are solely located at the outer boundary of transport layers, i.e., $\boldsymbol{\Gamma}^D \cap \overline{\boldsymbol{\Omega}}_{\text{intr}} = \emptyset$, see Figure 3.1. The outer boundary conditions are for $t \geq 0$ modeled via

$$\psi(\mathbf{x}, t) = \psi_0(\mathbf{x}) + U(\mathbf{x}, t), \quad \varphi_{\text{n}}(\mathbf{x}, t) = \varphi_{\text{p}}(\mathbf{x}, t) = U(\mathbf{x}, t), \qquad \mathbf{x} \in \boldsymbol{\Gamma}^D, \tag{3.7a}$$

$$\nabla\psi(\mathbf{x}, t) \cdot \boldsymbol{\nu}(\mathbf{x}) = \mathbf{j}_{\text{n}}(\mathbf{x}, t) \cdot \boldsymbol{\nu}(\mathbf{x}) = \mathbf{j}_{\text{p}}(\mathbf{x}, t) \cdot \boldsymbol{\nu}(\mathbf{x}) = 0, \qquad \mathbf{x} \in \boldsymbol{\Gamma}^N, \tag{3.7b}$$

where U corresponds to an externally applied time-dependent voltage and $\boldsymbol{\nu}$ is the outward pointing unit normal to $\boldsymbol{\Gamma}^N$. The potential ψ_0 can be computed iteratively, implicitly or explicitly when assuming a Boltzmann relation, as described in Section 2.6.1. Concerning the anion vacancies, we impose no flux Neumann boundary conditions on the whole intrinsic boundary, namely,

$$\mathbf{j}_{\text{a}}(\mathbf{x}, t) \cdot \boldsymbol{\nu}_{\text{intr}}(\mathbf{x}) = 0, \quad \mathbf{x} \in \partial\boldsymbol{\Omega}_{\text{intr}}, \ t \geq 0, \tag{3.8}$$

where $\boldsymbol{\nu}_{\text{intr}}$ is the outward pointing unit normal to $\partial\boldsymbol{\Omega}_{\text{intr}}$. In Section 5.2, we will perform simulations on a perovskite solar cell using these time-dependent outer boundary conditions.

Remark 3.1. (Time-independent ohmic contacts) Under the assumption of time-independent boundary conditions we will study the underlying finite volume discretization scheme and prove the existence of a discrete solution in Chapter 4. More precisely, let the Dirichlet values $\psi^D, \varphi^D \in W^{1,\infty}(\mathbf{\Omega})$ be given. Then, we adjust the outer boundary conditions (3.7a) to

$$\psi(\mathbf{x},t) = \psi^D(\mathbf{x}), \quad \varphi_\mathrm{n}(\mathbf{x},t) = \varphi_\mathrm{p}(\mathbf{x},t) = \varphi^D(\mathbf{x}), \qquad \mathbf{x} \in \mathbf{\Gamma}^D, \ t \geq 0. \tag{3.9}$$

When comparing (3.7a) and (3.9), this means the boundary values are fixed to $\psi^D := \psi_0 + \overline{U}$ and $\varphi^D := \overline{U}$, where $\overline{U}$ is a constant-in-time applied voltage. We note that the same Dirichlet value φ^D is imposed on both quasi Fermi potentials.

3.1.3.2. Internal boundary conditions

Due to the heterojunctions between the perovskite and the transport layers, we need additional internal boundary conditions at the interfaces between neighboring subdomains. The traces of the potentials φ_n, φ_p, and ψ coincide on both sides of the internal boundaries $\mathbf{\Sigma}_\mathrm{ETL}$ and $\mathbf{\Sigma}_\mathrm{HTL}$, which contain a point in the one-dimensional case, an edge in two dimensions and a face in three dimensions. Moreover, we assume continuity of the corresponding fluxes across internal boundaries. More precisely, for $t \geq 0$ and $k \in \{\mathrm{ETL}, \mathrm{HTL}\}$ we have

$$\Big(\varepsilon_s \nabla\psi(\mathbf{x},t;k) - \varepsilon_s \nabla\psi(\mathbf{x},t;\mathrm{intr})\Big) \cdot \boldsymbol{\nu}_\mathrm{intr}(\mathbf{x}) = 0, \quad \mathbf{x} \in \mathbf{\Sigma}_k, \tag{3.10a}$$

$$\Big(\mathbf{j}_\mathrm{n}(\mathbf{x},t;k) - \mathbf{j}_\mathrm{n}(\mathbf{x},t;\mathrm{intr})\Big) \cdot \boldsymbol{\nu}_\mathrm{intr}(\mathbf{x}) = 0, \quad \mathbf{x} \in \mathbf{\Sigma}_k, \tag{3.10b}$$

$$\Big(\mathbf{j}_\mathrm{p}(\mathbf{x},t;k) - \mathbf{j}_\mathrm{p}(\mathbf{x},t;\mathrm{intr})\Big) \cdot \boldsymbol{\nu}_\mathrm{intr}(\mathbf{x}) = 0, \quad \mathbf{x} \in \mathbf{\Sigma}_k. \tag{3.10c}$$

Here, we use the notation that for an arbitrary function $\mathbf{f}$ the expression $\mathbf{f}(\mathbf{x},t;k)$ denotes the trace of $\mathbf{f}$, where $\mathbf{f}$ is restricted onto $\mathbf{\Omega}_k$, $k \in \{\mathrm{ETL}, \mathrm{intr}, \mathrm{HTL}\}$ and evaluated at the respective interface between transport and perovskite layer $\mathbf{x} \in \mathbf{\Sigma}_k$. It is possible to introduce surface recombination rates via the right-hand sides of the electron and hole equations (3.10b), (3.10c), as demonstrated in, e.g., [28, 48]. An extensive discussion and inclusion of this effect will be neglected in this thesis.

Remark 3.2. (Conservation of mass for anion vacancies) Observe that by integrating the continuity equation (3.1c) over $\mathbf{\Omega}_\mathrm{intr}$, using Gauss' theorem, and the Neumann boundary conditions (3.8) the total mass of anion vacancies is conserved, namely,

$$\int_{\mathbf{\Omega}_\mathrm{intr}} n_\mathrm{a}(\mathbf{x},t)\,d\mathbf{x} = \int_{\mathbf{\Omega}_\mathrm{intr}} n_\mathrm{a}^0(\mathbf{x})\,d\mathbf{x}, \quad \text{for all } t \geq 0.$$

An equivalent condition does not hold for electron and hole densities due to the boundary conditions and the recombination/photogeneration terms.

3.1.4. Non-dimensionalization

In this subsection, we derive the relevant non-dimensional parameters of the model, following [50] and [163, Section 2.4]. Starting from the bulk equations (3.1), we rewrite the equations in terms of the scaled variables given as the ratio of the unscaled physical quantity to the scaling factors defined in Table 3.1. In the following, we make several simplifications to simplify the presentation and the forthcoming computations. More precisely, we assume from now on that the mobilities μ_n and μ_p, the dielectric permittivity ε_s, and the effective conduction and valence density of states N_n and N_p are constant in the domain $\mathbf{\Omega}$, as well as the parameters entering the process-dependent recombination rate r_r in (3.3), if not mentioned otherwise. Moreover, we assume that the band-edge energies $E_\mathrm{n}, E_\mathrm{p}, E_\mathrm{a}$ are zero, $\mu_\mathrm{n} = \mu_\mathrm{p}$, and $N_\mathrm{n} = N_\mathrm{p}$. In Table 3.1, the timescale is chosen for the anion vacancies. By replacing $\tilde{\mu}_\mathrm{a}$ with $\tilde{\mu}$ in the time variable scaling factor, one could write the dimensionless version adapted to the electrons and holes timescale. We assume that the scaling factor $\tilde{N}$ is precisely equal to $N_\mathrm{n} = N_\mathrm{p}$ and that $\tilde{N}_\mathrm{a} = N_\mathrm{a}$. Similarly, since we assumed, for simplicity, that the mobilities are constant in the overall spatial domain, we take $\tilde{\mu}_\mathrm{a} = \mu_\mathrm{a}$ and $\tilde{\mu} = \mu_\mathrm{n} = \mu_\mathrm{p}$.

In practice, the previous quantities vary in each subdomain. All the analyses of Section 3.3.2 and Section 4.2 can be adapted without the previous simplifications. However, apart from creating a notational overhead, the fundamental ideas remain the same. Moreover, the location vector is rescaled with respect to the device thickness. By denoting the scaled quantities with the same symbol as the corresponding unscaled quantities, the dimensionless version of the mass balance equations (3.1a), (3.1b), (3.1c) read

$$\begin{aligned}
\nu\, z_\mathrm{n}\partial_t n_\mathrm{n} + \nabla\cdot\mathbf{j}_\mathrm{n} &= z_\mathrm{n}\Big(\gamma\, G - R(n_\mathrm{n}, n_\mathrm{p})\Big), && \mathbf{x}\in\mathbf{\Omega},\ t\geq 0, && \text{(Pa)}\\
\nu\, z_\mathrm{p}\partial_t n_\mathrm{p} + \nabla\cdot\mathbf{j}_\mathrm{p} &= z_\mathrm{p}\Big(\gamma\, G - R(n_\mathrm{n}, n_\mathrm{p})\Big), && \mathbf{x}\in\mathbf{\Omega},\ t\geq 0, && \text{(Pb)}\\
z_\mathrm{a}\partial_t n_\mathrm{a} + \nabla\cdot\mathbf{j}_\mathrm{a} &= 0, && \mathbf{x}\in\mathbf{\Omega}_\mathrm{intr},\ t\geq 0, && \text{(Pc)}
\end{aligned}$$

coupled to the non-dimensionalized version of the Poisson equation (3.1d)

$$-\lambda^2\Delta\psi = \begin{cases} \delta\Big(z_\mathrm{n}n_\mathrm{n} + z_\mathrm{p}n_\mathrm{p} + C\Big), & \mathbf{x}\in\mathbf{\Omega}_\mathrm{HTL}\cup\mathbf{\Omega}_\mathrm{ETL},\ t\geq 0,\\ \delta\Big(z_\mathrm{n}n_\mathrm{n} + z_\mathrm{p}n_\mathrm{p} + C\Big) + z_\mathrm{a}n_\mathrm{a}, & \mathbf{x}\in\mathbf{\Omega}_\mathrm{intr},\ t\geq 0. \end{cases} \qquad \text{(Pd)}$$

The charge carrier currents (3.1e) can be rewritten in non-dimensionalized form

$$\mathbf{j}_\alpha = -z_\alpha^2 n_\alpha \nabla\varphi_\alpha, \quad \alpha\in\{\mathrm{n},\mathrm{p},\mathrm{a}\}, \qquad \text{(Pe)}$$

Symbol	Meaning	Scaling factor	Order of magnitude
$\mathbf{x}$	Space variable	l	10^{-7} m
φ_α, φ^D, φ^0_α	Quasi Fermi potentials	U_T	10^{-2} V
ψ, ψ^D	Electric potential	U_T	10^{-2} V
C	Doping profile	$\tilde{N}$	10^{24} m^{-3}
n_n	Electron density	$\tilde{N}$	10^{24} m^{-3}
n_p	Hole density	$\tilde{N}$	10^{24} m^{-3}
n_a	Vacancy density	$\tilde{N}_\mathrm{a}$	10^{27} m^{-3}
$\mu_\mathrm{n}, \mu_\mathrm{p}$	Electron and hole mobility	$\tilde{\mu}$	10^{-4} m^2/(Vs)
μ_a	Vacancy mobility	$\tilde{\mu}_\mathrm{a}$	10^{-16} m^2/(Vs)
t	Time variable	$\frac{l^2}{\tilde{\mu}_\mathrm{a} U_T}$	10^4 s
$\mathbf{j}_\mathrm{n}$	Electron current density	$\frac{qU_T\tilde{N}\tilde{\mu}}{l}$	10^6 C/(m^{2}s)
$\mathbf{j}_\mathrm{p}$	Hole current density	$\frac{qU_T\tilde{N}\tilde{\mu}}{l}$	10^6 C/(m^{2}s)
$\mathbf{j}_\mathrm{a}$	Vacancy current density	$\frac{qU_T\tilde{N}_\mathrm{a}\tilde{\mu}_\mathrm{a}}{l}$	10^{-3} C/(m^{2}s)
R	Recombination rate	$\frac{\tilde{\mu}U_T\tilde{N}}{l^2}$	10^{32} 1/(m^{3}s)
G	Photogeneration rate	$F_\mathrm{ph}\alpha_g$	10^{28} 1/(m^{3}s)

Table 3.1.: Scaling factors of a perovskite solar cell device with MAPI as perovskite material related to the default parameters of [44, 48] (see also Table B.1) at $T = 298$ K.

and we have the following non-dimensionalized expression for the state equation (2.3)

$$n_\alpha = \mathcal{F}_\alpha\Big(z_\alpha(\varphi_\alpha - \psi)\Big), \quad \alpha \in \{\mathrm{n}, \mathrm{p}, \mathrm{a}\}. \tag{Pf}$$

There are four dimensionless parameters, the rescaled Debye length, which is taken with respect to the anion vacancy concentration

$$\lambda = \sqrt{\frac{\varepsilon_s U_T}{l^2 q \tilde{N}_\mathrm{a}}}, \tag{3.11}$$

the mobility parameter, defined as the relative mobility of anion vacancies with respect to the electron and hole mobility

$$\nu = \frac{\tilde{\mu}_\mathrm{a}}{\tilde{\mu}}, \tag{3.12}$$

the concentration parameter, given as the relative concentration of electrons and holes with respect to the anion vacancy concentration

$$\delta = \frac{\tilde{N}}{\tilde{N}_\mathrm{a}}, \tag{3.13}$$

and the photogeneration parameter, which rescales the photogeneration rate

$$\gamma = \frac{F_\mathrm{ph} \alpha_g l^2}{\tilde{\mu} U_T \tilde{N}}. \tag{3.14}$$

We can also interpret the parameter ν as the ratio of the ionic carrier to the electric timescale. In a typical device, the parameters ν, λ, δ, and γ are small (compared to 1). More precisely, for the values in Table 3.1, we have $\nu \approx 10^{-12}$, $\lambda \approx 10^{-2}$, $\delta \approx 10^{-3}$ and $\gamma \approx 10^{-4}$. In particular, the parameters ν and λ^2 generate important stiffness in the model, which motivates using a robust implicit-in-time numerical scheme (see Chapter 4).

To summarize, we have the set of unknowns $(\varphi_\mathrm{n}, \varphi_\mathrm{p}, \varphi_\mathrm{a}, \psi)$ solving the equations (P) with rescaled initial conditions (PIC) (see Section 3.1.3). As boundary conditions, we supply the model with non-dimensionalized versions of (3.7b), (3.8), (3.9), and (3.10). For $t \geq 0$ and $k \in \{\mathrm{HTL}, \mathrm{ETL}\}$, we have

$$\begin{aligned}
\nabla\psi(\mathbf{x},t) \cdot \boldsymbol{\nu}(\mathbf{x}) = \mathbf{j}_\mathrm{n}(\mathbf{x},t) \cdot \boldsymbol{\nu}(\mathbf{x}) = \mathbf{j}_\mathrm{p}(\mathbf{x},t) \cdot \boldsymbol{\nu}(\mathbf{x}) &= 0, && \mathbf{x} \in \boldsymbol{\Gamma}^N, && \text{(PBCa)} \\
\psi(\mathbf{x},t) = \psi^D(\mathbf{x}), \quad \varphi_\mathrm{n}(\mathbf{x},t) = \varphi_\mathrm{p}(\mathbf{x},t) &= \varphi^D(\mathbf{x}), && \mathbf{x} \in \boldsymbol{\Gamma}^D, && \text{(PBCb)} \\
\mathbf{j}_\mathrm{a}(\mathbf{x},t) \cdot \boldsymbol{\nu}_\mathrm{intr}(\mathbf{x}) &= 0, && \mathbf{x} \in \partial\boldsymbol{\Omega}_\mathrm{intr}, && \text{(PBCc)} \\
\Big(\lambda^2 \nabla\psi(\mathbf{x},t;k) - \lambda^2 \nabla\psi(\mathbf{x},t;\mathrm{intr})\Big) \cdot \boldsymbol{\nu}_\mathrm{intr}(\mathbf{x}) &= 0, && \mathbf{x} \in \boldsymbol{\Sigma}_k, && \text{(PBCd)} \\
\Big(\mathbf{j}_\mathrm{n}(\mathbf{x},t;k) - \mathbf{j}_\mathrm{n}(\mathbf{x},t;\mathrm{intr})\Big) \cdot \boldsymbol{\nu}_\mathrm{intr}(\mathbf{x}) &= 0, && \mathbf{x} \in \boldsymbol{\Sigma}_k, && \text{(PBCe)} \\
\Big(\mathbf{j}_\mathrm{p}(\mathbf{x},t;k) - \mathbf{j}_\mathrm{p}(\mathbf{x},t;\mathrm{intr})\Big) \cdot \boldsymbol{\nu}_\mathrm{intr}(\mathbf{x}) &= 0, && \mathbf{x} \in \boldsymbol{\Sigma}_k, && \text{(PBCf)}
\end{aligned}$$

where $\psi^D, \varphi^D \in W^{1,\infty}(\mathbf{\Omega})$. Until the end of Chapter 4, we exclusively deal with this PDE system for the charge transport in perovskite solar cells. Further, if referring to the initial conditions (PIC), we refer to a non-dimensionalized version of (PIC), if not mentioned otherwise.

3.2. Memristive devices

Two-dimensional layered transition metal dichalcogenides (TMDCs) are promising memristive materials for neuromorphic computing systems. These materials could solve the issue of high energy consumption associated with conventional von Neumann computer architectures, commonly used as hardware for artificial intelligence calculations [57, 146, 207, 252]. However, our understanding of the physics of lateral TMDC memristors still needs to be completed, and there is ongoing debate about the mechanisms responsible for resistive switching in these devices. Experimental evidence suggests different switching mechanisms, including the movement of chalcogen vacancies [150, 206]. In our context, understanding the key switching mechanism is related to understanding the origin of hysteresis in the current-voltage characteristics.

The existing models for lateral devices are based on analytical approximations of the current-voltage curve with numerous fitting parameters [207] or compact model formulations [226, 262]. While such models can be helpful for circuit simulations and design due to their computational efficiency, they fail to capture the complex dynamics of the switching process. To our knowledge, the first vacancy-assisted drift-diffusion model for describing lateral TMDC-based memristors is formulated in [DA5]. While drift-diffusion models describing charge transport in memristors based on other materials also exist [3, 229], they need to include a proper discussion of the limitation of vacancy accumulation, as demonstrated in [DA5].

3.2.1. Bulk equations

In contrast to a perovskite solar cell, the memristive device geometry is solely given by the semiconducting material layer, i.e., $\mathbf{\Omega} = \mathbf{\Omega}_{\text{intr}}$, where $\mathbf{\Omega} \subset \mathbb{R}^d$, $d \in \{1, 2, 3\}$, is an open, connected, and bounded spatial domain. Figure 3.2 illustrates a typical lateral memristive device geometry and its cross-section in the x-y plane. The device comprises a TMDC flake on a substrate, given by silicon dioxide (SiO_2) and silicon (Si). The flake is laterally sandwiched between two electrodes, usually composed of a titanium (Ti) and a gold (Au) layer. We can further simplify the model geometry and represent it by a one-dimensional (1D) conducting channel, defined by the flake length, in x direction, see Figure 3.2. As explained in Section 2.4.1.2, we assume vacancy

migration of chalcogen defects. The electron, hole, and chalcogen defect densities $n_\mathrm{n}, n_\mathrm{p}, n_\mathrm{a}$ satisfy the continuity equations

$$z_\alpha q \partial_t n_\alpha + \nabla \cdot \mathbf{j}_\alpha = 0, \quad \mathbf{x} \in \mathbf{\Omega},\ t \geq 0, \quad \text{for } \alpha \in \{\mathrm{n}, \mathrm{p}, \mathrm{a}\}, \tag{3.15a}$$

which are self-consistently coupled via the electrostatic potential ψ to the nonlinear Poisson equation

$$-\nabla \cdot (\varepsilon_s \nabla \psi) = q \sum_{\alpha \in \{\mathrm{n},\mathrm{p},\mathrm{a}\}} z_\alpha n_\alpha(\psi, \varphi_\alpha) + qC(\mathbf{x}), \quad \mathbf{x} \in \mathbf{\Omega},\ t \geq 0, \tag{3.15b}$$

where $C \in L^\infty(\mathbf{\Omega})$ denotes the background charge density. In our charge transport model, we assume a negligible vacancy generation and substantial n-type doping (i.e., $n_\mathrm{n} \gg n_\mathrm{p}$). Consequently, this leads to no reaction or production rates in (3.15a). Lastly, the current densities are defined as before (see (2.2))

$$\mathbf{j}_\alpha = -z_\alpha^2 q \mu_\alpha n_\alpha \nabla \varphi_\alpha, \quad \mathbf{x} \in \mathbf{\Omega},\ t \geq 0, \quad \text{for } \alpha \in \{\mathrm{n}, \mathrm{p}, \mathrm{a}\}. \tag{3.15c}$$

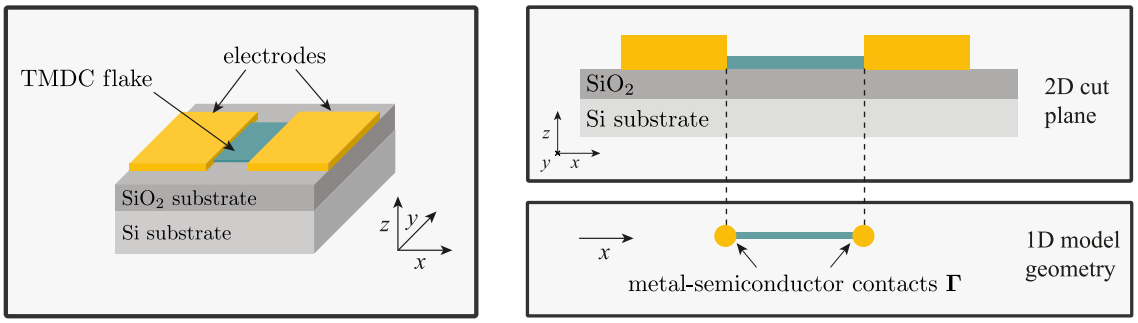

Figure 3.2.: Illustration of the three-dimensional geometry of a memristive device with indicated SiO_2/Si substrate, the TMDC flake and the contact electrodes (left), a two-dimensional view of the x-z cut plane (upper right), and a simplification of the geometry for a one-dimensional model (lower right). (From [DA5] with modifications.)

3.2.2. Initial and boundary conditions

The system (3.15) is supplied with initial conditions for $t = 0$

$$\varphi_\mathrm{n}(\mathbf{x}, 0) = \varphi_\mathrm{n}^0(\mathbf{x}), \quad \varphi_\mathrm{p}(\mathbf{x}, 0) = \varphi_\mathrm{p}^0(\mathbf{x}), \quad \varphi_\mathrm{a}(\mathbf{x}, 0) = \varphi_\mathrm{a}^0(\mathbf{x}), \quad \text{for } \mathbf{x} \in \mathbf{\Omega}, \tag{MIC}$$

where we assume $\varphi_\mathrm{n}^0, \varphi_\mathrm{p}^0, \varphi_\mathrm{a}^0 \in L^\infty(\mathbf{\Omega})$. As before, we define the initial densities $n_\alpha^0(\mathbf{x}) = N_\alpha \mathcal{F}_\alpha(\eta_\alpha(\varphi_\alpha^0, \psi(\mathbf{x}, 0)))$ for $\alpha \in \{\mathrm{n}, \mathrm{p}, \mathrm{a}\}$.

We divide the outer boundary of the device geometry $\mathbf{\Omega}$ into two parts: $\mathbf{\Gamma}$ and $\mathbf{\Gamma}^N$. Here, $\mathbf{\Gamma}$ refers to the interface between the flake and the electrodes and $\mathbf{\Gamma}^N$ to the remaining interfaces. We assume that $\mathbf{\Gamma}$ and $\mathbf{\Gamma}^N$ are closed subsets of $\partial\mathbf{\Omega}$ with $\partial\mathbf{\Omega} = \mathbf{\Gamma} \cup \mathbf{\Gamma}^N$. For the chalcogen defects all boundaries represent physical barriers

$$\mathbf{j}_\mathrm{a}(\mathbf{x}, t) \cdot \boldsymbol{\nu}(\mathbf{x}) = 0, \quad \mathbf{x} \in \partial\mathbf{\Omega},\ t \geq 0, \tag{3.16}$$

where $\boldsymbol{\nu}$ is the outward pointing unit normal to $\partial\mathbf{\Omega}$. At the isolating Neumann boundary we impose for the other species

$$\nabla\psi(\mathbf{x}, t) \cdot \boldsymbol{\nu}(\mathbf{x}) = \mathbf{j}_\mathrm{n}(\mathbf{x}, t) \cdot \boldsymbol{\nu}(\mathbf{x}) = \mathbf{j}_\mathrm{p}(\mathbf{x}, t) \cdot \boldsymbol{\nu}(\mathbf{x}) = 0, \quad \mathbf{x} \in \mathbf{\Gamma}^N,\ t \geq 0. \tag{3.17}$$

At the metal-semiconductor contact $\mathbf{\Gamma}$ it is possible to impose a range of boundary conditions. In Section 3.2.2.1 and Section 3.2.2.2, we assume that $\mathbf{\Gamma}$ represents a Schottky contact, where we use the notation $\mathbf{\Gamma}^S = \mathbf{\Gamma}$. Subsequently, in Section 3.2.2.3, we consider a scenario where the boundary $\mathbf{\Gamma}$ behaves like an ohmic contact, modeled by Dirichlet boundary conditions. There, we employ the notation $\mathbf{\Gamma}^D = \mathbf{\Gamma}$.

3.2.2.1. Schottky boundary conditions

In case of classical Schottky contacts at $\mathbf{\Gamma}^S$, thermionic emission [52] is described for electrons and holes with the boundary conditions

$$\mathbf{j}_\mathrm{n}(\mathbf{x}, t) \cdot \boldsymbol{\nu}(\mathbf{x}) = z_\mathrm{n} q v_\mathrm{n}(n_\mathrm{n}(\mathbf{x}, t) - n_{\mathrm{n},0}), \quad \mathbf{x} \in \mathbf{\Gamma}^S,\ t \geq 0, \tag{3.18a}$$

$$\mathbf{j}_\mathrm{p}(\mathbf{x}, t) \cdot \boldsymbol{\nu}(\mathbf{x}) = z_\mathrm{p} q v_\mathrm{p}(n_\mathrm{p}(\mathbf{x}, t) - n_{\mathrm{p},0}), \quad \mathbf{x} \in \mathbf{\Gamma}^S,\ t \geq 0. \tag{3.18b}$$

Here, $v_\mathrm{n}, v_\mathrm{p}$ are the electron and hole recombination velocities given by (with h as Planck constant)

$$v_\mathrm{n} = \frac{4\pi m_\mathrm{n}^*(k_B T)^2}{h^3 N_\mathrm{n}} \quad \text{and} \quad v_\mathrm{p} = \frac{4\pi m_\mathrm{p}^*(k_B T)^2}{h^3 N_\mathrm{p}}, \tag{3.19}$$

with the effective mass m_n^* and m_p^* of electrons and holes, respectively. The corresponding equilibrium carrier densities $n_{\mathrm{n},0}$, and $n_{\mathrm{p},0}$, at the contacts are

$$n_{\mathrm{n},0} = N_\mathrm{n} \mathcal{F}_\mathrm{n}\left(-\frac{\phi_0}{k_B T}\right) \quad \text{and} \quad n_{\mathrm{p},0} = N_\mathrm{p} \mathcal{F}_\mathrm{p}\left(-\frac{E_\mathrm{g} - \phi_0}{k_B T}\right), \tag{3.20}$$

where $\phi_0 = \phi_0(\mathbf{x}) > 0$ is an intrinsic Schottky energy barrier constant in time and $E_\mathrm{g} = E_\mathrm{n} - E_\mathrm{p}$ is the band gap. For the electrostatic potential at the metal-semiconductor contacts $\mathbf{\Gamma}^S$ we apply the Dirichlet condition

$$\psi(\mathbf{x}, t) = \psi_0(\mathbf{x}) + U(\mathbf{x}, t)\ , \quad \mathbf{x} \in \mathbf{\Gamma}^S,\ t \geq 0, \tag{3.21}$$

with $\psi_0 = -(\phi_0 - E_\mathrm{n})/q$ denoting an intrinsic electrostatic potential barrier, and U denoting a time-dependent applied voltage at the contact. The intrinsic Schottky barrier ϕ_0 is considered as a material and device parameter, i.e., for a given device, ψ_0 and ϕ_0 depend only on $\mathbf{x} \in \mathbf{\Gamma}^S$.

3.2.2.2. Image-charge-induced Schottky barrier lowering

The charge transport model (3.15) with the initial conditions (MIC) and classical Schottky boundary conditions (3.18)–(3.21) characterizes a system where the band-edges $\mathscr{E}_\mathrm{n} = E_\mathrm{n} - q\psi$, $\mathscr{E}_\mathrm{p} = E_\mathrm{p} - q\psi$ on the boundary $\mathbf{\Gamma}^S$ are prescribed by a Schottky barrier ϕ_0. In what follows, we denote the underlying electrostatic potential unaffected by any additional external charges by ψ_r and refer to it as residual electrostatic potential. Correspondingly, the electric potential energy for electrons is given by $\phi_r = q_\mathrm{n}\psi_r$ and is visualized in Figure 3.3 (right, gray curve). Here, $q_\mathrm{n} = z_\mathrm{n} q$ is the electrons' electric charge.

Without an external bias, the band-edge of electrons for the previously defined Schottky boundary model is defined as

$$\mathscr{E}_\mathrm{n} = E_\mathrm{n} + \phi, \quad \phi = \phi_r, \quad \text{in } \mathbf{\Omega}, \tag{3.22}$$

$$\mathscr{E}_\mathrm{n} = \phi_0, \quad \text{on } \mathbf{\Gamma}^S, \tag{3.23}$$

where ϕ denotes the electric potential energy in accordance with (2.25). However, any point charge near a metal-semiconductor junction induces an opposite polarity charge (*image charge*) in the metal through charge redistribution caused by the electric field (Figure 3.3, left).

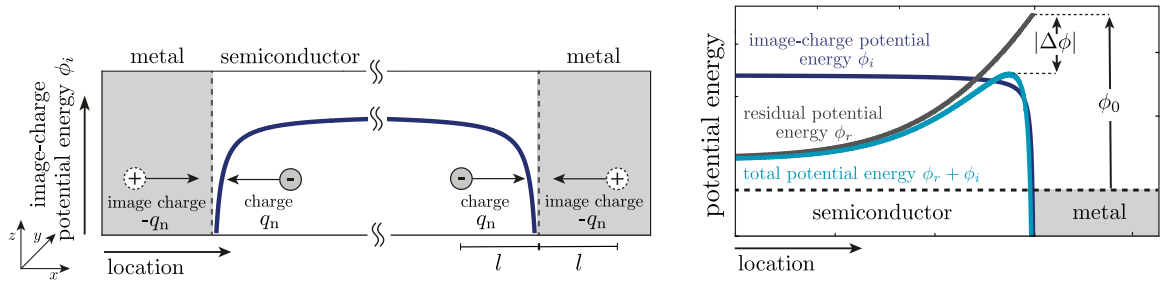

Figure 3.3.: Schematic illustration of an electron point charge q_n at the semiconductor-metal interfaces inducing an image charge $-q_\mathrm{n}$ in the metal electrode, which results in an attractive image-charge potential energy ϕ_i (left), and the superposition of the residual potential energy ϕ_r and the image-charge potential energy ϕ_i without an external bias. The superposition reduces the interfacial potential energy barrier maximum by $|\Delta\phi|$ relative to the value of ϕ_r at the interface (right). (From [DA5] with modifications.)

The induction of image charges adds a contribution ϕ_i (Figure 3.3, right, dark blue curve), to which we will refer as *image-charge potential energy* [52, 235], to the total electric potential energy

$$\phi = \phi_r + \phi_i, \quad \text{in } \mathbf{\Omega}. \tag{3.24}$$

The new total potential energy (3.24) has an impact on the band-edges $\mathscr{E}_\mathrm{n}$, $\mathscr{E}_\mathrm{p}$ and alters the boundary values of $\mathscr{E}_\mathrm{n}$, $\mathscr{E}_\mathrm{p}$ by some $\Delta\phi$ (see Figure 3.3, right, light blue curve). As will be demonstrated, in case of the electron band-edge this means when no external bias is applied

$$\begin{aligned} \mathscr{E}_\mathrm{n} &= E_\mathrm{n} + \phi, \quad \phi = \phi_r + \phi_i, && \text{in } \mathbf{\Omega}, \\ \mathscr{E}_\mathrm{n} &= \phi_0 + \Delta\phi, && \text{on } \mathbf{\Gamma}^S. \end{aligned} \tag{3.25}$$

This change in the boundary values of the potential energies can be schematically observed in Figure 3.3 (right). As shown, the total potential energy ϕ is indeed reduced due to the superposition of the residual potential energy ϕ_r with the image-charge potential energy ϕ_i, which is why this effect is known as *(image-charge-induced) Schottky barrier lowering*.

Now, we will carefully extend the classical Schottky boundary conditions (3.18)–(3.21) on $\mathbf{\Gamma}^S$ by identifying the barrier change $\Delta\phi$ caused by Schottky barrier lowering. To accomplish this, we rely on the following assumptions.

1. The semiconductor-metal interface is planar, with the device's width and thickness aligned perfectly with the y and z axes.
2. The electron point charge and the induced image charge are symmetric around the interface. Both are evaluated at the same distance l from the interface $\mathbf{\Gamma}^S$.
3. We focus only on the closest electrode's induced charge and image force, i.e., we ignore image forces from other metal contacts.

We proceed in two steps to find a suitable description of $\Delta\phi$ entering (3.25). First, we use Coulomb's law to calculate the energy induced by the image charge ϕ_i. Due to a planar setup, the Coulomb force reduces to a one-dimensional force, dependent on an arbitrary distance s between charges and the interface $\mathbf{\Gamma}^S$

$$F(s) = -\frac{q_\mathrm{n}^2}{4\pi\varepsilon_i}\frac{1}{(2s)^2}, \quad s \geq 0,$$

where the negative sign indicates attraction independent of direction. It is worth noting that we replaced the vacuum permittivity in Coulomb's law by an appropriate real-valued permittivity describing the semiconductor medium, the *image-force permittivity*

ε_i [234, 235]. We can calculate the image force potential energy ϕ_i by integrating F from a reference position to the exact position $s = l > 0$ assuming an infinitely far away reference position [98]

$$\phi_i = -\int_{\infty}^{l} F\, ds = -\frac{q_\mathrm{n}^2}{16\pi\varepsilon_i}\int_{l}^{\infty}\frac{1}{s^2}\, ds = -\frac{q_\mathrm{n}^2}{16\pi\varepsilon_i}\frac{1}{l}. \tag{3.26}$$

With (3.26) we have a suitable description for the image-charge potential energy ϕ_i.

Second, we must evaluate the residual potential energy $\phi_r = q_\mathrm{n}\psi_r$ at $\mathbf{\Gamma}^S$ to address modified boundary conditions. To do this, we perform a linear Taylor expansion in the opposite direction of the outward pointing unit normal to $\mathbf{\Gamma}^S$, denoted by $\boldsymbol{\nu}$,

$$\psi_r(\mathbf{x} - l\boldsymbol{\nu}) \approx \psi_r(\mathbf{x}) - l\nabla_{\boldsymbol{\nu}}\psi_r(\mathbf{x}), \quad \mathbf{x} \in \mathbf{\Gamma}^S, \tag{3.27}$$

where $\nabla_{\boldsymbol{\nu}}\psi_r = \nabla\psi_r \cdot \boldsymbol{\nu}$. With (3.24), (3.26), and (3.27), we can identify the total potential energy ϕ as a function of the distance l between the charges and the interface

$$\phi(l) = \phi_r(l) + \phi_i(l) = q_\mathrm{n}\left(\psi_r - l\nabla_{\boldsymbol{\nu}}\psi_r + \frac{q}{16\pi\varepsilon_i}\frac{1}{l}\right). \tag{3.28}$$

The total potential energy ϕ attains a maximum near the interface at

$$l^* = \sqrt{-\frac{q}{16\pi\varepsilon_i\nabla_{\boldsymbol{\nu}}\psi_r}}, \quad \text{if } \nabla_{\boldsymbol{\nu}}\psi_r < 0,$$

where we omitted the non-physical solution resulting into a negative length. In the one-dimensional case and under the assumption of a planar interface, the condition $\nabla_{\boldsymbol{\nu}}\psi_r < 0$ indicates that ψ_r needs to be bent downwards. The total potential energy evaluated at $l = l^*$ reads

$$\phi(l^*) = q_\mathrm{n}\left(\psi_r + \sqrt{-\frac{q\nabla_{\boldsymbol{\nu}}\psi_r}{4\pi\varepsilon_i}}\right) =: q_\mathrm{n}\psi_r + \Delta\phi,$$

where the value of $\Delta\phi$ is set to the second term multiplied by the electrons' charge q_n. Assuming that l^* is negligibly small, the electron band-edge $\mathscr{E}_\mathrm{n}$ at the boundary can be approximated by

$$\mathscr{E}_\mathrm{n} = E_\mathrm{n} + \phi_r + \phi_i \approx (E_\mathrm{n} + q_\mathrm{n}\psi_r) + q_\mathrm{n}\sqrt{-\frac{q\nabla_{\boldsymbol{\nu}}\psi_r}{4\pi\varepsilon_i}} = \phi_0 + \Delta\phi, \quad \mathbf{x} \in \mathbf{\Gamma}^S, \tag{3.29}$$

where due to (3.22), we have $E_\mathrm{n} + q_\mathrm{n}\psi_r = \phi_0$ for boundary values $\mathbf{x} \in \mathbf{\Gamma}^S$. The equation (3.29) is consistent with (3.25). Since $q_\mathrm{n} < 0$, the formula in (3.29) demonstrates that the potential barrier at the boundary is indeed lowered by a value $|\Delta\phi|$, as illustrated

in Figure 3.3 (right). While the image-charge potential energy ϕ_i is constant in time, $\phi_r = q_\mathrm{n}\psi_r$ depends on the charge distribution within the semiconductor, which can influence $\Delta\phi$. In total, in case of Schottky barrier lowering, the electric potential boundary condition differs from (3.21) by the barrier change $\Delta\psi = \Delta\phi/q_\mathrm{n}$, i.e.,

$$\psi(\mathbf{x},t) = \psi_0(\mathbf{x}) + U(\mathbf{x},t) + \Delta\psi(\mathbf{x},t)\ , \quad \mathbf{x}\in\mathbf{\Gamma}^S,\ t\geq 0, \tag{3.30}$$

where

$$\Delta\psi = \begin{cases} \sqrt{-\frac{q\nabla_{\boldsymbol{\nu}}\psi_r}{4\pi\varepsilon_\mathrm{i}}}, & \nabla_{\boldsymbol{\nu}}\psi_r < 0, \\ 0, & \nabla_{\boldsymbol{\nu}}\psi_r \geq 0. \end{cases} \tag{3.31}$$

The latter case ($\nabla_{\boldsymbol{\nu}}\psi_r \geq 0$) assumes no barrier changes for non-physical negative lengths $l = l^*$. Furthermore, the equations for the equilibrium carrier densities at the metal contacts $\mathbf{\Gamma}^S$ in (3.20) must be altered to

$$n_{\mathrm{n},0} = N_\mathrm{n}\mathcal{F}_\mathrm{n}\left(-\frac{\phi_0+\Delta\phi}{k_BT}\right), \quad n_{\mathrm{p},0} = N_\mathrm{p}\mathcal{F}_\mathrm{p}\left(-\frac{E_\mathrm{g}-(\phi_0+\Delta\phi)}{k_BT}\right), \tag{3.32}$$

to consider the change in the Schottky barrier.

As previously indicated, the residual electrostatic potential ψ_r solves a Poisson equation with the same volumetric space charge density as for ψ in (3.15b), supplied with Dirichlet boundary conditions at the metal contacts $\mathbf{\Gamma}^S$ and no flux boundary conditions on the remaining interfaces $\mathbf{\Gamma}^N$. Consequently, we solve a system of five coupled partial differential equations with five unknowns, namely, the three quasi Fermi potentials $\varphi_\mathrm{n}, \varphi_\mathrm{p}, \varphi_\mathrm{a}$, and the two electrostatic potentials ψ and ψ_r.

Let $\rho(\psi) = q\sum_{\alpha\in\{\mathrm{n,p,a}\}} z_\alpha n_\alpha(\psi,\varphi_\alpha) + qC$ denote the right-hand side of the Poisson equation (3.15b). Then, the initial boundary value problem for $t \geq 0$ can be summarized by the bulk equations

$$-\nabla\cdot(\varepsilon_s\nabla\psi) = \rho(\psi), \qquad \mathbf{x}\in\mathbf{\Omega}, \tag{3.33a}$$
$$-\nabla\cdot(\varepsilon_s\nabla\psi_r) = \rho(\psi), \qquad \mathbf{x}\in\mathbf{\Omega}, \tag{3.33b}$$
$$z_\alpha q\partial_t n_\alpha + \nabla\cdot\mathbf{j}_\alpha = 0, \quad \text{for } \alpha\in\{\mathrm{n,p,a}\}, \quad \mathbf{x}\in\mathbf{\Omega}, \tag{3.33c}$$

with zero-flux boundary conditions on $\mathbf{\Gamma}^N$ and the Schottky barrier lowering conditions at the metal contacts $\mathbf{\Gamma}^S$ for $t \geq 0$

$$\psi = \psi_0 + U + \Delta\psi(\nabla_{\boldsymbol{\nu}}\psi_r), \quad \mathbf{x}\in\mathbf{\Gamma}^S, \tag{3.33d}$$
$$\psi_r = \psi_0 + U, \qquad \mathbf{x}\in\mathbf{\Gamma}^S, \tag{3.33e}$$
$$\mathbf{j}_\mathrm{n}\cdot\boldsymbol{\nu} = z_\mathrm{n}qv_\mathrm{n}(n_\mathrm{n}-n_{\mathrm{n},0}), \qquad \mathbf{x}\in\mathbf{\Gamma}^S, \tag{3.33f}$$
$$\mathbf{j}_\mathrm{p}\cdot\boldsymbol{\nu} = z_\mathrm{p}qv_\mathrm{p}(n_\mathrm{p}-n_{\mathrm{p},0}), \qquad \mathbf{x}\in\mathbf{\Gamma}^S, \tag{3.33g}$$
$$\mathbf{j}_\mathrm{a}\cdot\boldsymbol{\nu} = 0, \qquad \mathbf{x}\in\mathbf{\Gamma}^S, \tag{3.33h}$$

where $\boldsymbol{\nu}$ is the outward pointing unit normal to $\boldsymbol{\Gamma}^S$ and (3.32) defines the equilibrium densities $n_{\mathrm{n},0}$, $n_{\mathrm{p},0}$. Lastly, we supply the problem with the initial conditions (MIC).

Classical Schottky boundary $\boldsymbol{\Gamma}^S$

unknowns: $\varphi_\mathrm{n}, \varphi_\mathrm{p}, \varphi_\mathrm{a}, \psi$
given: ϕ_0 (intrinsic Schottky barrier)

1. $\psi = \psi_0 + U$ on $\boldsymbol{\Gamma}^S$

2. $\mathbf{j}_\mathrm{n}(\psi)\cdot\boldsymbol{\nu} = z_\mathrm{n} q v_\mathrm{n}\Big(n_\mathrm{n}(\psi) - n_{\mathrm{n},0}(\phi_0)\Big)$ on $\boldsymbol{\Gamma}^S$
   $\mathbf{j}_\mathrm{p}(\psi)\cdot\boldsymbol{\nu} = z_\mathrm{p} q v_\mathrm{p}\Big(n_\mathrm{p}(\psi) - n_{\mathrm{p},0}(\phi_0)\Big)$ on $\boldsymbol{\Gamma}^S$

3. $\mathbf{j}_\mathrm{a}(\psi)\cdot\boldsymbol{\nu} = 0$ on $\boldsymbol{\Gamma}^S$

Image-charge induced Schottky boundary $\boldsymbol{\Gamma}^S$

unknowns: $\varphi_\mathrm{n}, \varphi_\mathrm{p}, \varphi_\mathrm{a}, \psi, \psi_r$
given: ϕ_0 (intrinsic Schottky barrier)

1. a. $\psi = \psi_0 + U + \Delta\psi(\nabla_{\boldsymbol{\nu}}\psi_r)$ on $\boldsymbol{\Gamma}^S$

   b. $\psi_r = \psi_0 + U$ on $\boldsymbol{\Gamma}^S$
   $-\nabla\cdot(\varepsilon_s\nabla\psi_r) = qC + q\sum_{\alpha\in\{\mathrm{n,p,a}\}} z_\alpha n_\alpha(\psi)$ in $\boldsymbol{\Omega}$

2. $\mathbf{j}_\mathrm{n}(\psi)\cdot\boldsymbol{\nu} = z_\mathrm{n} q v_\mathrm{n}\Big(n_\mathrm{n}(\psi) - n_{\mathrm{n},0}(\phi_0, \nabla_{\boldsymbol{\nu}}\psi_r)\Big)$ on $\boldsymbol{\Gamma}^S$
   $\mathbf{j}_\mathrm{p}(\psi)\cdot\boldsymbol{\nu} = z_\mathrm{p} q v_\mathrm{p}\Big(n_\mathrm{p}(\psi) - n_{\mathrm{p},0}(\phi_0, \nabla_{\boldsymbol{\nu}}\psi_r)\Big)$ on $\boldsymbol{\Gamma}^S$

3. $\mathbf{j}_\mathrm{a}(\psi)\cdot\boldsymbol{\nu} = 0$ on $\boldsymbol{\Gamma}^S$

Figure 3.4.: Summary of the classical Schottky (left) and the image-charge induced Schottky boundary model (right), where the dependencies on the electric potentials ψ, ψ_r are highlighted. The latter boundary model introduces the residual electric potential ψ_r as an additional unknown.

We note that the Poisson equation with respect to ψ in (3.33b) is *nonlinear* in ψ, while (3.33c) is *linear* in ψ_r. In Figure 3.4, the equations for the classical and the image-charge induced Schottky boundary model are summarized. Including Schottky barrier lowering adds a term $\Delta\psi(\nabla_{\boldsymbol{\nu}}\psi_r)$ to the electric potential boundary condition (3.21). This term depends on the projected gradient of the additional unknown, the residual electric potential ψ_r, which solves the Poisson equation for the same material charge density as ψ.

In Section 5.3.2, we will conduct simulations to study how reducing the Schottky barrier heights due to the introduced boundary model will impact the current-voltage characteristics of TMDC memristors and compare the results with measurements found in literature.

3.2.2.3. Ohmic contacts

Similar to the PSC model, we can supply the memristive charge transport model with ohmic boundary conditions. For this, we replace $\boldsymbol{\Gamma}^S$ by $\boldsymbol{\Gamma}^D$. As the outer boundary conditions on $\boldsymbol{\Gamma}^D$, we have

$$\psi(\mathbf{x},t) = \psi_0(\mathbf{x}) + U(\mathbf{x},t), \quad \varphi_\mathrm{n}(\mathbf{x},t) = \varphi_\mathrm{p}(\mathbf{x},t) = U(\mathbf{x},t), \qquad \mathbf{x}\in\boldsymbol{\Gamma}^D,\ t\geq 0, \tag{3.34}$$

with the locally electroneutral solution ψ_0 and an externally applied voltage U, as introduced in Section 3.1.3.1.

Under the assumption of time-independent ohmic boundary conditions, we will also prove the existence of solutions $(\varphi_\mathrm{n}, \varphi_\mathrm{p}, \varphi_\mathrm{a}, \psi)$ to an implicit-in-time finite volume discretization scheme in Chapter 4. In consistency with Remark 3.1, we apply

$$\psi(\mathbf{x},t) = \psi^D(\mathbf{x}), \quad \varphi_\mathrm{n}(\mathbf{x},t) = \varphi_\mathrm{p}(\mathbf{x},t) = \varphi^D(\mathbf{x}), \qquad \mathbf{x} \in \mathbf{\Gamma}^D, \ t \geq 0, \tag{3.35}$$

where $\psi^D, \varphi^D \in W^{1,\infty}(\mathbf{\Omega})$ are given Dirichlet values.

3.2.3. Non-dimensionalization

As in Section 3.1.4, we will formulate a non-dimensionalized model for the charge transport in TMDC memristive devices, which serves as a reference model for the numerical analysis in Chapter 4. We rewrite the equations in terms of the scaled variables given as the ratio of the unscaled physical quantity to the scaling factors defined in Table 3.2. For this, we use the parameter set S_1 (Table B.3, Table B.4).

We assume for the electron and hole mobility $\mu_\mathrm{n} = \mu_\mathrm{p}$ and for all band-edge energies $E_\alpha = 0$ with $\alpha = \{\mathrm{n}, \mathrm{p}, \mathrm{a}\}$. However, we allow in contrast to Section 3.1.4 different magnitudes of electron and hole densities. For the introduced scaling factors $\tilde{C}, \tilde{N}_\mathrm{n}, \tilde{N}_\mathrm{a}$ in Table 3.2, we assume $\tilde{C} = N_\mathrm{p}$, $\tilde{N}_\mathrm{n} = N_\mathrm{n}$, $\tilde{N}_\mathrm{a} = N_\mathrm{a}$. Similarly, we take $\tilde{\mu}_\mathrm{a} = \mu_\mathrm{a}$, and $\tilde{\mu} = \mu_\mathrm{n} = \mu_\mathrm{p}$. As before, we choose the timescale of chalcogen vacancies. Moreover, the location vector is rescaled with respect to the channel length.
The dimensionless versions of the mass balance equations (3.15a) read

$$\nu\, z_\mathrm{n} \partial_t n_\mathrm{n} + \nabla \cdot \mathbf{j}_\mathrm{n} = 0, \qquad \mathbf{x} \in \mathbf{\Omega}, \ t \geq 0, \tag{Ma}$$

$$\nu\, z_\mathrm{p} \partial_t n_\mathrm{p} + \nabla \cdot \mathbf{j}_\mathrm{p} = 0, \qquad \mathbf{x} \in \mathbf{\Omega}, \ t \geq 0, \tag{Mb}$$

$$z_\mathrm{a} \partial_t n_\mathrm{a} + \nabla \cdot \mathbf{j}_\mathrm{a} = 0, \qquad \mathbf{x} \in \mathbf{\Omega}, \ t \geq 0, \tag{Mc}$$

which are self-consistently coupled to the non-dimensionalized Poisson equation

$$-\lambda^2 \Delta \psi = \delta_\mathrm{n}\Big(z_\mathrm{n} n_\mathrm{n} + \delta_\mathrm{p}\left(z_\mathrm{p} n_\mathrm{p} + C\right)\Big) + z_\mathrm{a} n_\mathrm{a}, \qquad \mathbf{x} \in \mathbf{\Omega}, \ t \geq 0. \tag{Md}$$

The dimensionless charge carrier currents are given as

$$\mathbf{j}_\alpha = -z_\alpha^2 n_\alpha \nabla \varphi_\alpha, \quad \alpha \in \{\mathrm{n}, \mathrm{p}, \mathrm{a}\}, \tag{Me}$$

and the non-dimensionalized version of the state equation (2.3) equals

$$n_\alpha = \mathcal{F}_\alpha\Big(z_\alpha(\varphi_\alpha - \psi)\Big), \quad \alpha \in \{\mathrm{n}, \mathrm{p}, \mathrm{a}\}. \tag{Mf}$$

There are four dimensionless parameters, the rescaled Debye length, which is taken with respect to the vacancy concentration

$$\lambda = \sqrt{\frac{\varepsilon_s U_T}{l^2 q \tilde{N}_\mathrm{a}}} \approx 10^{-5}, \tag{3.36}$$

Symbol	Meaning	Scaling factor	Order of magnitude
$\mathbf{x}$	Space variable	l	10^{-6} m
φ_α, φ^D, φ^0_α	Quasi Fermi potentials	U_T	10^{-2} V
ψ, ψ^D	Electric potential	U_T	10^{-2} V
C	Doping profile	$\tilde{C}$	10^{21} m^{-3}
n_n	Electron density	$\tilde{N}_\mathrm{n}$	10^{25} m^{-3}
n_p	Hole density	$\tilde{C}$	10^{21} m^{-3}
n_a	Vacancy density	$\tilde{N}_\mathrm{a}$	10^{28} m^{-3}
$\mu_\mathrm{n}, \mu_\mathrm{p}$	Electron and hole mobility	$\tilde{\mu}$	10^{-4} m^2/(Vs)
μ_a	Vacancy mobility	$\tilde{\mu}_\mathrm{a}$	10^{-14} m^2/(Vs)
t	Time variable	$\frac{l^2}{\tilde{\mu}_\mathrm{a} U_T}$	10^4 s
$\mathbf{j}_\mathrm{n}$	Electron current density	$\frac{q U_T \tilde{N}_\mathrm{n} \tilde{\mu}}{l}$	10^6 C/(m^{2}s)
$\mathbf{j}_\mathrm{p}$	Hole current density	$\frac{q U_T \tilde{C} \tilde{\mu}}{l}$	10^2 C/(m^{2}s)
$\mathbf{j}_\mathrm{a}$	Vacancy current density	$\frac{q U_T \tilde{N}_\mathrm{a} \tilde{\mu}_\mathrm{a}}{l}$	10^{-1} C/(m^{2}s)

Table 3.2.: Scaling factors of a MoS_2-based memristive device related to the parameter set S_1 (Table B.3, Table B.4) at $T = 300$ K. Since the doping and hole densities are small compared to the electron and vacancy densities, we use the same scaling factor.

the mobility parameter, given as the relative mobility of chalcogen vacancies with respect to the mobility of electrons and holes

$$\nu = \frac{\tilde{\mu}_\mathrm{a}}{\tilde{\mu}} \approx 10^{-10}, \tag{3.37}$$

the electron concentration parameter, defined as the relative concentration of electrons

with respect to the chalcogen vacancy concentration

$$\delta_{\mathrm{n}} = \frac{\tilde{N}_{\mathrm{n}}}{\tilde{N}_{\mathrm{a}}} \approx 10^{-3}, \tag{3.38}$$

and the hole concentration parameter, given as the relative doping/hole concentration with respect to the electron concentration

$$\delta_{\mathrm{p}} = \frac{\tilde{C}}{\tilde{N}_{\mathrm{n}}} \approx 10^{-4}. \tag{3.39}$$

Similar to the non-dimensionalized PSC charge transport model, we have a stiff model, generated by λ^2 and ν. We use the non-dimensionalized version of (MIC) (see Section 3.2.2) as initial condition if not mentioned otherwise. As boundary conditions, we supply the model with a dimensionless version of the ohmic contact boundary model (3.35) at $\mathbf{\Gamma}^D = \mathbf{\Gamma}$, introduced in Section 3.2.2.3. Furthermore, on the isolating interface $\mathbf{\Gamma}^N$, we consider dimensionless versions of (3.16) and (3.17). Thus, for $t \geq 0$, we have

$$\begin{aligned}
\nabla\psi(\mathbf{x},t)\cdot\boldsymbol{\nu}(\mathbf{x}) = \mathbf{j}_{\mathrm{n}}(\mathbf{x},t)\cdot\boldsymbol{\nu}(\mathbf{x}) = \mathbf{j}_{\mathrm{p}}(\mathbf{x},t)\cdot\boldsymbol{\nu}(\mathbf{x}) = 0, \qquad & \mathbf{x}\in\mathbf{\Gamma}^N, && \text{(MBCa)}\\
\psi(\mathbf{x},t) = \psi^D(\mathbf{x}), \quad \varphi_{\mathrm{n}}(\mathbf{x},t) = \varphi_{\mathrm{p}}(\mathbf{x},t) = \varphi^D(\mathbf{x}), \qquad & \mathbf{x}\in\mathbf{\Gamma}^D, && \text{(MBCb)}\\
\mathbf{j}_{\mathrm{a}}(\mathbf{x},t)\cdot\boldsymbol{\nu}(\mathbf{x}) = 0, \qquad & \mathbf{x}\in\partial\mathbf{\Omega}, && \text{(MBCc)}
\end{aligned}$$

where $\psi^D, \varphi^D \in W^{1,\infty}(\mathbf{\Omega})$. Until the end of Chapter 4, we only deal with the PDE system (M), (MIC), (MBC) with the unknowns $(\varphi_{\mathrm{n}}, \varphi_{\mathrm{p}}, \varphi_{\mathrm{a}}, \psi)$ for the charge transport in TMDC-based memristors.

3.3. Entropy method to prove the existence of solution

A mathematical study of the charge transport model for perovskite solar cells has not been conducted yet. In contrast, the charge transport model for memristive devices was explored in [124]. There, the authors established various results, including the global existence of weak solutions, assuming that all charge carriers obey a Boltzmann relation with the time-independent boundary conditions (MBC).

In comparison, classical drift-diffusion models have been studied in detail, see, e.g., [89, 90, 122, 127, 163, 164, 174]. An essential *a priori* estimate for these models relies on the evolution of the physical *free energy* or a related energy functional. It allows us to study the well-posedness of the equations as well as the asymptotic behavior of

their solution [21, 89, 174]. The techniques relying on a well-chosen physically relevant Lyapunov functional have been used for many dissipative systems of PDEs and are usually referred to as *entropy methods* [4, 129]. For further information, we refer to the textbook [129] and the references therein. Due to that, we will use the term *entropy* instead of *free energy* even though the latter one is physically more appropriate.

From now on, we restrict ourselves to the non-dimensionalized version of the charge transport models. More precisely, we study for perovskite solar cells the model (P) with initial conditions (PIC) and boundary conditions (PBC) (see Section 3.1.4) and for TMDC memristive devices the drift-diffusion equations (M) supplemented with (MIC) and (MBC) (see Section 3.2.3). It is worth noting that the differences between both models are the physical interpretation of the vacancy carrier $\alpha = \mathrm{a}$, the scaling, and the device geometry.

Within this section, we will introduce useful entropy functions for both models and establish a continuous entropy-dissipation inequality. The discrete version of this inequality, which we will derive in Section 4.2, will allow us to deduce the existence of discrete solutions and assess the stability of the discretization schemes. We understand stability here in the sense that the discrete solutions remain bounded, independent of changes in the grid and time spacing.

3.3.1. Entropy functions

For $\alpha \in \{\mathrm{n}, \mathrm{p}, \mathrm{a}\}$, we define the *entropy function* Φ_α, associated with the statistics function $\mathcal{F}_\alpha$, as an antiderivative of the inverse of statistics function, namely,

$$\Phi_\alpha'(x) = \mathcal{F}_\alpha^{-1}(x), \quad x \geq 0. \tag{3.40}$$

Observe that the hypotheses on the statistics functions (H1) (see Section 2.3.1) and (H2) (see Section 2.4.2) imply that $\mathcal{F}_\alpha$ is strictly increasing and, therefore, that the entropy function Φ_α is strictly convex. Furthermore, we note that Φ_α enters the definition of the physical free energy (2.48). Of course, from (3.40), the entropy function Φ_α is only defined up to a constant, but the value of the constant is not crucial for electrons $\alpha = \mathrm{n}$ and holes $\alpha = \mathrm{p}$ in what follows because we will introduce *relative* entropies. The constant may be generally taken to ensure that Φ_α is non-negative and vanishes at only one point, which is a necessary condition for the vacancies $\alpha = \mathrm{a}$. We define the relative entropy H_α by

$$H_\alpha(x, y) = \Phi_\alpha(x) - \Phi_\alpha(y) - \Phi_\alpha'(y)(x - y), \quad x, y \geq 0. \tag{3.41}$$

Observe that H_α is non-negative due to the convexity of Φ_α.

Examples. In case of the Boltzmann approximation, i.e., $\mathcal{F}_{\mathrm{n}}(\eta) = \mathcal{F}_{\mathrm{p}}(\eta) = \exp(\eta)$, one may choose, for example, as entropy function

$$\Phi_{\mathrm{n}}(x) = \Phi_{\mathrm{p}}(x) = x\log(x) - x + 1, \quad x \geq 0.$$

In case of the Fermi-Dirac integral of order -1, i.e., $\mathcal{F}_{\mathrm{a}}(\eta) = (\exp(-\eta) + 1)^{-1}$, one has

$$\Phi_{\mathrm{a}}(x) = x\log(x) + (1-x)\log(1-x) + \log(2), \quad x \geq 0.$$

Let us now state some useful results for the entropy functions. The proofs can be found in Appendix A.2 and Appendix A.3.

Lemma 3.3. One has the following bounds on the entropy functions (3.40) and (3.41).

(i) Let $\alpha \in \{\mathrm{n}, \mathrm{p}\}$. Further, let $\mathcal{F}_\alpha$ be a statistics function satisfying (H1) and H_α be the associated relative entropy function. Then, for any $\varepsilon > 0$ and $y_0 \geq 0$, there exists a constant $c_{y_0,\varepsilon} > 0$ such that

$$x \leq c_{y_0,\varepsilon} + \varepsilon H_\alpha(x, y), \quad \text{for all } x \geq 0,\ y \in [0, y_0].$$

(ii) Let $\mathcal{F}_{\mathrm{a}}$ be a statistics function satisfying (H2) and Φ_{a} be the associated entropy function. Then, for any $\varepsilon > 0$, there exists a constant $c_\varepsilon > 0$ such that

$$x \leq c_\varepsilon + \varepsilon\Phi_{\mathrm{a}}(x), \quad \text{for all } x \geq 0.$$

Under the final additional assumption on the statistics functions of electrons and holes

$$\lim_{x\to+\infty} \frac{H_\alpha(x, y_0)}{\mathcal{F}_\alpha^{-1}(x)} = +\infty, \quad \text{for } y_0 \geq 0 \quad \text{and} \quad \alpha \in \{\mathrm{n}, \mathrm{p}\}, \tag{H3}$$

we have the following result.

Lemma 3.4. Let $\mathcal{F}_\alpha$ with $\alpha \in \{\mathrm{n}, \mathrm{p}\}$ be a statistics function satisfying (H1) and (H3). Then, for any $\varepsilon > 0$ and $y_0 \geq 0$, there exists a constant $c_{y_0,\varepsilon} \geq 0$ such that

$$\max\{\mathcal{F}_\alpha^{-1}(x), 0\} \leq c_{y_0,\varepsilon} + \varepsilon H_\alpha(x, y), \quad \text{for all } x \geq 0,\ y \in [0, y_0].$$

We will also show in Appendix A.1 that the Boltzmann statistics and the Fermi-Dirac statistics of order $1/2$ both satisfy (H1), (H3), while the Fermi-Dirac statistics of order -1 satisfies (H2). We proceed with establishing entropy-dissipation inequalities for both introduced non-dimensionalized charge transport models.

3.3.2. Entropy-dissipation inequality

The thermodynamic free energy, as introduced in Section 2.6.2, is of physical relevance. However, our current objective is to prove a mathematical entropy-dissipation inequality. For this reason, we examine a variation of the energy functional (2.48), which we will now refer to as the *total relative entropy* in agreement with the mathematical literature. Despite considering different device geometries and non-dimensionalizations for the PSC and the TMDC memristive model, we can establish, in both cases, an entropy-dissipation inequality. We start with the perovskite solar cell application.

Perovskite solar cells. We consider the problem (P) with the initial conditions (PIC) and the boundary conditions (PBC) (see Section 3.1.4). Adapting the functional of [18, 126] to our system, the total relative entropy with respect to the Dirichlet boundary values $\psi^D, \varphi^D \in W^{1,\infty}(\mathbf{\Omega})$ for $t \geq 0$ is given by

$$\mathbb{E}(t) = \frac{\lambda^2}{2} \int_{\mathbf{\Omega}} |\nabla(\psi - \psi^D)|^2 \, d\mathbf{x} + \int_{\mathbf{\Omega}_{\text{intr}}} \Phi_{\text{a}}(n_{\text{a}}) \, d\mathbf{x} + \delta \sum_{\alpha \in \{\text{n,p}\}} \int_{\mathbf{\Omega}} H_\alpha(n_\alpha, n_\alpha^D) \, d\mathbf{x}, \tag{3.42}$$

where the entropy functions Φ_{a}, H_{n} and H_{p} are defined in (3.40), (3.41). The densities n_{n}^D, n_{p}^D can be calculated by inserting φ^D, ψ^D into the dimensionless state equation (Pf). It is important to note that since we generally assume $\Phi_{\text{a}} \geq 0$ the middle term is non-negative as well which implies that the total entropy is non-negative.

In contrast to the energy functional (2.48), the relative entropy (3.42) takes the assumptions for the non-dimensionalization in Section 3.1.4 into account, in particular the assumption of vanishing band-edge energies. Furthermore, the energy contributions of the electric potential and the electron and hole quasi Fermi potentials are defined on the overall domain $\mathbf{\Omega}$, whereas the contribution with respect to the anion vacancies is solely defined on the intrinsic domain $\mathbf{\Omega}_{\text{intr}}$.

Taking into account the fact that $z_\alpha^2 = 1$ for $\alpha \in \{\text{n}, \text{p}\}$, the associated non-negative dissipation $\mathbb{D}$ for $t \geq 0$ is defined as

$$\begin{aligned} \mathbb{D}(t) = &\frac{\delta}{\nu} \int_{\mathbf{\Omega}} R(n_{\text{n}}, n_{\text{p}}) \, (\varphi_{\text{p}} - \varphi_{\text{n}}) \, d\mathbf{x} + \frac{\delta}{2\nu} \sum_{\alpha \in \{\text{n,p}\}} \int_{\mathbf{\Omega}} n_\alpha |\nabla \varphi_\alpha|^2 \, d\mathbf{x} \\ &+ \frac{z_{\text{a}}^2}{2} \int_{\mathbf{\Omega}_{\text{intr}}} n_{\text{a}} |\nabla \varphi_{\text{a}}|^2 \, d\mathbf{x}. \end{aligned} \tag{3.43}$$

The relative entropy $\mathbb{E}$ and the dissipation $\mathbb{D}$ satisfy the following inequality.

Theorem 3.5. (Continuous entropy-dissipation inequality for a PSC model) Consider a smooth solution to the model (P), with initial conditions (PIC) and boundary

conditions (PBC). Then, for any $\varepsilon > 0$, there is a constant $c_{\varepsilon,\mathbf{\Omega}} > 0$ such that

$$\frac{\mathrm{d}}{\mathrm{d}t}\mathbb{E}(t) + \mathbb{D}(t) \leq c_{\varepsilon,\mathbf{\Omega}} + \varepsilon\mathbb{E}(t), \quad t \geq 0, \tag{3.44}$$

where the entropy is defined in (3.42) and the dissipation in (3.43). The constant $c_{\varepsilon,\mathbf{\Omega}}$ depends only on ε, the measure of $\mathbf{\Omega}$, the boundary data and the photogeneration term via the norms $\|G\|_{L^\infty}$, $\|\varphi^D\|_{W^{1,\infty}}$ and $\|\psi^D\|_{W^{1,\infty}}$, as well as on z_a^2 and the dimensionless parameters δ, γ and ν.

Proof. Let $t \geq 0$. First, we take the derivative of (3.42) with respect to time

$$\begin{aligned}\frac{\mathrm{d}}{\mathrm{d}t}\mathbb{E}(t) = \lambda^2 \int_{\mathbf{\Omega}} (\partial_t \nabla\psi)\cdot\nabla(\psi-\psi^D)\,d\mathbf{x} \; + \int_{\mathbf{\Omega}_{\mathrm{intr}}} \mathcal{F}_\mathrm{a}^{-1}(n_\mathrm{a})\partial_t n_\mathrm{a}\,d\mathbf{x} \\ + \delta \sum_{\alpha\in\{\mathrm{n,p}\}} \int_{\mathbf{\Omega}} \left(\mathcal{F}_\alpha^{-1}(n_\alpha) - \mathcal{F}_\alpha^{-1}(n_\alpha^D)\right)\partial_t n_\alpha\,d\mathbf{x}.\end{aligned} \tag{3.45}$$

By integrating the first term by parts and using the Poisson equation (Pd) one obtains

$$\begin{aligned}\lambda^2 \int_{\mathbf{\Omega}} (\partial_t\nabla\psi)\cdot\nabla(\psi-\psi^D)\,d\mathbf{x} \; &= \delta \int_{\mathbf{\Omega}} (z_\mathrm{n}\partial_t n_\mathrm{n} + z_\mathrm{p}\partial_t n_\mathrm{p})(\psi-\psi^D)\,d\mathbf{x} \\ &\quad + \int_{\mathbf{\Omega}_{\mathrm{intr}}} z_\mathrm{a}\partial_t n_\mathrm{a}(\psi-\psi^D)\,d\mathbf{x},\end{aligned}$$

where all the boundary terms cancel thanks to the boundary conditions (PBCb) and (PBCd). Plugging the previous equality back into (3.45) and using the relation $\mathcal{F}_\alpha^{-1}(n_\alpha) + z_\alpha\psi = z_\alpha\varphi_\alpha$ (from the state equation (Pf)), we have

$$\frac{\mathrm{d}}{\mathrm{d}t}\mathbb{E}(t) = \; \delta \sum_{\alpha\in\{\mathrm{n,p}\}} \int_{\mathbf{\Omega}} z_\alpha\left(\varphi_\alpha - \varphi^D\right)\partial_t n_\alpha\,d\mathbf{x} + \int_{\mathbf{\Omega}_{\mathrm{intr}}} z_\mathrm{a}\left(\varphi_\mathrm{a} - \psi^D\right)\partial_t n_\mathrm{a}\,d\mathbf{x}.$$

Next, we insert the balance equations (Pa), (Pb), (Pc), the definition of the current densities (Pe), and integrate by parts

$$\begin{aligned}\frac{\mathrm{d}}{\mathrm{d}t}\mathbb{E}(t) &= -\frac{\delta}{\nu}\sum_{\alpha\in\{\mathrm{n,p}\}}\int_{\mathbf{\Omega}} \nabla\cdot\mathbf{j}_\alpha\left(\varphi_\alpha-\varphi^D\right)\,d\mathbf{x} \; - \int_{\mathbf{\Omega}_{\mathrm{intr}}} \nabla\cdot\mathbf{j}_a\left(\varphi_\mathrm{a}-\psi^D\right)\,d\mathbf{x} \\ &\quad + \frac{\delta}{\nu}\sum_{\alpha\in\{\mathrm{n,p}\}}\int_{\mathbf{\Omega}} z_\alpha\left(\gamma G - R\right)\left(\varphi_\alpha-\varphi^D\right)\,d\mathbf{x} \\ &= -\frac{\delta}{\nu}\sum_{\alpha\in\{\mathrm{n,p}\}}\int_{\mathbf{\Omega}} n_\alpha\nabla\varphi_\alpha\cdot\nabla\left(\varphi_\alpha-\varphi^D\right)\,d\mathbf{x} + \frac{\delta}{\nu}\int_{\mathbf{\Omega}}\left(\gamma G - R\right)\left(\varphi_\mathrm{p}-\varphi_\mathrm{n}\right)d\mathbf{x} \\ &\quad - \int_{\mathbf{\Omega}_{\mathrm{intr}}} z_\mathrm{a}^2 n_\mathrm{a}\nabla\varphi_\mathrm{a}\cdot\nabla\left(\varphi_\mathrm{a}-\psi^D\right)\,d\mathbf{x},\end{aligned}$$

where we used $z_\mathrm{n} = -1 = -z_\mathrm{p}$. The boundary terms vanish again thanks to (PBCa), (PBCb), (PBCc), (PBCe), and (PBCf). By expanding all contributions of the previous equality

$$\begin{aligned}\frac{\mathrm{d}}{\mathrm{d}t}\mathbb{E}(t) = &-\frac{\delta}{\nu}\sum_{\alpha\in\{\mathrm{n,p}\}}\int_{\mathbf{\Omega}} n_\alpha|\nabla\varphi_\alpha|^2\,d\mathbf{x} + \frac{\delta}{\nu}\sum_{\alpha\in\{\mathrm{n,p}\}}\int_{\mathbf{\Omega}} n_\alpha\nabla\varphi_\alpha\cdot\nabla\varphi^D\,d\mathbf{x}\\ &-\int_{\mathbf{\Omega}_\mathrm{intr}} z_\mathrm{a}^2 n_\mathrm{a}|\nabla\varphi_\mathrm{a}|^2\,d\mathbf{x} + \int_{\mathbf{\Omega}_\mathrm{intr}} z_\mathrm{a}^2 n_\mathrm{a}\nabla\varphi_\mathrm{a}\cdot\nabla\psi^D\,d\mathbf{x}\\ &+\frac{\delta\gamma}{\nu}\int_{\mathbf{\Omega}} G(\varphi_\mathrm{p}-\varphi_\mathrm{n})\,d\mathbf{x} - \frac{\delta}{\nu}\int_{\mathbf{\Omega}} R(\varphi_\mathrm{p}-\varphi_\mathrm{n})\,d\mathbf{x},\end{aligned}$$

and using Young's inequality for the cross terms ($ab \le a^2/2 + b^2/2$) we get

$$\begin{aligned}\frac{\mathrm{d}}{\mathrm{d}t}\mathbb{E}(t) + \mathbb{D}(t) \le &\frac{\delta}{2\nu}\sum_{\alpha\in\{\mathrm{n,p}\}}\int_{\mathbf{\Omega}} n_\alpha|\nabla\varphi^D|^2\,d\mathbf{x} + \frac{z_\mathrm{a}^2}{2}\int_{\mathbf{\Omega}_\mathrm{intr}} n_\mathrm{a}|\nabla\psi^D|^2\,d\mathbf{x}\\ &+\frac{\delta\gamma}{\nu}\int_{\mathbf{\Omega}} G\left(\varphi_\mathrm{p}-\varphi_\mathrm{n}\right)\,d\mathbf{x},\end{aligned} \tag{3.46}$$

where we also added the dissipation $\mathbb{D}$ defined in (3.43). It remains to bound the terms on the right-hand side. For the first two remainder terms on the right-hand side of (3.46) we use Lemma 3.3 to find for some $\varepsilon > 0$

$$\begin{aligned}&\frac{\delta}{2\nu}\sum_{\alpha\in\{\mathrm{n,p}\}}\int_{\mathbf{\Omega}} n_\alpha|\nabla\varphi^D|^2\,d\mathbf{x} + \frac{z_\mathrm{a}^2}{2}\int_{\mathbf{\Omega}_\mathrm{intr}} n_\mathrm{a}|\nabla\psi^D|^2\,d\mathbf{x}\\ &\le \frac{1}{2\nu}||\nabla\varphi^D||_{L^\infty}^2\delta\sum_{\alpha\in\{\mathrm{n,p}\}}\int_{\mathbf{\Omega}} n_\alpha\,d\mathbf{x} + \frac{z_\mathrm{a}^2}{2}||\nabla\psi^D||_{L^\infty}^2\int_{\mathbf{\Omega}_\mathrm{intr}} n_\mathrm{a}\,d\mathbf{x}\\ &\le \frac{1}{2\nu}||\nabla\varphi^D||_{L^\infty}^2\delta\sum_{\alpha\in\{\mathrm{n,p}\}}\int_{\mathbf{\Omega}}\left(c_{y_\alpha^D,\varepsilon} + \varepsilon H_\alpha(n_\alpha, n_\alpha^D)\right)\,d\mathbf{x}\\ &\quad+\frac{z_\mathrm{a}^2}{2}||\nabla\psi^D||_{L^\infty}^2\int_{\mathbf{\Omega}_\mathrm{intr}}\left(c_\varepsilon + \varepsilon\Phi_\mathrm{a}(n_\mathrm{a})\right)d\mathbf{x}\\ &\le \max\left\{\frac{1}{2\nu}||\nabla\varphi^D||_{L^\infty}^2, \frac{z_\mathrm{a}^2}{2}||\nabla\psi^D||_{L^\infty}^2\right\}\left((\delta c_{y_n^D,\varepsilon} + \delta c_{y_p^D,\varepsilon} + c_\varepsilon)|\mathbf{\Omega}| + \varepsilon\mathbb{E}\right),\end{aligned}$$

since the first term in (3.42) is non-negative. Here, H_α is defined in (3.41). The quantities $c_\varepsilon, c_{y_\mathrm{n}^D,\varepsilon}, c_{y_\mathrm{p}^D,\varepsilon}$ are the corresponding constants introduced in Lemma 3.3, where we set

$$y_\alpha^D = \mathcal{F}_\alpha(\|\varphi^D\|_{L^\infty} + \|\psi^D\|_{L^\infty}), \quad \alpha\in\{\mathrm{n,p}\}. \tag{3.47}$$

With help of Lemma 3.4 and the relation $z_\alpha\varphi_\alpha = \mathcal{F}_\alpha^{-1}(n_\alpha) + z_\alpha\psi$, the last remainder term of (3.46) is estimated by

$$\begin{aligned}\frac{\delta\gamma}{\nu}\int_{\mathbf{\Omega}} G\left(\varphi_{\mathrm{p}}-\varphi_{\mathrm{n}}\right)\,d\mathbf{x} &= \frac{\gamma}{\nu}\delta\sum_{\alpha\in\{\mathrm{n,p}\}}\int_{\mathbf{\Omega}} G\mathcal{F}_\alpha^{-1}(n_\alpha)\,d\mathbf{x}\\ &\le \frac{\gamma}{\nu}||G||_{L^\infty}\delta\sum_{\alpha\in\{\mathrm{n,p}\}}\int_{\mathbf{\Omega}}\max\{\mathcal{F}_\alpha^{-1}(n_\alpha),0\}\,d\mathbf{x}\\ &\le \frac{\gamma}{\nu}||G||_{L^\infty}\sum_{\alpha\in\{\mathrm{n,p}\}}\left(\delta c_{y_\alpha^D,\varepsilon}|\mathbf{\Omega}| + \varepsilon\delta\int_{\mathbf{\Omega}} H_\alpha\left(n_\alpha,n_\alpha^D\right)\,d\mathbf{x}\right)\\ &\le \frac{\gamma}{\nu}||G||_{L^\infty}\left(\delta c_{y_{\mathrm{n}}^D,\varepsilon}|\mathbf{\Omega}| + \delta c_{y_{\mathrm{p}}^D,\varepsilon}|\mathbf{\Omega}| + \varepsilon\mathbb{E}\right),\end{aligned}$$

since the other two contributions of the entropy are non-negative. The quantities $c_{y_{\mathrm{n}}^D,\varepsilon}$, $c_{y_{\mathrm{p}}^D,\varepsilon}$ are the constants introduced in Lemma 3.4 with $y_{\mathrm{n}}^D, y_{\mathrm{p}}^D$ defined in (3.47). Plugging these estimates back into (3.46) proves the entropy-dissipation estimate (up to a redefinition of ε) and with suitable $c_{\varepsilon,\mathbf{\Omega}}$. □

Under additional assumptions, we can expect a decay of the relative entropy in time.

Remark 3.6. Under the assumption of constant boundary data, i.e., $\nabla\varphi^D = \nabla\psi^D = \mathbf{0}$, and in the absence of external generation of electrons and holes, i.e., $G = 0$, the entropy-dissipation inequality simplifies to

$$\frac{\mathrm{d}}{\mathrm{d}t}\mathbb{E}(t) + \mathbb{D}(t) \le 0, \quad t \ge 0.$$

It becomes evident from the proof of Theorem 3.5, particularly from the immediate estimate (3.46), that the right-hand side of the entropy-dissipation inequality (3.44) vanishes in this specific scenario. In this case, the entropy $\mathbb{E}$ decays in time and the solution is expected to converge exponentially fast towards the equilibrium solution $(\varphi_{\mathrm{n}}^{\mathrm{eq}}, \varphi_{\mathrm{p}}^{\mathrm{eq}}, \varphi_{\mathrm{a}}^{\mathrm{eq}}, \psi^{\mathrm{eq}})$. This equilibrium is such that the quasi Fermi potentials for electrons and holes are constant on $\mathbf{\Omega}$

$$\varphi_{\mathrm{p}}^{\mathrm{eq}} = \varphi_{\mathrm{n}}^{\mathrm{eq}} = \varphi^D$$

and $\varphi_{\mathrm{a}}^{\mathrm{eq}}$ is constant on $\mathbf{\Omega}_{\mathrm{intr}}$, determined by the conservation of mass for anion vacancies

$$\int_{\mathbf{\Omega}_{\mathrm{intr}}} n_{\mathrm{a}}(\varphi_{\mathrm{a}}^{\mathrm{eq}}, \psi^{\mathrm{eq}})\,d\mathbf{x} = \int_{\mathbf{\Omega}_{\mathrm{intr}}} n_{\mathrm{a}}(\mathbf{x},0)\,d\mathbf{x},$$

which is consistent with Section 2.6.1. The electric potential ψ^{eq} satisfies the following

nonlinear Poisson equation

$$-\lambda^2\Delta\psi^{\mathrm{eq}} = \begin{cases} \delta\Big(n_{\mathrm{p}}(\varphi_{\mathrm{p}}^{\mathrm{eq}},\psi^{\mathrm{eq}}) - n_{\mathrm{n}}(\varphi_{\mathrm{n}}^{\mathrm{eq}},\psi^{\mathrm{eq}}) + C\Big), & \mathbf{x}\in\boldsymbol{\Omega}_{\mathrm{HTL}}\cup\boldsymbol{\Omega}_{\mathrm{ETL}}, \\ \delta\Big(n_{\mathrm{p}}(\varphi_{\mathrm{p}}^{\mathrm{eq}},\psi^{\mathrm{eq}}) - n_{\mathrm{n}}(\varphi_{\mathrm{n}}^{\mathrm{eq}},\psi^{\mathrm{eq}}) + C\Big) & \\ \quad + z_{\mathrm{a}}n_{\mathrm{a}}(\varphi_{\mathrm{a}}^{\mathrm{eq}},\psi^{\mathrm{eq}}), & \mathbf{x}\in\boldsymbol{\Omega}_{\mathrm{intr}}, \end{cases}$$

supplemented with the boundary conditions (PBCa), (PBC) for the electric potential. The proof of this asymptotic behavior is beyond the scope of this thesis but could be investigated following the lines of the seminal work of Gajewski [89].

We proceed with establishing an entropy-dissipation inequality for our second application, the TMDC-based memristive devices.

Memristive devices. The memristive model is given by (M), with initial conditions (MIC) and boundary conditions (MBC) (see Section 3.2.3). Analogously, we define a total relative entropy with respect to the Dirichlet boundary values $\psi^D, \varphi^D \in W^{1,\infty}(\boldsymbol{\Omega})$ for $t \geq 0$

$$\begin{aligned}\mathbb{E}(t) = \frac{\lambda^2}{2}\int_{\boldsymbol{\Omega}} |\nabla(\psi-\psi^D)|^2\,d\mathbf{x} \; + \int_{\boldsymbol{\Omega}} \Phi_{\mathrm{a}}(n_{\mathrm{a}})\,d\mathbf{x} \; + \delta_{\mathrm{n}}\int_{\boldsymbol{\Omega}} H_{\mathrm{n}}(n_{\mathrm{n}},n_{\mathrm{n}}^D)\,d\mathbf{x} \\ + \delta_{\mathrm{n}}\delta_{\mathrm{p}}\int_{\boldsymbol{\Omega}} H_{\mathrm{p}}(n_{\mathrm{p}},n_{\mathrm{p}}^D)\,d\mathbf{x},\end{aligned} \tag{3.48}$$

where Φ_{a}, H_{n} and H_{p} are given by (3.40), (3.41).

Like the entropy function for the PSC model (3.42), the relative entropy for the memristive model (3.48) considers the assumptions made for the non-dimensionalization in Section 3.2.3. This notably includes the assumption of vanishing band-edge energies. Furthermore, the domain $\boldsymbol{\Omega}$ now refers to the TMDC material layer, on which all potentials evolve. The dissipation rate for $t \geq 0$ is defined as

$$\mathbb{D}(t) = \frac{\delta_{\mathrm{n}}}{2\nu}\int_{\boldsymbol{\Omega}} n_{\mathrm{n}}|\nabla\varphi_{\mathrm{n}}|^2\,d\mathbf{x} \; + \frac{\delta_{\mathrm{n}}\delta_{\mathrm{p}}}{2\nu}\int_{\boldsymbol{\Omega}} n_{\mathrm{p}}|\nabla\varphi_{\mathrm{p}}|^2\,d\mathbf{x} \; + \frac{z_{\mathrm{a}}^2}{2}\int_{\boldsymbol{\Omega}} n_{\mathrm{a}}|\nabla\varphi_{\mathrm{a}}|^2\,d\mathbf{x}. \tag{3.49}$$

Observe that the entropy $\mathbb{E}$ as well as the dissipation $\mathbb{D}$ are non-negative. Now, we can formulate a continuous entropy-dissipation inequality.

Theorem 3.7. (Continuous entropy-dissipation inequality for a memristive model) Consider a smooth solution to the model (M), with initial conditions (MIC) and boundary conditions (MBC). Then, for any $\varepsilon > 0$, there is a constant $c_{\varepsilon,\boldsymbol{\Omega}} > 0$ such that

$$\frac{\mathrm{d}}{\mathrm{d}t}\mathbb{E}(t) + \mathbb{D}(t) \leq c_{\varepsilon,\boldsymbol{\Omega}} + \varepsilon\mathbb{E}(t), \quad t \geq 0, \tag{3.50}$$

where the entropy is defined in (3.48) and the dissipation in (3.49). The constant $c_{\varepsilon,\mathbf{\Omega}}$ depends only on ε, the measure of $\mathbf{\Omega}$ and the boundary data via the norms $\|\varphi^D\|_{W^{1,\infty}}$ and $\|\psi^D\|_{W^{1,\infty}}$, z_{a}^2, and the dimensionless parameters δ_{n}, δ_{p} and ν. □

The proof of Theorem 3.7 follows a similar structure as the proof of Theorem 3.5 and is therefore omitted here. Regarding constant boundary conditions, i.e., $\nabla\varphi^D = \nabla\psi^D = \mathbf{0}$, Remark 3.6 also applies to the memristive model. Specifically, the right-hand side of the entropy-dissipation inequality (3.50) also vanishes, indicating an exponential decay of the entropy $\mathbb{E}$.

Before concluding this chapter, we can deduce, with the help of Grönwall's lemma [66, 67, 100], immediate consequences of Theorem 3.5 for the entropy $\mathbb{E}$ in (3.42) and the dissipation $\mathbb{D}$ in (3.43) or of Theorem 3.7 for the entropy $\mathbb{E}$ in (3.48) and the dissipation $\mathbb{D}$ in (3.49). As time-dependent functions, $t \mapsto \mathbb{E}(t)$ and $t \mapsto \mathbb{D}(t)$ are locally bounded and locally integrable, respectively. To show this, we will employ a modified version of Grönwall's lemma, as presented in Lemma 3.8.

Lemma 3.8. (Grönwall's lemma) Let $t_F \in \mathbb{R}_{\geq 0}$ and suppose that $u, g, a : [0, t_F] \to \mathbb{R}$ are sufficiently smooth functions such that

$$u'(t) + g(t) \leq a(t)u(t), \quad \text{for } t \in [0, t_F],$$

where a, g are non-negative on $[0, t_F]$. Then,

$$u(t) + \int_0^t g(s)\,ds \leq u(0)\exp\left(\int_0^t a(s)\,ds\right), \quad \text{for } t \in [0, t_F].$$

The proof of Lemma 3.8 can be found in Appendix A.4. We formulate the following result, showing that the entropy $\mathbb{E}$ is locally bounded and the dissipation $\mathbb{D}$ is locally integrable. Moreover, for any but fixed $\varepsilon > 0$, we observe that the entropy is bounded by an exponential with respect to time.

Corollary 3.9. Let $\mathbb{E}$ and $\mathbb{D}$ either be given by (3.42), (3.43) or by (3.48) and (3.49). Then, for any $\varepsilon > 0$, one has

$$\mathbb{E}(t) + \int_0^t \mathbb{D}(s)\mathrm{d}s \leq e^{\varepsilon t}\mathbb{E}(0) + \frac{c_{\varepsilon,\mathbf{\Omega}}}{\varepsilon}(e^{\varepsilon t} - 1), \quad t \geq 0.$$

Proof. We define $\tilde{\mathbb{E}} := \mathbb{E} + \frac{c_{\varepsilon,\mathbf{\Omega}}}{\varepsilon}$. Reformulating now the entropy-dissipation inequalities in Theorem 3.5 and Theorem 3.7 with respect to $\tilde{\mathbb{E}}$, gives us

$$\frac{\mathrm{d}}{\mathrm{d}t}\tilde{\mathbb{E}}(t) + \mathbb{D}(t) \leq \varepsilon\tilde{\mathbb{E}}(t), \quad t \geq 0.$$

Setting now $u(t) = \tilde{\mathbb{E}}(t)$, $g(t) = \mathbb{D}(t)$, and $a(t) = \varepsilon$, applying Grönwall's lemma in Lemma 3.8, inserting $\tilde{\mathbb{E}}$, and rearranging terms, proves the claim. □

4. Numerical analysis of vacancy-assisted charge transport models

Extensive literature has been devoted to addressing suitable methods for solving drift-diffusion equations as given PDE systems, including discretization schemes based on the finite difference (FDM) or the finite element method (FEM). For instance, we refer to [10, 24, 75, 125, 148, 155, 174, 216, 242]. However, this thesis will focus exclusively on schemes derived from the finite volume method (FVM). FVM-based approaches are flexible with respect to the device geometry like FEM while still correctly reflecting physical phenomena such as local conservativity of fluxes or consistency to thermodynamic laws [70, 72]. The design and study of FVM numerical schemes for drift-diffusion models is also a mature but still very active field of research (e.g., [19, 30, 74, 86, 88, 125, 132, 157, 211]). In order to ensure the quality of the numerical simulation and the stability of the numerical method, efforts have been made towards the design of structure-preserving schemes [17, 34, 94, 107, 173]. They preserve the physical features of the original model, such as the decay of free energy or non-negativity of carrier densities.

In the context of perovskite solar cells, other researchers have used either a finite-difference [50, 77, 138], a finite-element discretization [29, 50] or commercial software packages [2, 81, 117, 182, 250]. However, as of our current knowledge, no drift-diffusion discretization schemes have been formulated explicitly for memristive devices.

This chapter is organized as follows: In Section 4.1, we formulate the numerical schemes for two models, namely, the PSC model defined by (P), (PIC), and (PBC), as well as the TMDC memristive model given by (M), (MIC), and (MBC). These models were introduced at the end of Section 3.1.4 and Section 3.2.3, respectively. Additionally, we provide in this section essential concepts and notations needed for a proper formulation of the discretization schemes. These finite volume schemes rely on a two-point flux approximation (TPFA) of the fluxes and a backward Euler scheme in time. As TPFA, we use the *excess chemical potential flux* scheme (frequently called *Sedan* scheme), which appears to be used for the first time in [255]. As in the continuous setting, we will show in Section 4.2 that entropy-dissipation relations also hold at the discrete level, ensuring stability and preservation of the physical structure of the models. After proving the existence of a discrete electric potential for given quasi Fermi potentials

(Section 4.2.2), we continue proving *a priori* estimates on the quasi Fermi potentials and the electric potential in Section 4.2.3. This chapter ends with the existence proofs in Section 4.2.4.

This chapter is based in large parts on [DA2]. Minor parts can be found in [DA4].

4.1. Discrete charge transport equations

This section presents the concepts and notations essential for formulating implicit-in-time finite volume discretization schemes. In Section 4.1.1, we will begin by introducing admissible meshes [70]. These meshes, which satisfy some orthogonality constraints, establish the structural framework for discretizing a computational domain $\mathbf{\Omega}$ into discrete cells. We continue in Section 4.1.2 with the development of suitable FVM discretization schemes. Finally, in Section 4.1.3 we discuss two-point flux approximations designed to describe the flow of charge carriers, and, we introduce the excess chemical potential scheme, our chosen method for discretizing the current densities, in this thesis.

In Chapter 3, we made a common assumption for both applications that the device domain $\mathbf{\Omega} \subset \mathbb{R}^d$, $d \in \{1, 2, 3\}$, is open, connected, and bounded. It is important to note that when dealing with the PSC model, the spatial domain is further divided into three subdomains $\overline{\mathbf{\Omega}} = \cup_k \overline{\mathbf{\Omega}}_k$, $k \in \{\mathrm{ETL}, \mathrm{intr}, \mathrm{HTL}\}$. In contrast, for the TMDC memristor application, the device geometry is represented solely by $\mathbf{\Omega}$. Differences in the discretizations due to different device geometries in our two applications will be explicitly highlighted.

4.1.1. Discretization meshes

An admissible mesh, following the definition in [70], can be characterized by the triplet $(\mathcal{T}, \mathcal{E}, \{\mathbf{x}_K\}_{K\in\mathcal{T}})$ under the additional assumption that the computational domain $\mathbf{\Omega}$ is polygonal (or polyhedral). In this context, $\mathcal{T}$ denotes a family of *control volumes*, $\mathcal{E}$ corresponds to a family of *faces*, and $\{\mathbf{x}_K\}_{K\in\mathcal{T}}$ describes a family of *nodes*. In the following, we describe the concept of an admissible mesh and its relevance to our discretization mesh. More precisely, $\mathcal{T}$ denotes a family of non-empty, convex, open, and polygonal (or polyhedral) control volumes (frequently called *cells*) $K \in \mathcal{T}$, whose Lebesgue measure is denoted by m_K. The union of the closure of all control volumes is equal to the closure of the spatial domain, i.e.,

$$\overline{\mathbf{\Omega}} = \bigcup_{K\in\mathcal{T}} \overline{K}.$$

Furthermore, we call $\mathcal{E}$ a family of faces, where $\sigma \in \mathcal{E}$ is a subset of $\overline{\mathbf{\Omega}}$ contained in a hyperplane of $\mathbb{R}^d$. Each face (or *edge*) σ has a strictly positive $(d-1)$-dimensional measure, denoted by m_σ. We use the abbreviation $\sigma = K|L = \partial K \cap \partial L$ for the intersection between two different control volumes $K \neq L$. The intersection $K|L$ is either empty or reduces to a face contained in $\mathcal{E}$. Also, for any cell $K \in \mathcal{T}$ we assume that there exists a subset of faces $\mathcal{E}_K \subset \mathcal{E}$ so that we can describe the boundary of a control volume by $\partial K = \bigcup_{\sigma \in \mathcal{E}_K} \sigma$ and, consequently, it follows that $\mathcal{E} = \bigcup_{K \in \mathcal{T}} \mathcal{E}_K$. We distinguish the faces that are on the boundary of $\mathbf{\Omega}$ by introducing the notations

$$\mathcal{E}^D = \{\sigma \in \mathcal{E} \text{ s.t. } \sigma \subset \mathbf{\Gamma}^D\}, \quad \mathcal{E}^N = \{\sigma \in \mathcal{E} \text{ s.t. } \sigma \subset \mathbf{\Gamma}^N\},$$

and assume that the Dirichlet and Neumann boundaries $\mathbf{\Gamma}^D, \mathbf{\Gamma}^N$ can be well described by the union of respective boundary faces, i.e., $\mathbf{\Gamma}^D = \bigcup_{\sigma \in \mathcal{E}^D} \sigma$ and $\mathbf{\Gamma}^N = \bigcup_{\sigma \in \mathcal{E}^N} \sigma$.

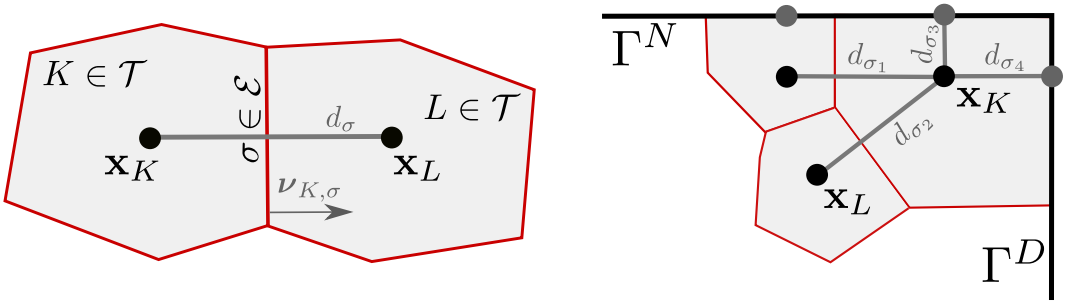

Figure 4.1.: Neighboring control volumes in the interior of the device domain (left) and near outer boundaries $\mathbf{\Gamma}^D$ and $\mathbf{\Gamma}^N$ (right). For our analysis, we assume that the cell centers (black points) of a boundary control volume are located in the interior of the computational domain. The boundary of the control volumes are highlighted in red. (From [DA2] with modifications.)

To each control volume $K \in \mathcal{T}$ we assign a node (also called *cell center* or *collocation point*) $\mathbf{x}_K \in K$, and we assume that the family of nodes $\{\mathbf{x}_K\}_{K \in \mathcal{T}}$ satisfies the *orthogonality condition*: If K and L share a face $\sigma = K|L$, then the vector

$$\overline{\mathbf{x}_K \mathbf{x}_L} \text{ is orthogonal to } \sigma = K|L.$$

We assume that each node $\mathbf{x}_K$ is located within the interior of $\mathbf{\Omega}$. In other words, for all $K \in \mathcal{T}$ with $\mathcal{E}_K \cap \partial\mathbf{\Omega} \neq \emptyset$, it holds that $\mathbf{x}_K \notin \partial\mathbf{\Omega}$. This condition is visualized in Figure 4.1 (right). It is important to note that the last assumption is not a constraint arising from the definition of admissible meshes but rather a requirement for the subsequent numerical analysis in this chapter. Indeed, it is possible to construct admissible meshes with nodes $\mathbf{x}_K$ located at the boundary $\partial\mathbf{\Omega}$, as will be discussed in Remark 4.1. Furthermore, for each edge $\sigma = K|L \in \mathcal{E}$, we define d_σ as the Euclidean

distance between two collocation points $\mathbf{x}_K$ and $\mathbf{x}_L$. If the edge $\sigma \in \mathcal{E}$ lies on the boundary $\partial\mathbf{\Omega}$, i.e., $\sigma = \partial K \cap \partial\mathbf{\Omega} \neq \emptyset$, then d_σ is defined as the Euclidean distance between $\mathbf{x}_K$ and the affine hyperplane spanned by σ (see Figure 4.1, right). Lastly, we introduce the transmissibility through the edge σ by $\tau_\sigma = m_\sigma / d_\sigma$. The notations are illustrated in Figure 4.1.

Additionally to the admissibility, we assume that the mesh $(\mathcal{T}, \mathcal{E}, \{\mathbf{x}_K\}_{K\in\mathcal{T}})$ is regular in the following sense. There is a constant $\xi > 0$, which does not depend on the size of the mesh $h_\mathcal{T} = \max_{K\in\mathcal{T}}\{\mathrm{diam}(K)\}$ such that

$$\forall K \in \mathcal{T},\ \forall \sigma \in \mathcal{E}_K,\ \begin{cases} d_\sigma \geq \xi\, \mathrm{diam}(K)\,, \\ m_K \geq \xi \sum_{\sigma\in\mathcal{E}_K} m_\sigma d_\sigma\,. \end{cases} \tag{4.1}$$

We can think of the regularity assumptions as an asymptotic property as $h_\mathcal{T} \to 0$, which have to be always satisfied on a given mesh due to the finite number of cells.

For the time discretization we decompose the interval $[0, t_F]$, for a given end time $t_F > 0$ into a finite and increasing number of time steps $0 = t^1 < \ldots < t^M = t_F$ with a step-size $\tau^m = t^m - t^{m-1}$ at time step $m = 2, \ldots, M$. We finally introduce $\Delta t = \max_{m=2,\ldots,M}\{\tau^m\}$.

In the PSC charge transport model (P), (PIC), and (PBC), the device domain is divided into three subdomains $\overline{\mathbf{\Omega}} = \cup_k \overline{\mathbf{\Omega}}_k$ with $k \in \{\mathrm{ETL}, \mathrm{intr}, \mathrm{HTL}\}$, where only the intrinsic perovskite region $\mathbf{\Omega}_\mathrm{intr}$ contains migrating anion vacancies. To incorporate this fact in the discretization, we denote the subset of control volumes in the intrinsic domain by $\mathcal{T}_\mathrm{intr} \subset \mathcal{T}$. It is assumed that

$$\overline{\mathbf{\Omega}}_\mathrm{intr} = \bigcup_{K\in\mathcal{T}_\mathrm{intr}} \overline{K}.$$

Furthermore, we use for the set of faces in the intrinsic domain the notation

$$\mathcal{E}_\mathrm{intr} = \{\sigma \in \mathcal{E} \text{ s.t. } \sigma \subset \overline{\mathbf{\Omega}}_\mathrm{intr}\}.$$

We also define the set of interior faces on the whole and the intrinsic domain as

$$\mathcal{E}^\mathrm{int} = \{\sigma \in \mathcal{E} \text{ s.t. } \sigma \not\subset \partial\mathbf{\Omega}\}, \quad \mathcal{E}^\mathrm{int}_\mathrm{intr} = \{\sigma \in \mathcal{E}_\mathrm{intr} \text{ s.t. } \sigma \not\subset \partial\mathbf{\Omega}_\mathrm{intr}\},$$

respectively.

Remark 4.1. (Boundary conforming Voronoi meshes) A particular type of discretization mesh can be generated using Voronoi diagrams and Delaunay triangulations (triangulation in two dimensions, tetrahedralization in three dimensions), which are

interdisciplinary concepts with various applications beyond computational mathematics [185]. Given a finite number of points $\{\mathbf{x}_K\}_{K\in\mathcal{T}} \subset \mathbb{R}^d$, $d \in \{1,2,3\}$, a Voronoi cell K contains all locations that are closest to the point $\mathbf{x}_K \in K$ from the given point set $\{\mathbf{x}_K\}_{K\in\mathcal{T}}$, i.e.,

$$K = \left\{\mathbf{x} \in \mathbb{R}^d : \|\mathbf{x} - \mathbf{x}_K\| < \|\mathbf{x} - \mathbf{x}_L\| \text{ for all } \mathbf{x}_L \in \{\mathbf{x}_K\}_{K\in\mathcal{T}}, \mathbf{x}_L \neq \mathbf{x}_K\right\}.$$

The dual of a Voronoi diagram is a Delaunay triangulation, in the sense that the Voronoi cells' vertices are the Delaunay triangles' circumcenters. As a result, explicitly calculating Voronoi cells is unnecessary to implement the finite volume method based on Voronoi meshes. Instead, we can work with a triangulation $\overline{\mathbf{\Omega}} = \bigcup_K \overline{T}_K$ of a computational domain $\mathbf{\Omega}$, where $\{T_K\}_K$ is the family of non-overlapping simplices and the simplicial contributions of the triangulation [71]. Delaunay triangulations of computational domains can be efficiently generated using software such as `Triangle` [218] for two-dimensional or `TetGen` [221] for three-dimensional domains. Figure 4.2 shows two partitions of a domain $\mathbf{\Omega}$, generated with `Triangle`, with the boundary of the Voronoi cells highlighted in red and the boundary of the Delaunay simplices in gray. Clearly, we see that the partition in Figure 4.2 (left) does not satisfy $\overline{\mathbf{\Omega}} = \bigcup_{K\in\mathcal{T}} \overline{K}$ (gray cells).

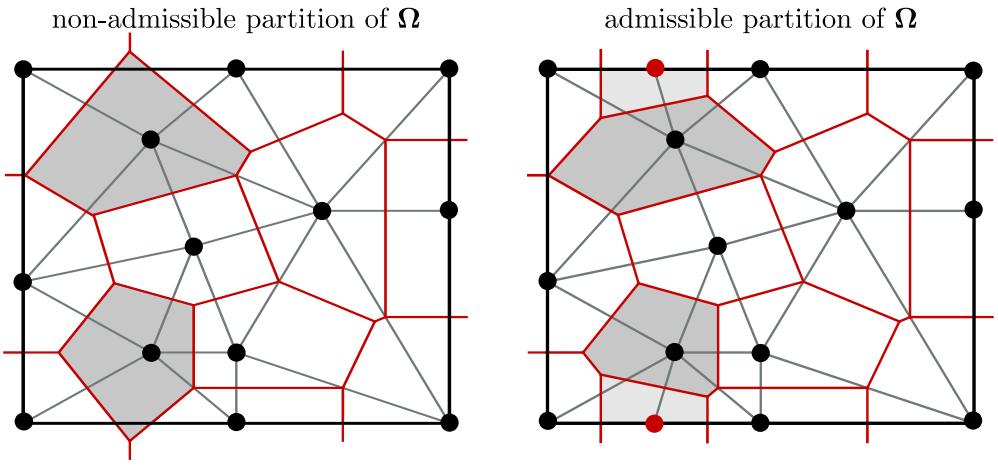

Figure 4.2.: Two Delaunay triangulations of a computational domain $\mathbf{\Omega}$ with the boundary of the Voronoi cells highlighted in red. In the left figure, the Voronoi cells do not satisfy $\overline{\mathbf{\Omega}} = \bigcup_{K\in\mathcal{T}} \overline{K}$ (see the gray cells), while the admissible Voronoi mesh in the right figure is a product of a boundary conforming Delaunay mesh generation, by adding additional points to the partition. The meshes are generated with `Triangle` [218].

However, by imposing additional constraints on the angles of Delaunay simplices and adding additional points (Figure 4.2, right in red), a concept known as *boundary*

conforming Delaunay triangulation [80, 91, 220, 222], we can construct admissible Voronoi meshes in the sense of [70], as depicted in Figure 4.2 (right). In contrast to our previous assumption that $\mathbf{x}_K \notin \partial\mathbf{\Omega}$, which does not come from the definition of admissible meshes, Figure 4.2 (right) illustrates that when a control volume K intersects with the boundary, i.e., $\overline{K} \cap \partial\mathbf{\Omega} \neq \emptyset$, we require that $\mathbf{x}_K \in \partial\mathbf{\Omega}$.

4.1.2. Finite volume discretization

Next, we formulate the implicit-in-time finite volume discretizations for the two charge transport models (P), (PIC), (PBC) and (M), (MIC), (MBC), stated at the end of Section 3.1.4 and Section 3.2.3, respectively. In what follows, the quantity u_K^m represents an approximation of the mean value of $u(\mathbf{x}, t)$ on the cell K at time t^m, where u is one of the potentials $\varphi_\mathrm{n}, \varphi_\mathrm{p}, \varphi_\mathrm{a}, \psi$. With this, we can define the vector $\boldsymbol{u}^m = (u_K^m)_{K\in\mathcal{T}}$. We note that for the anion vacancy quasi Fermi potential φ_a in the perovskite application the approximation is only given for $K \in \mathcal{T}_\mathrm{intr}$, so that we define $\boldsymbol{\varphi}_\mathrm{a}^m = (\varphi_{\mathrm{a},K}^m)_{K\in\mathcal{T}_\mathrm{intr}}$. The discretizations of the doping profile $C \in L^\infty(\mathbf{\Omega})$, the boundary data φ^D, $\psi^D \in W^{1,\infty}(\mathbf{\Omega})$, and the photogeneration rate $G \in L^\infty(\mathbf{\Omega})$ (for the PSC model) are expressed as integral averages over a cell K

$$\chi_K = \frac{1}{m_K}\int_K \chi(\mathbf{x})d\mathbf{x}, \quad K \in \mathcal{T},\ \chi = C,\, G,\, \psi^D \text{ or } \varphi^D. \tag{4.2a}$$

For the boundary data, this results in the vectors $\boldsymbol{\psi}^D = (\psi_K^D)_{K\in\mathcal{T}}$ and $\boldsymbol{\varphi}^D = (\varphi_K^D)_{K\in\mathcal{T}}$. We discretize in the same way the initial conditions φ_n^0, φ_p^0, φ_a^0, which lead to the corresponding vectors $\boldsymbol{\varphi}_\mathrm{n}^0$, $\boldsymbol{\varphi}_\mathrm{p}^0$ and $\boldsymbol{\varphi}_\mathrm{a}^0$. Furthermore, for a face $\sigma \in \mathcal{E}^D$ located at the Dirichlet boundary $\mathbf{\Gamma}^D$ the Dirichlet functions ψ^D, φ^D are given as integral averages over the face σ

$$\chi_\sigma = \frac{1}{m_\sigma}\int_\sigma \chi(\gamma)d\gamma, \quad \sigma \in \mathcal{E}^D,\ \chi = \psi^D,\, \varphi^D. \tag{4.2b}$$

The discrete densities can be calculated via the dimensionless state equations (see (Pf) and (Mf)) inside the domain and at the Dirichlet boundary, namely,

$$\boldsymbol{n}_\alpha^m = \mathcal{F}_\alpha\left(z_\alpha(\boldsymbol{\varphi}_\alpha^m - \boldsymbol{\psi}^m)\right), \qquad \alpha \in \{\mathrm{n},\mathrm{p},\mathrm{a}\},\ m \in \mathbb{N}, \tag{4.3a}$$

$$\boldsymbol{n}_\alpha^D = \mathcal{F}_\alpha\left(z_\alpha(\boldsymbol{\varphi}_\alpha^D - \boldsymbol{\psi}^D)\right), \qquad \alpha \in \{\mathrm{n},\mathrm{p}\}, \tag{4.3b}$$

$$n_{\alpha,\sigma}^D = \mathcal{F}_\alpha\left(z_\alpha(\varphi_\sigma^D - \psi_\sigma^D)\right), \qquad \alpha \in \{\mathrm{n},\mathrm{p}\},\ \sigma \in \mathcal{E}^D, \tag{4.3c}$$

where the statistics function is applied pointwise to the first two input vectors. We remark that the discrete values of the boundary densities, defined by (4.3b) and (4.3c), are bounded but that the upper bound may be larger than $\|n_\alpha^D\|_{L^\infty}$. Indeed, we have

$$\max\left\{\max_{K\in\mathcal{T}} n_{\alpha,K}^D, \max_{\sigma\in\mathcal{E}^D} n_{\alpha,\sigma}^D\right\} \leq \mathcal{F}_\alpha(\|\varphi^D\|_{L^\infty} + \|\psi^D\|_{L^\infty}) =: y_\alpha^D, \quad \text{for } \alpha \in \{\mathrm{n},\mathrm{p}\}. \tag{4.4}$$

Furthermore, we introduce the finite difference operator acting on vectors $\boldsymbol{u} = (u_K)_K$, denoted by $D_{K,\sigma}$. It is given by

$$D_{K,\sigma}\boldsymbol{u} = \begin{cases} u_L - u_K, & \text{if } \sigma = K|L, \\ u_\sigma^D - u_K, & \text{if } \sigma \in \mathcal{E}^D, \boldsymbol{u} \neq \boldsymbol{\varphi}_\mathrm{a}, \boldsymbol{u} \neq \boldsymbol{n}_\mathrm{a} \\ 0, & \text{otherwise.} \end{cases} \tag{4.5}$$

For the vacancy density $\boldsymbol{n}_\mathrm{a}$ and the quasi Fermi potential $\boldsymbol{\varphi}_\mathrm{a}$, we have in case of the PSC model that $\sigma = K|L \in \mathcal{E}_\mathrm{intr}^\mathrm{int}$, whereas in case of the memristive model $\sigma = K|L \in \mathcal{E}^\mathrm{int}$. Lastly, we discuss the choice of the time discretization method.

Because of the stiffness in drift-diffusion models arising from small non-dimensionalized parameters such as the rescaled Debye length λ, fully implicit-in-time numerical methods are usually preferred. Using the backward Euler method yields robustness of the discretization schemes and asymptotic preserving properties for drift-diffusion type models [18, 34]. To the best of our knowledge, there does not exist literature proving such properties for higher order time and spatial FVM discretizations in the context of drift-diffusion models. Hence, the discussion of other time discretizations is omitted here, and we also rely on the backward Euler method. We refer to, e.g., [102, 103, 115] on a general overview of temporal discretization methods.

The finite volume method follows a general procedure in which we integrate the bulk equations (P) and (M) over each control volume $K \in \mathcal{T}$ (*resp.* $K \in \mathcal{T}_\mathrm{intr}$ for the vacancies in the PSC model). We employ Gauss' law to account for the current densities and break down the surface integrals into the sum of integrals over the faces $\sigma \in \mathcal{E}_K$. For instance, for the left-hand side of the Poisson equation, this means

$$\int_K \Delta\psi \, d\mathbf{x} = \int_{\partial K} \nabla\psi \cdot \boldsymbol{\nu}_{K,\sigma} \, dS = \sum_{\sigma\in\mathcal{E}_K} \int_\sigma \nabla\psi \cdot \boldsymbol{\nu}_{K,\sigma} \, dS \approx \sum_{\sigma\in\mathcal{E}_K} m_\sigma \frac{D_{K,\sigma}\boldsymbol{\psi}^m}{d_\sigma},$$

where $\boldsymbol{\nu}_{K,\sigma}$ is the unit normal to the face σ outward from the control volume K, and, where we used a central difference flux approximation for $\nabla\psi \cdot \boldsymbol{\nu}_{K,\sigma}$. Furthermore, for the right-hand side of the Poisson equation, we can apply one-point quadrature rules. Similarly, we can formulate proper discrete counterparts of the other equations. We proceed with formulating the numerical schemes.

Perovskite solar cells The finite volume scheme for (P), (PIC), (PBC) (see Section 3.1.4) is given as follows. First, the discrete mass balance equations for the three

charge carriers are for each time step $m \in \mathbb{N}$ given by

$$\nu z_{\mathrm{n}} m_K \frac{n_{\mathrm{n},K}^m - n_{\mathrm{n},K}^{m-1}}{\tau^m} + \sum_{\sigma \in \mathcal{E}_K} J_{\mathrm{n},K,\sigma}^m = z_{\mathrm{n}} m_K \Big(\gamma G_K - R(n_{\mathrm{n},K}^m, n_{\mathrm{p},K}^m) \Big), \quad K \in \mathcal{T}, \tag{DPa}$$

$$\nu z_{\mathrm{p}} m_K \frac{n_{\mathrm{p},K}^m - n_{\mathrm{p},K}^{m-1}}{\tau^m} + \sum_{\sigma \in \mathcal{E}_K} J_{\mathrm{p},K,\sigma}^m = z_{\mathrm{p}} m_K \Big(\gamma G_K - R(n_{\mathrm{n},K}^m, n_{\mathrm{p},K}^m) \Big), \quad K \in \mathcal{T}, \tag{DPb}$$

$$z_{\mathrm{a}} m_K \frac{n_{\mathrm{a},K}^m - n_{\mathrm{a},K}^{m-1}}{\tau^m} + \sum_{\sigma \in \mathcal{E}_K} J_{\mathrm{a},K,\sigma}^m = 0, \qquad K \in \mathcal{T}_{\mathrm{intr}}. \tag{DPc}$$

They are coupled to the discrete Poisson equation for $m \in \mathbb{N}$

$$-\lambda^2 \sum_{\sigma \in \mathcal{E}_K} \tau_\sigma D_{K,\sigma} \boldsymbol{\psi}^m = \begin{cases} \delta m_K (z_{\mathrm{n}} n_{\mathrm{n},K}^m + z_{\mathrm{p}} n_{\mathrm{p},K}^m + C_K), & K \in \mathcal{T} \setminus \mathcal{T}_{\mathrm{intr}}, \\ \delta m_K (z_{\mathrm{n}} n_{\mathrm{n},K}^m + z_{\mathrm{p}} n_{\mathrm{p},K}^m + C_K) & \\ \quad + m_K z_{\mathrm{a}} n_{\mathrm{a},K}^m, & K \in \mathcal{T}_{\mathrm{intr}}. \end{cases} \tag{DPd}$$

Memristive devices The finite volume scheme for (M), (MIC), (MBC) (see Section 3.2.3) is given by the discrete mass balance equations for the three charge carriers. For $m \in \mathbb{N}$ we have

$$\nu z_{\mathrm{n}} m_K \frac{n_{\mathrm{n},K}^m - n_{\mathrm{n},K}^{m-1}}{\tau^m} + \sum_{\sigma \in \mathcal{E}_K} J_{\mathrm{n},K,\sigma}^m = 0, \qquad K \in \mathcal{T}, \tag{DMa}$$

$$\nu z_{\mathrm{p}} m_K \frac{n_{\mathrm{p},K}^m - n_{\mathrm{p},K}^{m-1}}{\tau^m} + \sum_{\sigma \in \mathcal{E}_K} J_{\mathrm{p},K,\sigma}^m = 0, \qquad K \in \mathcal{T}, \tag{DMb}$$

$$z_{\mathrm{a}} m_K \frac{n_{\mathrm{a},K}^m - n_{\mathrm{a},K}^{m-1}}{\tau^m} + \sum_{\sigma \in \mathcal{E}_K} J_{\mathrm{a},K,\sigma}^m = 0, \qquad K \in \mathcal{T}, \tag{DMc}$$

which are coupled to the discrete Poisson equation which reads for $m \in \mathbb{N}$ and $K \in \mathcal{T}$

$$-\lambda^2 \sum_{\sigma \in \mathcal{E}_K} \tau_\sigma D_{K,\sigma} \boldsymbol{\psi}^m = \delta_{\mathrm{n}} m_K \Big(z_{\mathrm{n}} n_{\mathrm{n},K}^m + \delta_{\mathrm{p}} (z_{\mathrm{p}} n_{\mathrm{p},K}^m + C_K) \Big) + m_K z_{\mathrm{a}} n_{\mathrm{a},K}^m. \tag{DMd}$$

In both numerical schemes (DP), (DM), we assume for $\alpha \in \{\mathrm{n}, \mathrm{p}, \mathrm{a}\}$ that the discrete current density $J_{\alpha,K,\sigma}^m$ is a locally conservative and consistent approximation of $\int_\sigma \mathbf{j}_\alpha \cdot \boldsymbol{\nu}_{K,\sigma} \, dS$ with $\boldsymbol{\nu}_{K,\sigma}$ as the unit normal to the face σ outward from the control volume K. We understand locally conservative in the sense that for $\sigma = K|L$ the flux approximation shall satisfy

$$J_{\alpha,K,\sigma}^m + J_{\alpha,L,\sigma}^m = 0, \quad \alpha \in \{\mathrm{n}, \mathrm{p}, \mathrm{a}\}. \tag{4.6}$$

We note that the finite difference operator $D_{K,\sigma}$, defined in (4.5), is also locally conservative. As a consequence of (4.6), the locally conservative fluxes agree up to sign for any interior edge σ. This allows us to introduce for the finite difference operator the notation

$$D_\sigma \boldsymbol{u} = |D_{K,\sigma}\boldsymbol{u}|, \qquad \text{for } \sigma \in \mathcal{E}_K. \tag{4.7}$$

A discussion of possible choices for the numerical charge carrier fluxes will be part of the following section.

4.1.3. Charge carrier flux discretization

A correct choice of the discrete current densities $J^m_{\alpha,K,\sigma}$ is a rather delicate issue as the wrong choice may lead to instabilities or violation of thermodynamic principles. For example, when choosing a second-order accurate central finite difference flux for $J^m_{\alpha,K,\sigma}$, rigorous numerical analysis can be performed [30], but does not reflect physical phenomena adequately generally, such as positivity of carrier densities or a discrete maximum principle [71]. Furthermore, the first-order accurate upwind flux discretizations exist, which take the flow direction of the drift component of the continuous current densities into account [243]. In the context of drift-diffusion models, they were analyzed in, e.g., [19, 37, 38]. Moreover, we have the exponential fitting schemes. In case of Boltzmann statistics (2.21), the resulting scheme was independently derived several times [54, 111, 158, 203, 210]. In the framework of this thesis, we call this family of discretizations *Scharfetter-Gummel schemes*, a name frequently used in semiconductor physics [76, 203].

For a Boltzmann approximation as statistics function $\mathcal{F}_\alpha$, the classical Scharfetter-Gummel scheme [210] (which corresponds to linear diffusion) results in a stable and thermodynamically consistent two-point flux approximation scheme. The scheme is proven to exhibit second-order convergence in the L^2 norm for sufficiently smooth solutions of two-dimensional problems [145]. The classical Scharfetter-Gummel approximation simplifies to the upwind scheme when the drift component dominates over diffusion. Conversely, when the electric field, and consequently the drift, vanishes, it coincides with the central difference flux [71]. A computationally costly generalization can be formulated for statistics functions beyond the Boltzmann approximation but cannot be expressed in closed form [68].

Hence, several modified numerically stable Scharfetter-Gummel flux discretizations, which preserve the physical properties of the model, have recently been developed and/or analyzed [19, 71–73, 85, 139, 140, 190]. These schemes deal with nonlinear diffusion within the continuous current densities (see (2.28), (2.37)). In our following

analysis, we maintain consistency with the descriptions of electron and hole current densities (2.28) by assuming a constant mobility for the vacancies. This assumption results in nonlinear diffusion within the drift-diffusion current density (2.37). For a discussion of schemes for current densities that involve linear diffusion but a modified drift component as stated in (2.38), we refer to, e.g., [DA6, 31–33, 105]. It is worth noting that Scharfetter-Gummel based schemes, similar to those mentioned, have been successfully employed in commercial software such as [46, 223, 233].

In the following, we use the excess chemical potential approximation as TPFA scheme for $J^m_{\alpha,K,\sigma}$. The earliest reference, we could find for this thermodynamically consistent discretization scheme is [255] which was later numerically analyzed in [30, 92] and compared in [DA9, 132]. The derivation of the numerical flux is based on an equivalent reformulation of the non-dimensionalized current densities $\mathbf{j}_\alpha = -z_\alpha^2 n_\alpha \nabla\varphi_\alpha$ (see (Pe), (Me)) with respect to the dimensionless *excess chemical potential* $\eta^{\mathrm{ex}} := \eta - \eta^{\mathrm{id}}$. Here, $\eta^{\mathrm{id}} := \log n_\alpha$ denotes the ideal dimensionless chemical potential. For instance, for the Boltzmann approximation, the dimensionless chemical potential reads $\eta = \log n_\alpha$, which results in $\eta^{\mathrm{ex}} = \log n_\alpha - \eta^{\mathrm{id}} = 0$. Thus, we can identify the excess chemical potential η^{ex} as a measure of degeneracy of the chemical potential from a Boltzmann setup [15].

Using the dimensionless relation $z_\alpha\varphi_\alpha = \eta_\alpha + z_\alpha\psi$ and the fact that $\nabla\eta^{\mathrm{id}} = \nabla n_\alpha / n_\alpha$, we reformulate the current densities (Pe), (Me) to

$$\begin{aligned}\mathbf{j}_\alpha = -z_\alpha^2 n_\alpha \nabla\varphi_\alpha \ &= -z_\alpha n_\alpha \nabla\Big(\eta + z_\alpha\psi + \eta^{\mathrm{id}} - \eta^{\mathrm{id}}\Big) \\ &= -z_\alpha\Big(\nabla n_\alpha + n_\alpha\nabla(z_\alpha\psi + \eta^{\mathrm{ex}})\Big) \qquad \text{for } \alpha \in \{\mathrm{n},\mathrm{p},\mathrm{a}\}. \\ &= -z_\alpha\Big(\nabla n_\alpha + n_\alpha\nabla(z_\alpha\varphi_\alpha - \log n_\alpha)\Big),\end{aligned} \tag{4.8}$$

In the classical Scharfetter-Gummel scheme derivation, we assume that both the electric field $-\nabla\psi$, and the current density $\mathbf{j}_\alpha$ remain constant along the connecting vector $\overline{\mathbf{x}_K\mathbf{x}_L}$ between two neighboring control volumes K, L, see, e.g., [71]. Suppose we additionally assume that the excess chemical potential gradient $\nabla\eta^{\mathrm{ex}}$ is also constant along the vector $\overline{\mathbf{x}_K\mathbf{x}_L}$. In that case, we can similarly derive the excess chemical potential flux approximation which takes the following form for $\alpha \in \{\mathrm{n},\mathrm{p},\mathrm{a}\}$

$$J^m_{\alpha,K,\sigma} = \begin{cases} -z_\alpha\tau_\sigma\Big(B\left(-Q^m_{\alpha,K,\sigma}\right)n^m_{\alpha,L} - B\left(Q^m_{\alpha,K,\sigma}\right)n^m_{\alpha,K}\Big), & \text{if } \sigma = K|L, \\ -z_\alpha\tau_\sigma\Big(B\left(-Q^m_{\alpha,K,\sigma}\right)n^D_{\alpha,\sigma} - B\left(Q^m_{\alpha,K,\sigma}\right)n^m_{\alpha,K}\Big), & \text{if } \sigma \in \mathcal{E}^D, \alpha \neq \mathrm{a}, \\ 0, & \text{otherwise,} \end{cases} \tag{DFa}$$

where the quantity $Q^m_{\alpha,K,\sigma}$ is defined as

$$Q^m_{\alpha,K,\sigma} = D_{K,\sigma}\left(z_\alpha \boldsymbol{\varphi}^m_\alpha - \log \boldsymbol{n}^m_\alpha\right). \tag{DFb}$$

In the previous formula, the logarithm is applied componentwise. Lastly, the function B denotes the Bernoulli function

$$B(x) = \frac{x}{\exp(x) - 1}, \text{ for } x \in \mathbb{R} \setminus \{0\} \quad \text{and} \quad B(0) = 1. \tag{4.9}$$

It is worth noting that in case of the PSC discretization scheme (DP), if $\alpha = \mathrm{a}$ in (DF), then the face $\sigma = K|L$ is only contained in the set of intrinsic interior faces, i.e., $\sigma \in \mathcal{E}^{\mathrm{int}}_{\mathrm{intr}}$ and not in the set of all interior faces $\sigma \in \mathcal{E}^{\mathrm{int}}$.

Remark 4.2. (Physical parameters) As explained at the beginning of Section 3.1.4 and Section 3.2.3 (non-dimensionalization of models), we introduced several simplifications for the physical parameters to enhance clarity in our presentation. To extend our current schemes to include non-constant and/or different parameters, we must make these parameters edge-dependent, involving the mobilities $\mu_{\mathrm{n}}, \mu_{\mathrm{p}}$, the permittivity ε_s, and the effective densities of states $N_{\mathrm{n}}, N_{\mathrm{p}}$. Edge-dependent parameters must then be introduced into the flux discretization schemes (DF) as well as the sum of the left-hand side of the Poisson equations (DPd), (DMd). For the effective density of states, we must adapt the definitions of densities via the state equations (4.3) accordingly. To consider non-zero but piecewise constant band-edge energies E_α, we need to add the corresponding term in the state equations (4.3). Finally, we must modify the definitions of the PSC discrete mass balances (DPa) and (DPb) to include non-constant recombination parameters entering (3.3).

Remark 4.3. (Boundary conditions) Observe that all the boundary conditions have been considered in the definition of the schemes. The external Neumann (PBCa), (MBCa) and Dirichlet boundary conditions (PBCb), (MBCb) for the electric potential are handled in the definition of the finite difference operator (4.5). For the quasi Fermi potentials of electrons and holes external boundary conditions are included in the definition of the finite difference operator (4.5) as well as in the flux discretization scheme (DF) (and in the discrete state equation (4.3c) entering the flux discretization). The Neumann boundary conditions for the vacancies of both applications (PBCc), (MBCc) are included in the definition of (DF). Finally, observe that for the discretization scheme of PSCs the continuity of fluxes of electrons, holes and electric potential through the interfaces $\boldsymbol{\Sigma}_{\mathrm{ETL}}$ and $\boldsymbol{\Sigma}_{\mathrm{HTL}}$ ((PBCd), (PBCe), and (PBCf)) is automatically ensured thanks to the flux conservation property (4.6).

At first glance, it might not be obvious why the flux scheme (DF) is a discrete version of the current density $\mathbf{j}_\alpha = -z_\alpha^2 n_\alpha \nabla \varphi_\alpha$ (see (Pe) and (Me)). It turns out that we can define for $\alpha \in \{\mathrm{n}, \mathrm{p}, \mathrm{a}\}$

$$\overline{n}_{\alpha,\sigma}^m := \begin{cases} \dfrac{B(-Q_{\alpha,K,\sigma}^m) n_{\alpha,L}^m - B(Q_{\alpha,K,\sigma}^m) n_{\alpha,K}^m}{z_\alpha(\varphi_{\alpha,L}^m - \varphi_{\alpha,K}^m)}, & \text{if } \sigma = K|L, \\ \dfrac{B(-Q_{\alpha,K,\sigma}^m) n_{\alpha,\sigma}^D - B(Q_{\alpha,K,\sigma}^m) n_{\alpha,K}^m}{z_\alpha(\varphi_\sigma^D - \varphi_{\alpha,K}^m)}, & \text{if } \sigma \in \mathcal{E}^D \cap \mathcal{E}_K, \alpha \neq \mathrm{a}, \\ 0, & \text{otherwise}, \end{cases} \tag{4.10}$$

and equivalently rewrite the excess chemical potential scheme (DF) to

$$J_{\alpha,K,\sigma}^m = -z_\alpha^2 \tau_\sigma \overline{n}_{\alpha,\sigma}^m D_{K,\sigma} \boldsymbol{\varphi}_\alpha^m, \quad \text{for all } \alpha \in \{\mathrm{n}, \mathrm{p}, \mathrm{a}\}. \tag{4.11}$$

We note that, as before, in case of the finite volume scheme for the perovskite solar cell charge transport model, we have in case of halide vacancies $\alpha = \mathrm{a}$ for the faces only $\sigma = K|L \in \mathcal{E}_{\mathrm{intr}}^{\mathrm{int}}$ in (4.10), whereas in all other cases $\sigma = K|L \in \mathcal{E}^{\mathrm{int}}$. Moreover, $\overline{n}_{\alpha,\sigma}^m$ is well-defined in the sense that thanks to the conservation property (4.6), $\overline{n}_{\alpha,\sigma}^m$ depends only on the edge (and not nodal values) as well as the fact that a boundary edge has only one associated control volume. The reformulation of the discrete fluxes (4.11) now is closer to the continuous current density $\mathbf{j}_\alpha = -z_\alpha^2 n_\alpha \nabla \varphi_\alpha$ (see (Pe) and (Me)), but the analogy would not be complete, if $\overline{n}_{\alpha,\sigma}^m$ is not consistent with the density at the interface σ. This is actually the case as the following lemma shows which is adapted from [30, Lemma 3.1].

Lemma 4.4. Let $\alpha \in \{\mathrm{n}, \mathrm{p}, \mathrm{a}\}$. The interface value $\overline{n}_{\alpha,\sigma}^m$ defined by (4.10) is a convex combination of $n_{\alpha,K}^m$ and $n_{\alpha,L}^m$ (*resp.* $n_{\alpha,\sigma}^D$ for $\alpha \neq \mathrm{a}$), if $\sigma = K|L$ (*resp.* $\sigma \in \mathcal{E}^D$ for $\alpha \neq \mathrm{a}$). In particular, it is enclosed between the minimum and the maximum of the two values $n_{\alpha,K}^m$ and $n_{\alpha,L}^m$ (*resp.* $n_{\alpha,\sigma}^D$ for $\alpha \neq \mathrm{a}$).

Proof. Let $\alpha \in \{\mathrm{n}, \mathrm{p}, \mathrm{a}\}$. It suffices to observe that for $\sigma = K|L$ (the boundary case can be readily adapted),

$$\overline{n}_{\alpha,\sigma}^m = \frac{B(y) - B(x)}{x - y} n_{\alpha,L}^m + \frac{B(-x) - B(-y)}{x - y} n_{\alpha,K}^m, \tag{4.12}$$

with $x = D_{K,\sigma} \log \boldsymbol{n}_\alpha^m$ and $y = -Q_{\alpha,K,\sigma}^m$. Using the fact that the Bernoulli function is decreasing, $B(y) - B(-y) = -y$, and $B(-x) - B(x) = x$, we observe that the coefficients in (4.12) are non-negative and sum to 1. Hence, the claim follows. We refer to [30] for additional details concerning this computation. □

4.2. Existence of a discrete solution

The goal of this section is to establish the existence of a discrete solution corresponding to the two implicit-in-time TPFA finite volume schemes (DP), (DM) with the flux approximation (DF). The discretizations consist of a nonlinear system of equations at each time step. Knowing the solution at step $m-1$, we establish the existence of a solution at time step m. We consider the quasi Fermi potentials and the electrostatic potential as unknowns of the nonlinear system of equations, as the charge carrier densities are functions of these potentials through the statistical relation (4.3).

The primary tool of our analysis is a discrete counterpart of the continuous entropy-dissipation inequalities in Theorem 3.5 and Theorem 3.7. For further information on the entropy method for finite volume schemes, we refer to [36]. We proceed as follows: In Section 4.2.1, we adapt the arguments of the continuous entropy-dissipation calculations to show in Theorem 4.5 and Theorem 4.6 that an analogous inequality also holds for a solution of the implicit-in-time FVM schemes. We continue in Section 4.2.2 with showing the existence and uniqueness of a discrete electric potential for given quasi Fermi potentials associated with the Poisson equation. Then, we prove in Section 4.2.3 some *a priori* estimates on the quasi Fermi and electrostatic potentials, obtained as consequences of the bounds on the entropy and the dissipation. Lastly, Section 4.2.4 shows the existence of quasi Fermi potentials, which finalizes the proof of the existence of discrete solutions stated in Theorem 4.15 and Theorem 4.16. The proofs rely on a corollary of Brouwer's fixed point theorem for the quasi Fermi potentials, coupled with the minimization of a convex functional for the electric potential.

4.2.1. Discrete entropy-dissipation inequality

This section aims to prove the discrete entropy-dissipation inequalities presented in Theorem 4.5 and Theorem 4.6, which serve as discrete counterparts of Theorem 3.5 and Theorem 3.7.

Perovskite solar cells We consider the problem (P) with the initial conditions (PIC) and the boundary conditions (PBC) (see Section 3.1.4). The implicit-in-time finite volume scheme is given by (DP), (DF). In the following, we derive a discrete counterpart of Theorem 3.5 for the discrete relative entropy ($m \in \mathbb{N}$)

$$\begin{aligned}\mathbb{E}_{\mathcal{T}}^m = \frac{\lambda^2}{2}\sum_{\sigma\in\mathcal{E}}\tau_\sigma\left(D_\sigma(\boldsymbol{\psi}^m-\boldsymbol{\psi}^D)\right)^2 + \delta\sum_{\alpha\in\{\mathrm{n,p}\}}\sum_{K\in\mathcal{T}} m_K H_\alpha(n_{\alpha,K}^m, n_{\alpha,K}^D)\\ + \sum_{K\in\mathcal{T}_{\mathrm{intr}}} m_K\Phi_{\mathrm{a}}(n_{\mathrm{a},K}^m),\end{aligned} \tag{4.13}$$

where $\Phi_{\mathrm{a}}' = \mathcal{F}_{\mathrm{a}}^{-1}$ (see (3.40)) and $H_\alpha(x,y) = \Phi_\alpha(x) - \Phi_\alpha(y) - \Phi_\alpha'(y)(x-y)$ (see (3.41)). Furthermore, we introduced the notation $D_\sigma \boldsymbol{u} = |D_{K,\sigma}\boldsymbol{u}|$ (see (4.7)). Since we assume that $\Phi_{\mathrm{a}} \geq 0$, the overall discrete entropy $\mathbb{E}_{\mathcal{T}}^m$ is non-negative. Taking into account the fact that $z_\alpha^2 = 1$ for $\alpha \in \{\mathrm{n},\mathrm{p}\}$, the corresponding discrete non-negative dissipation $\mathbb{D}_{\mathcal{T}}^m$ for $m \in \mathbb{N}$ is given by

$$\begin{aligned}\mathbb{D}_{\mathcal{T}}^m =& \frac{\delta}{\nu} \sum_{K\in\mathcal{T}} m_K R(n_{\mathrm{n},K}^m, n_{\mathrm{p},K}^m)\left(\varphi_{\mathrm{p},K}^m - \varphi_{\mathrm{n},K}^m\right) + \frac{\delta}{2\nu} \sum_{\alpha\in\{\mathrm{n},\mathrm{p}\}} \sum_{\sigma\in\mathcal{E}} \tau_\sigma \overline{n}_{\alpha,\sigma}^m (D_\sigma \boldsymbol{\varphi}_\alpha^m)^2 \\ &+ \frac{z_{\mathrm{a}}^2}{2} \sum_{\sigma\in\mathcal{E}_{\mathrm{intr}}^{\mathrm{int}}} \tau_\sigma \overline{n}_{\mathrm{a},\sigma}^m (D_\sigma \boldsymbol{\varphi}_{\mathrm{a}}^m)^2.\end{aligned} \tag{4.14}$$

With this, we formulate the discrete entropy-dissipation inequality for the PSC model.

Theorem 4.5. (Discrete entropy-dissipation inequality for a PSC model) Let $m \in \mathbb{N}$. For any solution to the finite volume scheme (DP), (DF) and any $\varepsilon > 0$ one has the following entropy-dissipation inequality: There is a constant $c_{\varepsilon,\boldsymbol{\Omega},\xi} > 0$ such that

$$\frac{\mathbb{E}_{\mathcal{T}}^m - \mathbb{E}_{\mathcal{T}}^{m-1}}{\tau^m} + \mathbb{D}_{\mathcal{T}}^m \leq c_{\varepsilon,\boldsymbol{\Omega},\xi} + \varepsilon \mathbb{E}_{\mathcal{T}}^m, \tag{4.15}$$

where the entropy $\mathbb{E}_{\mathcal{T}}^m$ is defined in (4.13) and the dissipation $\mathbb{D}_{\mathcal{T}}^m$ in (4.14). The constant $c_{\varepsilon,\boldsymbol{\Omega},\xi}$ depends solely on ε, the measure of $\boldsymbol{\Omega}$, the mesh regularity $\xi > 0$, the boundary data and the photogeneration term via the norms $\|G\|_{L^\infty}$, $\|\varphi^D\|_{W^{1,\infty}}$ and $\|\psi^D\|_{W^{1,\infty}}$, as well as on z_{a}^2 and the dimensionless parameters δ, γ and ν. If $G = 0$ and $\nabla\varphi^D = \nabla\psi^D = \mathbf{0}$, then the right-hand side of (4.15) vanishes.

Proof. Let $m \in \mathbb{N}$. We start by considering the difference of the entropy $\mathbb{E}_{\mathcal{T}}^m$ defined in (4.13) evaluated at time t^m and t^{m-1}, that is

$$\begin{aligned}\mathbb{E}_{\mathcal{T}}^m - \mathbb{E}_{\mathcal{T}}^{m-1} =& \frac{\lambda^2}{2} \sum_{\sigma\in\mathcal{E}} \tau_\sigma \left(\left(D_\sigma(\boldsymbol{\psi}^m - \boldsymbol{\psi}^D)\right)^2 - \left(D_\sigma(\boldsymbol{\psi}^{m-1} - \boldsymbol{\psi}^D)\right)^2 \right) \\ &+ \delta \sum_{K\in\mathcal{T}} m_K \left(\Phi_{\mathrm{n}}(n_{\mathrm{n},K}^m) - \Phi_{\mathrm{n}}(n_{\mathrm{n},K}^{m-1}) - \Phi_{\mathrm{n}}'\left(n_{\mathrm{n},K}^D\right)\left(n_{\mathrm{n},K}^m - n_{\mathrm{n},K}^{m-1}\right)\right) \\ &+ \delta \sum_{K\in\mathcal{T}} m_K \left(\Phi_{\mathrm{p}}(n_{\mathrm{p},K}^m) - \Phi_{\mathrm{p}}(n_{\mathrm{p},K}^{m-1}) - \Phi_{\mathrm{p}}'\left(n_{\mathrm{p},K}^D\right)\left(n_{\mathrm{p},K}^m - n_{\mathrm{p},K}^{m-1}\right)\right) \\ &+ \sum_{K\in\mathcal{T}_{\mathrm{intr}}} m_K \left(\Phi_{\mathrm{a}}(n_{\mathrm{a},K}^m) - \Phi_{\mathrm{a}}(n_{\mathrm{a},K}^{m-1})\right).\end{aligned} \tag{4.16}$$

First, we apply $-b^2 \leq -a^2 + 2(a-b)a$ for $a, b \in \mathbb{R}$ to the electric potential contribution

$$\left(\left(D_\sigma(\boldsymbol{\psi}^m - \boldsymbol{\psi}^D)\right)^2 - \left(D_\sigma(\boldsymbol{\psi}^{m-1} - \boldsymbol{\psi}^D)\right)^2\right) \leq 2 D_{K,\sigma}\left(\boldsymbol{\psi}^m - \boldsymbol{\psi}^{m-1}\right) D_{K,\sigma}\left(\boldsymbol{\psi}^m - \boldsymbol{\psi}^D\right).$$

Second, since Φ_α is convex, i.e., $-\Phi_\alpha(y) \le -\Phi_\alpha(x) + \Phi'_\alpha(x)(x-y)$ for $x, y \in \mathbb{R}$, we can estimate for $\alpha \in \{\mathrm{n}, \mathrm{p}, \mathrm{a}\}$

$$-\Phi_\alpha(n_{\alpha,K}^{m-1}) \le -\Phi_\alpha(n_{\alpha,K}^m) + \Phi'_\alpha(n_{\alpha,K}^m)(n_{\alpha,K}^m - n_{\alpha,K}^{m-1}).$$

Applying now the previous two estimates to the right-hand side of (4.16), we receive

$$\begin{aligned}\mathbb{E}_{\mathcal{T}}^m - \mathbb{E}_{\mathcal{T}}^{m-1} \le{}& \lambda^2 \sum_{\sigma\in\mathcal{E}} \tau_\sigma D_{K,\sigma}\left(\boldsymbol{\psi}^m - \boldsymbol{\psi}^{m-1}\right) D_{K,\sigma}\left(\boldsymbol{\psi}^m - \boldsymbol{\psi}^D\right) \\ &+ \delta \sum_{\alpha\in\{\mathrm{n},\mathrm{p}\}} \sum_{K\in\mathcal{T}} m_K \left(\mathcal{F}_\alpha^{-1}(n_{\alpha,K}^m) - \mathcal{F}_\alpha^{-1}\left(n_{\alpha,K}^D\right)\right)\left(n_{\alpha,K}^m - n_{\alpha,K}^{m-1}\right) \\ &+ \sum_{K\in\mathcal{T}_{\mathrm{intr}}} m_K \mathcal{F}_{\mathrm{a}}^{-1}(n_{\mathrm{a},K}^m)\Big(n_{\mathrm{a},K}^m - n_{\mathrm{a},K}^{m-1}\Big),\end{aligned} \tag{4.17}$$

where we used $\Phi'_\alpha = \mathcal{F}_\alpha^{-1}$. Furthermore, for the first sum in the above inequality,

$$S := \lambda^2 \sum_{\sigma\in\mathcal{E}} \tau_\sigma D_{K,\sigma}\left(\boldsymbol{\psi}^m - \boldsymbol{\psi}^{m-1}\right) D_{K,\sigma}\left(\boldsymbol{\psi}^m - \boldsymbol{\psi}^D\right),$$

we use a discrete integration by parts, stated in Lemma A.7(i), with $\boldsymbol{u} = \boldsymbol{\psi}^m - \boldsymbol{\psi}^{m-1}$, and insert the discrete Poisson equation (DPd) to get

$$\begin{aligned}S ={}& -\lambda^2 \sum_{K\in\mathcal{T}} \sum_{\sigma\in\mathcal{E}_K} \tau_\sigma D_{K,\sigma}\left(\boldsymbol{\psi}^m - \boldsymbol{\psi}^{m-1}\right)\left(\psi_K^m - \psi_K^D\right) \\ ={}& \delta \sum_{\alpha\in\{\mathrm{n},\mathrm{p}\}} \sum_{K\in\mathcal{T}} m_K z_\alpha \left(n_{\alpha,K}^m - n_{\alpha,K}^{m-1}\right)\left(\psi_K^m - \psi_K^D\right) \\ &+ \sum_{K\in\mathcal{T}_{\mathrm{intr}}} m_K z_{\mathrm{a}} \left(n_{\mathrm{a},K}^m - n_{\mathrm{a},K}^{m-1}\right)\left(\psi_K^m - \psi_K^D\right).\end{aligned}$$

Plugging this relation back into the initial estimate (4.17), and using the relation $z_\alpha \varphi_\alpha = \mathcal{F}_\alpha^{-1}(n_\alpha) + z_\alpha \psi$, we obtain

$$\begin{aligned}\mathbb{E}_{\mathcal{T}}^m - \mathbb{E}_{\mathcal{T}}^{m-1} \le{}& \delta \sum_{\alpha\in\{\mathrm{n},\mathrm{p}\}} \sum_{K\in\mathcal{T}} m_K z_\alpha \left(\varphi_{\alpha,K}^m - \varphi_K^D\right)\left(n_{\alpha,K}^m - n_{\alpha,K}^{m-1}\right) \\ &+ \sum_{K\in\mathcal{T}_{\mathrm{intr}}} m_K z_{\mathrm{a}} \left(\varphi_{\mathrm{a},K}^m - \psi_K^D\right)\left(n_{\mathrm{a},K}^m - n_{\mathrm{a},K}^{m-1}\right).\end{aligned} \tag{4.18}$$

Now, we divide by the time step size τ^m and insert the mass balance equations (DPa), (DPb), (DPc)

$$\begin{aligned}\frac{\mathbb{E}_{\mathcal{T}}^m - \mathbb{E}_{\mathcal{T}}^{m-1}}{\tau^m} \le{}& -\frac{\delta}{\nu} \sum_{\alpha\in\{\mathrm{n},\mathrm{p}\}} \sum_{K\in\mathcal{T}} \sum_{\sigma\in\mathcal{E}_K} J_{\alpha,K,\sigma}^m \left(\varphi_{\alpha,K}^m - \varphi_K^D\right) - \sum_{K\in\mathcal{T}_{\mathrm{intr}}} \sum_{\sigma\in\mathcal{E}_K} J_{\mathrm{a},K,\sigma}^m \left(\varphi_{\mathrm{a},K}^m - \psi_K^D\right) \\ &+ \frac{\delta}{\nu} \sum_{\alpha\in\{\mathrm{n},\mathrm{p}\}} \sum_{K\in\mathcal{T}} z_\alpha m_K \Big(\gamma G_K - R_K^m\Big)\left(\varphi_{\alpha,K}^m - \varphi_K^D\right),\end{aligned}$$

where we introduce the abbreviation $R_K^m := R(n_{\mathrm{n},K}^m, n_{\mathrm{p},K}^m)$. Next, we perform a discrete integration by parts (see Lemma A.7(ii) and (iii)) and use $z_\mathrm{n} = -1 = -z_\mathrm{p}$ to deduce

$$\begin{aligned}\frac{\mathbb{E}_\mathcal{T}^m - \mathbb{E}_\mathcal{T}^{m-1}}{\tau^m} \le{}& \frac{\delta}{\nu} \sum_{\alpha\in\{\mathrm{n},\mathrm{p}\}} \sum_{\sigma\in\mathcal{E}} J_{\alpha,K,\sigma}^m D_{K,\sigma}\left(\boldsymbol{\varphi}_\alpha^m - \boldsymbol{\varphi}^D\right) + \sum_{\sigma\in\mathcal{E}_\mathrm{intr}^\mathrm{int}} J_{\mathrm{a},K,\sigma}^m D_{K,\sigma}\left(\boldsymbol{\varphi}_\mathrm{a}^m - \boldsymbol{\psi}^D\right)\\ &- \frac{\delta}{\nu}\sum_{K\in\mathcal{T}} m_K R_K^m\left(\varphi_{\mathrm{p},K}^m - \varphi_{\mathrm{n},K}^m\right) + \frac{\delta\gamma}{\nu}\sum_{K\in\mathcal{T}} m_K G_K\left(\varphi_{\mathrm{p},K}^m - \varphi_{\mathrm{n},K}^m\right).\end{aligned}$$

Furthermore, we insert the fluxes $J_{\alpha,K,\sigma}^m = -z_\alpha^2\tau_\sigma\overline{n}_{\alpha,\sigma}^m D_{K,\sigma}\boldsymbol{\varphi}_\alpha^m$ (see (4.11)) dependent on the interface density $\overline{n}_{\alpha,\sigma}^m$ defined in (4.10) and use $z_\mathrm{n}^2 = z_\mathrm{p}^2 = 1$

$$\begin{aligned}\frac{\mathbb{E}_\mathcal{T}^m - \mathbb{E}_\mathcal{T}^{m-1}}{\tau^m} \le{}& -\frac{\delta}{\nu}\sum_{\alpha\in\{\mathrm{n},\mathrm{p}\}}\sum_{\sigma\in\mathcal{E}} \tau_\sigma\overline{n}_{\alpha,\sigma}^m D_{K,\sigma}\boldsymbol{\varphi}_\alpha^m D_{K,\sigma}\left(\boldsymbol{\varphi}_\alpha^m - \boldsymbol{\varphi}^D\right)\\ &- z_\mathrm{a}^2\sum_{\sigma\in\mathcal{E}_\mathrm{intr}^\mathrm{int}} \tau_\sigma\overline{n}_{\mathrm{a},\sigma}^m D_{K,\sigma}\boldsymbol{\varphi}_\mathrm{a}^m D_{K,\sigma}\left(\boldsymbol{\varphi}_\mathrm{a}^m - \boldsymbol{\psi}^D\right)\\ &- \frac{\delta}{\nu}\sum_{K\in\mathcal{T}} m_K R_K^m\left(\varphi_{\mathrm{p},K}^m - \varphi_{\mathrm{n},K}^m\right) + \frac{\delta\gamma}{\nu}\sum_{K\in\mathcal{T}} m_K G_K\left(\varphi_{\mathrm{p},K}^m - \varphi_{\mathrm{n},K}^m\right).\end{aligned}$$

After using the inequality $-a(a-b) \le -(a^2-b^2)/2$ for $a, b \in \mathbb{R}$ in the first two sums and adding the dissipation defined in $\mathbb{D}_\mathcal{T}^m$ in (4.14), we obtain

$$\begin{aligned}\frac{\mathbb{E}_\mathcal{T}^m - \mathbb{E}_\mathcal{T}^{m-1}}{\tau^m} + \mathbb{D}_\mathcal{T}^m \le{}& \frac{\delta}{2\nu}\sum_{\alpha\in\{\mathrm{n},\mathrm{p}\}}\sum_{\sigma\in\mathcal{E}} \tau_\sigma\overline{n}_{\alpha,\sigma}^m\left(D_\sigma\boldsymbol{\varphi}^D\right)^2 + \frac{z_\mathrm{a}^2}{2}\sum_{\sigma\in\mathcal{E}_\mathrm{intr}^\mathrm{int}} \tau_\sigma\overline{n}_{\mathrm{a},\sigma}^m\left(D_\sigma\boldsymbol{\psi}^D\right)^2\\ &+ \frac{\delta\gamma}{\nu}\sum_{K\in\mathcal{T}} m_K G_K\left(\varphi_{\mathrm{p},K}^m - \varphi_{\mathrm{n},K}^m\right),\end{aligned} \tag{4.19}$$

where $D_\sigma\boldsymbol{u} = |D_{K,\sigma}\boldsymbol{u}|$ (see (4.7)). At this stage, it is evident that if $G = 0$ and $\nabla\varphi^D = \nabla\psi^D = \mathbf{0}$, then our claim holds for a vanishing right-hand side, and we can formulate a discrete equivalent of Remark 3.6. In the general case, it remains to estimate the different remainder terms in the right-hand side of (4.19), which we denote by S_1, S_2 and S_3, respectively. We need the following intermediate result for the remainder terms S_1 and S_2 in (4.19). Let $\sigma = K|L \in \mathcal{E}^\mathrm{int}$. Then, we have the following estimates for the discrete approximation $\boldsymbol{\varphi}^D = (\varphi^D)_{K\in\mathcal{T}}$ of the boundary data $\varphi^D \in W^{1,\infty}(\boldsymbol{\Omega})$

$$\begin{aligned}\frac{D_\sigma\boldsymbol{\varphi}^D}{d_\sigma} &\le \frac{1}{d_\sigma m_K m_L}\int_K\int_L |\varphi^D(\mathbf{x}) - \varphi^D(\mathbf{y})|\,d\mathbf{x}\,d\mathbf{y}\\ &\le \frac{\mathrm{diam}(K) + \mathrm{diam}(L)}{d_\sigma}\|\nabla\varphi^D\|_{L^\infty} \le \frac{2}{\xi}\|\nabla\varphi^D\|_{L^\infty}.\end{aligned} \tag{4.20}$$

The last inequality holds also when $\sigma \in \mathcal{E}^D$ or when replacing $\boldsymbol{\varphi}^D$ with $\boldsymbol{\psi}^D$. We can prove the first inequality by using the integral average descriptions (4.2), the second with the mean value theorem, and the last inequality with the help of the first regularity assumption (4.1) ($d_\sigma \geq \xi \operatorname{diam}(K)$). Going back to the first remainder term of (4.19), we set

$$S_1 = \frac{\delta}{2\nu} \sum_{\alpha\in\{\mathrm{n,p}\}} \sum_{\sigma\in\mathcal{E}} \frac{m_\sigma}{d_\sigma} \overline{n}^m_{\alpha,\sigma} (D_\sigma \boldsymbol{\varphi}^D)^2,$$

where we inserted $\tau_\sigma = m_\sigma/d_\sigma$. Since the interface value $\overline{n}^m_{\alpha,\sigma}$ is the convex combination of the two neighboring non-negative densities (see Lemma 4.4), it is bounded from above by the sum of these densities, i.e.,

$$\sum_{\sigma\in\mathcal{E}} \overline{n}^m_{\alpha,\sigma} = \sum_{\sigma\in\mathcal{E}^{\mathrm{int}}} \overline{n}^m_{\alpha,\sigma} + \sum_{\sigma\in\mathcal{E}^D} \overline{n}^m_{\alpha,\sigma} \leq 2 \sum_{K\in\mathcal{T}} \sum_{\sigma\in\mathcal{E}_K} n^m_{\alpha,K} + \sum_{\sigma\in\mathcal{E}^D} \overline{n}^m_{\alpha,\sigma},$$

where due to the definition in (4.10) we have $\overline{n}^m_{\alpha,\sigma} = 0$ for $\sigma \in \mathcal{E}^D$. The previous estimate and $D_\sigma \boldsymbol{\varphi}^D/d_\sigma \leq \frac{2}{\xi}\|\nabla\varphi^D\|_{L^\infty}$ (see (4.20)) yield for S_1

$$\begin{aligned} S_1 &\leq \frac{2\delta}{\nu\xi^2}\|\nabla\varphi^D\|^2_{L^\infty} \sum_{\alpha\in\{\mathrm{n,p}\}} \sum_{\sigma\in\mathcal{E}} m_\sigma\, d_\sigma \overline{n}^m_{\alpha,\sigma} \\ &\leq \frac{2\delta}{\nu\xi^2}\|\nabla\varphi^D\|^2_{L^\infty} \sum_{\alpha\in\{\mathrm{n,p}\}} \Big(2 \sum_{K\in\mathcal{T}} n^m_{\alpha,K} \sum_{\sigma\in\mathcal{E}_K} m_\sigma\, d_\sigma + \sum_{\sigma\in\mathcal{E}^D} m_\sigma\, d_\sigma \overline{n}^m_{\alpha,\sigma}\Big) \\ &\leq \frac{2\delta}{\nu\xi^2}\|\nabla\varphi^D\|^2_{L^\infty} \sum_{\alpha\in\{\mathrm{n,p}\}} \Big(\frac{2}{\xi} \sum_{K\in\mathcal{T}} m_K n^m_{\alpha,K} + |\boldsymbol{\Omega}| y^D_\alpha\Big), \end{aligned} \tag{4.21}$$

where we used the second regularity assumption in (4.1) ($m_K \geq \xi \sum_{\sigma\in\mathcal{E}_K} m_\sigma d_\sigma$) and estimated the interface density by the upper bounds $y^D_\alpha = \mathcal{F}_\alpha(\|\varphi^D\|_{L^\infty} + \|\psi^D\|_{L^\infty})$ for $\alpha \in \{\mathrm{n,p}\}$ (see (4.4)). Similarly, we define the remainder term in (4.19) corresponding to the vacancy contribution as S_2 and establish the estimate

$$S_2 = \frac{z_{\mathrm{a}}^2}{2} \sum_{\sigma\in\mathcal{E}^{\mathrm{int}}_{\mathrm{intr}}} \tau_\sigma \overline{n}^m_{\mathrm{a},\sigma} (D_\sigma \boldsymbol{\psi}^D)^2 \leq \frac{4 z_{\mathrm{a}}^2}{\xi^3}\|\nabla\psi^D\|^2_{L^\infty} \sum_{K\in\mathcal{T}_{\mathrm{intr}}} m_K n^m_{\mathrm{a},K}. \tag{4.22}$$

With (4.21), (4.22) and Lemma 3.3, we find for some $\varepsilon > 0$ with the corresponding

constants $c_\varepsilon, c_{y_\mathrm{n}^D,\varepsilon}, c_{y_\mathrm{p}^D,\varepsilon} > 0$

$$\begin{aligned}
S_1 + S_2 \leq & \frac{4}{\nu\xi^3}\|\nabla\varphi^D\|_{L^\infty}^2\delta \sum_{\alpha\in\{\mathrm{n,p}\}}\sum_{K\in\mathcal{T}} m_K n_{\alpha,K}^m + \frac{4z_\mathrm{a}^2}{\xi^3}\|\nabla\psi^D\|_{L^\infty}^2 \sum_{K\in\mathcal{T}_\mathrm{intr}} m_K n_{\mathrm{a},K}^m \\
& + \frac{2\delta}{\nu\xi^2}\|\nabla\varphi^D\|_{L^\infty}^2|\boldsymbol{\Omega}|(y_\mathrm{n}^D + y_\mathrm{p}^D) \\
& \leq \frac{4}{\nu\xi^3}\|\nabla\varphi^D\|_{L^\infty}^2\delta \sum_{\alpha\in\{\mathrm{n,p}\}}\sum_{K\in\mathcal{T}} m_K\Big(c_{y_\alpha^D,\varepsilon} + \varepsilon H_\alpha(n_{\alpha,K}^m, n_{\alpha,K}^D)\Big) \\
& + \frac{4z_\mathrm{a}^2}{\xi^3}\|\nabla\psi^D\|_{L^\infty}^2 \sum_{K\in\mathcal{T}_\mathrm{intr}} m_K\Big(c_\varepsilon + \varepsilon\Phi_\mathrm{a}(n_{\mathrm{a},K}^m)\Big) + \frac{2\delta}{\nu\xi^2}\|\nabla\varphi^D\|_{L^\infty}^2|\boldsymbol{\Omega}|(y_\mathrm{n}^D + y_\mathrm{p}^D) \\
& \leq c_\xi\Big(c_{\varepsilon,\boldsymbol{\Omega},\xi} + \varepsilon\delta \sum_{\alpha\in\{\mathrm{n,p}\}}\sum_{K\in\mathcal{T}} m_K H_\alpha(n_{\alpha,K}^m, n_{\alpha,K}^D) + \varepsilon \sum_{K\in\mathcal{T}_\mathrm{intr}} m_K\Phi_\mathrm{a}(n_{\mathrm{a},K}^m)\Big) \\
& \leq c_\xi\left(c_{\varepsilon,\boldsymbol{\Omega},\xi} + \varepsilon\mathbb{E}_\mathcal{T}^m\right),
\end{aligned}$$

since the first term of the entropy (4.13) is non-negative. We set the constants to

$$\begin{aligned}
c_\xi &= \max\Big\{\frac{4}{\nu\xi^3}\|\nabla\varphi^D\|_{L^\infty}^2, \frac{4z_\mathrm{a}^2}{\xi^3}\|\nabla\psi^D\|_{L^\infty}^2\Big\}, \\
c_{\varepsilon,\boldsymbol{\Omega},\xi} &= \delta c_{y_\mathrm{n}^D,\varepsilon}|\boldsymbol{\Omega}| + \delta c_{y_\mathrm{p}^D,\varepsilon}|\boldsymbol{\Omega}| + c_\varepsilon|\boldsymbol{\Omega}_\mathrm{intr}| + \frac{2\delta}{\nu\xi^2 c_\xi}\|\nabla\varphi^D\|_{L^\infty}^2|\boldsymbol{\Omega}|(y_\mathrm{n}^D + y_\mathrm{p}^D).
\end{aligned}$$

For the last remainder term coming from the photogeneration we have

$$S_3 = \frac{\delta\gamma}{\nu}\sum_{K\in\mathcal{T}} m_K G_K\left(\varphi_{\mathrm{p},K}^m - \varphi_{\mathrm{n},K}^m\right) = \frac{\delta\gamma}{\nu}\sum_{\alpha\in\{\mathrm{n,p}\}}\sum_{K\in\mathcal{T}} m_K G_K \mathcal{F}_\alpha^{-1}(n_{\alpha,K}^m),$$

where we used $\varphi_\alpha = \mathcal{F}_\alpha^{-1}(n_\alpha)/z_\alpha + \psi$ and $z_\mathrm{n} = -1 = -z_\mathrm{p}$. Furthermore, we use Lemma 3.4 to estimate

$$\begin{aligned}
S_3 &\leq \frac{\delta\gamma}{\nu}\left(\max_{K\in\mathcal{T}} G_K\right)\sum_{\alpha\in\{\mathrm{n,p}\}}\sum_{K\in\mathcal{T}} m_K \max\{\mathcal{F}_\alpha^{-1}(n_{\alpha,K}^m), 0\} \\
&\leq \frac{\gamma}{\nu}||G||_{L^\infty}\delta\sum_{\alpha\in\{\mathrm{n,p}\}}\sum_{K\in\mathcal{T}} m_K\left(c_{y_\alpha^D,\varepsilon} + \varepsilon H_\alpha(n_{\alpha,K}^m, n_{\alpha,K}^D)\right) \\
&\leq \frac{\gamma}{\nu}||G||_{L^\infty}\left(\delta c_{y_\mathrm{n}^D,\varepsilon}|\boldsymbol{\Omega}| + \delta c_{y_\mathrm{p}^D,\varepsilon}|\boldsymbol{\Omega}| + \varepsilon\mathbb{E}_\mathcal{T}^m\right),
\end{aligned}$$

since the other two contributions of the entropy $\mathbb{E}_\mathcal{T}^m$ defined in (4.13) are non-negative. If we combine everything back into (4.19) for redefined constants $c_\xi, c_{\varepsilon,\boldsymbol{\Omega},\xi} > 0$ depending on all the aforementioned quantities, we find

$$\frac{\mathbb{E}_\mathcal{T}^m - \mathbb{E}_\mathcal{T}^{m-1}}{\tau^m} + \mathbb{D}_\mathcal{T}^m \leq S_1 + S_2 + S_3 \leq c_\xi\Big(c_{\varepsilon,\boldsymbol{\Omega},\xi} + 2\varepsilon\mathbb{E}_\mathcal{T}^m\Big). \tag{4.23}$$

Since c_ξ does not depend on ε, this is equivalent to the desired inequality (4.15) up to a redefinition of ε and $c_{\varepsilon,\mathbf{\Omega},\xi}$. □

In the same way, we can prove a discrete entropy-dissipation inequality for TMDC-based memristors.

Memristive devices The memristive model is given by (M), with initial conditions (MIC) and boundary conditions (MBC) (see Section 3.2.3). The underlying implicit-in-time finite volume scheme is formulated in (DM), (DF). Analogously to (4.13), we define a total relative entropy for $m \in \mathbb{N}$

$$\begin{aligned}\mathbb{E}_{\mathcal{T}}^m = \frac{\lambda^2}{2}\sum_{\sigma\in\mathcal{E}} \tau_\sigma \left(D_\sigma(\boldsymbol{\psi}^m - \boldsymbol{\psi}^D)\right)^2 &+ \delta_{\mathrm{n}} \sum_{K\in\mathcal{T}} m_K H_{\mathrm{n}}(n_{\mathrm{n},K}^m, n_{\mathrm{n},K}^D) \\ + \delta_{\mathrm{n}}\delta_{\mathrm{p}} \sum_{K\in\mathcal{T}} m_K H_{\mathrm{p}}(n_{\mathrm{p},K}^m, n_{\mathrm{p},K}^D) &+ \sum_{K\in\mathcal{T}} m_K \Phi_{\mathrm{a}}(n_{\mathrm{a},K}^m),\end{aligned} \tag{4.24}$$

where $\Phi_{\mathrm{a}}' = \mathcal{F}_{\mathrm{a}}^{-1}$ (see (3.40)) and $H_\alpha(x,y) = \Phi_\alpha(x) - \Phi_\alpha(y) - \Phi_\alpha'(y)(x-y)$ for $\alpha \in \{\mathrm{n},\mathrm{p}\}$ (see (3.41)). Since we assume that $\Phi_{\mathrm{a}} \geq 0$, the overall discrete entropy $\mathbb{E}_{\mathcal{T}}^m$ is non-negative. The non-negative dissipation rate for $m \in \mathbb{N}$ is defined as

$$\begin{aligned}\mathbb{D}_{\mathcal{T}}^m = \frac{\delta_{\mathrm{n}}}{2\nu}\sum_{\sigma\in\mathcal{E}} \tau_\sigma \overline{n}_{\mathrm{n},\sigma}^m (D_\sigma \boldsymbol{\varphi}_{\mathrm{n}}^m)^2 &+ \frac{\delta_{\mathrm{n}}\delta_{\mathrm{p}}}{2\nu}\sum_{\sigma\in\mathcal{E}} \tau_\sigma \overline{n}_{\mathrm{p},\sigma}^m (D_\sigma \boldsymbol{\varphi}_{\mathrm{p}}^m)^2 \\ + \frac{z_{\mathrm{a}}^2}{2}\sum_{\sigma\in\mathcal{E}} \tau_\sigma \overline{n}_{\mathrm{a},\sigma}^m (D_\sigma \boldsymbol{\varphi}_{\mathrm{a}}^m)^2,\end{aligned} \tag{4.25}$$

and with this, we can formulate a discrete entropy-dissipation inequality.

Theorem 4.6. (Discrete entropy-dissipation inequality for a memristive model) Let $m \in \mathbb{N}$. For any solution to the finite volume scheme (DM), (DF) and any $\varepsilon > 0$ one has the following entropy-dissipation inequality: There is a constant $c_{\varepsilon,\mathbf{\Omega},\xi} > 0$ such that

$$\frac{\mathbb{E}_{\mathcal{T}}^m - \mathbb{E}_{\mathcal{T}}^{m-1}}{\tau^m} + \mathbb{D}_{\mathcal{T}}^m \leq c_{\varepsilon,\mathbf{\Omega},\xi} + \varepsilon \mathbb{E}_{\mathcal{T}}^m, \tag{4.26}$$

where the entropy $\mathbb{E}_{\mathcal{T}}^m$ is defined in (4.24) and the dissipation $\mathbb{D}_{\mathcal{T}}^m$ in (4.25). The constant $c_{\varepsilon,\mathbf{\Omega},\xi}$ depends solely on ε, the measure of $\mathbf{\Omega}$, the mesh regularity $\xi > 0$, the boundary data via the norms $\|\varphi^D\|_{W^{1,\infty}}$ and $\|\psi^D\|_{W^{1,\infty}}$, as well as on z_{a}^2 and the dimensionless parameters δ_{n}, δ_{p} and ν. If $\nabla\varphi^D = \nabla\psi^D = \mathbf{0}$, then the right-hand side of (4.26) vanishes. □

The proof of Theorem 4.6 follows a similar structure as the proof of Theorem 4.5 and is therefore omitted here. From the discrete entropy-dissipation inequality in

Theorem 4.5 (*resp.* Theorem 4.6), we can deduce some bounds on the entropy $\mathbb{E}_{\mathcal{T}}^m$ in (4.13) (*resp.* (4.24)) and on the cumulated dissipation $\sum_{k=1}^m \tau^k \mathbb{D}_{\mathcal{T}}^k$ for any $m \geq 1$ with $\mathbb{D}_{\mathcal{T}}^k$ defined in (4.14) (*resp.* (4.25)). The proof relies on similar ideas to those used in the proof of Grönwall's lemma, as explained in Appendix A.4.

Corollary 4.7. Let $\mathbb{E}_{\mathcal{T}}^m$ and $\mathbb{D}_{\mathcal{T}}^m$ be given by (4.13) and (4.14) (*resp.* (4.24) and (4.25)). Provided that $\varepsilon < (\Delta t)^{-1}$, where $\Delta t = \max_{m\in\mathbb{N}}\{\tau^m\}$, one has for any $m \geq 1$ that

$$\mathbb{E}_{\mathcal{T}}^m + \sum_{j=1}^m \tau^j \mathbb{D}_{\mathcal{T}}^j \leq (1-\varepsilon\Delta t)^{-m}\mathbb{E}_{\mathcal{T}}^0 + \frac{C_{\varepsilon,\boldsymbol{\Omega},\xi}}{\varepsilon}\Big((1-\varepsilon\Delta t)^{-m} - 1\Big). \tag{4.27}$$

Proof. For $j \in \mathbb{N}$ we define $\mathbb{K}_{\mathcal{T}}^j = \mathbb{E}_{\mathcal{T}}^j + \frac{C_{\varepsilon,\boldsymbol{\Omega},\xi}}{\varepsilon}$. It is worth noting that by using (4.15) (*resp.* (4.26)) we get

$$\mathbb{K}_{\mathcal{T}}^j - \mathbb{K}_{\mathcal{T}}^{j-1} + \tau^j \mathbb{D}_{\mathcal{T}}^j \leq \varepsilon\tau^j \mathbb{K}_{\mathcal{T}}^j \leq \varepsilon\Delta t \mathbb{K}_{\mathcal{T}}^j, \quad j \in \mathbb{N}, \tag{4.28}$$

where we multiplied (4.15) (*resp.* (4.26)) with τ^j. Furthermore, for $j \in \mathbb{N}$, we define $w^j = \mathbb{K}_{\mathcal{T}}^j(1-\varepsilon\Delta t)^j$. Using (4.28) we obtain that

$$\begin{aligned} w^j - w^{j-1} + (1-\varepsilon\Delta t)^{j-1}\tau^j\mathbb{D}_{\mathcal{T}}^j &= (1-\varepsilon\Delta t)^{j-1}\Big[\mathbb{K}_{\mathcal{T}}^j - \mathbb{K}_{\mathcal{T}}^{j-1} + \tau^j\mathbb{D}_{\mathcal{T}}^j - \varepsilon\Delta t\mathbb{K}_{\mathcal{T}}^j\Big] \\ &\leq 0, \end{aligned}$$

and summing over j, we get

$$w^m - w^0 + \sum_{j=1}^m (1-\varepsilon\Delta t)^{j-1}\tau^j\mathbb{D}_{\mathcal{T}}^j \leq 0.$$

We now multiply the last inequality by $(1-\varepsilon\Delta t)^{-m}$ which yields

$$\mathbb{K}_{\mathcal{T}}^m + \sum_{j=1}^m (1-\varepsilon\Delta t)^{-(m-j+1)}\tau^j\mathbb{D}_{\mathcal{T}}^j \leq (1-\varepsilon\Delta t)^{-m}\mathbb{K}_{\mathcal{T}}^0.$$

Since $(1-\varepsilon\Delta t)^{-(m-j+1)} \geq 1$, we find

$$\mathbb{K}_{\mathcal{T}}^m + \sum_{j=1}^m \tau^j\mathbb{D}_{\mathcal{T}}^j \leq (1-\varepsilon\Delta t)^{-m}\mathbb{K}_{\mathcal{T}}^0,$$

which proves (4.7) after inserting $\mathbb{K}_{\mathcal{T}}^0$, $\mathbb{K}_{\mathcal{T}}^m$ and rearranging terms. □

Corollary 4.7 provides the discrete counterpart to Corollary 3.9, demonstrating that the discrete entropy $\mathbb{E}_{\mathcal{T}}^m$ and the cumulated dissipation $\sum_{k=1}^m \tau^k\mathbb{D}_{\mathcal{T}}^k$ remain locally bounded by an exponential for $m \in \mathbb{N}$. This result is based on the observation that for any fixed $\varepsilon > 0$, we have $(1-\varepsilon\Delta t)^{-m} = \exp(m\log(\frac{1}{1-\varepsilon\Delta t}))$ and $0 < \varepsilon\Delta t < 1$. In particular, the boundedness of the entropy and the dissipation for a fixed time are needed to establish the existence of discrete solutions in Section 4.2.4.

4.2.2. Existence of electric potential

In the following, we neglect the superscript m, and denote by $\mathbf{X}$ the vector containing the unknown quasi Fermi potentials which we define by

$$\mathbf{X} = \Big((\varphi_{\mathrm{n},K} - \varphi^D_{\mathrm{n},K})_{K\in\mathcal{T}}, (\varphi_{\mathrm{p},K} - \varphi^D_{\mathrm{p},K})_{K\in\mathcal{T}}, (\varphi_{\mathrm{a},K} - \psi^D_K)_{K\in\mathcal{T}_\mathrm{a}} \Big), \tag{4.29}$$

where in case of the PSC discretization scheme (DP), (DF) we have $\mathcal{T}_\mathrm{a} := \mathcal{T}_\mathrm{intr}$. Analogously, we set for the memristive device scheme (DM), (DF) the family of control volumes to $\mathcal{T}_\mathrm{a} := \mathcal{T}$.

This section aims to show the existence of a unique electric potential $\boldsymbol{\psi} = (\psi_K)_{K\in\mathcal{T}}$ solving the Poisson equation of the discretization schemes dependent on the vector of unknowns $\mathbf{X}$.

Lemma 4.8. (Existence of electric potential) Let $\mathbf{X}$ denote the vector containing the unknown quasi Fermi potentials as defined in (4.29). Suppose that $\mathbf{X}$ is given. Then, there exists a unique solution $\boldsymbol{\psi}(\mathbf{X})$ to the discrete nonlinear Poisson equation (DPd) (*resp.* (DMd)). Furthermore, the mapping $\mathbf{X} \mapsto \boldsymbol{\psi}(\mathbf{X})$ is continuous.

For the proof of Lemma 4.8, we rely on the following lemma, which addresses the conditions under which a real-valued function f has a (unique) global minimum.

Lemma 4.9. (Existence of (unique) global minimum) Let $N \in \mathbb{N}$ and $f : \mathbb{R}^N \to \mathbb{R}$ be a continuous and coercive function.

(i) Then, f has at least one global minimum $\mathbf{x}^* \in \mathbb{R}^N$.

(ii) Suppose that f is additionally differentiable and strictly convex. Then, the global minimum $\mathbf{x}^* \in \mathbb{R}^N$ of f is unique.

To establish Lemma 4.9, we will employ the extreme value theorem, which can be found in, e.g., [205, Theorem 4.16]. We will state the theorem without a proof.

Theorem 4.10. (Extreme value theorem) Let $\mathbf{D} \subset \mathbb{R}^N$ be compact and $f : \mathbf{D} \to \mathbb{R}$ be a continuous function. Then, f attains its maximum and minimum on $\mathbf{D}$. □

Proof of Lemma 4.9. We start with the proof of (i). On the one hand, according to the extreme value theorem (see Theorem 4.10), we can deduce the existence of a local minimum $\mathbf{x}^* \in \overline{B(\mathbf{0}, M)}$ with $M > 0$, which satisfies

$$f(\mathbf{0}) \geq f(\mathbf{x}^*), \quad \text{for } \mathbf{0}, \mathbf{x}^* \in \overline{B(\mathbf{0}, M)}.$$

On the other hand, due to the coercivity of f, we know that as $\|\mathbf{x}\| \to +\infty$, $f(\mathbf{x}) \to +\infty$, which implies that for a sufficiently large $M > 0$, we have

$$f(\mathbf{x}) > f(\mathbf{0}) \geq f(\mathbf{x}^*), \quad \text{for } \|\mathbf{x}\| > M.$$

The above inequality shows that $\mathbf{x}^*$ is a global minimum. The assumption in (ii) that f is strictly convex and differentiable implies that f satisfies for $\mathbf{x}, \mathbf{y} \in \mathbb{R}^N$

$$f(\mathbf{y}) > f(\mathbf{x}) + \nabla f(\mathbf{x})^T(\mathbf{y} - \mathbf{x}).$$

Therefore, for an existing global minimum $\mathbf{x}^*$, for which it holds $\nabla f(\mathbf{x}^*) = \mathbf{0}$, we can conclude that $f(\mathbf{y}) > f(\mathbf{x}^*)$ for all $\mathbf{y} \in \mathbb{R}^N$. This means that the global minimum $\mathbf{x}^* \in \mathbb{R}^N$ is unique. □

We continue by proving the existence of a discrete electric potential for given quasi Fermi potentials, as stated in Lemma 4.8.

Proof of Lemma 4.8. We will only demonstrate the claim for the discrete Poisson equation associated with the PSC discretization scheme (DPd). The proof for the Poisson equation associated with the memristive model (DMd) follows a similar logic. It is worth noting that the boundary conditions are already incorporated in both (DPd) and (DMd), as indicated by Remark 4.3. We define the discrete functional $\mathcal{J}$ for $\mathbf{\Psi} = (\Psi_K)_K \in \mathbb{R}^N$ as follows:

$$\begin{aligned}\mathcal{J}(\mathbf{\Psi}) = &-\delta \sum_{K\in\mathcal{T}} m_K C_K \Psi_K + \delta \sum_{\alpha\in\{\mathrm{n,p}\}} \sum_{K\in\mathcal{T}} m_K \mathcal{G}_\alpha(z_\alpha(\varphi_{\alpha,K} - \Psi_K)) \\ &+ \frac{\lambda^2}{2} \sum_{\sigma\in\mathcal{E}} \tau_\sigma (D_\sigma \mathbf{\Psi})^2 + \sum_{K\in\mathcal{T}_{\mathrm{intr}}} m_K \mathcal{G}_{\mathrm{a}}(z_{\mathrm{a}}(\varphi_{\mathrm{a},K} - \Psi_K)).\end{aligned}$$

Here, $\mathcal{G}_\alpha$ denotes an antiderivative of $\mathcal{F}_\alpha$ for $\alpha \in \{\mathrm{n}, \mathrm{p}, \mathrm{a}\}$. Since $\mathcal{G}_\alpha$ is increasing and $\mathcal{F}_\alpha$ vanishes at $-\infty$ (due to (H1) and (H2), stated in Section 2.3.1 and Section 2.4.2), the antiderivative $\mathcal{G}_\alpha$ is bounded from below. Furthermore, the K-th component of $\nabla\mathcal{J}$ is given by

$$\frac{\partial \mathcal{J}}{\partial \Psi_K} = \begin{cases} -\delta m_K \Big(C_K + \displaystyle\sum_{\alpha\in\{\mathrm{n,p}\}} z_\alpha \mathcal{F}_\alpha(z_\alpha(\varphi_{\alpha,K} - \Psi_K)) \Big) \\ -\lambda^2 \displaystyle\sum_{\sigma\in\mathcal{E}_K} \tau_\sigma D_{K,\sigma} \mathbf{\Psi}, & K \in \mathcal{T} \setminus \mathcal{T}_{\mathrm{intr}}, \\ -\delta m_K \Big(C_K + \displaystyle\sum_{\alpha\in\{\mathrm{n,p}\}} z_\alpha \mathcal{F}_\alpha(z_\alpha(\varphi_{\alpha,K} - \Psi_K)) \Big) \\ -\lambda^2 \displaystyle\sum_{\sigma\in\mathcal{E}_K} \tau_\sigma D_{K,\sigma} \mathbf{\Psi} - m_K z_{\mathrm{a}} \mathcal{F}_{\mathrm{a}}(z_{\mathrm{a}}(\varphi_{\mathrm{a},K} - \Psi_K)), & K \in \mathcal{T}_{\mathrm{intr}}. \end{cases}$$

We conclude that a solution $\boldsymbol{\psi}$ to the discrete Poisson equation (DPd) satisfies $\nabla\mathcal{J}(\boldsymbol{\psi}) = \mathbf{0}$. Therefore, finding a unique minimizer $\boldsymbol{\psi}$ of $\mathcal{J}$ is equivalent to finding a unique solution $\boldsymbol{\psi}$ to the discrete Poisson equation. The existence of such unique global minimum follows from Lemma 4.9. Therefore, we need to demonstrate that the assumptions of Lemma 4.9 are satisfied. Indeed, $\mathcal{J}$ is continuous and differentiable. Since $\mathcal{G}_\alpha$ is bounded from below, the coercivity of $\mathcal{J}$ follows from the coercivity of $\mathcal{H}(\boldsymbol{\Psi}) = \frac{\lambda^2}{2}\sum_{\sigma\in\mathcal{E}}\tau_\sigma(D_\sigma\boldsymbol{\Psi})^2 - \delta\sum_{K\in\mathcal{T}} m_K C_K \Psi_K$. We can establish the coercivity of $\mathcal{H}$ as follows. The discrete Poincaré inequality [70, Lemma 3.1] shows that we can bound the first term of $\mathcal{H}$ from below. Furthermore, Hölder's inequality implies that $\|\Psi\|_{L^1} \leq M_H\|\Psi\|_{L^2}$ for some constant $M_H > 0$, where we specifically refer to the discrete approximations of the L^p norms [149]. In total, we obtain

$$\begin{aligned}\mathcal{H}(\boldsymbol{\Psi}) = \frac{\lambda^2}{2}\sum_{\sigma\in\mathcal{E}}\tau_\sigma(D_\sigma\boldsymbol{\Psi})^2 - \delta\sum_{K\in\mathcal{T}} m_K C_K\Psi_K &\geq \frac{\lambda^2}{2|\boldsymbol{\Omega}|^2}\|\Psi\|_{L^2}^2 - \delta|\boldsymbol{\Omega}|\|C\|_{L^\infty}\|\Psi\|_{L^1}\\ &\geq \frac{\lambda^2}{2|\boldsymbol{\Omega}|^2}\|\Psi\|_{L^2}^2 - \delta M_H|\boldsymbol{\Omega}|\|C\|_{L^\infty}\|\Psi\|_{L^2},\end{aligned}$$

where the right-hand side tends to $+\infty$ as $\|\Psi\|_{L^2} \to +\infty$. This means that $\mathcal{H}$ is coercive, and consequently, $\mathcal{J}$ is also coercive. From Lemma 4.9(i) we can conclude the existence of a global minimum $\boldsymbol{\Psi} = \boldsymbol{\psi}$. The strict convexity of $\mathcal{J}$, due to being a sum of a strictly convex and convex functions, gives the uniqueness of this minimum at $\boldsymbol{\Psi} = \boldsymbol{\psi}$ (see Lemma 4.9(ii)). Therefore, the original claim, that there exists a unique solution to the discrete Poisson equation (DPd) for given quasi Fermi potentials $\mathbf{X}$, is established. Finally, we can prove the continuity of $\mathbf{X} \mapsto \boldsymbol{\psi}(\mathbf{X})$ by applying the implicit function theorem to $\nabla\mathcal{J}$. To do this, we need to demonstrate that the Hessian of $\mathcal{J}$ with respect to $\boldsymbol{\Psi}$ is non-singular. This can be achieved by showing that the Hessian of $\mathcal{J}$ is strictly diagonally dominant [241, Theorem 1.21], which is straightforward given the description of the diagonal entries of the Hessian of $\mathcal{J}$

$$\frac{\partial^2\mathcal{J}}{\partial\Psi_K\partial\Psi_K} = \begin{cases} \delta m_K \sum_{\alpha\in\{\mathrm{n,p}\}} z_\alpha^2\mathcal{F}_\alpha'(z_\alpha(\varphi_{\alpha,K} - \Psi_K)) + \lambda^2\sum_{\sigma\in\mathcal{E}_K}\tau_\sigma, & K\in\mathcal{T}\setminus\mathcal{T}_{\mathrm{intr}},\\ \delta m_K \sum_{\alpha\in\{\mathrm{n,p}\}} z_\alpha^2\mathcal{F}_\alpha'(z_\alpha(\varphi_{\alpha,K} - \Psi_K)) + \lambda^2\sum_{\sigma\in\mathcal{E}_K}\tau_\sigma & \\ \quad + m_K z_{\mathrm{a}}^2\mathcal{F}_{\mathrm{a}}'(z_{\mathrm{a}}(\varphi_{\mathrm{a},K} - \psi_K)), & K\in\mathcal{T}_{\mathrm{intr}}, \end{cases}$$

and the fact that the off-diagonal components solely contain information about the scaled transmissibility τ_σ of one edge. Moreover, due to (H1) and (H2) we have $\mathcal{F}_\alpha' > 0$ for $\alpha \in \{\mathrm{n,p,a}\}$ which completes the proof. □

As a consequence of Lemma 4.8 we can interpret the discrete electric potential as a continuous map $\boldsymbol{\psi} = \boldsymbol{\psi}(\mathbf{X})$.

4.2.3. A priori estimates

Due to Lemma 4.8, we denote the discrete entropies (4.13), (4.24) by $\mathbb{E}_{\mathcal{T}}(\mathbf{X})$ and its associated dissipation functionals (4.14), (4.25) by $\mathbb{D}_{\mathcal{T}}(\mathbf{X})$, where $\mathbf{X}$ is defined in (4.29). In this dissipation, we may distinguish the contributions of electrons, holes, and vacancies. Therefore, we introduce the following notation $\mathbb{D}_{\mathcal{T},\alpha}$ for $\alpha \in \{\mathrm{n},\mathrm{p},\mathrm{a}\}$. In case of the PSC discretization scheme (DP), (DF), we have

$$\mathbb{D}_{\mathcal{T},\alpha}(\mathbf{X}) = \frac{\delta}{2\nu}\sum_{\sigma\in\mathcal{E}} \tau_\sigma \overline{n}_{\alpha,\sigma}(D_\sigma \boldsymbol{\varphi}_\alpha)^2, \quad \text{for all } \alpha \in \{\mathrm{n},\mathrm{p}\}, \tag{4.30}$$

$$\mathbb{D}_{\mathcal{T},\mathrm{a}}(\mathbf{X}) = \frac{z_\mathrm{a}^2}{2}\sum_{\sigma\in\mathcal{E}_{\mathrm{intr}}^{\mathrm{int}}} \tau_\sigma \overline{n}_{\mathrm{a},\sigma}(D_\sigma \boldsymbol{\varphi}_\mathrm{a})^2, \tag{4.31}$$

and, analogously, for the TMDC memristive device discretization scheme (DM), (DF), we set

$$\mathbb{D}_{\mathcal{T},\mathrm{n}}(\mathbf{X}) = \frac{\delta_\mathrm{n}}{2\nu}\sum_{\sigma\in\mathcal{E}} \tau_\sigma \overline{n}_{\mathrm{n},\sigma}(D_\sigma \boldsymbol{\varphi}_\mathrm{n})^2, \quad \mathbb{D}_{\mathcal{T},\mathrm{p}}(\mathbf{X}) = \frac{\delta_\mathrm{n}\delta_\mathrm{p}}{2\nu}\sum_{\sigma\in\mathcal{E}} \tau_\sigma \overline{n}_{\mathrm{p},\sigma}(D_\sigma \boldsymbol{\varphi}_\mathrm{p})^2, \tag{4.32}$$

$$\mathbb{D}_{\mathcal{T},\mathrm{a}}(\mathbf{X}) = \frac{z_\mathrm{a}^2}{2}\sum_{\sigma\in\mathcal{E}} \tau_\sigma \overline{n}_{\mathrm{a},\sigma}(D_\sigma \boldsymbol{\varphi}_\mathrm{a})^2. \tag{4.33}$$

In the following, we prove some *a priori* estimates on the set of unknowns following from bounds on the entropy and dissipation. We start in Lemma 4.11 with a bound on the electric potential.

Lemma 4.11. (Bound for electrostatic potential) Assume that there exists a constant $M_E > 0$ such that $\mathbb{E}_{\mathcal{T}}(\mathbf{X}) \le M_E$. Then, there exists some $M_B > 0$ depending on M_E, λ, $\mathcal{T}$, and ψ^D such that

$$-M_B \le \psi_K \le M_B, \quad \forall K \in \mathcal{T}. \tag{4.34}$$

Proof. As the (relative) entropy contributions of the charge carriers $\alpha \in \{\mathrm{n},\mathrm{p},\mathrm{a}\}$ are non-negative, the bound on $\mathbb{E}_{\mathcal{T}}(\mathbf{X})$ directly implies a bound on the electric energy contribution,

$$\frac{\lambda^2}{2}\sum_{\sigma\in\mathcal{E}} \tau_\sigma (D_\sigma(\boldsymbol{\psi} - \boldsymbol{\psi}^D))^2 \le M_E,$$

where the difference operator $D_\sigma \boldsymbol{u} = |D_{K,\sigma}\boldsymbol{u}|$ is defined in (4.5) and (4.7) for some $\boldsymbol{u}$. We deduce (4.34) by starting with a fixed control volume $K^* \in \mathcal{T}$ so that $\mathcal{E}_K \cap \mathcal{E}^D \neq \emptyset$. This means that K^* has a face σ located on the Dirichlet boundary. For such

$\sigma^* \in \mathcal{E}_{K^*} \cap \mathcal{E}^D \neq \emptyset$, it holds

$$\begin{aligned}\frac{\lambda^2}{2}\tau_{\sigma^*}|\psi_{K^*} - \psi^D_{K^*}|^2 = \frac{\lambda^2}{2}\tau_{\sigma^*}|D_{K^*,\sigma^*}(\boldsymbol{\psi} - \boldsymbol{\psi}^D)|^2 &= \frac{\lambda^2}{2}\tau_{\sigma^*}(D_{\sigma^*}(\boldsymbol{\psi} - \boldsymbol{\psi}^D))^2 \\ &\leq \frac{\lambda^2}{2}\sum_{\sigma\in\mathcal{E}_{K^*}}\tau_\sigma(D_\sigma(\boldsymbol{\psi} - \boldsymbol{\psi}^D))^2 \\ &\leq \frac{\lambda^2}{2}\sum_{\sigma\in\mathcal{E}}\tau_\sigma(D_\sigma(\boldsymbol{\psi} - \boldsymbol{\psi}^D))^2 \leq M_E.\end{aligned}$$

Since $\psi^D \in W^{1,\infty}(\boldsymbol{\Omega})$, we can deduce a bound on $|\psi_{K^*}|$ depending on M_E, λ, ψ^D and also $\mathcal{T}$ (due to the occurrence of $\tau_\sigma = m_\sigma/d_\sigma$). Proceeding now with an interior edge $\sigma = K^*|L$, we observe that

$$\begin{aligned}\frac{\lambda^2}{2}\tau_\sigma(|\psi_L - \psi^D_L| - |\psi_{K^*} - \psi^D_{K^*}|)^2 \leq \frac{\lambda^2}{2}\tau_\sigma(|\psi_L - \psi_{K^*} - (\psi^D_L - \psi^D_{K^*})|)^2 \\ = \frac{\lambda^2}{2}\tau_\sigma(D_\sigma(\boldsymbol{\psi} - \boldsymbol{\psi}^D))^2 \leq M_E,\end{aligned}$$

which shows that $|\psi_L|$ is also bounded due to the boundedness of $\psi_{K^*}, \psi^D_{K^*}$, and ψ^D_L. From these bounds, and by using the connectedness of the mesh and the finite number of control volumes one can inductively get a uniform finite bound for all $(\psi_K)_{K\in\mathcal{T}}$ dependent on all the aforementioned quantities. □

Next, we prove bounds on the electron and hole quasi Fermi potentials, where we stay close to the proof in [30, Lemma 3.7]. Due to different hypotheses on the statistics function $\mathcal{F}_\alpha$ and boundary conditions in [30], an adapted version of [30, Lemma 3.2] is stated in Lemma A.8 and proven in Appendix A.6.

Lemma 4.12. (Bound for electron and hole quasi Fermi potentials) Let $\alpha \in \{\mathrm{n}, \mathrm{p}\}$. Assume that there exists $M_E > 0$ such that $\mathbb{E}_\mathcal{T}(\mathbf{X}) \leq M_E$ and $M_D > 0$ such that $\mathbb{D}_{\mathcal{T},\alpha}(\mathbf{X}) \leq M_D$. Then, there exists some $M_B > 0$ depending on M_E, M_D, $\mathcal{T}$, ψ^D, φ^D, z_α, and the dimensionless constants ν and δ (*resp.* $\delta_\mathrm{n}, \delta_\mathrm{p}$) such that

$$-M_B \leq \varphi_{\alpha,K} \leq M_B, \quad \forall K \in \mathcal{T}. \tag{4.35}$$

In the following proof, we utilize the definition (4.30) associated with the PSC model for $\mathbb{D}_{\mathcal{T},\mathrm{n}}(\mathbf{X}), \mathbb{D}_{\mathcal{T},\mathrm{p}}(\mathbf{X})$. If we instead use the definition (4.32) associated with the memristor model, we only need to adapt the prefactors of the dissipation within the following proof. In that case, M_B in (4.35) additionally depends on other parameters. Specifically, in the case of the memristive model, we have dependencies on $\delta_\mathrm{n}, \delta_\mathrm{p}$ for $\mathbb{D}_{\mathcal{T},\mathrm{p}}(\mathbf{X})$, and on δ_n for $\mathbb{D}_{\mathcal{T},\mathrm{n}}(\mathbf{X})$.

Proof of Lemma 4.12. Let $\alpha \in \{\mathrm{n}, \mathrm{p}\}$. First, we rewrite $\mathbb{D}_{\mathcal{T},\alpha}(\mathbf{X})$ as defined in (4.30) by using $J^m_{\alpha,K,\sigma} = -z_\alpha^2 \tau_\sigma \overline{n}^m_{\alpha,\sigma} D_{K,\sigma} \boldsymbol{\varphi}^m_\alpha$ (see (4.11))

$$\mathbb{D}_{\mathcal{T},\alpha}(\mathbf{X}) = -\frac{\delta}{2\nu} \sum_{\sigma\in\mathcal{E}} J_{\alpha,K,\sigma} D_{K,\sigma} \boldsymbol{\varphi}_\alpha,$$

where we used $z_\mathrm{n}^2 = 1 = z_\mathrm{p}^2$. The main proof idea is based on reformulating $\mathbb{D}_{\mathcal{T},\alpha}$ in terms of a discrete functional $\mathcal{D}_\alpha$. With the help of another functional associated to $\mathcal{D}_\alpha$, we can iteratively deduce the boundedness of $\varphi_{\alpha,K}$ for all $K \in \mathcal{T}$. To define $\mathcal{D}_\alpha$, we introduce the function $\mathcal{K}_\alpha : \mathbb{R}\times\mathbb{R} \to \mathbb{R}$ with

$$\mathcal{K}_\alpha(x,a) = \log(\mathcal{F}_\alpha(x-a)) - x, \quad \forall (x,a) \in \mathbb{R}\times\mathbb{R},$$

and we note that

$$Q_{\alpha,K,\sigma} = \mathcal{K}_\alpha(z_\alpha\varphi_{\alpha,K}, z_\alpha\psi_K) - \mathcal{K}_\alpha(z_\alpha\varphi_{\alpha,K,\sigma}, z_\alpha\psi_{K,\sigma}),$$

where $\varphi_{\alpha,K,\sigma}$ and $\psi_{K,\sigma}$ stand for $\varphi_{\alpha,L}, \psi_L$, if $\sigma = K|L \in \mathcal{E}^{\mathrm{int}}$ and for $\varphi^D_\sigma, \psi^D_\sigma$, if $\sigma \in \mathcal{E}^D$. With the help of $\mathcal{K}_\alpha$, we introduce the face dissipation functional $\mathcal{D}_\alpha : \mathbb{R}^4 \to \mathbb{R}$ defined by (with $\mathcal{D}_\alpha = \mathcal{D}_\alpha(x,y,a,b)$)

$$\mathcal{D}_\alpha = (x-y)\Big[B\Big(\mathcal{K}_\alpha(x,a) - \mathcal{K}_\alpha(y,b)\Big)\mathcal{F}_\alpha(x-a) - B\Big(\mathcal{K}_\alpha(y,b) - \mathcal{K}_\alpha(x,a)\Big)\mathcal{F}_\alpha(y-b)\Big].$$

Indeed, $\mathbb{D}_{\mathcal{T},\alpha}(\mathbf{X})$ can be rewritten in terms of $\mathcal{D}_\alpha$

$$\mathbb{D}_{\mathcal{T},\alpha}(\mathbf{X}) = \frac{\delta}{2\nu} \sum_{\sigma\in\mathcal{E}} \tau_\sigma \mathcal{D}_\alpha\big(z_\alpha\varphi_{\alpha,K}, z_\alpha\varphi_{\alpha,K,\sigma}, z_\alpha\psi_K, z_\alpha\psi_{K,\sigma}\big). \tag{4.36}$$

Similarly to [30, Lemma 3.7], we introduce another functional associated to $\mathcal{D}_\alpha$, $\Upsilon_{\overline{\Phi},\overline{\Psi}} : \mathbb{R} \to \mathbb{R}$, defined by

$$\Upsilon_{\overline{\Phi},\overline{\Psi}}(x) = \inf\left\{\mathcal{D}_\alpha(x,y,a,b);\ -\overline{\Phi} \le y \le \overline{\Phi}, -\overline{\Psi} \le a,b \le \overline{\Psi}\right\}, \tag{4.37}$$

and we establish (see Appendix A.6, Lemma A.8) that

$$\lim_{x\to-\infty} \Upsilon_{\overline{\Phi},\overline{\Psi}}(x) = +\infty \quad \text{and} \quad \lim_{x\to+\infty} \Upsilon_{\overline{\Phi},\overline{\Psi}}(x) = +\infty. \tag{4.38}$$

Especially, Lemma 4.9(i) guarantees that $\Upsilon_{\overline{\Phi},\overline{\Psi}}$ is bounded from below, which will eventually ensure the boundedness of $\varphi_{\alpha,K}$ for all $K \in \mathcal{T}$. As in the proof of Lemma 4.11, we begin by demonstrating the boundedness of the potential φ_{α,K^*} at a specific control volume K^* situated at the Dirichlet boundary. Let $K^* \in \mathcal{T}$ be a control volume, for which there exists a face $\sigma^* \in \mathcal{E}_K \cap \mathcal{E}^D \neq \emptyset$. Next, we verify whether $\Upsilon_{\overline{\Phi},\overline{\Psi}}$ in (4.37) is

well-defined for σ^*. Thanks to the regularity assumptions on the boundary data, i.e., $\varphi^D, \psi^D \in W^{1,\infty}(\mathbf{\Omega})$, and the bound on the discrete electric potential (see Lemma 4.11), there exist $\overline{\Phi}, \overline{\Psi} > 0$ such that

$$-\overline{\Phi} \leq \varphi^D_{\sigma^*} \leq \overline{\Phi} \quad \text{and} \quad -\overline{\Psi} \leq \psi_{K^*}, \psi^D_{\sigma^*} \leq \overline{\Psi},$$

which shows that $\Upsilon_{\overline{\Phi},\overline{\Psi}}(z_\alpha \varphi_{\alpha,K^*})$ exists. We consider the description (4.36) of $\mathbb{D}_{\mathcal{T},\alpha}$. The assumption $\mathbb{D}_{\mathcal{T},\alpha}(\mathbf{X}) < M_D$ and the boundedness of $\Upsilon_{\overline{\Phi},\overline{\Psi}}(z_\alpha \varphi_{\alpha,K^*})$ from below, particularly imply for $\sigma^* \in \mathcal{E}_K \cap \mathcal{E}^D \neq \emptyset$

$$-\infty < \Upsilon_{\overline{\Phi},\overline{\Psi}}(z_\alpha \varphi_{\alpha,K^*}) \leq \mathcal{D}_\alpha\big(z_\alpha \varphi_{\alpha,K^*}, z_\alpha \varphi^D_{\sigma^*}, z_\alpha \psi_{K^*}, z_\alpha \psi^D_{\sigma^*}\big) \leq \frac{2\nu}{\delta \tau_{\sigma^*}} M_D.$$

Hence, φ_{α,K^*} is bounded. This property propagates from cell to cell due to the connectedness of the mesh. Since we have a finite number of control volumes, the claim follows. □

Lastly, Lemma 4.13 gives a bound on the vacancy quasi Fermi potential. Regarding the numerical schemes for the charge transport in PSCs, we identify $\alpha = \mathrm{a}$ as halide vacancies and set $\mathcal{T}_\mathrm{a} := \mathcal{T}_\mathrm{intr}$. In contrast, for the TMDC-based memristive devices, we can think of chalcogen vacancies, where we have $\mathcal{T}_\mathrm{a} := \mathcal{T}$. The difference in the dissipation $\mathbb{D}_{\mathcal{T},\mathrm{a}}$ for both models is only the set of faces in the sum, where we have $\sigma \in \mathcal{E}^\mathrm{intr}_\mathrm{intr}$ for the perovskite model and $\sigma \in \mathcal{E}$ for the memristor model (see (4.31) and (4.33)).

Lemma 4.13. (Bound for vacancy quasi Fermi potential) Assume that there exists $M_D > 0$ such that $\mathbb{D}_{\mathcal{T},\mathrm{a}}(\mathbf{X}) \leq M_D$ and that there also exists $\bar{n} \in (0,1)$ such that

$$\frac{1}{|\mathbf{\Omega}|} \sum_{K \in \mathcal{T}_\mathrm{a}} m_K n_{\mathrm{a},K} = \bar{n}. \tag{4.39}$$

Then, there exists some $M_B > 0$ depending on M_D, $\bar{n}$ and $\mathcal{T}$ such that

$$-M_B \leq \varphi_{\mathrm{a},K} \leq M_B, \quad \forall K \in \mathcal{T}_\mathrm{a}. \tag{4.40}$$

Proof. We note that the statistics function $\mathcal{F}_\mathrm{a}$ is monotonically increasing due to hypothesis (H2). Thus, the result stated in Lemma 4.13 is equivalent to the fact that there exists $\varepsilon \in (0,1)$ satisfying

$$\varepsilon \leq n_{\mathrm{a},K} \leq 1 - \varepsilon, \quad \forall K \in \mathcal{T}_\mathrm{a}. \tag{4.41}$$

Under the conditions specified in Lemma 4.13, the inequality (4.41) was previously demonstrated in [30, Lemma 3.7]. The proof method employed there is similar to the approach used to establish Lemma 4.12. It involves a reformulation of the dissipation functions, the introduction of a coercive face dissipation functional ([30, Lemma 3.2]), and identifying a control volume that ensures the boundedness of at least one $n_{\mathrm{a},K}$ (which is guaranteed by the mass conservation (4.39)). □

4.2.4. Main existence result

Finally, we can prove the existence of discrete solutions. In order to establish the existence results, we rely on a corollary of Brouwer's fixed point theorem [67, Section 9.1] which reads as follows and is stated here without a proof.

Lemma 4.14. (From [67, Section 9.1]) Let $N \in \mathbb{N}$ and $\mathbf{P} : \mathbb{R}^N \to \mathbb{R}^N$ be a continuous vector field. Assume that there exists $M_B > 0$ such that $\mathbf{P}(\mathbf{X}) \cdot \mathbf{X} \geq 0$, if $\|\mathbf{X}\| = M_B$. Then, there exists $\mathbf{X}^* \in \mathbb{R}^N$ such that $\mathbf{P}(\mathbf{X}^*) = \mathbf{0}$ and $\|\mathbf{X}^*\| \leq M_B$. □

Lemma 4.14 will ensure the existence of quasi Fermi potentials associated to the discrete continuity equations. For example, for the perovskite solar cell discretization scheme the discrete continuity equations (DPa), (DPb), and (DPc) and for the memristive application the corresponding equations (DMa), (DMb), and (DMc) at the time step m constitute a nonlinear system of equations. More precisely, we can introduce a continuous vector field $\mathbf{P}_m : \mathbb{R}^{\theta_\mathbf{X}} \to \mathbb{R}^{\theta_\mathbf{X}}$ with $\theta_\mathbf{X} = 2\mathrm{Card}(\mathcal{T}) + \mathrm{Card}(\mathcal{T}_{\mathrm{intr}})$ (*resp.* $\theta_\mathbf{X} = 3\mathrm{Card}(\mathcal{T})$) such that $\mathbf{P}_m(\mathbf{X}^m) = \mathbf{0}$ is equivalent to the continuity equations (DPa), (DPb), and (DPc) (*resp.* (DMa), (DMb), and (DMc)), where $\mathbf{X}^m$ is defined by (4.29), noting that we have omitted the superscript m there. The vector $\mathbf{X}^m$ contains the unknown quasi Fermi potentials.

Within the existence proofs, we will use an estimate that relates the scalar product $\mathbf{P}_m(\mathbf{X}^m) \cdot \mathbf{X}^m$ to the discrete entropy-dissipation inequalities (see Appendix A.7). To establish this estimate, the components of $\mathbf{P}_m(\mathbf{X}^m)$ are build as follows. For the electron and hole components, we put every term of the equations (DPa) and (DPb) (*resp.* (DMa) and (DMb)) on the left-hand side and rescale by a factor $\delta\tau^m/\nu$ (*resp.* $\delta_\mathrm{n}\tau^m/\nu$ and $\delta_\mathrm{n}\delta_\mathrm{p}\tau^m/\nu$). The vacancy-related components are given by (DPc) (*resp.* (DMc)), rescaled by τ^m. Furthermore, we will apply Lemma 4.14 to a regularized version of $\mathbf{P}_m$ and then consider the limit with respect to the regularization parameter.

In case of perovskite solar cells, the existence result reads as follows.

Theorem 4.15. (Existence of discrete solution to the PSC discretization scheme) For all time steps $m \geq 1$, the implicit-in-time finite volume scheme (DP), (DF) for the PSC charge transport model (P), (PIC), (PBC) has at least one solution $(\boldsymbol{\varphi}_\mathrm{n}^m, \boldsymbol{\varphi}_\mathrm{p}^m, \boldsymbol{\varphi}_\mathrm{a}^m, \boldsymbol{\psi}^m) \in \mathbb{R}^\theta$ with $\theta = 3\mathrm{Card}(\mathcal{T}) + \mathrm{Card}(\mathcal{T}_{\mathrm{intr}})$. Moreover, this solution satisfies the following L^∞ bounds. There exists $M_B > 0$ depending on the data and on the mesh such that

$$-M_B \leq \boldsymbol{\varphi}_\mathrm{n}^m, \boldsymbol{\varphi}_\mathrm{p}^m, \boldsymbol{\varphi}_\mathrm{a}^m, \boldsymbol{\psi}^m \leq M_B, \quad \text{for all } m \geq 1,$$

holds componentwise.

Proof. First, we prove the existence of quasi Fermi potentials $\mathbf{X}$, where for the sake of readability, we omit the superscript m. We recall that Lemma 4.8 guarantees the existence of a continuous and uniquely determined map $\mathbf{X} \mapsto \boldsymbol{\psi}(\mathbf{X})$ solving the nonlinear Poisson equation (DPd) for any given vector of quasi Fermi potentials $\mathbf{X}$. Thus, $\mathbf{P}_m$ is well-defined and continuous. We have established the following inequality within the proof of Theorem 4.5 for $\varepsilon > 0$ (see Lemma A.9)

$$\mathbf{P}_m(\mathbf{X}) \cdot \mathbf{X} \geq (1 - \varepsilon\tau^m)\mathbb{E}_{\mathcal{T}}(\mathbf{X}) - \mathbb{E}_{\mathcal{T}}(\mathbf{X}^{m-1}) + \tau^m \mathbb{D}_{\mathcal{T}}(\mathbf{X}) - \tau^m c_{\varepsilon,\boldsymbol{\Omega},\xi}, \tag{4.42}$$

where $c_{\varepsilon,\boldsymbol{\Omega},\xi} > 0$ and $\mathbf{X}^{m-1}$ denotes the known solution at the previous time step $m-1$. The scalar product $\mathbf{P}_m(\mathbf{X}) \cdot \mathbf{X}$ is given in (A.12) up to a rescaling with τ^m. For a suitable, but fixed ε, the constant $c_{\varepsilon,\boldsymbol{\Omega},\xi}$ is bounded. Consequently, there exists a constant $\tilde{M} > 0$ such that $\varepsilon\tau^m < 1/2$ and $\mathbb{E}_{\mathcal{T}}(\mathbf{X}^{m-1}) + \tau^m c_{\varepsilon,\boldsymbol{\Omega},\xi} < \tilde{M}$. Therefore, we can further estimate (4.42) as follows,

$$\mathbf{P}_m(\mathbf{X}) \cdot \mathbf{X} \geq \frac{1}{2}\mathbb{E}_{\mathcal{T}}(\mathbf{X}) + \tau^m \mathbb{D}_{\mathcal{T}}(\mathbf{X}) - \tilde{M}. \tag{4.43}$$

Our goal is to utilize Lemma 4.14 to demonstrate the existence of a solution at time step m. Rather than directly applying this lemma to $\mathbf{P}_m$, and specifically showing now the non-negativity of the scalar product $\mathbf{P}_m(\mathbf{X}) \cdot \mathbf{X}$, we introduce a parameter-dependent regularization of $\mathbf{P}_m$. This regularization satisfies the assumptions of Lemma 4.14: For a given $\mu > 0$, we define $\mathbf{P}_m^\mu(\mathbf{X}) = \mathbf{P}_m(\mathbf{X}) + \mu\mathbf{X}$. It holds

$$\mathbf{P}_m^\mu(\mathbf{X}) \cdot \mathbf{X} = \mathbf{P}_m(\mathbf{X}) \cdot \mathbf{X} + \mu\|\mathbf{X}\|^2 \geq \mu\|\mathbf{X}\|^2 - \tilde{M} \geq 0, \quad \text{for } \|\mathbf{X}\| \geq \sqrt{\tilde{M}/\mu}, \tag{4.44}$$

where we used the estimate (4.43) and the non-negativity of $\mathbb{E}_{\mathcal{T}}(\mathbf{X})$ and $\mathbb{D}_{\mathcal{T}}(\mathbf{X})$. Then, Lemma 4.14 shows the existence of $\mathbf{X}^{m,\mu} \in B(\mathbf{0}, \sqrt{\tilde{M}/\mu})$ such that

$$\mathbf{P}_m^\mu(\mathbf{X}^{m,\mu}) = \mathbf{0}, \quad \text{for } \|\mathbf{X}^{m,\mu}\| \leq \sqrt{\tilde{M}/\mu}. \tag{4.45}$$

Next, we need to show that $\mathbf{X}^{m,\mu}$ is actually uniformly bounded in μ. To achieve this, we will verify the hypotheses of Lemma 4.12 and Lemma 4.13. We begin by demonstrating the validity of the assumption (4.39) of Lemma 4.13. To do this, we take the scalar product of $\mathbf{P}_m^\mu(\mathbf{X}^{m,\mu})$ with the vector $\mathbf{V} = (\mathbf{0}_{\mathcal{T}}, \mathbf{0}_{\mathcal{T}}, \mathbf{1}_{\mathcal{T}_{\text{intr}}})$. Since the sum over all fluxes in the intrinsic region vanishes due to the local conservativity of the flux discretization scheme, we obtain

$$\sum_{K \in \mathcal{T}_{\text{intr}}} z_{\text{a}} m_K n_{\text{a},K}^{m,\mu} - \sum_{K \in \mathcal{T}_{\text{intr}}} z_{\text{a}} m_K n_{\text{a},K}^{m-1} + \mu \mathbf{X}^{m,\mu} \cdot \mathbf{V} = 0,$$

and, therefore, after rescaling with the measure of $\mathbf{\Omega}$, we have

$$\begin{aligned}\left|\frac{1}{|\mathbf{\Omega}|}\sum_{K\in\mathcal{T}_{\mathrm{intr}}} z_{\mathrm{a}} m_K n_{\mathrm{a},K}^{m,\mu} - \frac{1}{|\mathbf{\Omega}|}\sum_{K\in\mathcal{T}_{\mathrm{intr}}} z_{\mathrm{a}} m_K n_{\mathrm{a},K}^{m-1}\right| &\leq \frac{\mu}{|\mathbf{\Omega}|}\|\mathbf{X}^{m,\mu}\|\|\mathbf{V}\| \\ &\leq \frac{\sqrt{\tilde{M}\mu}}{|\mathbf{\Omega}|}\|\mathbf{V}\|,\end{aligned} \tag{4.46}$$

where we used $\|\mathbf{X}^{m,\mu}\| \leq \sqrt{\tilde{M}/\mu}$. But since the solution at the previous time step exists and hence is bounded, there exists $\varepsilon^{(m-1)} \in (0,1)$ such that $\frac{1}{|\mathbf{\Omega}|}\sum_{K\in\mathcal{T}_{\mathrm{intr}}} m_K n_{\mathrm{a},K}^{m-1} \in (\varepsilon^{(m-1)}, 1-\varepsilon^{(m-1)})$. Consequently, we deduce from (4.46) that for a sufficiently small μ, the vector $\mathbf{X}^{m,\mu}$ satisfies for $\varepsilon^{(m)} = \varepsilon^{(m-1)}/2$

$$\frac{1}{|\mathbf{\Omega}|}\sum_{K\in\mathcal{T}_{\mathrm{intr}}} m_K n_{\mathrm{a},K}^{m,\mu} \in (\varepsilon^{(m)}, 1-\varepsilon^{(m)}),$$

where $(\varepsilon^{(m-1)}, 1-\varepsilon^{(m-1)}) \subset (\varepsilon^{(m)}, 1-\varepsilon^{(m)})$. Thus, the condition (4.39) of Lemma 4.13 is satisfied. Moreover, due to (4.43), (4.44), (4.45), and $\mu\|\mathbf{X}^{m,\mu}\|^2 \geq 0$,

$$0 = \mathbf{P}_m^{\mu}(\mathbf{X}^{m,\mu})\cdot\mathbf{X}^{m,\mu} \geq \frac{1}{2}\mathbb{E}_{\mathcal{T}}(\mathbf{X}^{m,\mu}) + \tau^m\mathbb{D}_{\mathcal{T}}(\mathbf{X}^{m,\mu}) - \tilde{M},$$

we see that $\mathbb{E}_{\mathcal{T}}(\mathbf{X}^{m,\mu})$ and $\mathbb{D}_{\mathcal{T}}(\mathbf{X}^{m,\mu})$ are uniformly bounded in μ. Hence, we can apply Lemma 4.12 and Lemma 4.13 to deduce that $\|\mathbf{X}^{m,\mu}\|$ is bounded uniformly in μ, for sufficiently small μ. Finally, we can extract a subsequence, which converges to a limit denoted by $\mathbf{X}^m$ as μ tends to 0. Due to (4.45), this limit satisfies $\mathbf{P}_m^0(\mathbf{X}^m) = \mathbf{0}$. On the other hand, due to the definition of the regularization $\mathbf{P}_m^{\mu}$, we have $\mathbf{P}_m(\mathbf{X}^m) = \mathbf{P}_m^0(\mathbf{X}^m) = \mathbf{0}$. Thus, we have found quasi Fermi potentials which solve the discrete system (DPa), (DPb), and (DPc). It remains to show the existence of a uniquely determined and bounded $\boldsymbol{\psi}(\mathbf{X}^m)$ which solves the Poisson equation (DPd). However, this follows from Lemma 4.8 and Lemma 4.11 which ends the proof of Theorem 4.15. □

Analogously, we can formulate an existence result for the memristor application.

Theorem 4.16. (Existence of discrete solution to the TMDC-based memstrive device discretization scheme) For all time steps $m \geq 1$, the implicit-in-time finite volume scheme (DM), (DF) for the TMDC-based memristor charge transport model (M), (MIC), (MBC) has at least one solution $(\boldsymbol{\varphi}_{\mathrm{n}}^m, \boldsymbol{\varphi}_{\mathrm{p}}^m, \boldsymbol{\varphi}_{\mathrm{a}}^m, \boldsymbol{\psi}^m) \in \mathbb{R}^{\theta}$ with $\theta = 4\mathrm{Card}(\mathcal{T})$. Moreover, this solution satisfies the following L^{∞} bounds. There exists $M_B > 0$ depending on the data and on the mesh such that

$$-M_B \leq \boldsymbol{\varphi}_{\mathrm{n}}^m, \boldsymbol{\varphi}_{\mathrm{p}}^m, \boldsymbol{\varphi}_{\mathrm{a}}^m, \boldsymbol{\psi}^m \leq M_B, \quad \text{for all } m \geq 1,$$

holds componentwise. □

The proof of Theorem 4.16 follows a similar structure to the proof of Theorem 4.15 and is therefore omitted here. We end this chapter with a remark on the convergence of both introduced discretization schemes.

Remark 4.17. (Convergence of both schemes) In addition to the existence of a solution to the numerical schemes, it is expected that the entropy-dissipation inequalities, serving as *a priori* estimates, will provide the necessary bounds to prove convergence towards weak solutions of the PDE systems [36]. For instance, Corollary 4.7 demonstrates that both the discrete entropy and the discrete dissipation remain bounded for a fixed time. If we closely examine the definitions of the entropy $\mathbb{E}_{\mathcal{T}}^m$ in (4.13) and (4.24) and the dissipation $\mathbb{D}_{\mathcal{T}}^m$ in (4.14) and (4.25), we may identify with Corollary 4.7 uniform estimates for the electric potential, the densities, and the gradients of quasi Fermi potentials in a suitable Bochner space $L^p(0, t_F; X)$, $1 \leq p \leq \infty$, where X is some Banach space, and t_F is the end time. We can potentially find a convergent sequence of approximate solutions by establishing these estimates and employing compactness and/or convergence arguments. In simpler models, the convergence of the schemes concerning the excess chemical flux approximation has already been demonstrated (e.g., [30], for the Fermi-Dirac integral of order -1 as the statistics function). However, in our context, we expect more technical challenges due to multiple domains (in the case of the PSC model) and various species. Furthermore, developing new nonlinear estimates to handle general statistics functions will be crucial.

5. Simulation results

In Chapter 2, we derived suitable drift-diffusion equations for vacancy-assisted charge transport in crystalline semiconductors. Chapter 3 extended these equations to describe the transport in perovskite solar cells and TMDC-based memristive devices. Then, we translated the continuous model into discrete counterparts and proved the existence of discrete solutions in Chapter 4. Finally, in this chapter, we complement our theoretical results with numerical experiments.

We can realize the simulations with the help of commercial software packages (see, e.g., [77, 81, 117]). Major drawbacks of commercial software are the limitation in flexibility and transparency. Thus, there is also a rise in (partially) open-access software tools to simulate vacancy-assisted charge transport in perovskite solar cells in one dimension [28, 44, 138]. To our knowledge, no open-access software exists for simulating vacancy-assisted charge transport in TMDC-based memristive devices. As another alternative, we rely in this thesis on the open source software `ChargeTransport.jl` [DA7] for simulating charge transport in semiconductors via the Voronoi finite volume method as implemented in `VoronoiFVM.jl` [DA8]. The packages are written in the programming language Julia, which received remarkable attention in recent years due to its exceptional performance capabilities, combining high-level syntax with execution speeds comparable to low-level languages [20].

This chapter starts by verifying properties of the finite volume schemes, such as a special case of the entropy-dissipation inequalities and the spatial convergence rate (Section 5.1). Furthermore, we pay particular attention to the large time behavior and the decay of a relative free entropy with respect to the steady state solution for physically meaningful setups of PSCs and TMDC-based memristive devices. We continue in Section 5.2 with a study of volume exclusion effects and its influence on a PSC setup with MAPI as perovskite material by comparing the electric potential, the vacancy carrier density and the current-voltage curves of a charge transport model based on two different ionic current densities. Lastly, we validate in Section 5.3 the vacancy-assisted model with experimental hysteresis and pulse measurement data found in literature for lateral 2D MoS_2-based memristive devices, strongly corroborating the relevance of vacancy dynamics in TMDC devices. While Section 5.1 considers exclusively the drift-diffusion models with time-independent Dirichlet conditions, we

use time-dependent boundary conditions in Section 5.2 and Section 5.3. In these sections, we supply the PSC model with ohmic contact boundary conditions (see Section 3.1.3.1). For the TMDC-based memristors, we simulate the Schottky boundary conditions (see Section 3.2.2.1) as well as the image-charge-induced Schottky barrier lowering conditions (see Section 3.2.2.2). For all simulations, we use the backward Euler method for the time discretization, as explained in Section 4.1.2. Moreover, the linear system of equations resulting from applying the Newton method is solved via a sparse LU factorization [DA8]. In the following, when referring to the L^p norms, $1 \leq p \leq \infty$, we specifically refer to the discrete approximations [149] of these norms at a fixed time t^m. All Julia files to generate and visualize the simulation data are available in [DA1], which can be used to verify the presented results.

The main parts of this chapter are based on [DA2, DA3, DA5]. To be more precise, Section 5.1.1 is published in [DA2], the findings of Section 5.2 are based on [DA3] and, lastly, Section 5.3 can be found in [DA5].

5.1. Large time behavior, convergence order and entropy decay

In this section we are interested in the large time behavior of both non-dimensionalized charge transport models (P), (PIC), (PBC) and (M), (MIC), (MBC), introduced at the end of Section 3.1.4 and Section 3.2.3, respectively. We refer to the solutions for $t \to +\infty$ as *steady state* solutions, denoted by $(\varphi_{\mathrm{n}}^{\infty}, \varphi_{\mathrm{p}}^{\infty}, \varphi_{\mathrm{a}}^{\infty}, \psi^{\infty})$, and introduce an entropy with respect to the steady state solutions

$$\mathbb{E}_{\infty}(t) = \frac{\lambda^2}{2} \int_{\mathbf{\Omega}} |\nabla(\psi - \psi^{\infty})|^2 \, d\mathbf{x} + \sum_{\alpha \in \{\mathrm{n,p,a}\}} \delta_{\mathbb{E},\alpha} \int_{\mathbf{\Omega}_\alpha} H_\alpha(n_\alpha, n_\alpha^{\infty}) \, d\mathbf{x}, \tag{5.1}$$

where $H_\alpha(x,y) = \Phi_\alpha(x) - \Phi_\alpha(y) - \Phi_\alpha'(y)(x-y)$ (see (3.41)). The steady state densities can be calculated via the non-dimensionalized state equations $n_\alpha^{\infty} = \mathcal{F}_\alpha\left(z_\alpha(\varphi_\alpha^{\infty} - \psi^{\infty})\right)$ (see (Pf) and (Mf)) from the steady state solutions. In both charge transport models, electrons and holes migrate throughout the device, i.e., $\mathbf{\Omega}_{\mathrm{n}} = \mathbf{\Omega}_{\mathrm{p}} = \mathbf{\Omega}$. For PSC devices, the vacancy domain is $\mathbf{\Omega}_{\mathrm{a}} = \mathbf{\Omega}_{\mathrm{intr}}$, whereas for TMDC-based memristive devices, we define $\mathbf{\Omega}_{\mathrm{a}} = \mathbf{\Omega}$. The quantity $\delta_{\mathbb{E},\alpha} \geq 0$ denotes the dimensionless concentration parameter. Comparing the previously defined continuous entropy functionals (3.42), (3.48) with (5.1), we set for the perovskite application $\delta_{\mathbb{E},\mathrm{n}} = \delta_{\mathbb{E},\mathrm{p}} = \delta$ and $\delta_{\mathbb{E},\mathrm{a}} = 1$. In the case of memristive devices, we define $\delta_{\mathbb{E},\mathrm{n}} = \delta_{\mathrm{n}}$, $\delta_{\mathbb{E},\mathrm{p}} = \delta_{\mathrm{n}}\delta_{\mathrm{p}}$ and $\delta_{\mathbb{E},\mathrm{a}} = 1$.

The non-negative, dimensionless functional $\mathbb{E}_\infty$ in (5.1) can be seen as a measure

of the distance between a solution at time t and the model's steady state, which vanishes if and only if the solution at time t and the steady state coincide almost everywhere. Furthermore, from an analytical point of view, $\mathbb{E}_\infty$ may help to prove the convergence of the discrete solution to the discrete steady state [34]. Tracing back the non-dimensionalizations and assumptions in Section 3.1.4 and Section 3.2.3, we can formulate a dimensionalized version of (5.1)

$$\mathbb{E}_\infty(t) = \frac{1}{2}\int_{\mathbf{\Omega}} \varepsilon_s |\nabla(\psi - \psi^\infty)|^2 \, d\mathbf{x} + \sum_{\alpha\in\{\mathrm{n,p,a}\}} \int_{\mathbf{\Omega}_\alpha} H_\alpha(n_\alpha, n_\alpha^\infty)\, d\mathbf{x}, \tag{5.2}$$

where we now use the dimensionalized state equation (2.3) to calculate the steady state densities n_α^∞. In the case of $\mathcal{F}_\mathrm{n} = \mathcal{F}_\mathrm{p} = \exp$ and $\mathcal{F}_\mathrm{a} = F_{-1}$, the following functions enter H_α

$$\Phi_\alpha(x) = k_B T x \left(\log\left(\frac{x}{N_\alpha}\right) - 1\right) - z_\alpha E_\alpha x, \qquad \text{for } \alpha \in \{\mathrm{n,p}\}, \tag{5.3a}$$

$$\Phi_\mathrm{a}(x) = k_B T \left(x \log\left(\frac{x}{N_\mathrm{a}}\right) + (N_\mathrm{a} - x)\log\left(1 - \frac{x}{N_\mathrm{a}}\right)\right) - z_\mathrm{a} E_\mathrm{a} x. \tag{5.3b}$$

We note that the functions in (5.3) are exactly the contributions entering the thermodynamic free energy (2.49). This means, we extend the contributions of the relative entropy with respect to the steady state such that they are consistent with the physical free energy in Section 2.6.2.

5.1.1. Perovskite solar cells

We consider the perovskite charge transport model, formulated in (P), (PIC), (PBC) with its discrete counterpart (DP), (DF) (see Section 4.1.2 and Section 4.1.3). In the following, we start with a toy problem resulting from the perovskite application with non-physical choices of the dimensional parameters and end with a realistic study of the large time behavior of the perovskite model at a constant applied voltage. This scenario corresponds in a physical sense to investigating the influence of *preconditioning* [51] a PSC before current-voltage measurements.

5.1.1.1. Initial test problem

Within this section, we assume a one-dimensional and dimensionless domain $\Omega = (0, 6)$ and set $\Omega_\mathrm{HTL} = (0, 2), \Omega_\mathrm{intr} = (2, 4)$, $\Omega_\mathrm{ETL} = (4, 6)$. We chose 511 interior nodes per subdomain, and additional points at the outer $x = 0, 6$ and inner boundaries $x = 2, 4$, resulting in a total of 1537 nodes with a grid spacing $h \approx 3.9 \times 10^{-3}$. The time domain is given by $[0, 80]$, which we discretize with a uniform time step of $\Delta t = 1.0 \times 10^{-1}$.

We set the rescaled Debye length to $\lambda = 1$, the mobility parameter to $\nu = 1$, the concentration parameter to $\delta = 1$, and the photogeneration parameter to $\gamma = 0$.

Equal boundary values. In the first setup, we study the implications of Remark 3.6, i.e., we assume constant boundary functions $\varphi^D, \psi^D \in W^{1,\infty}(\Omega)$ and the absence of external generation of electrons and holes. To this end, we have a constant doping $C = 0.1$ and no photogeneration and recombination, i.e., $G = R = 0$. The Dirichlet functions (PBCb) are chosen as constant functions $\varphi^D = 0.5$ and $\psi^D = \operatorname{arcsinh}(C/2) + 0.5$ in the whole domain Ω. The sinusoidal initial conditions (IC) for the electron and hole quasi Fermi potentials, as well as for the electric potential, and the constant initial condition for the vacancy quasi Fermi potential, along with the steady state solutions, are depicted in Figure 5.1 (left). In Figure 5.1 (right), we show the respective steady state densities.

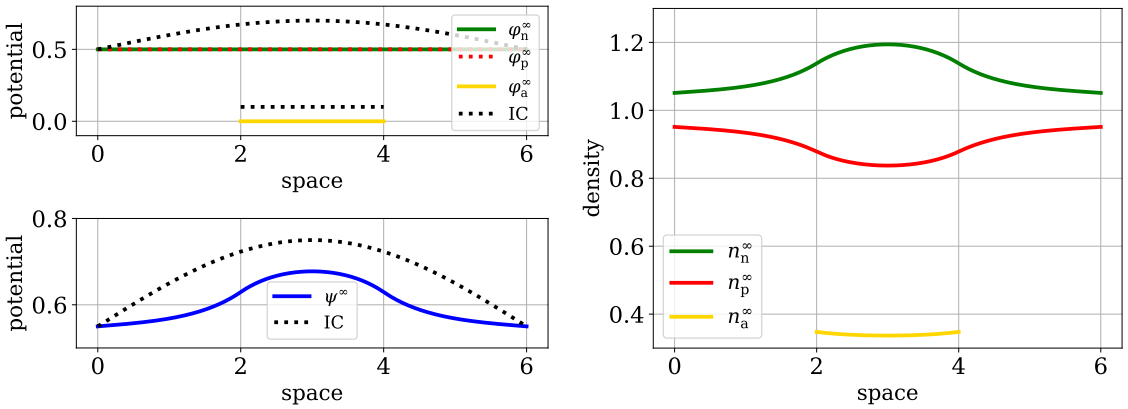

Figure 5.1.: Steady state solutions $(\varphi_n^\infty, \varphi_p^\infty, \varphi_a^\infty, \psi^\infty)$ with the respective initial conditions (IC) as dotted lines (left) and the associated steady state densities (right) for a three-layer test problem with equal boundary values. (From [DA2] with modifications.)

Since for these specific choices, we have $\mathbf{0} = \nabla\varphi^D = \nabla\psi^D$ and $G = 0$, Remark 3.6 indicates that the relative entropy with respect to the Dirichlet boundary values (3.42) does not increase in time, i.e., $\frac{d}{dt}\mathbb{E} \leq 0$. This result can be numerically verified, as shown in Figure 5.2 (left in blue). Due to a non-constant steady state electric potential ψ^∞ (Figure 5.1, left in blue) and the choice $\psi^D = \operatorname{arcsinh}(C/2) + 0.5$, we have $|\nabla(\psi - \psi^D)| \neq 0$ for all time steps. Thus, the relative entropy with respect to the boundary values (3.42) (Figure 5.2, left in blue) levels off after an initial decrease. Furthermore, the relative entropy with respect to the steady state (5.1) (Figure 5.2, left in green) as well as the quadratic L^2 errors between the steady state and a solution at time t (Figure 5.2, right) decay exponentially with a similar slope, reaching machine precision at a similar time. Hence, the expected exponential convergence towards

steady state, as stated in Remark 3.6, is confirmed through numerical simulations for the two measures (relative entropy with respect to steady state and quadratic L^2 errors) for the deviation of a solution at time t from the steady state.

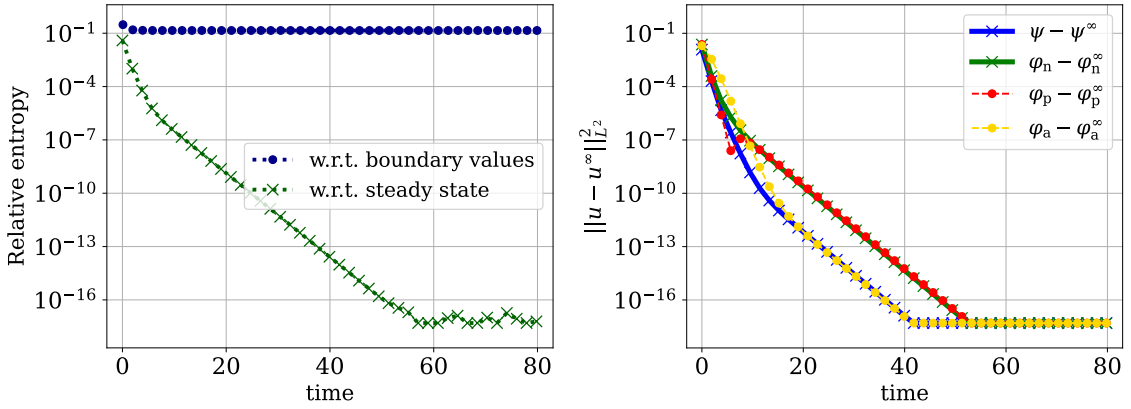

Figure 5.2.: Left: Time evolution of the relative entropy with respect to the Dirichlet boundary functions (3.42) as well as the relative entropy with respect to the steady state (5.1). Right: Time evolution of the quadratic L^2 errors between the computed and the steady state solutions. All quantities are calculated for a three-layer test problem with equal boundary values. (From [DA2] with modifications.)

Non-equal boundary values. In most applications, the constraint of having equal boundary values is too limiting. Therefore, we examine in the following the large time behavior of solutions and the relative entropy when non-equal boundary values are considered.

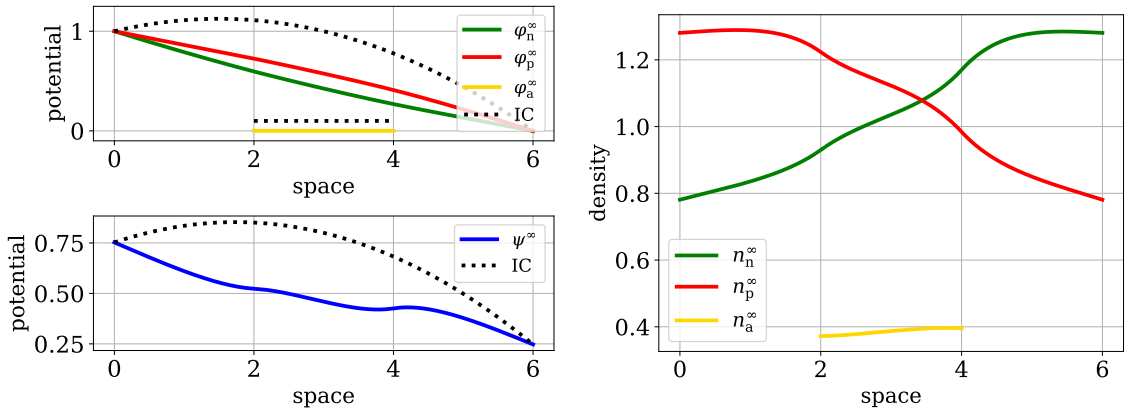

Figure 5.3.: Steady state potentials with the respective initial conditions as dotted lines (left) and the associated steady state densities (right) for a three-layer test problem with non-equal boundary values. (From [DA2] with modifications.)

We assume that the doping C is a piecewise constant function given by 0.5 in Ω_{ETL}

and by -0.5 in $\Omega_{\mathrm{HTL}} \cup \Omega_{\mathrm{intr}}$. The boundary values are set to $\varphi^D|_{x=0} = 1, \varphi^D|_{x=6} = 0$, $\psi^D|_{x=0} = \operatorname{arcsinh}(-0.5/2) + 1, \psi^D|_{x=6} = \operatorname{arcsinh}(0.5/2)$. We choose quadratic initial conditions for the electron and hole quasi Fermi potentials, as well as the electric potential and a constant initial condition for the vacancy quasi Fermi potential.

The initial conditions are additionally to the steady state solutions depicted in Figure 5.3 (left) as black dotted lines. Furthermore, Figure 5.3 (right) shows the steady state densities. For this setup, the relative entropy with respect to the steady state and the quadratic L^2 errors are shown in Figure 5.4 (left and middle). Also, for non-equal boundary values, these curves decay exponentially as before and reach machine precision with a similar slope, even though this setup is not covered by Remark 3.6.

Finally, we complete this section with an investigation of the spatial convergence behavior. Suppose $n_* \in \mathbb{N}$ is given, then $2 \cdot 2^{n_*-1} - 1$ interior nodes are chosen in each of the three subdomains along with four additional boundary nodes at $x = 0, 2, 4, 6$. In total, we have $n_{\mathrm{tot}} = 3 \cdot (2 \cdot 2^{n_*-1} - 1) + 4$ nodes. We calculate a reference solution on a grid with $n_* = 9$ corresponding to 1537 nodes with a grid spacing $h_* \approx 3.9 \times 10^{-3}$. The L^2 errors between the solution u_{n_*}, for $n_* = 2, \dots, 8$, and the reference solution projected onto the coarser mesh evaluated at the final time are shown in Figure 5.4 (right). Since for the final time $t_F = 80$, the system is already within machine precision of the steady state, the error shown is purely due to the spatial discretization. We observe second-order convergence in the L^2 norm.

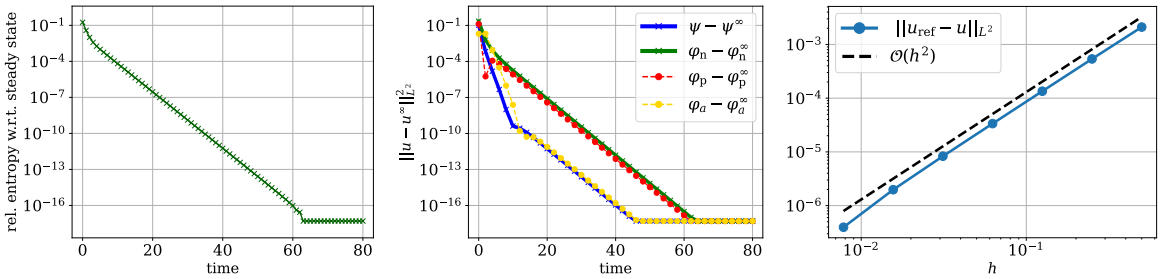

Figure 5.4.: Time evolution of the relative entropy (5.1) for non-equal boundary values (left) and of the quadratic L^2 errors between steady state and solutions at time t (middle). On the right, the L^2 error with respect to the grid spacing h is shown. All quantities are calculated for a three-layer test problem with non-equal boundary values. (From [DA2] with modifications.)

Next, we discuss the large time behavior and the entropy decay for a physically meaningful PSC setup.

5.1.1.2. PSC preconditioning scan protocol

In the following, we choose the rescaling factors and non-dimensionalized parameters introduced in Section 3.1.4 in such a way that the resulting solutions correspond to a realistic three-layer PSC device with MAPI as perovskite material, indicating that the vacancy carrier evolving in Ω_{intr} corresponds to iodide vacancies. In particular, we allow for regionwise-constant parameters in the whole domain Ω, non-zero band-edge energies and a present photogeneration. We use the parameter set provided in [44, 48], which is summarized in Table B.1. The one-dimensional domain $\Omega = (0, 700)$ nm is subdivided into $\Omega_{\text{ETL}} = (0, 100)$ nm, $\Omega_{\text{intr}} = (100, 500)$ nm, and $\Omega_{\text{HTL}} = (500, 700)$ nm. The mesh is given by 385 nodes with a uniform grid spacing in each layer, namely, $h_{\text{ETL}} \approx 0.78$ nm, $h_{\text{HTL}} \approx 1.6$ nm in the transport layers, and $h_{\text{intr}} \approx 3.1$ nm in the perovskite layer. The uniform time mesh is built with a step size of $\Delta t = 0.5$ s and the final time is given by $t_F = 220$ s.

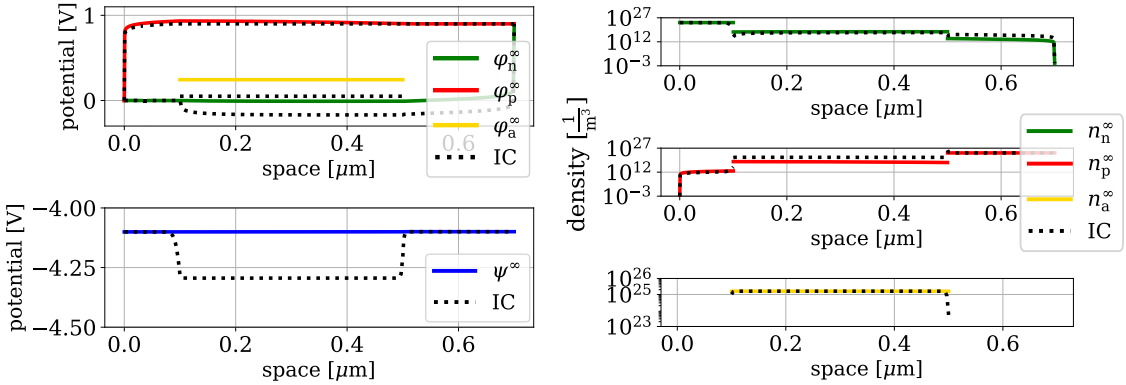

Figure 5.5.: Steady state potentials (left) and the associated steady state densities (right) with the respective initial conditions as black dotted lines for a PSC three-layer device with realistic parameters including photogeneration and non-equal boundary values. (From [DA2] with modifications.)

In experimental measurements, a PSC device typically undergoes a preconditioning protocol [51] where it is held at a constant voltage for several seconds, allowing ionic charges to equilibrate. Subsequently, scan protocols involving an applied voltage varying with time are applied to investigate the device's physics. Mathematically, during the preconditioning protocol, *time-independent* boundary conditions are applied. Then, when accurately modeling the scan protocol, the *time-dependent* voltage is incorporated via the Dirichlet boundary conditions (3.7a). Thus, the steady state potentials and their respective densities depicted in Figure 5.5 (left and right) can be considered as the solutions after a successful preconditioning scan and before a voltage-varying measurement protocol. In the presented configuration, the constant

applied voltage is chosen such that the steady state electric potential ψ^∞ remains constant. This behavior of a constant ψ^∞ can be well observed in Figure 5.5 (left, in blue). The chosen initial conditions (black dotted lines) correspond to a solution of the charge transport model with a non-constant vacancy concentration (see Figure 5.5, right). As before, we consider the large time behavior of the quadratic L^2 errors and the relative entropy with respect to the steady state. It is worth noting that we now consider the dimensional form of this functional, given in (5.2), supplied with (5.3). Specifically, this implies that non-zero band-edge energies enter the relative entropy with respect to the steady state.

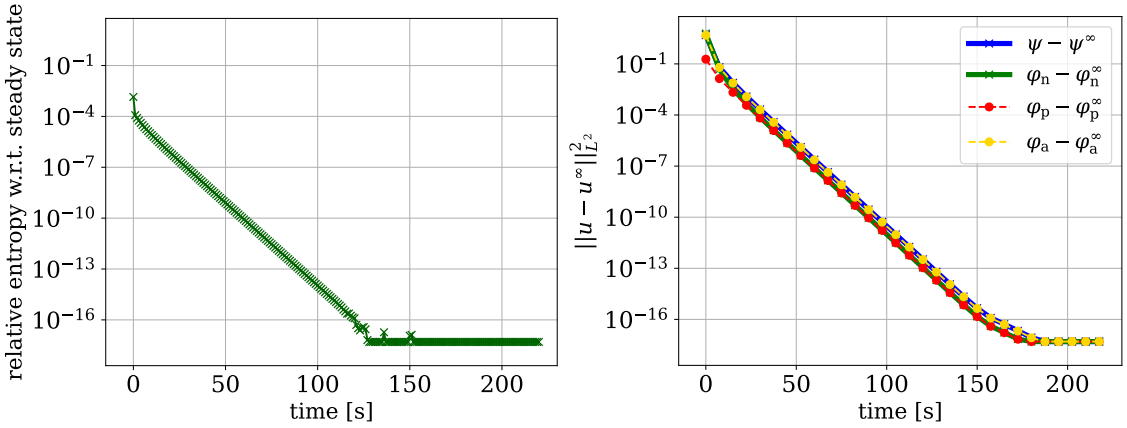

Figure 5.6.: Time evolution of the relative entropy with respect to the steady state (5.2) (left) and of the quadratic L^2 errors between the computed and the steady state solutions (right). All quantities are calculated for a PSC three-layer device with realistic parameters including photogeneration and non-equal boundary values. (From [DA2] with modifications.)

It is worth noting that the presented setup is not covered by Remark 3.6. Still, Figure 5.6 indicates an exponential decay towards zero of the dimensionalized relative entropy with respect to the steady state (5.2) and the quadratic L^2 errors. In contrast to the observations made in the previous section, where the relative entropy and the quadratic L^2 errors reach machine precision with a similar slope, the relative entropy vanishes faster in this example. This may be explained by a present photogeneration rate or by the additional terms in (5.3) due to non-zero band-edge energies, which influence the convergence behavior. Nevertheless, we see again, as in the previous setups, a similar and exponential convergence rate of the two introduced measures, the relative entropy (Figure 5.6, left) and the quadratic L^2 errors (Figure 5.6, right), for the deviation of a solution at time t from the steady state.

We conclude our study on the large time behavior of the relative entropy and the quadratic L^2 errors for vacancy-assisted charge transport with a physically reasonable

memristive device application.

5.1.2. Memristive devices

Usually, when analyzing memristive devices, periodic piecewise linear and time-dependent voltage cycles are applied to identify the origin of the hysteretic behavior of the current-voltage curve, which is crucial for understanding the underlying switching mechanisms of the device. For example, Section 5.3 deals with such a study and relates the I-V hysteresis to forming local vacancy depletion zones. Most of these studies consider time-dependent boundary conditions modeling ohmic, Schottky, or Schottky barrier lowering contacts (via a time-varying applied voltage) as described in Section 3.2.2. However, to gain further insight into the device behavior and reliability, we investigate the large time behavior of solutions at a given constant voltage U_* within a voltage cycle. In this context, the initial conditions correspond to the solutions at a time $t_* > 0$, which represents the time after the completion of one voltage cycle, and when the voltage U_* is once again reached, as illustrated in Figure 5.7. Starting from $t = t_*$, we study in the following the large time behavior of these solutions. It is important to note that the initial configuration at $t = t_*$ is a consequence of the previously applied voltage cycle and the specific initial conditions chosen at $t = 0$ s. Therefore, the initial condition at $t = t_*$ is not chosen arbitrarily.

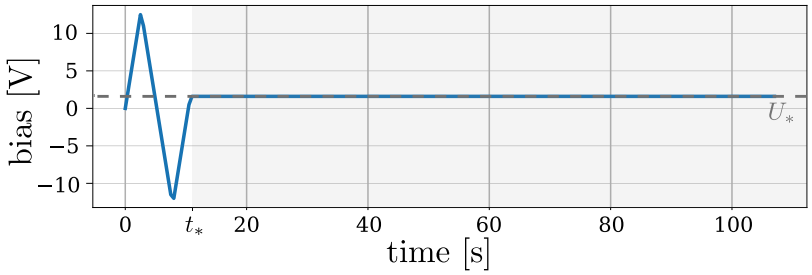

Figure 5.7.: Illustration of the applied voltage as a function of time applied at the right contact. After a given threshold voltage U_*, the applied voltage is chosen to be constant. The time regime of interest for a large time behavior study is highlighted in gray.

In this example, we choose again the rescaling factors and non-dimensionalized parameters introduced in Section 3.2.3 such that the resulting solutions correspond to a realistic TMDC-based memristive device with MoS_2 as TMDC material. Consequently, we assume the transport of sulfur vacancies additionally to the electron and hole transport. We use the parameter set S_1 (Table B.3, Table B.4), and as a representative voltage at the beginning of the second cycle, we choose $U_* = 1.6$ V and a start time $t_* = 10.72$ s, following Figure 5.7.

In contrast to the PSC setup, we have solely one domain $\Omega = [0.0, 1.0]$ µm, on which all potentials evolve. We consider a non-uniform grid spacing with 213 nodes, a minimum spacing of $h_{\min} \approx 3 \times 10^{-4}$ µm near the contact boundaries, and a maximum spacing of $h_{\max} \approx 2 \times 10^{-2}$ µm in the bulk. For the temporal discretization, we use non-uniform time steps between $\Delta t_{\min} = 1.0$ µs and $\Delta t_{\max} = 5.0 \times 10^{-1}$ s with an end time $t_F = 250$ s and a total number of 1005 nodes. The boundary values are set to $\varphi^D = 0$ V, $\psi^D = (E_n - \phi_0(x_1))/q = -4.001$ V at the left contact and to $\varphi^D = U_* = 1.6$ V, $\psi^D = (E_n - \phi_0(x_2))/q + U_* = -2.401$ V at the right contact.

We set the average vacancy concentration C_a as the ratio of the overall vacancy charge to the measure of the device domain, i.e.,

$$C_a = \frac{1}{|\Omega|} \int_{\Omega} n_a(\mathbf{x}, t)\, d\mathbf{x} = \frac{1}{|\Omega|} \int_{\Omega} n_a^0(\mathbf{x})\, d\mathbf{x}, \quad \text{for all } t \geq 0, \tag{5.4}$$

which is constant in space and time due to the conservation of mass, as mentioned in Remark 3.2. We observe that the initial condition $n_a^0 = N_a \mathcal{F}_a(\eta_a(\varphi_a^0, \psi(x, 0)))$ is directly connected to C_a. For MoS_2 as the TMDC material and the selected device geometry, DFT calculations [106, 195] predict average vacancy concentrations C_a up to $\approx 1 \times 10^{25}$ m^{-3}. The precise value of the average vacancy concentration C_a is not only a matter of numerical interest (due to the initial condition), but also serves as a critical physical parameter, strongly depending on the device's microstructure. In the following, we assume $C_a \approx 6.4 \times 10^{23}$ m^{-3}. This choice will be shown in Section 5.3.1 to align well with experimental measurements found in literature.

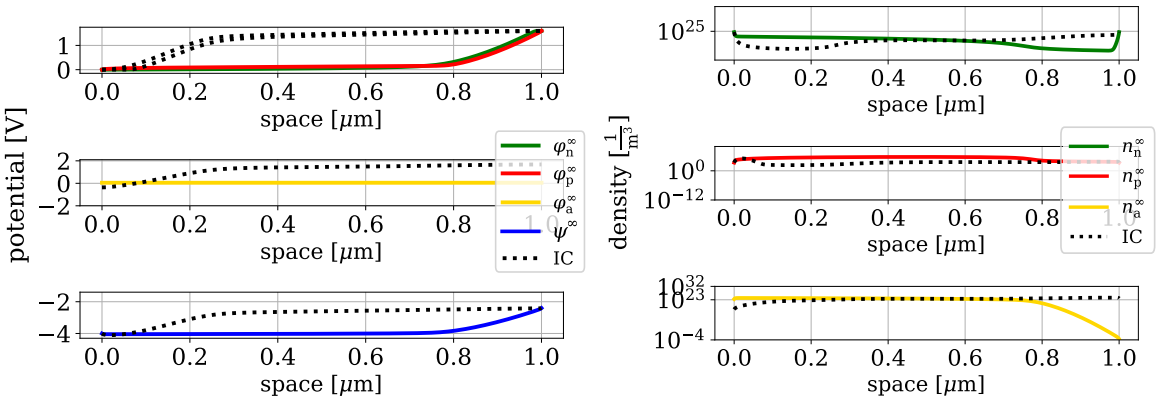

Figure 5.8.: Steady state potentials (left) and associated densities (right) with the respective initial conditions as black dotted lines for a realistic TMDC memristor. In this case, we have an average vacancy concentration of $C_a \approx 6.4 \times 10^{23}$ m^{-3}.

Figure 5.8 shows the steady state solutions (left) and the associated densities (right) along with the initial conditions as black dotted lines. In the vacancy quasi Fermi

potential initial condition (Figure 5.8, right, third row), we observe a decrease at the left electrode, leading to a local depletion region of vacancies in this regime. As time evolves, this depletion region moves towards the right contact, also portrayed in the steady state vacancy density in Figure 5.8 (right, third row). For further details on the physical interpretation, we refer to Section 5.3.1. Furthermore, in Figure 5.9, we observe an exponential decay of the relative entropy with respect to the steady state (5.2) (left) and the quadratic L^2 errors (right), both approaching zero. Similar to the physically relevant perovskite example in Section 5.1.1.2, both measures vanish at different times, although with a similar and exponential rate.

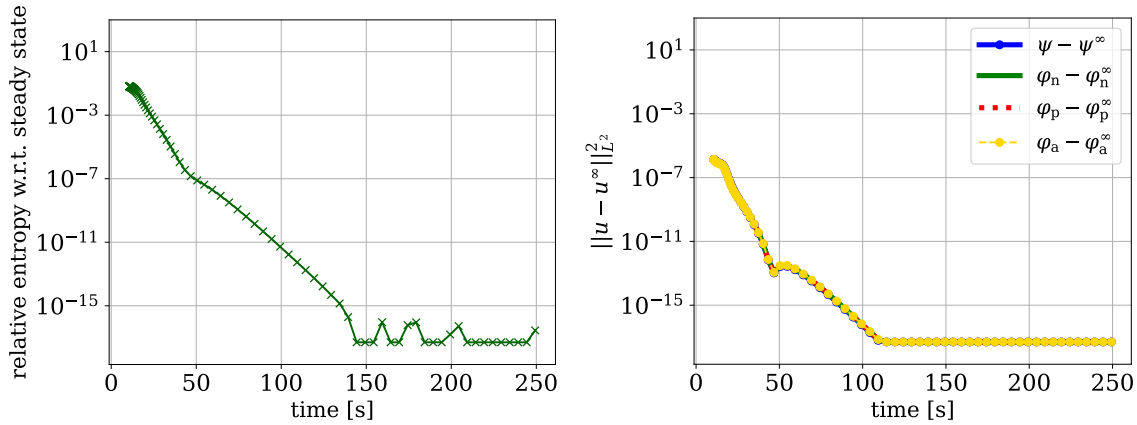

Figure 5.9.: Time evolution of the relative entropy with respect to the steady state (5.2) (left) and of the quadratic L^2 errors between the computed and the steady state solutions (right) for a realistic TMDC memristor. In this case, we have an average vacancy concentration of $C_a \approx 6.4 \times 10^{23}$ m^{-3}.

The number of vacancy sites significantly relies on the fabrication process of each memristive device. Therefore, we investigate how the large time behavior depends on the average vacancy concentration C_a which is directly connected to the choice of initial condition, as described in (5.4). We performed simulations for different values of C_a between $4.5 \times 10^{14} - 1.0 \times 10^{27}$ m^{-3} and visualized in Figure 5.10 the convergence times, i.e., the time at which the relative entropy and the quadratic L^2 errors reach machine precision. We use the backward Euler method for all average vacancy concentrations and adjust the time steps non-uniformly for varying C_a.

For all considered C_a a decay of the relative entropy and the quadratic L^2 errors is witnessed. In the range of 1.0×10^{24} m^{-3} $< C_a <$ 1.0×10^{25} m^{-3}, we see a peak in the convergence time for both, the relative entropy and the quadratic L^2 errors, differing by a factor of 2. Interestingly, this range corresponds to the physically meaningful regime for C_a. However, for small average vacancy concentrations ($C_a < 1.0 \times 10^{21}$ m^{-3}) and

large average vacancy concentrations ($C_\mathrm{a} > 1.0 \times 10^{26}$ m^{-3}), the relative entropy and the quadratic L^2 errors reach machine precision much faster. The observed peak in the convergence time can be better understood by examining the density profiles for a small ($C_\mathrm{a} \approx 1.0 \times 10^{17}$ m^{-3}) and a large ($C_\mathrm{a} \approx 1.0 \times 10^{27}$ m^{-3}) average vacancy concentration, corresponding to values, where the convergence times for the relative entropy and the quadratic L^2 errors are comparably small (see Figure 5.10).

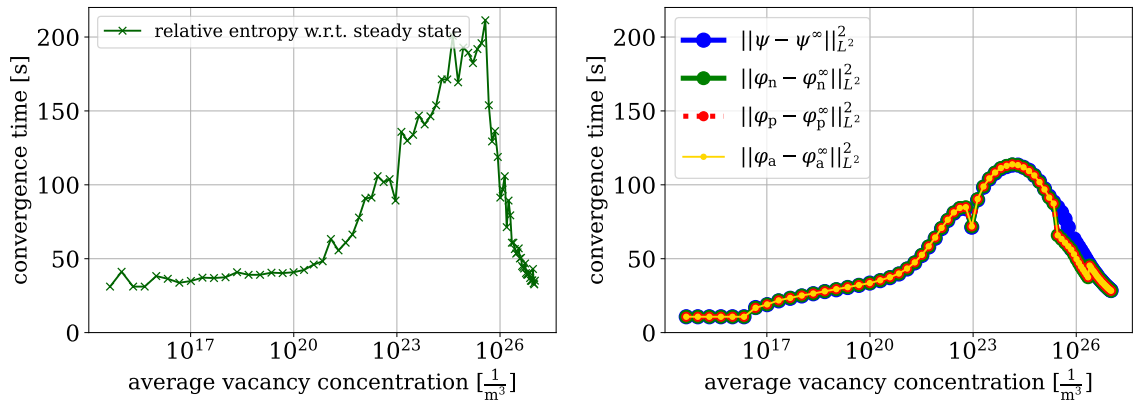

Figure 5.10.: Convergence times defined as the time at which machine precision is reached of the relative entropy with respect to the steady state (5.2) (left) and of the quadratic L^2 errors between the computed and the steady state solutions (right) in dependence of the average vacancy concentration C_a.

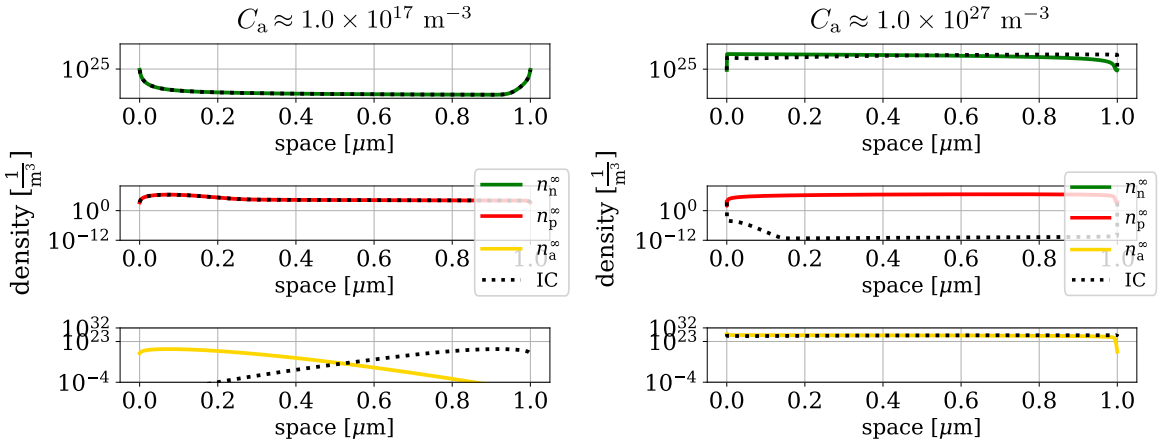

Figure 5.11.: Steady state densities with initial conditions for a realistic TMDC-based memristive device with an average vacancy concentration of $C_\mathrm{a} \approx 1.0 \times 10^{17}$ m^{-3} (left) and a concentration of $C_\mathrm{a} \approx 1.0 \times 10^{27}$ m^{-3} (right).

For smaller average vacancy concentrations (Figure 5.11, left), we clearly see that

the initial electron and hole densities remain close to the steady state configuration. Although there is a more pronounced trend of forming depletion zones at the left contact for the initial condition and at the right contact for the steady state of the vacancy density, in comparison to Figure 5.8 (right), the vacancy density appears to be so small that the steady state solution is quickly reached for all carriers.

Contrarily, we observe discrepancies in the initial conditions and steady state densities of electrons and holes for larger average vacancy concentrations (Figure 5.11, right). However, unlike the physically realistic case of $C_{\mathrm{a}} \approx 6.4 \times 10^{23}$ m^{-3}, depicted in Figure 5.8, these differences appear to be minor, allowing the steady state solution to be reached more rapidly. Additionally, the scenario of moving local depletion zones is not observed at all.

Summarizing, for the memristive devices, we also observe an exponential decay of the relative entropy with respect to the steady state (5.2) and the quadratic L^2 errors towards zero for all chosen average vacancy concentrations. This study underlines the importance of selecting initial conditions that are physically justified and aligned with the specific characteristics of the device. In the regime 1.0×10^{24} m^{-3} $< C_{\mathrm{a}} <$ 1.0×10^{25} m^{-3}, which corresponds to values near those predicted in literature, the relative entropy and the quadratic L^2 errors vanish slower. In this range, the vacancy dynamics clearly influences the dynamics of electrons and holes, as reflected by the larger convergence times. For smaller and larger vacancy concentrations, we observe faster convergence times. However, these concentration values tend to underestimate the influence of vacancy dynamics, as seen in Figure 5.11.

5.2. Volume exclusion effects in perovskite charge transport modeling

So far, we gained in this chapter insight into the large time behavior and the entropy decay of two vacancy-assisted charge transport models. However, as indicated in Section 2.4.3, when considering volume exclusion effects, the question arises of choosing the mobility or the diffusion coefficient as constant, while the other remains density-dependent. This section comprehensively compares two different ionic current densities, where we either assume a given mobility or diffusion coefficient. We will first carefully design a reasonable benchmark for perovskite solar cells. Then, in the framework of this benchmark, we will discuss the influence of the two different ionic current densities on the electric potential, the vacancy carrier density and the current-voltage characteristics for a model based on the ohmic contact boundary conditions, described in Section 3.1.3.1.

5.2.1. Design of benchmark

Until now, we assumed a constant mobility $\overline{\mu}_\mathrm{a}$ and a density-dependent diffusion coefficient D_a in the model formulations and in the numerical analysis of the implicit-in-time TPFA finite volume schemes (restated from (2.37))

$$\mathbf{j}_{\mathrm{a,ND}} = -z_\mathrm{a} q \overline{\mu}_\mathrm{a} U_T \left(g_\mathrm{a}\left(\frac{n_\mathrm{a}}{N_\mathrm{a}}\right) \nabla n_\mathrm{a} + \frac{z_\mathrm{a}}{U_T} n_\mathrm{a} \nabla \psi \right). \tag{5.5}$$

Indeed, there exist approaches [15, 44, 51] where, instead of a constant mobility, a density-dependence of the mobility is incorporated into the model, while the diffusion coefficient $\overline{D}_\mathrm{a}$ is regarded as constant (restated from (2.38))

$$\mathbf{j}_{\mathrm{a,MD}} = -z_\mathrm{a} q \overline{D}_\mathrm{a} \left(\nabla n_\mathrm{a} + \frac{z_\mathrm{a}}{U_T g_\mathrm{a}\left(\frac{n_\mathrm{a}}{N_\mathrm{a}}\right)} n_\mathrm{a} \nabla \psi \right). \tag{5.6}$$

In the following, we call $\mathbf{j}_{\mathrm{a,ND}}$ a current density based on *nonlinear diffusion* and $\mathbf{j}_{\mathrm{a,MD}}$ a current density with a *modified drift*. Following the discussion in Section 2.4.3, suppose that the mobility and the diffusion coefficient of both descriptions are proportional, i.e., $\overline{\mu}_\mathrm{a} U_T \sim \overline{D}_\mathrm{a}$. Then, the nonlinear diffusion current density $\mathbf{j}_{\mathrm{a,ND}}$ and the modified drift current density $\mathbf{j}_{\mathrm{a,MD}}$ are also proportional with respect to the diffusion enhancement g_a (restated from (2.39))

$$\mathbf{j}_{\mathrm{a,ND}} \sim g_\mathrm{a}\left(\frac{n_\mathrm{a}}{N_\mathrm{a}}\right) \mathbf{j}_{\mathrm{a,MD}}. \tag{5.7}$$

Now, we aim to understand the implications that the multiplication with the diffusion enhancement g_a in (5.7) has. To this end, we further assume that the vacancy concentration n_a is approximately equal to the fixed average vacancy concentration C_a, which is incorporated into the model via the right-hand side of the Poisson equation (3.1d) through the doping $C = -C_\mathrm{a}$ in the intrinsic layer, i.e., $n_\mathrm{a} \approx C_\mathrm{a}$. Then, the diffusion enhancement can be approximated by

$$g_\mathrm{a}\left(\frac{n_\mathrm{a}}{N_\mathrm{a}}\right) \approx g_\mathrm{a}\left(\frac{C_\mathrm{a}}{N_\mathrm{a}}\right) = \frac{1}{1-\frac{C_\mathrm{a}}{N_a}} = \frac{1}{1-\epsilon}, \tag{5.8}$$

where we introduce the dimensionless scaling factor

$$\epsilon = \frac{C_\mathrm{a}}{N_\mathrm{a}} = \frac{\text{average anion vacancy density}}{\text{maximum anion vacancy density}}. \tag{5.9}$$

Here, N_a is the saturation limit and a model parameter entering the state equation (2.3). If ϵ tends to zero ($g_\mathrm{a} \searrow 1$), we neglect the finite size of ions, resulting in

a Boltzmann relation between n_a and φ_a (see Remark 2.3 and the right column in Figure 5.12). Contrarily, if ϵ tends to 1 ($g_a \nearrow +\infty$), then ionic movement is suppressed, which can be well observed in Figure 5.12 (left column), and, thus, the model reduces to the classical van Roosbroeck system [204]. Since $g_a \geq 1$, the relation in (5.7) along with (5.8) indicates a slower evolution of the vacancy profile in the case of the modified drift current density and large choices of ϵ.

In the following, a small ϵ indicates *low exclusion*, while a larger ϵ indicates *high exclusion*. We can calculate a lower bound for the scaling factor ϵ, introduced in (5.9). To do this, we introduce the largest possible vacancy density $\overline{N}_a$, which is the ideal density of halide sites in a unit cell (see (2.31) and the subsequent discussion). Defining $\bar{\epsilon} := C_a/\overline{N}_a$, we indeed have $\bar{\epsilon} \leq \epsilon$, since $N_a \leq \overline{N}_a$. However, the precise choice of ϵ is strongly dependent on the perovskite material. For clarity, we assume a constant average vacancy concentration C_a. Thus, we can consider variations in ϵ to represent different maximum vacancy densities N_a, where $C_a < N_a < \overline{N}_a$. A choice of $N_a < \overline{N}_a$ indicates that only a certain percentage of ion sites, rather than all, becoming vacant is sufficient to, e.g., reproduce experimentally observed accumulation (see Figure 5.12, middle column).

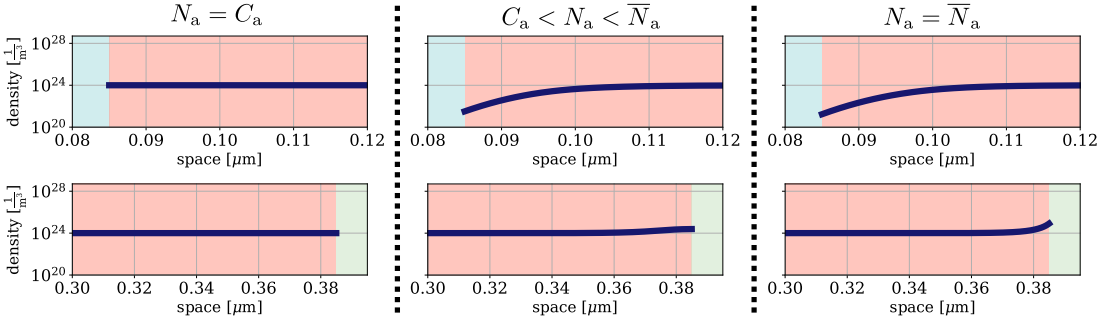

Figure 5.12.: Simulation of three possible equilibrium vacancy density configurations depending on the choice of the saturation limit N_a, portrayed in the perovskite layer (highlighted in red). The first row shows the vacancy density at the ETL/perovskite interface while the second row corresponds to the vacancy density at the perovskite/HTL interface. The simulation is based on the parameter set in Table B.2 and the device domain in Figure 5.13.

We use the parameter set in Table B.2 with $C_a = 1.0 \times 10^{24}$ m^{-3} and $\overline{N}_a = 1.21 \times 10^{28}$ m^{-3}. With $\overline{\mu}_a = 1 \times 10^{-14}$ m^2/(Vs) and $\overline{D}_a = 2.59 \times 10^{-16}$ m^2/s, we have $\overline{\mu}_a U_T = \overline{D}_a$. This choice of mobility and diffusion coefficient shows in the simulations that, given sufficient relaxation time, we receive the same steady state solution for the PSC charge transport based either on the flux (5.5) or the flux (5.6). Thus, of particular interest is the simulation of current-voltage scan protocols, where the model is far from an equilibrium state. To this end, we simulate a three-layer PSC device, where the

perovskite is sandwiched between two doped non-perovskite semiconductor transport layers. To be more precise, MAPI is used as the perovskite material, while PCBM is chosen for the electron and PEDOT:PSS for the hole transport layer. A schematic of the device architecture is shown in Figure 5.13. We note that the iodide vacancies move solely within the perovskite (red area), whereas electrons, holes, and the electric potential are defined across the whole device. The simulations are performed in one dimension. Furthermore, we apply a linear I-V scan protocol with a scan rate of 40 mV/s for an applied bias between 0 V and 1.2 V via the time-dependent Dirichlet conditions (3.7a), meaning that the scan ends at $t = 30$ s. During the scan, the outer boundary conditions for the ohmic contacts vary with time, and the steady state is not reached.

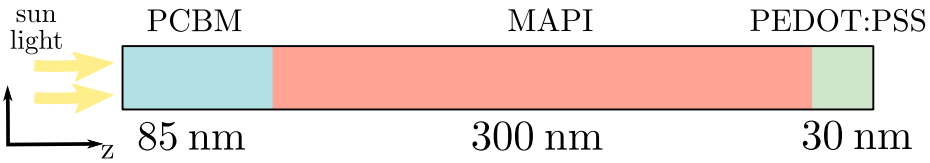

Figure 5.13.: Schematic diagram of the simulated PSC device configuration with ohmic contacts as described in Section 3.1.3.1. The electron transport layer (blue) is given by PCBM, whereas for the hole transport layer (green) PEDOT:PSS is used. As perovskite material (red layer), we use MAPI. (From [DA3].)

We validate the solutions calculated with `ChargeTransport.jl` [DA7] with additional simulations performed in the open source tool `Ionmonger` [44, 50]. While `ChargeTransport.jl` uses a finite volume method for the spatial discretization as described in Chapter 4, `Ionmonger` is based on a finite element method written in Matlab. The same non-uniform grid spacing as introduced by [44, 48] is used, whereas a uniform time mesh is utilized in `ChargeTransport.jl` and an adaptive one in `Ionmonger`. Information on the flux discretizations can be found in [DA6]. To primarily focus on the impact of the different current density descriptions, other effects, such as photogeneration and surface recombination, are neglected in the simulations. In the following, we look closer at the numerical performances of the solutions for the two current densities introduced in (5.5) and (5.6) for the described setup.

5.2.2. Discussion of results

Figure 5.14 shows the evolution of the electric potential within the perovskite layer (area shaded in red). Additionally, the evolution of the vacancy density in the vicinity of each perovskite/transport layer interface is depicted in Figure 5.15. Both profiles are visualized for a model based on the nonlinear diffusion current density (5.5) and a

model based on the modified drift current density (5.6) for two choices of ϵ reflecting low and high volume exclusion. The colored lines correspond to a solution calculated with `ChargeTransport.jl`, whereas the black dotted lines indicate respective solutions calculated with `Ionmonger`. Brighter colors indicate a later time. First, both software tools based on different discretization techniques yield near-identical results. Hence, we can compare the impact of the different current density descriptions independent of the numerical method.

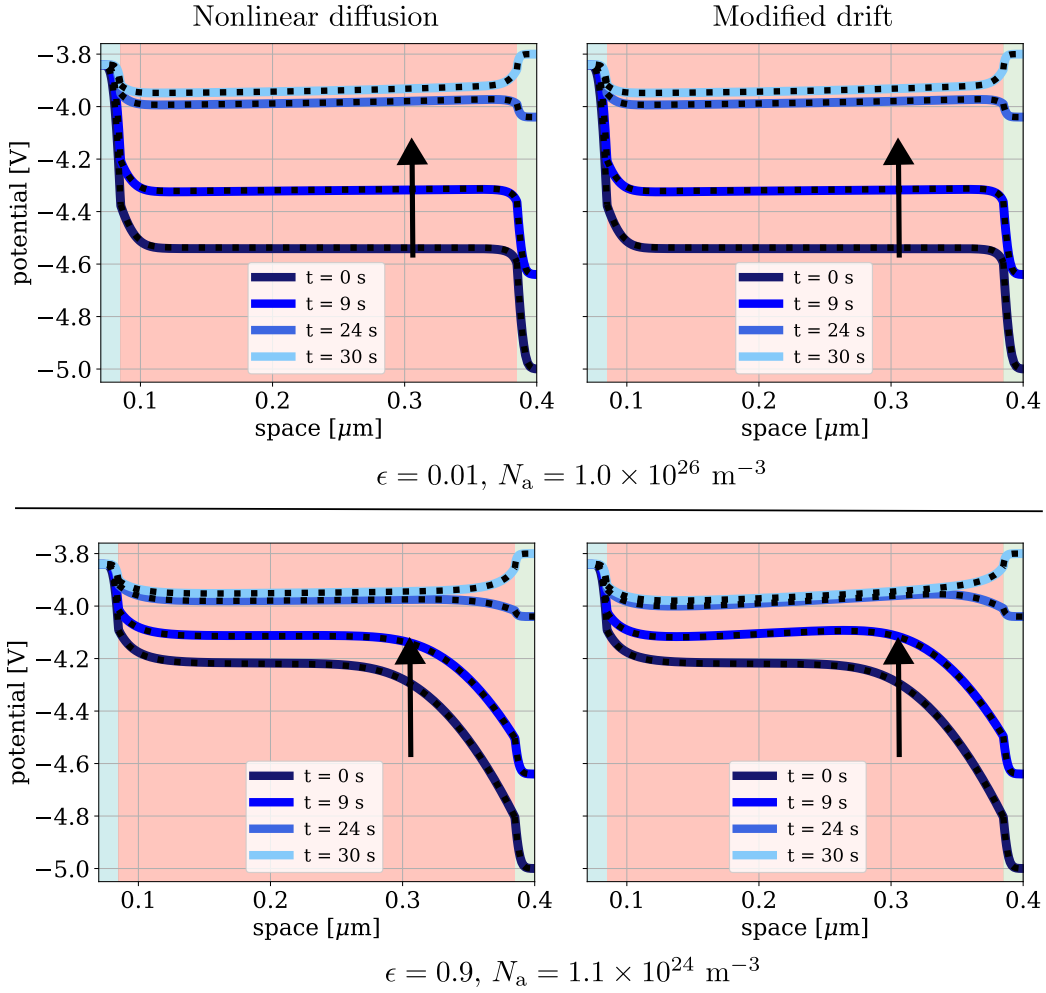

Figure 5.14.: Evolution of the electric potential ψ in the perovskite layer solving the PSC charge transport model based on the nonlinear diffusion (5.5) (first column) and for the model based on the modified drift current density (5.6) (second column). The first row shows the case of $\epsilon = 0.01$ (low exclusion) and the second row of $\epsilon = 0.9$ (high exclusion). The arrows indicate the direction of increasing time. (From [DA3] with modifications.)

Not surprisingly, for $\epsilon = 0.01$, no difference in the electrostatic potential evolution

(Figure 5.14, first row) and in the vacancy density profiles (Figure 5.15, top set of four) can be observed. We can explain this behavior using (5.8), which shows that for $\epsilon = 0.01$, $g_\mathrm{a} \approx 1$. Consequently, both current density descriptions coincide, as indicated by the relationship (5.7) and the equality $\overline{\mu}_\mathrm{a} U_T = \overline{D}_\mathrm{a}$. This particular case is also described in Remark 2.3.

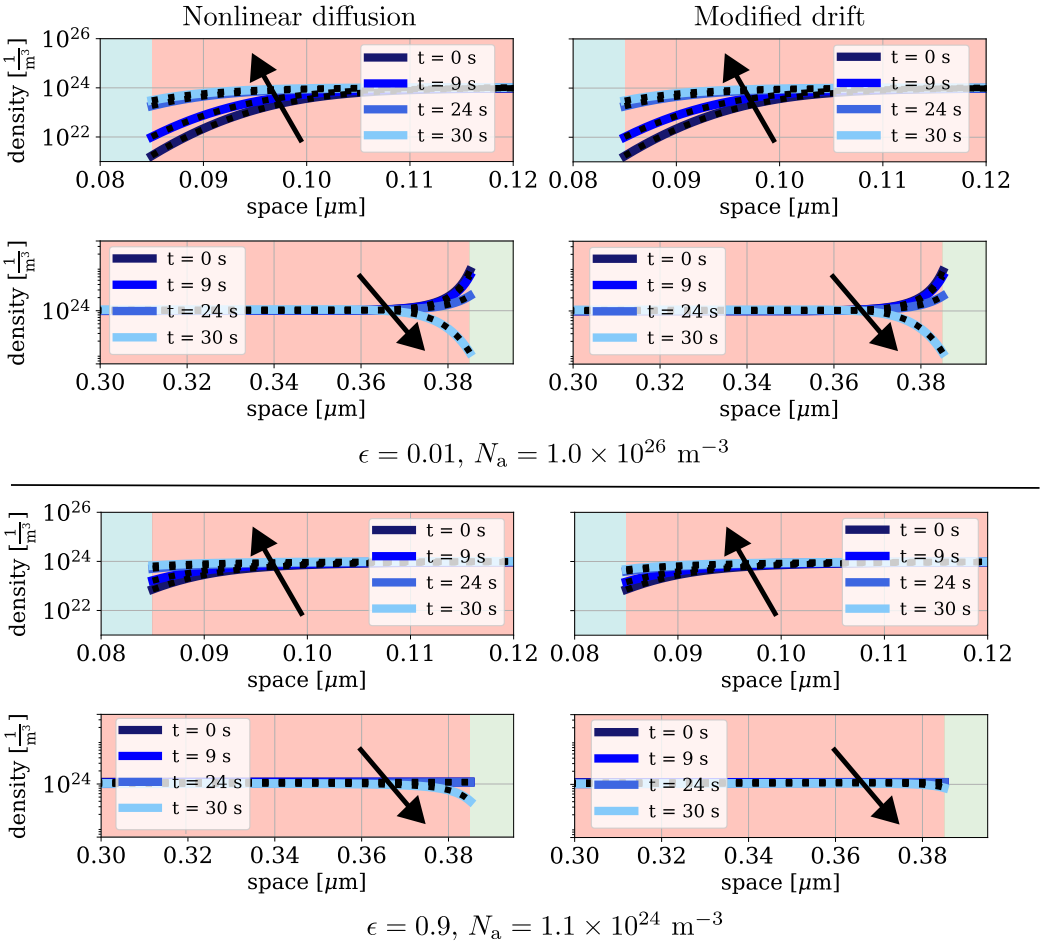

Figure 5.15.: Evolution of the vacancy density n_a at the left and right perovskite/transport layer interface for the PSC charge transport model based on the nonlinear diffusion current density (5.5) (first column) and for a model based on the modified drift current density (5.6) (second column). The first set of rows shows the case of $\epsilon = 0.01$ and the second set of rows (below the line) corresponds to $\epsilon = 0.9$. The arrows indicate the direction of increasing time. No differences can be observed in the case of low exclusion, whereas a slower evolution of the ion profile can be observed in the case of high exclusion and a modified drift current density. (From [DA3] with modifications.)

Contrarily, for high volume exclusion (larger ϵ), the modified drift current density (5.6)

causes a slower decrease of the ion density at the right perovskite interface (Figure 5.15, second set of rows). Again, this behavior can be explained via the relation (5.7) and the equality $\overline{\mu}_{\mathrm{a}} U_T = \overline{D}_{\mathrm{a}}$. Moreover, the diffusion enhancement g_{a} enters the diffusion part of the nonlinear diffusion current density $\mathbf{j}_{\mathrm{a,ND}}$, defined in (5.5). In this case, as g_{a} increases (larger ϵ), the diffusion of the vacancies in case of nonlinear diffusion current density (5.5) also increases. Therefore, it is only in the case of both high exclusion and modified drift current density (Figure 5.15, second set of rows) that we see a slower evolution.

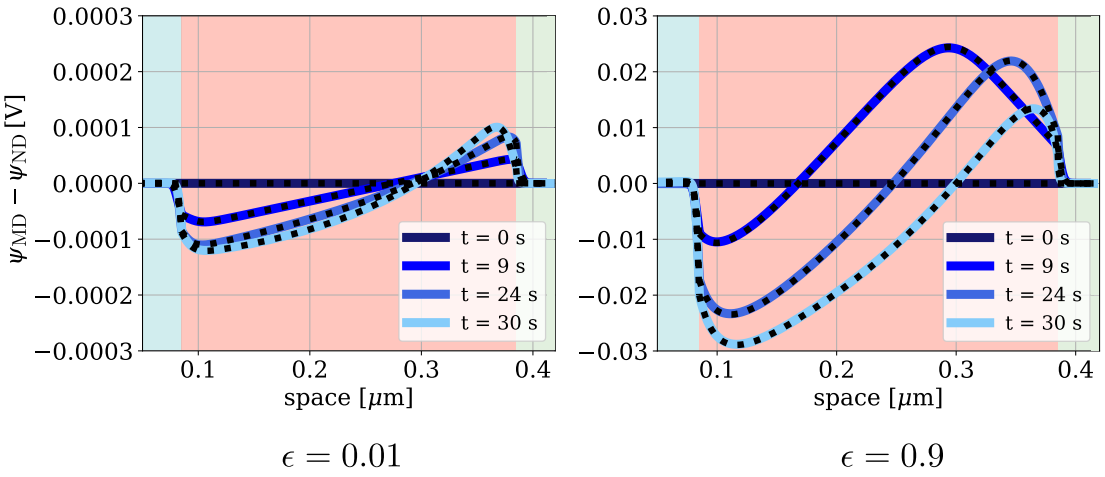

Figure 5.16.: Difference between calculated electrostatic potentials depicted in Figure 5.14 based on either a modified drift or a nonlinear diffusion approach, i.e., the error $\psi_{\mathrm{MD}} - \psi_{\mathrm{ND}}$ is shown for $\epsilon = 0.01$ (left) and $\epsilon = 0.9$ (right). The scale of the y-axes differs by two orders of magnitudes. (From [DA3] with modifications.)

Furthermore, the difference in the calculated electric potentials, i.e., $\psi_{\mathrm{MD}} - \psi_{\mathrm{ND}}$, is approximately two orders of magnitude larger for high volume exclusion (Figure 5.16). Both configurations (nonlinear diffusion and modified drift) start with the same initial condition, so the difference in electric potentials is negligible at $t = 0$ s. However, for later times t, the difference $\psi_{\mathrm{MD}} - \psi_{\mathrm{ND}}$ attains a peak at both of the perovskite/transport layer interface. A similar behavior can be observed in the vacancy density differences, depicted in Figure 5.17. The largest differences occur near the junction between the perovskite and transport layers. Again, for high volume exclusion, the difference in vacancy densities (Figure 5.17) is approximately two orders of magnitude larger. In case of high excluded-volume effects, the difference between the calculated vacancy densities at the end time $t = 30$ s is significantly larger than at previous times (Figure 5.17, right), agreeing with the previously made observations concerning Figure 5.15.

This trend of increasing error can be likewise observed for different choices of ϵ in Figure 5.18, where the L^∞ error between the calculated electric potentials and the vacancy densities with respect to ϵ are depicted. Both L^∞ errors are increasing with higher effects of excluded-volume for all visualized times $t > 0$ s. The difference in the vacancy densities seems most visible for larger times and larger ϵ (Figure 5.18, right) and increases the most for the end time $t = 30$ s.

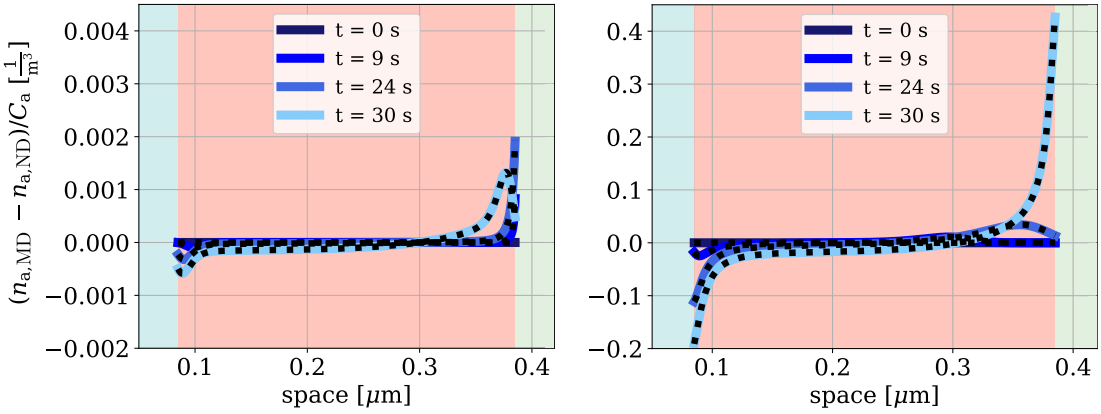

$\epsilon = 0.01$ $\epsilon = 0.9$

Figure 5.17.: Difference between calculated vacancy densities depicted in Figure 5.15 based on either a modified drift or a nonlinear diffusion approach scaled by the average vacancy density for $\epsilon = 0.01$ (left) and $\epsilon = 0.9$ (right). The scale of the y-axes differs by two orders of magnitudes. (From [DA3] with modifications.)

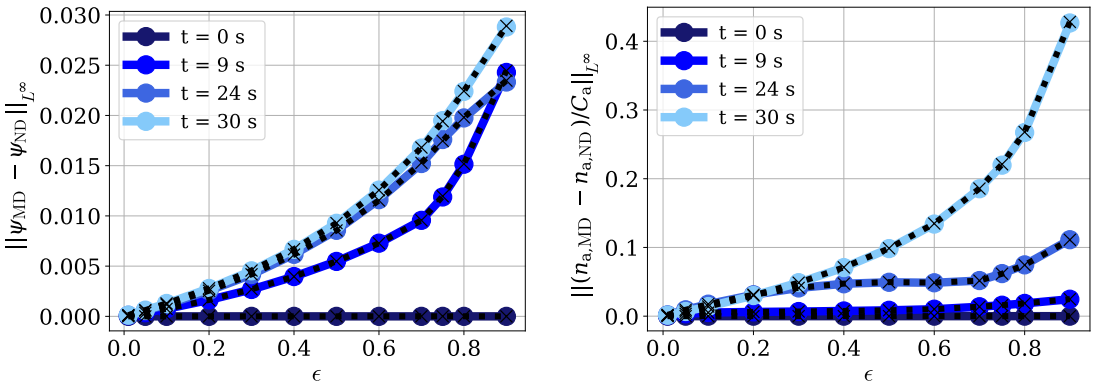

Figure 5.18.: L^∞ error between the electric potentials (left) and the vacancy densities (right) calculated from a model based on either a nonlinear diffusion (5.5) or a modified drift current density (5.6) for different values of ϵ. (From [DA3] with modifications.)

It is worth noting that the end time $t = 30$ s corresponds to the end of the scan

protocol rather than the time when a steady state solution is reached. Holding the perovskite solar cell at the constant end voltage $U = 1.2$ V while increasing the time allows us to calculate the steady state solutions as t approaches infinity. Figure 5.19 (first row) shows that for low exclusion effects, the quadratic L^2 errors between the steady state and a solution at time t reach machine precision at a similar time for both current density descriptions. However, the steady state solution is attained more slowly when using the modified drift approach for cases with high volume exclusion effects, as shown in Figure 5.19 (second row). In this case, the resulting quadratic L^2 errors take approximately two to three times longer to vanish with the modified drift current density.

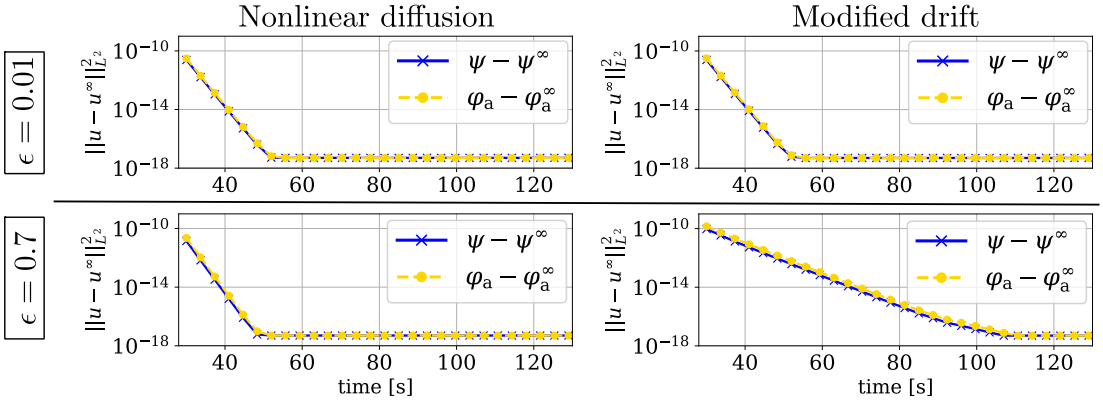

Figure 5.19.: Time evolution of the quadratic L^2 errors between the computed solutions at time t and the steady state solutions for low exclusion (first row) and high exclusion effects (second row). The steady state solution is calculated for a constant applied voltage $U = 1.2$ V. For high volume exclusion effects, the steady state solution is reached at different converging times.

Lastly, the influence of the different current density descriptions on the current-voltage curves without illumination is investigated in Figure 5.20 and Figure 5.21. Again, the colored curves correspond to solutions calculated with `ChargeTransport.jl`, while black dotted lines are the solutions received using `Ionmonger`. Brighter colors indicate higher volume exclusion, reflected in the choice of ϵ.

Figure 5.20 illustrates for low exclusion effects ($\epsilon = 0.01$) that the currents for either a nonlinear diffusion (5.5) or a modified drift current density (5.6) are identical. Moreover, for a model based on the modified drift current density (Figure 5.20, left), the impact of volume exclusion in the I-V curves becomes already observable for smaller choices of ϵ ($\epsilon = 0.5$). In contrast, for the nonlinear diffusion approach, differences in the I-V curve become only apparent for larger values (Figure 5.20, right, $\epsilon = 0.9$). However, both current density approaches reveal in Figure 5.20 that as ϵ increases, the

corresponding I-V characteristics shifts to the left, indicating that the current starts to flow at a lower voltage. The trends in the currents can be explained, as in [47], in terms of the distribution of the electric potential across the cell.

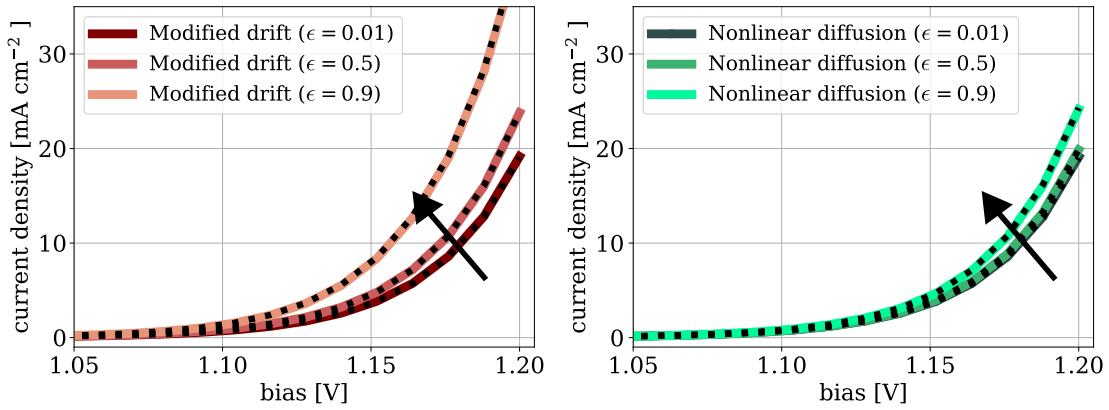

Figure 5.20.: Current-voltage curves for modified drift (left) and nonlinear diffusion (right) for variations of ϵ. The arrows indicate the direction of increasing ϵ. For larger values of ϵ the diode opens earlier. (From [DA3] with modifications.)

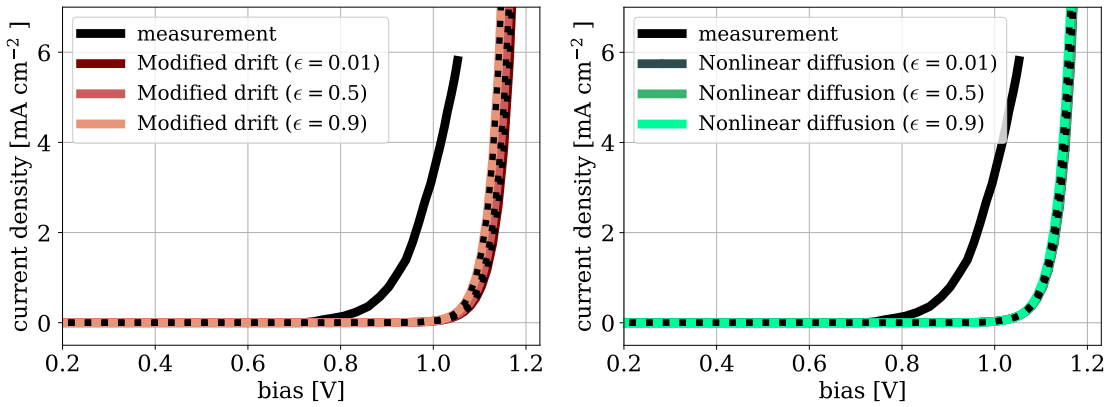

Figure 5.21.: Simulated I-V curves for modified drift (left) and nonlinear diffusion (right) for variations of ϵ in comparison with measurements [29]. (From [DA3] with modifications.)

At earlier times ($t = 0,9$ s in Figure 5.14), it can be seen that low exclusion leads to smaller potential drops within the perovskite layer and larger potential drops within the neighboring transport layers. Large drops can suppress recombination (by keeping minority carriers away from recombination sites) by forming barriers. However, at later times ($t = 24,30$ s), we observe that the electric field at the perovskite/HTL interface decreases for increasing ϵ. Smaller positive fields/larger negative fields allow more holes from the transport layer to enter the perovskite, leading to increased

recombination and higher currents, as shown in Figure 5.20. For the modified drift current density, at large ϵ, a negative electric field also emerges across the bulk of the perovskite due to the slower migration of ions (see Figure 5.15, second set of rows), further enhancing the currents.

Figure 5.21 compares the simulated I-V curves to the measurements from [29] for the same device setup, as illustrated in Figure 5.13. Indeed, Figure 5.21 shows that in comparison to the experimental measurements, the difference between nonlinear diffusion or modified drift current density are minor. However, it is important to note that for the sake of simplicity, this study excluded other effects, such as surface mechanisms or general trap states.

In summary, our study reveals that when dealing with high exclusion, the modified drift current density leads to a slower evolution of the vacancy profile, affecting the electric potential profile and the I-V characteristics. While this indicates a greater influence of volume exclusion effects on model predictions based on a modified drift current density description, in our specific comparison with a measurement curve, this influence is negligible. Nevertheless, additional physical effects or other scan protocols may exhibit a different behavior depending on whether a charge transport model is based on nonlinear diffusion or modified drift current densities.

5.3. Role of vacancy dynamics in two-dimensional memristive devices

We end this chapter by analyzing the origin of hysteresis, the influence of vacancy dynamics, and image-charge-induced Schottky barrier lowering for TMDC-based memristive devices. The discussion includes the cases of vanishing Schottky barriers and significant Schottky barrier heights. In addition, we examine the case without vacancy migration, leading to the classical semiconductor device equations [204]. Furthermore, the simulations are compared with experimental studies found in literature.

We use physically realistic parameters for MoS_2 as representative material, as stated in Table B.3. This includes the relative permittivity ε_r, the band-edge energies $E_\mathrm{n}, E_\mathrm{p}$, and the effective densities of states $N_\mathrm{n}, N_\mathrm{p}$. While the abovementioned parameters are obtained directly from the literature and used for all simulations, other parameters such as the mobilities $\mu_\mathrm{n}, \mu_\mathrm{p}, \mu_\mathrm{a}$, the intrinsic Schottky barriers ϕ_0, and the vacancy energy level E_a are expected to be highly sensitive to the sample's microstructure. These parameters are stated in Table B.4 for the two considered simulation scenarios. The measurements are from [150] and were performed on MoS_2-based memristive

devices fabricated with a mechanical shear exfoliation technique followed by a plasma treatment step to induce sulfur vacancies. Auger-electron spectroscopy measurements are performed on these devices, confirming vacancy migration. We refer to [150] for further information on the fabrication and measurement processes.

In the following, we have a one-dimensional device geometry, as illustrated in Figure 3.2 (bottom right), and apply a periodic piecewise linear voltage at the right contact, as shown in Figure 5.22. The scan protocol depends on the maximum voltage, the sweep rate and the number of cycles, specified in Table B.4. We denote the left contact by x_1 and the right contact by x_2.

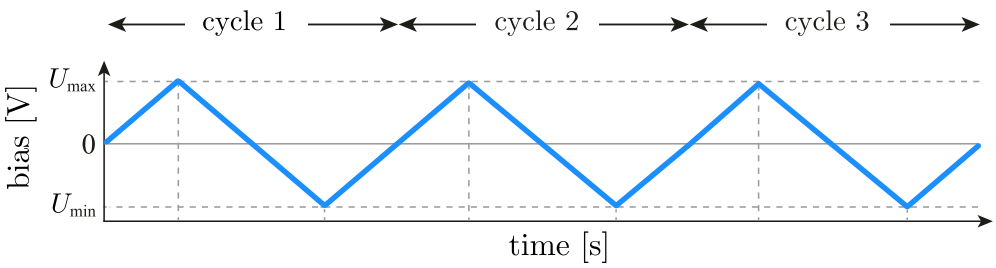

Figure 5.22.: Illustration of the time-dependent periodic piecewise linear voltage applied at the right contact for three consecutive voltage cycles.

5.3.1. Vacancy depletion and mobility

For the first case, we consider the parameter set S_1 (Table B.3 and Table B.4) with negligible Schottky barriers $\phi_0(x_1) = \phi_0(x_2) = 1$ meV. We supply the model with the classical Schottky boundary model (Section 3.2.2.1). The minimum and the maximum applied voltages are $U_{\min} = -13$ V, $U_{\max} = 13$ V, and one cycle lasts 10.4 s.

Figure 5.23 shows eight consecutively simulated I-V curves (middle). Additionally, we see a comparison of the experimentally measured curve with the second cycle simulation (left) and with two simulated I-V cycles without vacancy migration (right). The magnitude of the measured curve $|I|$ (Figure 5.23, gray circles) is smooth with approximately equal maximum current magnitudes at $U_{\min}$ and $U_{\max}$. While $|I(U)|$ is more or less symmetric around $U = 0$ V, the right hysteresis branch ($U > 0$ V) has a slightly larger area compared to the left branch ($U < 0$ V). The hysteresis direction is clockwise in the right and counterclockwise in the left branch (Figure 5.23, right). The second cycle I-V curve closely mirrors the characteristics of the measured curve, including the hysteresis direction and the transitions from the low-resistive state (LRS) to the high-resistive state (HRS) and vice versa (Figure 5.23, left).

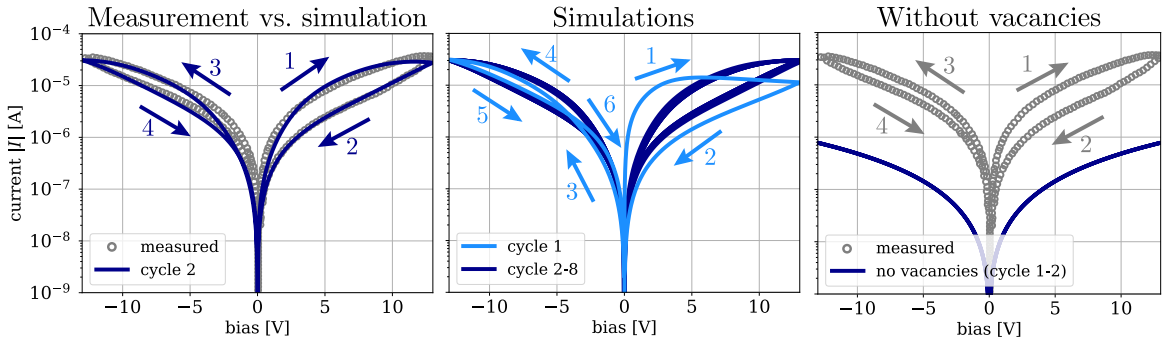

Figure 5.23.: Comparison between the simulated second cycle I-V with a symmetric I-V measurement curve from [150] (left) and illustration of eight consecutively simulated current-voltage cycles (middle). Furthermore, simulations without vacancy migration are compared to the measurements (right). The simulations are based on the parameter set S_1 (Table B.3 and Table B.4). (Left and middle figure from [DA5] with modifications.)

In Figure 5.23 (middle), we observe a notable difference in the I-V curves of the first cycle (light blue) compared to the following seven cycles (dark blue). Particularly, the first cycle I-V curve is highly asymmetric, with an initial rise in the current, which quickly saturates and almost remains constant until U_{max} is reached. In the left hysteresis branch ($U < 0$ V) of the first cycle I-V curve (light blue) a current crossing is visible, resulting in a change of the hysteresis direction from clockwise to counterclockwise indicated by arrows. The consecutive I-V curves (dark blue) behave differently, compared to the initial cycle. However, they consistently reproduce the I-V characteristics of the measured curve.

Moreover, we do not observe at all a hysteretic behavior when simulating the charge transport without accounting for vacancy migration (Figure 5.23, right). Furthermore, neglecting vacancy migration results in an underestimation of the current magnitude by a factor of two orders.

The different I-V characteristics for the initial cycle and the subsequent ones in Figure 5.23 (middle) arise from variations in the initial vacancy quasi Fermi potential φ_{a} configuration at the beginning of each cycle. At the beginning of the first cycle ($t = 0$ s, $U = 0$ V), the system is in equilibrium, wherein all quasi Fermi potentials remain constant, i.e., $\varphi_\alpha = \varphi_{\text{p}} = \varphi_{\text{a}} = 0$ V, as shown in the band diagram (Figure 5.24, left). Similarly, at the beginning of the second cycle ($t = 10.4$ s, $U = 0$ V) the electrons and holes still remain close to their initial configuration at $t = 0$ s (Figure 5.24, right). Contrarily, the small vacancy mobility results in a deviation from equilibrium of φ_{a} at the left contact as seen in Figure 5.24 (right, yellow dotted). Such a non-equilibrium configuration is reproducibly reached after each cycle following the first one.

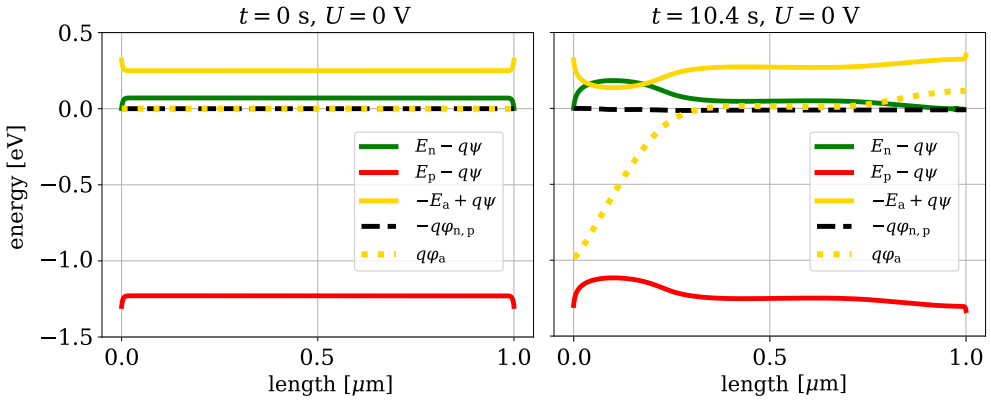

Figure 5.24.: Simulated band diagram of the initial equilibrium configuration at $t = 0$ s, and an applied voltage $U = 0$ V (left) and of the non-equilibrium configuration at the beginning of the second cycle at $t = 10.4$ s ($U = 0$ V). (From [DA5] with modifications.)

This difference between the first and the subsequent hysteresis loops can be linked to a more general dynamic phenomenon, which will become clearer in the subsequent discussion. We focus on the second cycle I-V curve as a more reproducible and representative I-V curve. Figure 5.25 shows the vacancy density at selected applied voltages during the second cycle. Additionally, its steady state limit, i.e., the configuration attained under a constant applied voltage as $t \to +\infty$, is shown in gray.

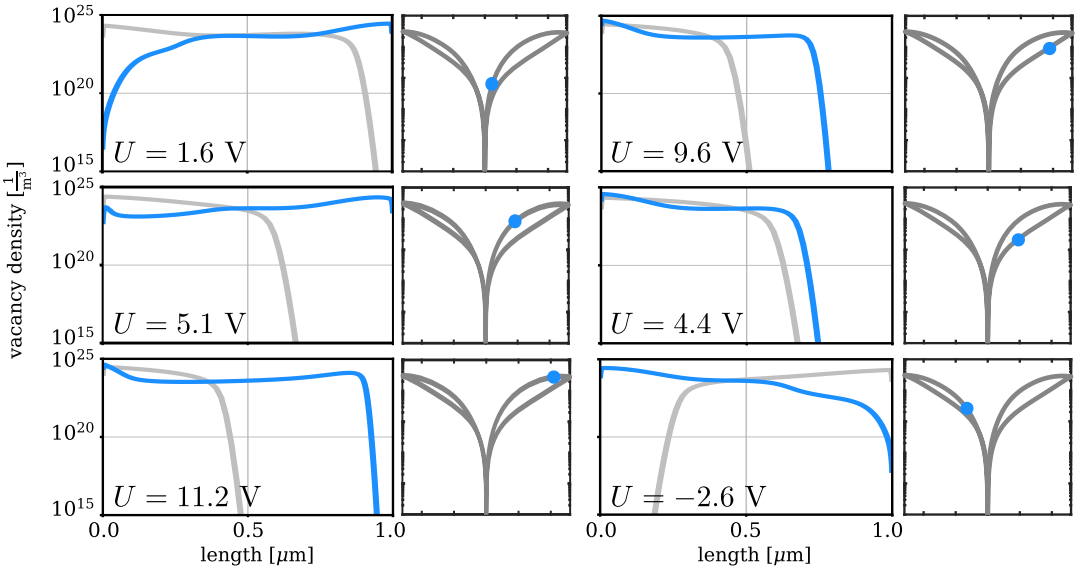

Figure 5.25.: Vacancy density configurations n_a for selected positions in the second cycle I-V curve shown in Figure 5.23 (left, darkblue), together with its steady state limit (gray). (From [DA5] with modifications.)

At the beginning of the cycle, the previously discussed drop in the vacancy quasi Fermi potential results in a local depletion of vacancies at the left contact ($n_\mathrm{a} \ll 10^{10}$ m^{-3}, Figure 5.25, $U = 1.6$ V). Initially, this depletion zone limits the current, but it vanishes quickly as the voltage increases (Figure 5.25, $U = 5.1$ V). Therefore, the device is in a high-conductance state at the beginning of the second cycle. As the applied voltage increases, the current also increases until a depletion zone forms at the right contact (Figure 5.25, $U = 11.2$ V). This depletion zone limits the current just before $U_\mathrm{max} = 13$ V is reached and grows, while the voltage decreases again (Figure 5.25, $U = 11.2$ V, $U = 9.6$ V, $U = 4.4$ V). The forming of the depletion zone at the right contact reduces the current, and, hence, the device is in the low-conductance state.

At $U = 0$ V, the system strives to restore equilibrium where no depletion zone exists. Because of the small vacancy mobility, the depletion zone is not entirely annihilated at the beginning of the left hysteresis branch (Figure 5.25, $U = -2.6$ V) leading to a mirrored vacancy density configuration similar to the one at the beginning of the right cycle (Figure 5.25, $U = 1.6$ V). This implies that the I-V curve is overall symmetric around $U = 0$ V, and the device starts in a high-conductance state at the beginning of the left hysteresis branch, portraying the behavior of the measured curve Figure 5.23 (left).

Next, we examine how the vacancy mobility μ_a impacts the I-V curve. As μ_a approaches zero or infinity, we expect the vacancy density to remain stationary. Further simulations, as detailed in [DA5], confirm this and reveal that significant hysteresis occurs only within the range of $\mu_\mathrm{a} \approx 10^{-15}$ m^2/(Vs) to $\mu_\mathrm{a} \approx 10^{-12}$ m^2/(Vs). Selected hysteresis curves with varying mobilities are portrayed in Figure 5.26.

As the mobility exceeds small values $\mu_\mathrm{a} \geq 10^{-15}$ m^2/(Vs), clockwise oriented hysteresis in both branches can be observed (Figure 5.26, first row). A transition of the hysteresis direction occurs in the left hysteresis branch from clockwise to counterclockwise at mobilities around $\mu_\mathrm{a} \approx 10^{-14}$ m^2/(Vs) (Figure 5.26, $\mu_\mathrm{a} = 3 \times 10^{-14}$ m^2/(Vs) and $\mu_\mathrm{a} = 5 \times 10^{-14}$ m^2/(Vs)). During this transition, the current in the left hysteresis branch intersects at a *crossover voltage* U_c (Figure 5.26, $\mu_\mathrm{a} = 3 \cdot 10^{-14}$ m^2/(Vs)), which moves towards $U = 0$ V as the mobility increases until the entire left hysteresis branch is directed counterclockwise (Figure 5.26, second row). Origin of this transition is the shorter time required for vacancies with a larger mobility to reach a steady state, which causes a faster annihilation of the depletion zone before $U < 0$ V is reached.

Further increasing the vacancy mobility (Figure 5.26, second row) results in the formation of maxima at voltages $U < U_\mathrm{max}$ (and $U > U_\mathrm{min}$), a symmetric I-V curve, and an overall reduced maximum current. This behavior reflects the formation dynamics of the depletion zone: In the high-mobility regime, the depletion zone can

form before $U_{\min}$ or $U_{\max}$ is reached, leading to maxima at earlier voltages and a drop in the current. Simultaneously, the vacancy density is close to its steady state limit, resulting in the symmetry around $U = 0$ V and $U_c \approx 0$ V.

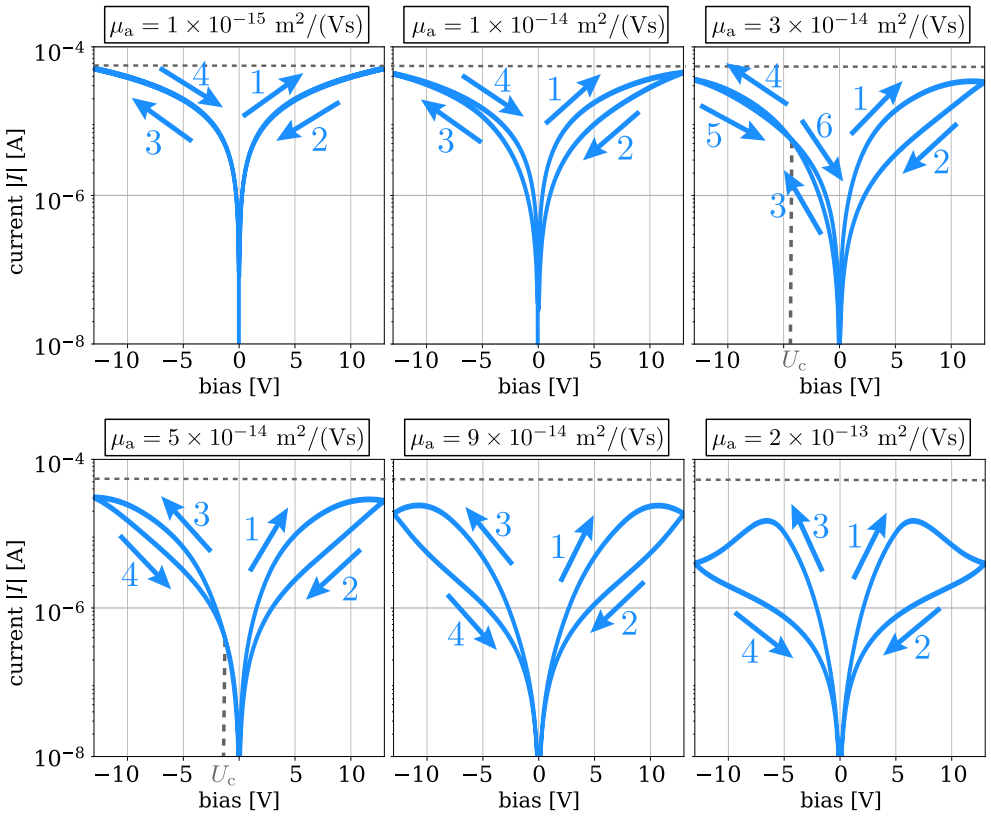

Figure 5.26.: Example hysteresis loops of the second cycle I-V simulation for selected vacancy mobility values. (From [DA5] with modifications.)

Additional simulations in [DA5] reveal that the crossover voltage consistently converges to $U_c = 0$ V after a sufficiently large number of voltage cycles. Higher mobility values result in faster reaching $U_c = 0$ V, requiring fewer cycles. Moreover, variations in the voltage sweep rate solely shift the range of mobilities for which hysteresis becomes observable.

In summary, the hysteresis and its symmetry originate from the formation and annihilation dynamics of the vacancy depletion zone. Hysteresis occurs in a small vacancy mobility range, in which the vacancies are sufficiently mobile to follow the other carriers but slow enough to be in non-equilibrium. Furthermore, the asymmetry and intersection in the left hysteresis branch are volatile features, influenced by both vacancy mobility and the number of cycles, vanishing after enough voltage cycles.

In this example, the intrinsic Schottky barriers are so small that SBL is negligible.

However, SBL is debated as a substantial mechanism contributing to hysteresis [150, 226, 262]. Therefore, the influence of SBL on the I-V curve is explored next.

5.3.2. Schottky barrier lowering

For the second case, we consider a similar parameter set S_2 (Table B.3 and Table B.4) as before but introduce intrinsic Schottky barriers $\phi_0(x_1) = 0.144$ eV and $\phi_0(x_2) = 0.11$ eV with a slightly smaller value at the right contact. The case *with SBL* refers to the Schottky barrier lowering model in Section 3.2.2.2, while *without/no SBL* refers to the Schottky boundary model in Section 3.2.2.1. The minimum and maximum applied voltages are $U_{\text{min}} = -10$ V, $U_{\text{max}} = 10$ V and one cycle lasts 8 s. This section deals exclusively with the second cycle I-V curves.

Figure 5.27 shows a comparison of the experimentally measured curve [151] with the simulated I-V with Schottky barrier lowering (left), without SBL (middle), and without vacancies (right). We observe good agreement of the measured I-V curve with the simulated I-V with SBL (Figure 5.27, left). Both have the same clockwise direction in the right branch and a counterclockwise direction in the left branch. In comparison to the measured I-V curve in Figure 5.23 (left), the asymmetry around $U = 0$ V of the measured curve in this section (Figure 5.27, left) is more pronounced, the two maximum current magnitudes are different, and the right hysteresis area is smaller than the left area.

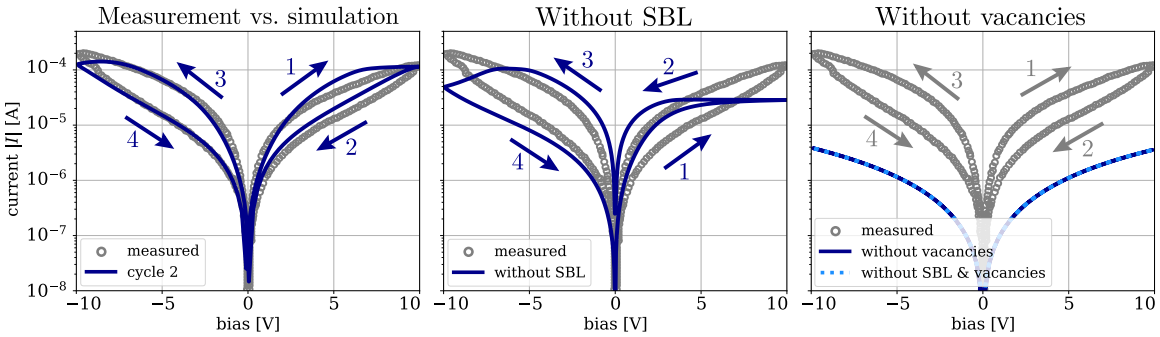

Figure 5.27.: Comparison between measurements of an asymmetric hysteresis curve from [150] and simulations with SBL (left) and without SBL (middle). Furthermore, simulations without vacancy migration based on both considered boundary models are compared to the measurements (right). The simulations are based on the parameter set S_2 (Table B.3 and Table B.4). (Left and middle figure from [DA5] with modifications.)

In contrast, the current-voltage characteristics without SBL (Figure 5.27, middle) shows a qualitative different behavior. Without SBL, the hysteresis direction of the

right branch is counterclockwise. Furthermore, we have significant differences in the maximum currents and the hysteresis areas of the left and right branches. Additionally, if we neglect vacancies (Figure 5.27, right), the current magnitude is underestimated by a factor of two orders and no hysteresis can be observed. For both boundary models (with and without SBL), the absence of vacancies results in identical I-V curves.

In equilibrium ($t = 0$ s), SBL reduces the contact barriers by approximately 25 % and 18 %. This results in new equilibrium barrier values of ≈ 0.11 eV (without SBL: 0.144 eV) at the left and ≈ 0.09 eV (without SBL: 0.11 eV) at the right contact, altering the electron band-edge boundary values (Figure 5.28, left). A similar reduction can be noticed in the band-edges of holes and vacancies. Next, we investigate how the barrier change at the left $|\Delta\phi(x_1)|$ and at the right contact $|\Delta\phi(x_2)|$ entering the SBL boundary model evolves over time. The barrier change $\Delta\phi$ is incorporated into the model through the electric potential boundary condition (3.30), (3.31) via the relation $\Delta\phi = -q\Delta\psi$. Figure 5.28 (middle) shows the applied bias and the changes in the Schottky barrier heights with respect to time during the first two voltage cycles. In our one-dimensional case, the condition $\nabla_{\boldsymbol{\nu}}\psi_r < 0$ in (3.31) indicates an upwards bending of the band-edges. Initially, for a positive bias, the band-edges at the left contact are bent upwards ($\nabla_{\boldsymbol{\nu}}\psi_r < 0$), leading to an increased Schottky barrier change $|\Delta\phi(x_1)| > 0$. Meanwhile, at the right contact, $\nabla_{\boldsymbol{\nu}}\psi_r$ becomes positive, i.e., $\nabla_{\boldsymbol{\nu}}\psi_r \geq 0$, indicating a downwards bent band-edge. Consequently, the change in the right Schottky barrier remains zero, i.e., $\Delta\phi(x_2) = 0$, during most of the right hysteresis cycle ($U > 0$). When the bias becomes negative, the situation reverses: The change in Schottky barriers is $\Delta\phi(x_1) = 0$ and $|\Delta\phi(x_2)| > 0$ during most of the left hysteresis cycle ($U < 0$).

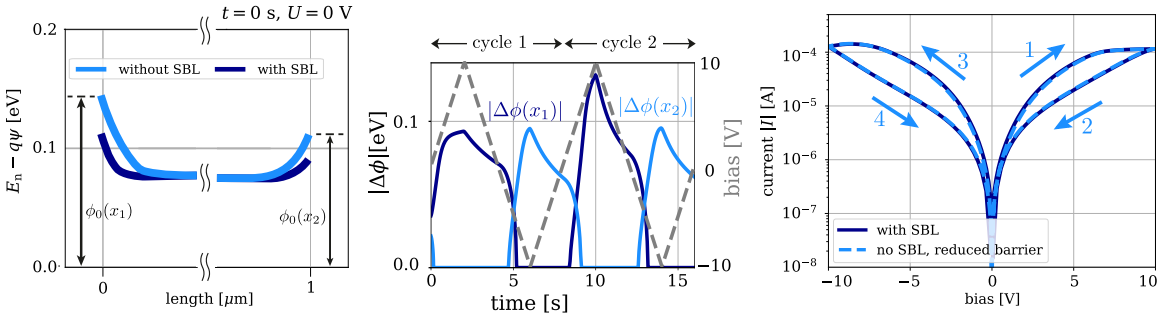

Figure 5.28.: Equilibrium electron band-edge with and without SBL (left) and the Schottky barrier change along with the applied voltage with respect to time (middle). Furthermore, a comparison between the simulated I-V curves with SBL (Figure 5.27, left) and without SBL but with reduced intrinsic Schottky barriers are shown (right). (From [DA5] with modifications.)

An additional I-V simulation was performed without SBL using the reduced equilibrium Schottky barriers obtained from the simulation with SBL as intrinsic Schottky barriers ϕ_0, (Figure 5.28, right; No SBL, reduced barrier). The resulting I-V curve aligns closely with the one obtained with SBL. This comparison shows that the hysteresis is primarily governed by the formation of the depletion zone as described in the previous section. Consequently, while SBL significantly affects the I-V curve, it does not explain the origin of hysteresis in this example.

Further simulations in [DA5] with varying intrinsic Schottky barriers at the left or right contact show a symmetric I-V curve for identical left and right Schottky barrier values. However, as the Schottky barrier heights at the left and right contacts differ, increasing asymmetry becomes noticeable in the I-V curve. Depending on the specific barrier values, this asymmetry can change the hysteresis direction in either the left or right branch. Other features were observed, such as the formation of a maximum at $U < U_{\max}$ and a reduction in maximum current with increasing barrier difference.

The analysis of the current-voltage dynamics resulting from asymmetric Schottky contacts is also investigated in [DA5]. There, the I-V curves show an initial asymmetry that decreases slightly but remains constant during more than 100 voltage cycles. Higher vacancy mobilities led to a faster convergence to this stable configuration, although it did not alter the underlying asymmetry. This observation suggests that the asymmetry in the hysteretic I-V characteristics, resulting from different Schottky barriers, is a non-volatile feature. This finding contrasts with the volatility observed in Section 5.3.1 for the case of negligible Schottky barriers.

5.3.3. Pulse simulation

For applications such as analog computing and the emulation of synaptic behavior, the devices are operated by applying repetitively short voltage pulses accompanied by a low-amplitude voltage pulse to read out the resistance via the current. Running such pulse simulations is challenging and computationally expensive due to the broad range of timescales involved. Each pulse lasts just a few microseconds to milliseconds, while the entire set of pulses can extend over many seconds to minutes. Moreover, the detailed behavior depends significantly on the pulse parameters, resulting in different maximum currents and symmetry of the set and reset currents. Like the I-V curve simulations, the pulse simulations start from an ideal equilibrium configuration, which is not necessarily ensured in the measurements. Considering these challenges, the pulse simulations in [DA5] show that our vacancy-assisted charge transport model can reproduce the overall experimental pulse-update behavior of two representative devices from [150].

5.3.4. Summary and conclusion

Our findings indicate that the hysteresis in both types of I-V characteristics, with and without significant Schottky barriers, arises from mobile charged vacancies. The vacancy dynamics leads to the formation and annihilation of a vacancy depletion region, locally reducing the conductivity and limiting the current. With this switching process, we can match experimentally observed I-V curves and explain other features, such as the formation of a maximum at $U < U_{\max}$ [118, 206, 207], hysteresis crossing [118], and different hysteresis directions [118, 150, 207].

Experimental studies have previously often explained different hysteresis directions with different switching mechanisms [118, 150, 262]. However, our simulations reveal that the vacancy depletion mechanism can account for both hysteresis directions, depending on minor changes in parameters like Schottky barriers, mobilities, and sweep cycles. In all our simulations, the hysteresis crossing results from slightly modifying the vacancy's dynamic response rather than an entirely new mechanism. Moreover, our study reveals that, while SBL notably affects the I-V curves, we did not identify any configuration where solely the effect of SBL reproduces the experimental measured I-V curve. Indeed, we showed that we can link the hysteresis behavior to the vacancy dynamics by modifying the Schottky barriers and using the classical Schottky boundary model. This result offers new insights into the frequently discussed hypothesis that SBL might be a primary mechanism for hysteresis in such devices [150, 226, 262]. In conclusion, our study highlights the importance of considering vacancy-assisted migration when designing and analyzing lateral memristive devices.

6. Conclusion and outlook

As the central concepts have been outlined in the preceding chapters, we will now summarize and draw conclusions based on the insights gained from this thesis. Additionally, we will provide an overview of potential avenues for future investigations.

6.1. Conclusion

A well-structured derivation and formulation of charge transport models, complemented by physically consistent numerical discretizations and simulations, are valuable tools for theoretical analysis. Furthermore, these tools can potentially guide future technological advancements, including developing technologies like perovskite solar cells and memristive devices. These innovations are promising in addressing our time's escalating global energy challenges.

In Chapter 2, we started with deriving general semi-classical macroscopic drift-diffusion equations. The resulting equations allow for an arbitrary number of mobile vacancies. Furthermore, they effectively include the physics of mobile point defects, particularly their nonlinear dynamics and volume exclusion effects, which capture the density saturation prescribed by the material's structure. Then, we continued in Chapter 3 by formulating drift-diffusion charge transport models tailored to PSCs and TMDC memristors. Moreover, we developed a self-consistent framework to account for image-charge-induced Schottky barrier lowering, which allows us to capture the influence of the applied voltage and the charge carriers on the Schottky barriers. In addition to these developments, we formulated in Chapter 4 implicit-in-time finite volume schemes based on the excess chemical potential flux as TPFA which preserves relevant physical properties such as positivity of densities or constant equilibrium quasi Fermi potentials. We looked closer to the numerical analysis of the discrete schemes, by proving an entropy-dissipation inequality which helped us to establish the existence of discrete solutions at every time step. Finally, in Chapter 5, we performed numerical simulations with `ChargeTransport.jl` [DA7]. These simulations allow us to validate and test our theoretical findings.

Our numerical experiments consistently demonstrate an exponential decay towards the discrete steady state solution for two error measure functionals. Moreover, the

relative entropy concerning non-zero band-edge energies exhibits an exponential convergence towards zero for both charge transport models. Our investigations also reveal that varying initial vacancy densities notably impact the convergence time towards the steady state, emphasizing the critical importance of aligning material parameters with existing literature for meaningful comparisons. Furthermore, we conducted a numerical comparison between two ionic current density descriptions when incorporating volume exclusion effects in a perovskite solar cell setup, using MAPI as the perovskite material. Notably, both models recover special cases of the charge transport model in the limit of ignoring the finite size of ions or suppressing ionic movement. In cases with high exclusion effects, we observed that the modified drift current density results in a slower evolution of the ion profile. This highlights the significant influence of volume exclusion effects on model predictions, particularly in scenarios involving a modified drift current density description. Lastly, we validated our charge transport model with I-V and pulse measurements found in literature for lateral 2D MoS_2-based memristive devices. These experiments strongly corroborated the relevance of vacancy dynamics in TMDC devices and offered a new perspective on the switching mechanisms. The insights gained from this study can also extend the functional behavior of 2D TMDC memristive devices, making them promising candidates for future neuromorphic computing applications.

6.2. Outlook

So far, we established a framework for describing and numerically solving the charge transport in crystalline semiconductors with additional vacancy migration. However, in addition to vacancy migration, other effects discussed in the literature influence the current-voltage characteristics and, consequently, the device performance. For instance, the impact of trap states has been explored in the context of perovskite-based solar cells (see, e.g., [110, 147, 183]) and TMDC memristors (see, e.g., [64, 113, 231]). From a modeling perspective, this involves coupling the drift-diffusion model to another continuity equation for the trap density, as proposed for perovskites in [77, 182]. Both, vacancy-assisted migration and charged trap states, alter the overall charge density, influencing the total device current. Thus, quantitative physical models can help by separating such effects, which are experimentally challenging to access or distinguish.

Concerning the discretization schemes, investigating the model behavior with non-zero and even irregular band-edge energies, as successfully applied in LED simulations [73], is from a mathematical and physical point of view of interest in the future. Additionally, studying the impact of time-dependent Dirichlet functions aligned with

physically realistic measurement techniques for PSCs and TMDC memristors can be a topic of future research. Within the scope of this thesis, we also did not discuss the convergence of the schemes for charge carriers evolving on different timescales. Furthermore, we have omitted an examination of the parameter sensitivity of physical parameters, following existing literature for the perovskite solar cells. Given this consideration, a logical next step involves a theoretical study of PSCs, similar to our approach for the TMDC memristive devices, by validating the model through experimental measurements. The presented ideas naturally extend this thesis and underline the importance of the interplay between theoretical findings, such as the modeling and discretization, and physical measurements.

A. Selected proofs

Within Chapter 2, we formulated the hypotheses (H1) and (H2), which deal with the regularity of the electrons and holes statistics functions

$$\begin{cases} \mathcal{F}_{\mathrm{n}}, \mathcal{F}_{\mathrm{p}} : \mathbb{R} \to (0,\infty) \text{ are } C^1\text{- diffeomorphisms;} \\ 0 < \mathcal{F}'_\alpha(\eta) \le \mathcal{F}_\alpha(\eta) \le \exp(\eta), \quad \eta \in \mathbb{R},\ \alpha \in \{\mathrm{n},\mathrm{p}\}, \end{cases} \tag{H1}$$

and the regularity of the vacancy statistics function

$$\begin{cases} \mathcal{F}_{\mathrm{a}} : \mathbb{R} \to (0,1) \text{ is a } C^1\text{- diffeomorphism;} \\ 0 < \mathcal{F}'_{\mathrm{a}}(\eta) \le \mathcal{F}_{\mathrm{a}}(\eta) \le \exp(\eta), \quad \eta \in \mathbb{R}. \end{cases} \tag{H2}$$

In this chapter, we show in Appendix A.1 that the examples of Fermi-Dirac and Boltzmann statistics (2.20), (2.21), and (2.23) indeed satisfy these assumptions. Then, we deal with the estimates concerning statistics and entropy functions (Lemma 3.3 and Lemma 3.4). We provide the proof of Lemma 3.3 in Appendix A.2 and Lemma 3.4 in Appendix A.3, which are stated under the assumption of (H1), (H2), and/or (H3). The hypothesis (H3) reads

$$\lim_{x\to+\infty} \frac{H_\alpha(x,y_0)}{\mathcal{F}_\alpha^{-1}(x)} = +\infty, \quad \text{for } y_0 \ge 0 \quad \text{and} \quad \alpha \in \{\mathrm{n},\mathrm{p}\}, \tag{H3}$$

where $H_\alpha(x,y) = \Phi_\alpha(x) - \Phi_\alpha(y) - \Phi'_\alpha(y)(x-y)$ is the relative entropy, defined in (3.41). We proceed by proving Grönwall's lemma (Lemma 3.8) in Appendix A.4 and a discrete integration by parts in Appendix A.5. Lastly, we establish two auxiliary results. One is needed for the proof of Lemma 4.12 (see Appendix A.6), and the other is required for the proofs of existence in Theorem 4.15 and Theorem 4.16 (see Appendix A.7).

A.1. Boltzmann and Fermi-Dirac statistics functions

We relate the Fermi-Dirac integral of order 1/2 in (2.20), and the Boltzmann approximation (2.21) to the hypotheses (H1) and (H3). Furthermore, we relate the Fermi-Dirac integral of order -1 in (2.23) to the hypothesis (H2).

Lemma A.1. (Boltzmann) Assume that the statistics for electrons and holes is the Boltzmann statistics (2.21), namely,

$$\mathcal{F}_\alpha(\eta) = e^\eta\,, \quad \eta \in \mathbb{R}\,,\ \alpha \in \{\mathrm{n},\mathrm{p}\}.$$

Then, $\mathcal{F}_\alpha$ satisfies (H1) and (H3). □

Lemma A.2. (Fermi-Dirac of order -1) Assume that the statistics for vacancies is the Fermi-Dirac integral of order -1 in (2.23), namely,

$$\mathcal{F}_\mathrm{a}(\eta) = F_{-1}(\eta) = \frac{1}{\exp(-\eta)+1}\,, \quad \eta \in \mathbb{R}\,.$$

Then, $\mathcal{F}_\mathrm{a}$ satisfies (H2). □

Lemma A.3. (Fermi-Dirac of order $1/2$) Assume that the statistics for electrons and holes is the Fermi-Dirac integral of order $1/2$ in (2.20), namely,

$$\mathcal{F}_\alpha(\eta) = F_{1/2}(\eta) = \frac{2}{\sqrt{\pi}}\int_0^\infty \frac{\xi^{1/2}}{\exp(\xi-\eta)+1}\,\mathrm{d}\xi\,, \quad \eta \in \mathbb{R}\,,\ \alpha \in \{\mathrm{n},\mathrm{p}\}. \tag{A.1}$$

Then, $\mathcal{F}_\alpha$ satisfies (H1) and (H3).

We only give a proof in the case of the Fermi-Dirac statistics of order $1/2$ since the results are essentially trivial for the other statistics functions.

Proof of Lemma A.3. Let $\alpha \in \{\mathrm{n},\mathrm{p}\}$. First, observe that $\mathcal{F}_\alpha$ is smooth and strictly increasing with limits 0 and $+\infty$, when $\eta \to -\infty$ and $\eta \to +\infty$, respectively. Then,

$$F_{1/2}(\eta)\exp(-\eta) = \frac{2}{\sqrt{\pi}}\int_0^\infty \frac{\xi^{1/2}}{\exp(\xi)+\exp(\eta)}\,\mathrm{d}\xi \le \frac{2}{\sqrt{\pi}}\int_0^\infty \xi^{1/2}\exp(-\xi)\,\mathrm{d}\xi = 1.$$

Moreover,

$$F'_{1/2}(\eta) = \frac{2}{\sqrt{\pi}}\int_0^\infty \frac{\xi^{1/2}\exp(\xi-\eta)}{(\exp(\xi-\eta)+1)^2}\,\mathrm{d}\xi \le F_{1/2}(\eta).$$

This proves (H1). Now let us focus on the behavior at infinity of $F_{1/2}$. We claim the existence of constants $c_1, c_2 > 0$ such that

$$c_1\eta^{3/2} \le F_{1/2}(\eta) \le c_2\eta^{3/2}, \quad \text{for } \eta \ge 1. \tag{A.2}$$

With (A.2) we can conclude $F_{1/2}^{-1}(s) = \mathcal{O}(s^{2/3})$ for $s \to +\infty$. Therefore, the associated entropy function behaves like $\mathcal{O}(s^{5/3})$ and (H3) readily follows. To see that (A.2) is

indeed satisfied, we consider (A.1) on the two intervals $[0,\eta]$ and $[\eta,+\infty)$, where the respective integrals are denoted by I_1, I_2. This yields $F_{1/2}(\eta) = \frac{2}{\sqrt{\pi}}(I_1 + I_2)$ with

$$I_1 = \int_0^\eta \frac{\xi^{1/2}}{\exp(\xi-\eta)+1}\,d\xi \quad \text{and} \quad I_2 = \int_0^\infty \frac{(z+\eta)^{1/2}}{\exp(z)+1}\,dz,$$

where we substitute $z = \xi - \eta$ in I_2. We bound I_1 and I_2 separately. On the one hand, since $0 \le \exp(\xi-\eta) \le 1$ for $\xi \le \eta$, we obtain

$$\frac{1}{3}\eta^{3/2} \le I_1 \le \frac{2}{3}\eta^{3/2}.$$

On the other hand, we split I_2 into an integral over $[0,\eta]$ and one over $[\eta,+\infty)$ and bound each term

$$\begin{aligned} I_2 &= \int_0^\eta \frac{(z+\eta)^{1/2}}{\exp z+1}\,dz + \int_\eta^\infty \frac{(z+\eta)^{1/2}}{\exp z+1}\,dz \\ &\le 2^{1/2}\eta^{1/2}\int_0^\eta \frac{1}{\exp z+1}\,dz + 2^{1/2}\int_\eta^\infty \frac{z^{1/2}}{\exp z+1}\,dz. \end{aligned}$$

But,

$$\int_0^\eta \frac{1}{\exp z+1}\,dz \le \int_0^\eta \exp(-z)dz \le 1$$

and

$$\int_\eta^\infty \frac{z^{1/2}}{\exp z+1}\,dz \le \int_0^\infty \frac{z^{1/2}}{\exp z}\,dz = \Gamma(3/2),$$

where Γ is the Euler's Gamma function, satisfying $\Gamma(3/2) = \frac{\sqrt{\pi}}{2}$. Hence, assuming $\eta \ge 1$, we receive for I_2

$$0 \le I_2 \le \sqrt{2}\Big(\eta^{1/2} + \frac{\sqrt{\pi}}{2}\Big) \le \sqrt{2}\eta^{3/2}\Big(1 + \frac{\sqrt{\pi}}{2}\Big).$$

With $c_1 = \frac{2}{3\sqrt{\pi}}$ and $c_2 = \frac{2}{\sqrt{\pi}}(\frac{2}{3} + \sqrt{2}(1+\frac{\sqrt{\pi}}{2}))$ the claim in (A.2) is shown. □

A.2. Proof of Lemma 3.3

Lemma 3.3. One has the following bounds on the entropy functions $\Phi'_\alpha = \mathcal{F}_\alpha^{-1}$ in (3.40) and $H_\alpha(x,y) = \Phi_\alpha(x) - \Phi_\alpha(y) - \Phi'_\alpha(y)(x-y)$ in (3.41).

(i) Let $\alpha \in \{\mathrm{n}, \mathrm{p}\}$. Further, let $\mathcal{F}_\alpha$ be a statistics function satisfying (H1) and H_α be the associated relative entropy function. Then, for any $\varepsilon > 0$ and $y_0 \geq 0$, there exists a constant $c_{y_0,\varepsilon} > 0$ such that

$$x \leq c_{y_0,\varepsilon} + \varepsilon H_\alpha(x, y), \quad \text{for all } x \geq 0,\ y \in [0, y_0].$$

(ii) Let $\mathcal{F}_\mathrm{a}$ be a statistics function satisfying (H2) and Φ_a be the associated entropy function. Then, for any $\varepsilon > 0$, there exists a constant $c_\varepsilon > 0$ such that

$$x \leq c_\varepsilon + \varepsilon \Phi_\mathrm{a}(x), \quad \text{for all } x \geq 0. \tag{A.3}$$

Proof. First, we show (i). Let $\mathcal{F}_\alpha$ with $\alpha \in \{\mathrm{n}, \mathrm{p}\}$ be a statistics function satisfying (H1) and H_α be the associated relative entropy function. Let $\varepsilon > 0$ and $y_0 \geq 0$. We note that the Legendre transform of the strictly convex function $x \mapsto \varepsilon H_\alpha(x, y)$ exists as a sum of a strictly convex and convex function. The Legendre transform reads $L(z) = \sup_{x \in \mathbb{R}} (xz - \varepsilon H_\alpha(x, y))$. For $x \geq 0$ and $y \in [0, y_0]$ one has

$$x \leq \sup_{x \in \mathbb{R}} (x - \varepsilon H_\alpha(x, y)) + \varepsilon H_\alpha(x, y),$$

where we evaluated the Legendre transform at 1. The value is exactly given by $L(1) = \bar{x} - \varepsilon H_\alpha(\bar{x}, y)$ with $\bar{x} = \mathcal{F}_\alpha\left(\frac{1}{\varepsilon} + \mathcal{F}_\alpha^{-1}(y)\right)$. In turn, one has

$$x \leq c_{y_0,\varepsilon} + \varepsilon H_\alpha(x, y), \quad \text{for all } x \geq 0,\ y \in [0, y_0],$$

for $c_{y_0,\varepsilon} := \mathcal{F}_\alpha\left(\frac{1}{\varepsilon} + \mathcal{F}_\alpha^{-1}(y_0)\right) > 0$ since $\mathcal{F}_\alpha$ is increasing.

For (ii), where $\mathcal{F}_\mathrm{a}$ is a statistics function satisfying (H2) and Φ_a is the associated non-negative entropy function, an analogous calculation will prove the estimate

$$x \leq c_\varepsilon + \varepsilon \Phi_\mathrm{a}(x), \quad \text{for all } x \geq 0,$$

with $c_\varepsilon := \mathcal{F}_\mathrm{a}\left(\frac{1}{\varepsilon}\right) > 0$, where we use now the Legendre transform of $x \mapsto \varepsilon \Phi_\mathrm{a}(x)$, given as $L(z) = \sup_{x \in \mathbb{R}} (xz - \varepsilon \Phi_\mathrm{a}(x))$. □

A.3. Proof of Lemma 3.4

Lemma 3.4. Let $\mathcal{F}_\alpha$ with $\alpha \in \{\mathrm{n}, \mathrm{p}\}$ be a statistics function satisfying (H1) and (H3). Then, for any $\varepsilon > 0$ and $y_0 \geq 0$, there exists a constant $c_{y_0,\varepsilon} \geq 0$ such that

$$\max\{\mathcal{F}_\alpha^{-1}(x), 0\} \leq c_{y_0,\varepsilon} + \varepsilon H_\alpha(x, y), \quad \text{for all } x \geq 0,\ y \in [0, y_0].$$

Proof. Let us consider $\mathcal{F}_\alpha$ with $\alpha \in \{\mathrm{n}, \mathrm{p}\}$ as a statistics function satisfying (H1) and (H3). Let $\varepsilon > 0$ and $y_0 \geq 0$. Because of (H3) there exists $x_0 \geq 0$, depending on y_0 and ε such that

$$0 \leq \mathcal{F}_\alpha^{-1}(x) \leq \varepsilon H_\alpha(x, y_0), \quad \text{for all } x \geq x_0. \tag{A.4}$$

Furthermore, the calculation $\partial_y H_\alpha(x, y) = -\Phi_\alpha''(y)(x - y) \leq 0$ reveals that $y \mapsto H_\alpha(x, y)$ is non-increasing for all $y \in [0, y_0], y \leq x$, due to the convexity of Φ_α. This eventually implies that (A.4) does not only hold for $y = y_0$, but also for $y \in [0, y_0]$ with $y_0 \leq x$. Hence,

$$0 \leq \mathcal{F}_\alpha^{-1}(x) \leq \varepsilon H_\alpha(x, y), \quad \text{for all } y \in [0, y_0],\ x \geq \max\{x_0, y_0\} =: \bar{x}.$$

This proves the claim with $c_{y_0,\varepsilon} = 0$ in case of $x \geq \bar{x}$. For $0 \leq x \leq \bar{x}$ we have

$$\mathcal{F}_\alpha^{-1}(x) \leq \mathcal{F}_\alpha^{-1}(\bar{x}),$$

since $\mathcal{F}_\alpha^{-1}$ is monotonously increasing. Due to the positivity of $\varepsilon H_\alpha(x, y)$, the claim directly follows with $c_{y_0,\varepsilon} = \mathcal{F}_\alpha^{-1}(\bar{x})$. Hence, in total, we set $c_{y_0,\varepsilon} := \min\{0, \mathcal{F}_\alpha^{-1}(\bar{x})\}$, which ends the proof. □

A.4. Proof of Grönwall's lemma

Lemma 3.8. (Grönwall's lemma) Let $t_F \in \mathbb{R}_{\geq 0}$ and suppose that $u, g, a : [0, t_F] \to \mathbb{R}$ are sufficiently smooth functions such that

$$u'(t) + g(t) \leq a(t)u(t), \quad \text{for } t \in [0, t_F], \tag{A.5}$$

where a, g are non-negative on $[0, t_F]$. Then,

$$u(t) + \int_0^t g(s)\, ds \leq u(0) \exp\left(\int_0^t a(s)\, ds\right), \quad \text{for } t \in [0, t_F]. \tag{A.6}$$

Proof. Additionally, let $h : [0, t_F] \to \mathbb{R}$ be a sufficiently smooth function. We can establish our claim directly by demonstrating that if

$$h'(t) \leq a(t)h(t), \quad \text{for } t \in [0, t_F], \tag{A.7a}$$

then

$$h(t) \leq h(0) \exp\left(\int_0^t a(s)\, ds\right), \quad \text{for } t \in [0, t_F]. \tag{A.7b}$$

To see that our original claim (A.6) follows from (A.7), we define $h(t) = u(t) + \int_0^t g(s)\,ds$. Due to the assumption (A.5), we have for $t \in [0, t_F]$

$$h'(t) = u'(t) + g(t) \leq a(t)u(t) \leq a(t)h(t) + a(t)\int_0^t g(s)\,ds \leq a(t)h(t),$$

since both functions, a and g, are non-negative. This means that h satisfies (A.7a). Thus, from (A.7b), it follows for $t \in [0, t_F]$

$$u(t) + \int_0^t g(s)\,ds = h(t) \leq h(0)\exp\left(\int_0^t a(s)\,ds\right) = u(0)\exp\left(\int_0^t a(s)\,ds\right),$$

which proves the claim (A.6). To conclude the proof, we demonstrate that (A.7a) indeed implies (A.7b). We define $\tilde{h}(r) = \exp(-\int_0^r a(s)\,ds)h(r)$, for $r \in [0, t]$. From (A.7a) the non-negativity of $\tilde{h}'$ follows, i.e.,

$$\tilde{h}'(r) = \exp\left(-\int_0^r a(s)\,ds\right)(h'(r) - a(r)h(r)) \leq 0, \quad \text{for } r \in [0, t].$$

Integrating $\tilde{h}'$ from 0 to t gives us $\tilde{h}(t) - \tilde{h}(0) \leq 0$, where

$$\tilde{h}(t) - \tilde{h}(0) = \exp\left(-\int_0^t a(s)\,ds\right)h(t) - h(0), \quad \text{for } t \in [0, t_F],$$

which shows (A.7b) after rearranging terms and multiplication with $\exp(\int_0^t a(s)\,ds)$. □

A.5. Proof of a discrete integration by parts

Lemma A.7. (Discrete integration by parts) Let $(\mathcal{T}, \mathcal{E}, \{\mathbf{x}_K\}_{K\in\mathcal{T}})$ be an admissible mesh and the finite difference operator $D_{K,\sigma}$ be given by (4.5).

(i) Let $\boldsymbol{\psi}^m = (\psi_K^m)_{K\in\mathcal{T}}$ be the approximation of the electric potential ψ at time t^m and $\boldsymbol{\psi}^D = (\psi_K^D)_{K\in\mathcal{T}}$ be the approximation of the boundary data $\psi^D \in W^{1,\infty}(\boldsymbol{\Omega})$. Similarly, we define the approximation of some function u as $\boldsymbol{u} = (u_K)_{K\in\mathcal{T}}$. Then,

$$\sum_{\sigma\in\mathcal{E}} D_{K,\sigma}\boldsymbol{u}\, D_{K,\sigma}(\boldsymbol{\psi}^m - \boldsymbol{\psi}^D) = -\sum_{K\in\mathcal{T}}\sum_{\sigma\in\mathcal{E}_K} D_{K,\sigma}\boldsymbol{u}(\psi_K^m - \psi_K^D).$$

(ii) Let $\alpha \in \{\mathrm{n}, \mathrm{p}\}$ and the flux approximation $J_{\alpha,K,\sigma}^m$ be given by (DF). Furthermore, let $\boldsymbol{\varphi}_\alpha^m = (\varphi_{\alpha,K}^m)_{K\in\mathcal{T}}$ and $\boldsymbol{\varphi}^D = (\varphi_K^D)_{K\in\mathcal{T}}$ be the approximations of the electron and hole quasi Fermi potentials at time t^m and the boundary data $\varphi^D \in W^{1,\infty}(\boldsymbol{\Omega})$, respectively. Then,

$$\sum_{\sigma\in\mathcal{E}} J_{\alpha,K,\sigma}^m D_{K,\sigma}(\boldsymbol{\varphi}_\alpha^m - \boldsymbol{\varphi}^D) = -\sum_{K\in\mathcal{T}}\sum_{\sigma\in\mathcal{E}_K} J_{\alpha,K,\sigma}^m(\varphi_{\alpha,K}^m - \varphi_K^D), \quad \text{for } \alpha \in \{\mathrm{n}, \mathrm{p}\}.$$

(iii) Let $\boldsymbol{\varphi}_{\mathrm{a}}^m = (\varphi_{\mathrm{a},K}^m)_{K\in\mathcal{T}_{\mathrm{a}}}$ be the approximation of the vacancy quasi Fermi potential φ_{a} at time t^m and $J_{\mathrm{a},K,\sigma}^m$ be the corresponding flux approximation (DF). Furthermore, let $\boldsymbol{\psi}^D = (\psi_K^D)_{K\in\mathcal{T}}$ be the approximation of $\psi^D \in W^{1,\infty}(\boldsymbol{\Omega})$. Then,

$$\sum_{\sigma\in\mathcal{E}_{\mathrm{a}}} J_{\mathrm{a},K,\sigma}^m D_{K,\sigma}(\boldsymbol{\varphi}_{\mathrm{a}}^m - \boldsymbol{\psi}^D) = -\sum_{K\in\mathcal{T}_{\mathrm{a}}}\sum_{\sigma\in\mathcal{E}_K} J_{\mathrm{a},K,\sigma}^m(\varphi_{\mathrm{a},K}^m - \psi_K^D).$$

In case of the PSC model, we have $\mathcal{T}_{\mathrm{a}} = \mathcal{T}_{\mathrm{intr}}$ and $\mathcal{E}_{\mathrm{a}} = \mathcal{E}_{\mathrm{intr}}^{\mathrm{int}}$, whereas in case of the TMDC memristor model, we have $\mathcal{T}_{\mathrm{a}} = \mathcal{T}$ and $\mathcal{E}_{\mathrm{a}} = \mathcal{E}$.

Proof. All proofs rely on the same idea: We reorder the sums by using the local conservativity of the finite difference operator $D_{K,\sigma}$ in (4.5) and the flux approximation $J_{\alpha,K,\sigma}^m$ in (DF) for $\alpha \in \{\mathrm{n},\mathrm{p},\mathrm{a}\}$, i.e., for $\sigma = K|L$ it holds

$$0 = J_{\alpha,K,\sigma}^m + J_{\alpha,L,\sigma}^m = D_{K,\sigma}\boldsymbol{u} + D_{L,\sigma}\boldsymbol{u}.$$

Therefore, it suffices to prove (i). We begin by splitting the sum on the left-hand side

$$\begin{aligned}\sum_{\sigma\in\mathcal{E}} D_{K,\sigma}\boldsymbol{u}\, D_{K,\sigma}(\boldsymbol{\psi}^m - \boldsymbol{\psi}^D) &= \sum_{\sigma\in\mathcal{E}^{\mathrm{int}}} D_{K,\sigma}\boldsymbol{u}\, D_{K,\sigma}(\boldsymbol{\psi}^m - \boldsymbol{\psi}^D)\\ &\quad + \sum_{\sigma\in\mathcal{E}^D} D_{K,\sigma}\boldsymbol{u}\, D_{K,\sigma}(\boldsymbol{\psi}^m - \boldsymbol{\psi}^D)\\ &\quad + \sum_{\sigma\in\mathcal{E}^N} D_{K,\sigma}\boldsymbol{u}\, D_{K,\sigma}(\boldsymbol{\psi}^m - \boldsymbol{\psi}^D) =: S_1 + S_2 + S_3,\end{aligned}$$

and use the definition of the finite difference operator (4.5) to rewrite S_1 for $\sigma = K|L$

$$\begin{aligned}S_1 &= \sum_{\sigma\in\mathcal{E}^{\mathrm{int}}} D_{K,\sigma}\boldsymbol{u}\, D_{K,\sigma}(\boldsymbol{\psi}^m - \boldsymbol{\psi}^D) = \sum_{\sigma\in\mathcal{E}^{\mathrm{int}}} D_{K,\sigma}\boldsymbol{u}\left(\psi_L^m - \psi_K^m - \psi_L^D + \psi_K^D\right)\\ &= \sum_{\sigma\in\mathcal{E}^{\mathrm{int}}}\Big(D_{K,\sigma}\boldsymbol{u}\left(\psi_L^m - \psi_L^D\right) - D_{K,\sigma}\boldsymbol{u}\left(\psi_K^m - \psi_K^D\right)\Big)\\ &= -\sum_{\sigma\in\mathcal{E}^{\mathrm{int}}}\Big(D_{L,\sigma}\boldsymbol{u}\left(\psi_L^m - \psi_L^D\right) + D_{K,\sigma}\boldsymbol{u}\left(\psi_K^m - \psi_K^D\right)\Big),\end{aligned}$$

where $D_{K,\sigma}\boldsymbol{u} = -D_{L,\sigma}\boldsymbol{u}$ since $D_{K,\sigma}$ is locally conservative. It is important to note that we count edges twice when summing over cells. Therefore, we obtain

$$S_1 = -\sum_{K\in\mathcal{T}}\sum_{\sigma\in\mathcal{E}_K\cap\mathcal{E}^{\mathrm{int}}} D_{K,\sigma}\boldsymbol{u}\left(\psi_K^m - \psi_K^D\right),$$

which proves the claim for all interior faces. Furthermore, we can rewrite S_2 such that

$$\begin{aligned}S_2 &= \sum_{\sigma\in\mathcal{E}^D} D_{K,\sigma}\boldsymbol{u}\, D_{K,\sigma}(\boldsymbol{\psi}^m - \boldsymbol{\psi}^D) = \sum_{\sigma\in\mathcal{E}^D} D_{K,\sigma}\boldsymbol{u}\,\left((\psi_\sigma^D - \psi_K^m) - (\psi_\sigma^D - \psi_K^D)\right)\\ &= -\sum_{K\in\mathcal{T}}\sum_{\sigma\in\mathcal{E}_K\cap\mathcal{E}^D} D_{K,\sigma}\boldsymbol{u}\left(\psi_K^m - \psi_K^D\right),\end{aligned}$$

which proves the claim for all faces located at the Dirichlet boundary. Lastly, due to the definition of the finite difference operator $D_{K,\sigma}$ for $\sigma \in \mathcal{E}^N$, we have

$$0 = \sum_{\sigma \in \mathcal{E}^N} D_{K,\sigma}\boldsymbol{u}\, D_{K,\sigma}(\boldsymbol{\psi}^m - \boldsymbol{\psi}^D) = -\sum_{K \in \mathcal{T}} \sum_{\sigma \in \mathcal{E}_K \cap \mathcal{E}^N} D_{K,\sigma}\boldsymbol{u}\left(\psi_K^m - \psi_K^D\right).$$

Thus, we proved (i) for all $\sigma \in \mathcal{E}$. □

A.6. Auxiliary result needed to establish Lemma 4.12

In this section, we establish a technical result which is crucial for the proof of bounds satisfied by the quasi Fermi potentials of electrons and holes, see Lemma 4.12.

Lemma A.8. Let $\alpha \in \{\mathrm{n}, \mathrm{p}\}$. Assume that the statistics function $\mathcal{F}_\alpha$ satisfies the hypothesis (H1). Let us define $\mathcal{K}_\alpha : (x, a) \in \mathbb{R}^2 \mapsto \mathcal{K}_\alpha(x, a) \in \mathbb{R}$ with

$$\mathcal{K}_\alpha(x, a) = \log(\mathcal{F}_\alpha(x - a)) - x,$$

and $\mathcal{D}_\alpha : (x, y, a, b) \in \mathbb{R}^4 \mapsto \mathcal{D}_\alpha(x, y, a, b) \in \mathbb{R}$ with

$$\mathcal{D}_\alpha = (x - y)\Big[B\Big(\mathcal{K}_\alpha(x, a) - \mathcal{K}_\alpha(y, b)\Big)\mathcal{F}_\alpha(x - a) - B\Big(\mathcal{K}_\alpha(y, b) - \mathcal{K}_\alpha(x, a)\Big)\mathcal{F}_\alpha(y - b)\Big].$$

Then, for all $\overline{\Phi}, \overline{\Psi} \in \mathbb{R}$, the function $\Upsilon_{\overline{\Phi},\overline{\Psi}} : \mathbb{R} \to \mathbb{R}$ defined by

$$\Upsilon_{\overline{\Phi},\overline{\Psi}}(x) = \inf\left\{\mathcal{D}_\alpha(x, y, a, b);\ -\overline{\Phi} \le y \le \overline{\Phi}, -\overline{\Psi} \le a, b \le \overline{\Psi}\right\}$$

verifies

$$\lim_{x \to -\infty} \Upsilon_{\overline{\Phi},\overline{\Psi}}(x) = +\infty \quad \text{and} \quad \lim_{x \to +\infty} \Upsilon_{\overline{\Phi},\overline{\Psi}}(x) = +\infty.$$

Proof. Let $\overline{\Phi}$ and $\overline{\Psi}$ be given. First, we remark that the function $\mathcal{K}_\alpha$ is non-increasing with respect to both of its variables a and x, where $x \mapsto \mathcal{K}_\alpha(x, a)$ is non-increasing due to (H1). We note that the Bernoulli function B is also non-increasing on $\mathbb{R}$. The regularity of the functions $\mathcal{K}_\alpha$ and $\mathcal{F}_\alpha$ ensure that there exist positive constants $\lambda, \underline{\mu}, \overline{\mu}$ such that for all $-\overline{\Phi} \le y \le \overline{\Phi}$, $-\overline{\Psi} \le b \le \overline{\Psi}$

$$-\lambda \le \mathcal{K}_\alpha(y, b) \le \lambda \quad \text{and} \quad \underline{\mu} \le \mathcal{F}_\alpha(y - b) \le \overline{\mu}.$$

This implies the following inequalities, for $x \in \mathbb{R}$, $y \in [-\overline{\Phi}, \overline{\Phi}]$ and $a, b \in [-\overline{\Psi}, \overline{\Psi}]$,

$$\begin{aligned} B\Big(\mathcal{K}_\alpha(x, -\overline{\Psi}) + \lambda\Big) \le\ & B\Big(\mathcal{K}_\alpha(x, a) - \mathcal{K}_\alpha(y, b)\Big) \le B\Big(\mathcal{K}_\alpha(x, \overline{\Psi}) - \lambda\Big), \\ -B\Big(-\lambda - \mathcal{K}_\alpha(x, -\overline{\Psi})\Big) \le\ & -B\Big(\mathcal{K}_\alpha(y, b) - \mathcal{K}_\alpha(x, a)\Big) \le -B\Big(\lambda - \mathcal{K}_\alpha(x, \overline{\Psi})\Big), \end{aligned}$$

yielding the following bounds on $\mathcal{D}_\alpha(x,y,a,b)/(x-y)$

$$\begin{aligned}\frac{\mathcal{D}_\alpha(x,y,a,b)}{x-y} &\geq B\Big(\mathcal{K}_\alpha(x,-\overline{\Psi})+\lambda\Big)\mathcal{F}_\alpha(x-\overline{\Psi}) - B\Big(-\lambda-\mathcal{K}_\alpha(x,-\overline{\Psi})\Big)\overline{\mu},\\ \frac{\mathcal{D}_\alpha(x,y,a,b)}{x-y} &\leq B\Big(\mathcal{K}_\alpha(x,\overline{\Psi})-\lambda\Big)\mathcal{F}_\alpha(x+\overline{\Psi}) - B\Big(\lambda-\mathcal{K}_\alpha(x,\overline{\Psi})\Big)\underline{\mu}.\end{aligned} \tag{A.8}$$

First, we consider the case that $x \leq -\overline{\Phi}$. We can deduce from (A.8) that

$$\frac{\mathcal{D}_\alpha(x,y,a,b)}{x-y} \leq B\Big(\mathcal{K}_\alpha(-\overline{\Phi},\overline{\Psi})-\lambda\Big)\mathcal{F}_\alpha(x+\overline{\Psi}) - B\Big(\lambda-\mathcal{K}_\alpha(-\overline{\Phi},\overline{\Psi})\Big)\underline{\mu}.$$

But, due to (H1), $\lim_{x\to-\infty}\mathcal{F}_\alpha(x+\overline{\Psi})=0$, which implies that, for $-x$ large enough, the right-hand side of the last inequality is negative. Thus, for such x with $x \leq y$ we have

$$\mathcal{D}_\alpha(x,y,a,b) \geq (x-y)\Big[B\Big(\mathcal{K}_\alpha(-\overline{\Phi},\overline{\Psi})-\lambda\Big)\mathcal{F}_\alpha(x+\overline{\Psi}) - B\Big(\lambda-\mathcal{K}_\alpha(-\overline{\Phi},\overline{\Psi})\Big)\underline{\mu}\Big],$$

and, by taking the infimum in $y \in [-\overline{\Phi},\overline{\Phi}]$, we obtain

$$\Upsilon_{\overline{\Phi},\overline{\Psi}}(x) \geq (x+\overline{\Phi})\Big[B\Big(\mathcal{K}_\alpha(-\overline{\Phi},\overline{\Psi})-\lambda\Big)\mathcal{F}_\alpha(x+\overline{\Psi}) - B\Big(\lambda-\mathcal{K}_\alpha(-\overline{\Phi},\overline{\Psi})\Big)\underline{\mu}\Big].$$

As the first product in the right-hand side tends to 0, while the second one tends to $+\infty$, we deduce that

$$\lim_{x\to-\infty}\Upsilon_{\overline{\Phi},\overline{\Psi}}(x) = +\infty.$$

We may now consider that $x \geq \overline{\Phi}$. From (A.8), we deduce that

$$\frac{\mathcal{D}_\alpha(x,y,a,b)}{x-y} \geq \Big(B\big(\mathcal{K}_\alpha(\overline{\Phi},-\overline{\Psi})+\lambda\big)\mathcal{F}_\alpha(x-\overline{\Psi}) - B\big(-\lambda-\mathcal{K}_\alpha(\overline{\Phi},-\overline{\Psi})\big)\overline{\mu}\Big).$$

For x sufficiently large, the right-hand side of the last inequality is positive and

$$\Upsilon_{\overline{\Phi},\overline{\Psi}}(x) \geq (x-\overline{\Phi})\Big(B\big(\mathcal{K}_\alpha(\overline{\Phi},-\overline{\Psi})+\lambda\big)\mathcal{F}_\alpha(x-\overline{\Psi}) - B\big(-\lambda-\mathcal{K}_\alpha(\overline{\Phi},-\overline{\Psi})\big)\overline{\mu}\Big).$$

Therefore, we get

$$\lim_{x\to+\infty}\Upsilon_{\overline{\Phi},\overline{\Psi}}(x) = +\infty.$$

□

A.7. Auxiliary result needed to establish the existence of discrete solutions

In Lemma A.9, we relate the scalar product between a continuous vector field $\mathbf{P}_m(\mathbf{X})$ and the vector of quasi Fermi potentials $\mathbf{X}$, as defined in (4.29), with the discrete entropy-dissipation inequalities (see Theorem 4.5 and Theorem 4.6). This auxiliary result is crucial in proving the existence of discrete solutions, as formulated in Theorem 4.15 and Theorem 4.16.

Lemma A.9. Let $\mathbf{P}_m : \mathbb{R}^{\theta_\mathbf{X}} \to \mathbb{R}^{\theta_\mathbf{X}}$ with $\theta_\mathbf{X} = 2\mathrm{Card}(\mathcal{T}) + \mathrm{Card}(\mathcal{T}_{\mathrm{intr}})$ (*resp.* $\theta_\mathbf{X} = 3\mathrm{Card}(\mathcal{T})$) be a continuous vector field, where the components are related to the continuity equations (DPa), (DPb), and (DPc) (*resp.* (DMa), (DMb), and (DMc)) as follows. For the electron and hole components, we put every term of the equations (DPa) and (DPb) (*resp.* (DMa) and (DMb)) on the left-hand side and rescale by a factor $\delta\tau^m/\nu$ (*resp.* $\delta_\mathrm{n}\tau^m/\nu$ and $\delta_\mathrm{n}\delta_\mathrm{p}\tau^m/\nu$). The vacancy-related components are given by (DPc) (*resp.* (DMc)), rescaled by τ^m. Furthermore, let $\mathbf{X}$ denote the vector containing the unknown quasi Fermi potentials at time step m as defined in (4.29). Then, the following inequality holds for any $\varepsilon > 0$

$$(1-\varepsilon\tau^m)\mathbb{E}_\mathcal{T}(\mathbf{X}) - \mathbb{E}_\mathcal{T}(\mathbf{X}^{m-1}) + \tau^m\mathbb{D}_\mathcal{T}(\mathbf{X}) - \tau^m c_{\varepsilon,\mathbf{\Omega},\xi} \leq \mathbf{P}_m(\mathbf{X})\cdot\mathbf{X}, \tag{A.9}$$

where $c_{\varepsilon,\mathbf{\Omega},\xi}$ corresponds to the constant from the entropy-dissipation inequality in Theorem 4.5 (*resp.* Theorem 4.6) and $\mathbf{X}^{m-1}$ denotes the solution at time step $m-1$.

Proof. In the following, we will only prove the claim for the PSC charge transport model, as the proof for the TMDC-based memristor model is analogous. The claim was already established within the proof of Theorem 4.5, where we defined the following remainder terms

$$S_1 = \frac{\delta}{2\nu}\sum_{\alpha\in\{\mathrm{n,p}\}}\sum_{\sigma\in\mathcal{E}}\frac{m_\sigma}{d_\sigma}\overline{n}_{\alpha,\sigma}\left(D_\sigma\boldsymbol{\varphi}^D\right)^2, \quad S_2 = \frac{z_\mathrm{a}^2}{2}\sum_{\sigma\in\mathcal{E}_{\mathrm{intr}}^{\mathrm{int}}}\tau_\sigma\overline{n}_{\mathrm{a},\sigma}\left(D_\sigma\boldsymbol{\psi}^D\right)^2,$$

$$S_3 = \frac{\delta\gamma}{\nu}\sum_{K\in\mathcal{T}} m_K G_K\left(\varphi_{\mathrm{p},K}-\varphi_{\mathrm{n},K}\right).$$

With this, we can bound the dissipation rate defined in (4.14) as follows

$$\begin{aligned}\mathbb{D}_\mathcal{T}(\mathbf{X}) - S_1 - S_2 - S_3 \leq{}& \frac{\delta}{\nu}\sum_{\alpha\in\{\mathrm{n,p}\}}\sum_{K\in\mathcal{T}}\sum_{\sigma\in\mathcal{E}_K} J_{\alpha,K,\sigma}(\varphi_{\alpha,K}-\varphi_K^D)\\ &+\frac{\delta}{\nu}\sum_{K\in\mathcal{T}} m_K\Big(R_K-\gamma G_K\Big)(\varphi_{\mathrm{p},K}-\varphi_{\mathrm{n},K})\\ &+\sum_{K\in\mathcal{T}_{\mathrm{intr}}}\sum_{\sigma\in\mathcal{E}_K} J_{\mathrm{a},K,\sigma}(\varphi_{\mathrm{a},K}-\psi_K^D).\end{aligned} \tag{A.10}$$

The recombination and photogeneration term of the right-hand side of (A.10) is equal to the difference of the recombination-related term of the dissipation $\mathbb{D}_{\mathcal{T}}(\mathbf{X})$, i.e., $\delta/\nu \sum_{K\in\mathcal{T}} m_K R_K \left(\varphi_{\mathrm{p},K}^m - \varphi_{\mathrm{n},K}^m\right)$, and S_3. The remaining terms can be easily estimated by tracing back the reformulations within the proof of the entropy-dissipation inequality. For example, for the vacancies, we define $\mathbb{D}_{\mathcal{T},\mathrm{a}}(\mathbf{X}) := z_\mathrm{a}^2/2 \sum_{\sigma\in\mathcal{E}_{\mathrm{intr}}^{\mathrm{int}}} \tau_\sigma \overline{n}_{\mathrm{a},\sigma} (D_\sigma \boldsymbol{\varphi}_\mathrm{a})^2$ (see (4.31)). We can show the following inequality by using $(a^2-b^2)/2 \le a(a-b)$, the definition of the discrete flux (4.11) dependent on $\overline{n}_{\alpha,\sigma}^m$, and a discrete integration by parts (see Lemma A.7(iii))

$$\begin{aligned}
\mathbb{D}_{\mathcal{T},\mathrm{a}}(\mathbf{X}) - S_2 &= \frac{z_\mathrm{a}^2}{2} \sum_{\sigma\in\mathcal{E}_{\mathrm{intr}}^{\mathrm{int}}} \tau_\sigma \overline{n}_{\mathrm{a},\sigma} (D_\sigma \boldsymbol{\varphi}_\mathrm{a})^2 - \frac{z_\mathrm{a}^2}{2} \sum_{\sigma\in\mathcal{E}_{\mathrm{intr}}^{\mathrm{int}}} \tau_\sigma \overline{n}_{\mathrm{a},\sigma} \left(D_\sigma \boldsymbol{\psi}^D\right)^2 \\
&\le z_\mathrm{a}^2 \sum_{\sigma\in\mathcal{E}_{\mathrm{intr}}^{\mathrm{int}}} \tau_\sigma \overline{n}_{\mathrm{a},\sigma}\, D_{K,\sigma}\boldsymbol{\varphi}_\mathrm{a} D_{K,\sigma} \left(\boldsymbol{\varphi}_\mathrm{a} - \boldsymbol{\psi}^D\right) \\
&\le - \sum_{\sigma\in\mathcal{E}_{\mathrm{intr}}^{\mathrm{int}}} J_{\mathrm{a},K,\sigma} D_{K,\sigma} \left(\boldsymbol{\varphi}_\mathrm{a} - \boldsymbol{\psi}^D\right) \le \sum_{K\in\mathcal{T}_{\mathrm{intr}}} \sum_{\sigma\in\mathcal{E}_K} J_{\mathrm{a},K,\sigma} \left(\varphi_{\mathrm{a},K} - \psi_K^D\right).
\end{aligned}$$

A similar calculation can be applied to relate the remaining terms in (A.10). Moreover, within the proof of Theorem 4.5, we established (see (4.18) up to a division by τ^m)

$$\begin{aligned}
\frac{\mathbb{E}_{\mathcal{T}}(\mathbf{X}) - \mathbb{E}_{\mathcal{T}}(\mathbf{X}^{m-1})}{\tau^m} &\le \delta \sum_{\alpha\in\{\mathrm{n},\mathrm{p}\}} \sum_{K\in\mathcal{T}} m_K z_\alpha \left(\varphi_{\alpha,K} - \varphi_K^D\right) \frac{n_{\alpha,K} - n_{\alpha,K}^{m-1}}{\tau^m} \\
&\quad + \sum_{K\in\mathcal{T}_{\mathrm{intr}}} m_K z_\mathrm{a} \left(\varphi_{\mathrm{a},K} - \psi_K^D\right) \frac{n_{\mathrm{a},K} - n_{\mathrm{a},K}^{m-1}}{\tau^m}.
\end{aligned} \tag{A.11}$$

We observe that the right-hand sides of (A.10) and (A.11) are equal to scaled scalar product, given by $(\mathbf{P}_m(\mathbf{X})\cdot\mathbf{X})/\tau^m$,

$$\begin{aligned}
\frac{\mathbf{P}_m(\mathbf{X})\cdot\mathbf{X}}{\tau^m} &= \sum_{\alpha\in\{\mathrm{n},\mathrm{p}\}} \sum_{K\in\mathcal{T}} (\varphi_{\alpha,K} - \varphi_K^D) \Big(\delta m_K z_\alpha \frac{n_{\alpha,K} - n_{\alpha,K}^{m-1}}{\tau^m} + \frac{\delta}{\nu} \sum_{\sigma\in\mathcal{E}_K} J_{\alpha,K,\sigma} \Big) \\
&\quad + \frac{\delta}{\nu} \sum_{K\in\mathcal{T}} m_K \Big(R_K(\varphi_{\mathrm{p},K} - \varphi_{\mathrm{n},K}) - \gamma G_K(\varphi_{\mathrm{p},K} - \varphi_{\mathrm{n},K}) \Big) \\
&\quad + \sum_{K\in\mathcal{T}_{\mathrm{intr}}} (\varphi_{\mathrm{a},K} - \psi_K^D) \Big(m_K z_\mathrm{a} \frac{n_{\mathrm{a},K} - n_{\mathrm{a},K}^{m-1}}{\tau^m} + \sum_{\sigma\in\mathcal{E}_K} J_{\mathrm{a},K,\sigma} \Big).
\end{aligned} \tag{A.12}$$

Here, we used $z_\mathrm{n} = -1$ and $z_\mathrm{p} = 1$ and defined $R_K := R(n_{\mathrm{n},K}, n_{\mathrm{p},K})$. Thus, by combining (A.10) and (A.11) we can deduce the estimate

$$\frac{\mathbb{E}_{\mathcal{T}}(\mathbf{X}) - \mathbb{E}_{\mathcal{T}}(\mathbf{X}^{m-1})}{\tau^m} + \mathbb{D}_{\mathcal{T}}(\mathbf{X}) - (S_1 + S_2 + S_3) \le \frac{\mathbf{P}_m(\mathbf{X})\cdot\mathbf{X}}{\tau^m}. \tag{A.13}$$

Moreover, we verified within the proof of Theorem 4.5 (see (4.23))

$$S_1 + S_2 + S_3 \leq \varepsilon \mathbb{E}_{\mathcal{T}}(\mathbf{X}) + c_{\varepsilon,\mathbf{\Omega},\xi}. \tag{A.14}$$

Substituting now (A.14) into (A.13) shows

$$\frac{\mathbb{E}_{\mathcal{T}}(\mathbf{X}) - \mathbb{E}_{\mathcal{T}}(\mathbf{X}^{m-1})}{\tau^m} + \mathbb{D}_{\mathcal{T}}(\mathbf{X}) - (\varepsilon \mathbb{E}_{\mathcal{T}}(\mathbf{X}) + c_{\varepsilon,\mathbf{\Omega},\xi}) \leq \frac{\mathbf{P}_m(\mathbf{X}) \cdot \mathbf{X}}{\tau^m}.$$

Finally, multiplying the last inequality by τ^m and rearranging terms completes the proof.

□

B. Summary of model parameters

All model parameters used for the simulations in Chapter 5 are summarized in this chapter. Appendix B.1 contains the parameters for the perovskite solar cell application and Appendix B.2 for the TMDC-based memristive devices.

B.1. Perovskite solar cells

We use Table B.1 in Section 5.1.1.2 to simulate a three-layer PSC device domain with TiO_2 as electron transport layer material and spiro-OMeTAD as material for the hole transport layer. Apart from $N_a = 1.0 \times 10^{27}$ m^{-3} and $E_a = -4.45$ eV, the parameter values are from [44, 48].

Physical quantity	Symbol	Value			Unit
		TiO_2	MAPI	spiro-OMeTAD	
Layer thickness		100	400	200	nm
Relative permittivity	ε_r	10	24.1	3	
Conduction band-edge energy	E_n	-4.0	-3.7	-3.4	eV
Valence band-edge energy	E_p	-5.8	-5.4	-5.1	eV
Vacancy energy level	E_a	–	-4.45	–	eV
Eff. conduction band DoS	N_n	5×10^{25}	8.1×10^{24}	5×10^{25}	m^{-3}
Eff. valence band DoS	N_p	5×10^{25}	5.8×10^{24}	5×10^{25}	m^{-3}
Max. vacancy density	N_a	–	1.0×10^{27}	–	m^{-3}
Doping density	C_n	1.0×10^{24}	0.0	0.0	m^{-3}
Doping density	C_p	0.0	0.0	1.0×10^{24}	m^{-3}
Average vacancy density	C_a	–	1.6×10^{25}	–	m^{-3}
Electron mobility	μ_n	3.89×10^{-4}	6.62×10^{-3}	3.89×10^{-5}	m^2/(Vs)
Hole mobility	μ_p	3.89×10^{-4}	6.62×10^{-3}	3.89×10^{-5}	m^2/(Vs)
Vacancy mobility	μ_a	–	3.39×10^{-16}	–	m^2/(Vs)
Radiative recombination coeff.	$r_{0,\mathrm{rad}}$	6.8×10^{-17}	3.6×10^{-18}	6.3×10^{-17}	m^3/s
SRH lifetime, electrons	τ_n	1.0×10^{100}	3.0×10^{-9}	1.0×10^{100}	s
SRH lifetime, holes	τ_p	1.0×10^{100}	3.0×10^{-7}	1.0×10^{100}	s
SRH trap energy	E_τ	-5.0	-4.55	-4.1	eV
Inc. photon flux	F_{ph}	0.0	1.4×10^{21}	0.0	1/(m^{2}s)
Absorption coefficient	α_g	0.0	1.3×10^7	0.0	1/m

Table B.1.: Parameter values from [44, 48] for the simulation of a three-layer perovskite solar cell at a temperature $T = 298$ K with TiO_2 as electron transport layer material and spiro-OMeTAD as hole transport layer material.

Furthermore, the simulations in Section 5.2 are based on Table B.2, where the parameters are from [28]. In this setup we use PCBM as electron transport layer material and PEDOT:PSS as hole transport layer material.

Physical quantity	Symbol	Value			Unit
		PCBM	MAPI	PEDOT:PSS	
Layer thickness		85	300	30	nm
Relative permittivity	ε_r	3	23.0	4	
Conduction band-edge energy	E_n	-3.8	-3.8	-3.0	eV
Valence band-edge energy	E_p	-6.2	-5.4	-5.1	eV
Eff. conduction band DoS	N_n	1×10^{25}	1.0×10^{25}	1×10^{26}	m^{-3}
Eff. valence band DoS	N_p	1×10^{25}	1×10^{25}	1×10^{26}	m^{-3}
Doping density	C_n	2.09×10^{24}	0.0	0.0	m^{-3}
Doping density	C_p	0.0	0.0	2.09×10^{24}	m^{-3}
Average vacancy density	C_a	–	1.0×10^{24}	–	m^{-3}
Electron mobility	μ_n	1.0×10^{-7}	2.0×10^{-3}	1.0×10^{-5}	$\mathrm{m}^2/(\mathrm{Vs})$
Hole mobility	μ_p	1.0×10^{-7}	2.0×10^{-3}	1.0×10^{-5}	$\mathrm{m}^2/(\mathrm{Vs})$
Vacancy mobility	μ_a	–	1.0×10^{-14}	–	$\mathrm{m}^2/(\mathrm{Vs})$
Radiative recombination coeff.	$r_{0,\mathrm{rad}}$	6.8×10^{-17}	3.6×10^{-18}	3.6×10^{-18}	m^3/s
SRH lifetime, electrons	τ_n	1.0×10^{100}	1.0×10^{-7}	1.0×10^{100}	s
SRH lifetime, holes	τ_p	1.0×10^{100}	1.0×10^{-7}	1.0×10^{100}	s
SRH trap energy	E_τ	-5.0	-4.6	-4.05	eV

Table B.2.: Parameter values from [28] for the simulation of a three-layer perovskite solar cell at a temperature $T = 300$ K with PCBM as electron transport layer material and PEDOT:PSS as hole transport layer material.

We note that with a lattice constant of $a = 6.28 \times 10^{-10}$ m (see [65]), we have an ideal halide density of $\overline{N}_\mathrm{a} = 1.21 \times 10^{28}\ \mathrm{m}^{-3}$. In the simulations in Section 5.2, when $N_\mathrm{a} = 1.0 \times 10^{26}\ \mathrm{m}^{-3}$ ($\epsilon = 0.01$), we choose $E_\mathrm{a} = -4.66$ eV and for $N_\mathrm{a} = 1.1 \times 10^{24}\ \mathrm{m}^{-3}$ ($\epsilon = 0.9$), we set $E_\mathrm{a} = -4.16$ eV. For all other choices of the tuple $(N_\mathrm{a}, E_\mathrm{a})$ we directly refer to the simulation files in [DA1]. In both parameter sets in Table B.1 and Table B.2, we set the doping to $C = C_\mathrm{n}$ in the electron transport layer, $C = -C_\mathrm{a}$ in the intrinsic perovskite layer and $C = -C_\mathrm{p}$ in the hole transport layer.

B.2. TMDC-based memristive devices

In the following, we have the material-dependent parameters collected from literature summarized in Table B.3. The sample specific parameters for the simulations in Section 5.1.2, Section 5.3.1 and Section 5.3.2 are summarized in Table B.4.

We calculate the valence band-edge energy with the relation $E_\mathrm{p} = E_\mathrm{n} - E_\mathrm{g}$ and the effective conduction and valence band densities of states $N_\mathrm{n}, N_\mathrm{p}$ via (2.19) by inserting

the effective masses from Table B.3. The saturation limit N_a can be estimated by the volume V and the number of sulfur sites in a 2H MoS_2 unit cell, see Figure 2.4. With the lattice constants $a = 0.316$ nm and $c = 1.229$ nm from [215], we have $N_a \leq 4/V \approx 4 \times 10^{28}$ m^{-3}. Lastly, we use an n-type, i.e., positive background doping concentration $C = 1.0 \times 10^{21}$ m^{-3}. This concentration value improves numerical stability and is sufficiently small to have no significant influence on the results.

Physical quantity	Symbol	Value used	Range	Unit	Reference
Channel length		1	–	µm	[150]
Channel width		10	–	µm	[150]
Channel thickness		0.015	–	µm	[150]
Relative permittivity	ε_r	10	–		[130]
Image-force permittivity	ε_i	10	$\geq \varepsilon_r$		[156, 176]
Conduction band-edge energy	E_n	-4.0	$[-4.3, -3.7]$	eV	[53, 104, 153, 184, 251]
Band gap	E_g	1.3	–	eV	[159]
Valence band-edge energy	E_p	-5.3	–	eV	
Electron effective mass	m_n^*	0.55	–	m_0	[257]
Electron effective mass	m_p^*	0.71	–	m_0	[257]
Eff. conduction band DoS	N_n	1×10^{25}	–	m^{-3}	
Eff. valence band DoS	N_p	1.5×10^{25}	–	m^{-3}	
Max. vacancy density	N_a	1×10^{28}	$\leq 4 \times 10^{28}$	m^{-3}	
Electron mobility	μ_n	–	$[1.0\times10^{-5}, 1.0\times10^{-2}]$	m^2/(Vs)	[151, 197, 256, 261]
Hole mobility	μ_p	–	$[1.0\times10^{-5}, 1.0\times10^{-2}]$	m^2/(Vs)	[151, 197, 256, 261]
Doping density	C	1.0×10^{21}	–	m^{-3}	

Table B.3.: Summary of the MoS_2 material parameters collected from the literature for a layer thickness of ≈ 15 nm and a constant temperature $T = 300$ K and comparison with the values used in the simulations. Here, m_0 denotes the electron rest mass.

Next, the sample-specific parameters are summarized in Table B.4. The used intrinsic vacancy energies result in average vacancy concentrations of $C_a \approx 6.4 \times 10^{23}$ m^{-3} ($E_a = -4.32$ eV) and $C_a \approx 5.4 \times 10^{23}$ m^{-3} ($E_a = -4.33$ eV). These average vacancy concentrations align well with DFT calculations [106, 195], which predicted areal densities of up to $\approx 4.6 \times 10^{17}$ m^{-2}. The areal densities should be divided by the channel thickness to obtain the average volumetric density, resulting in average vacancy concentrations C_a up to $\approx 1 \times 10^{25}$ m^{-3}.

We can relate the fitted vacancy mobilities μ_a to the vacancy activation energies ΔH_a via the Genreith-Schriever hopping model [93] which relates the vacancy mobility μ_a, the electric field strength E, the drift velocity v_d and the activation energy ΔH_a via $\mu_a = \min_E\{(\partial v_d/\partial E)(\Delta H_a, E)\}$. Assuming a vanishing entropy of migration $S_a = 0$, an attempted frequency of $v_0 = 1.0 \times 10^{12}$ Hz (see [59]) and setting the hopping distance to the lattice constant $a = 0.316$ nm (see [215]), the chosen vacancy mobilities in Table B.4 can be translated to the activation energies $H_a = 0.53 \pm 0.01$ eV (for

S_1) and $H_a = 0.503 \pm 0.001$ eV (for S_2). This matches particular well with previous estimations $H_a = 0.6$ eV for the devices [150]. In case of the parameter set S_1 one cycle lasts 10.4 s, while for S_2 one cycle takes 8 s.

Physical quantity	Symbol	S_1	S_2	Unit
Left Schottky barrier	$\phi_0(x_1)$	1.0×10^{-3}	0.144	eV
Right Schottky barrier	$\phi_0(x_2)$	1.0×10^{-3}	0.110	eV
Intrinsic vacancy energy	E_a	-4.32	-4.33	eV
Electron mobility	μ_n	2.5×10^{-4}	2.15×10^{-3}	$m^2/(Vs)$
Hole mobility	μ_p	2.5×10^{-4}	2.15×10^{-3}	$m^2/(Vs)$
Vacancy mobility	μ_a	5×10^{-14}	1.15×10^{-13}	$m^2/(Vs)$
Voltage amplitude	U_{max}	13	10	V

Table B.4.: Sample-specific parameter sets S_1 and S_2 obtained from the simulation fits to the experimental data in Figure 5.23 (right) with S_1 and in Figure 5.27 (left) with S_2. A sweep rate of 5 V/s was used for all fits.

Bibliography

[1] G. Albinus, H. Gajewski, and R. Hünlich. "Thermodynamic design of energy models of semiconductor devices". *Nonlinearity* 15.2 (2002), pp. 367–383. DOI: 10.1088/0951-7715/15/2/307 (cit. on pp. 5, 31).

[2] S. Altazin, C. Kirsch, E. Knapp, A. Stous, and B. Ruhstaller. "Refined drift-diffusion model for the simulation of charge transport across layer interfaces in organic semiconductor devices". *Journal of Applied Physics* 124.13 (2018), p. 135501. DOI: 10.1063/1.5043245 (cit. on p. 63).

[3] Y. Aoki, C. Wiemann, V. Feyer, H.-S. Kim, C. M. Schneider, H. Ill-Yoo, and M. Martin. "Bulk mixed ion electron conduction in amorphous gallium oxide causes memristive behaviour". *Nature Communications* 5.3473 (2014). DOI: 10.1038/ncomms4473 (cit. on pp. 10, 43).

[4] A. Arnold et al. "Entropies and Equilibria of Many-Particle Systems: An Essay on Recent Research". *Monatshefte für Mathematik* 142 (2004), pp. 35–43. DOI: 10.1007/s00605-004-0239-2 (cit. on p. 54).

[5] A. Al-Ashouri et al. "Monolithic perovskite/silicon tandem solar cell with $>29\%$ efficiency by enhanced hole extraction". *Science* 370.6522 (2020), pp. 1300–1309. DOI: 10.1126/science.abd4016 (cit. on p. 20).

[6] P. Atkins and J. De Paula. *Atkins' Physical Chemistry*. 8th ed. W. H. Freeman and Company, New York, 2006 (cit. on p. 25).

[7] M. Auf der Maur, T. Albes, and A. Gagliardi. "Thin-film solar cells". *Handbook of Optoelectronic Device Modeling and Simulation: Lasers, Modulators, Photodetectors, Solar Cells, and Numerical Methods, Vol. 2*. CRC Press Taylor & Francis Group, 2017, pp. 497–538 (cit. on p. 36).

[8] B. Bailey. *AI power consumption exploding*. https://semiengineering.com/ai-power-consumption-exploding (accessed 2023-10-20). 2022 (cit. on p. 3).

[9] U. Bandelow, H. Gajewski, and R. Hünlich. "Fabry-Perot Lasers: Thermodynamics-Based Modeling". 2005, pp. 63–85. DOI: 10.1007/0-387-27256-9_3 (cit. on p. 30).

[10] R. E. Bank, D. J. Rose, and W. Fichtner. "Numerical Methods for Semiconductor Device Simulation". *SIAM Journal on Scientific and Statistical Computing* 4.3 (1983), pp. 416–435. DOI: 10.1137/0904032 (cit. on pp. 6, 63).

[11] A. J. Bard and L. R. Faulkner. *Electrochemical Methods: Fundamentals and Applications*. 2nd ed. John Wiley & Sons, New York, 2001 (cit. on p. 13).

[12] C. Bataillon, F. Bouchon, C. Chainais-Hillairet, J. Fuhrmann, E. Hoarau, and R. Touzani. "Numerical methods for the simulation of a corrosion model with moving oxide layer". *Journal of Computational Physics* 231.18 (2012), pp. 6213–6231. DOI: 10.1016/j.jcp.2012.06.005 (cit. on p. 10).

[13] C. Bataillon et al. "Corrosion modelling of iron based alloy in nuclear waste repository". *Electrochimica Acta* 55.15 (2010), pp. 4451–4467. DOI: 10.1016/j.electacta.2010.02.087 (cit. on p. 10).

[14] R. J. Baxter. *Exactly Solved Models in Statistical Mechanics*. Academic Press, London, 1982 (cit. on p. 25).

[15] M. Z. Bazant. "Theory of Chemical Kinetics and Charge Transfer based on Nonequilibrium Thermodynamics". *Accounts of Chemical Research* 46.5 (2013), pp. 1144–1160. DOI: 10.1021/ar300145c (cit. on pp. 13, 22, 26, 27, 72, 108).

[16] E. Bellini. *KAUST claims 33.7% efficiency for perovskite/silicon tandem solar cell*. https://www.pv-magazine.com/2023/05/30/kaust-claims-33-7-efficiency-for-perovskite-silicon-tandem-solar-cell/ (accessed 2023-10-20). 2023 (cit. on pp. 2, 34).

[17] M. Bessemoulin-Chatard and C. Chainais-Hillairet. "Exponential decay of a finite volume scheme to the thermal equilibrium for drift–diffusion systems". *Journal of Numerical Mathematics* 25.3 (2017), pp. 147–168. DOI: 10.1515/jnma-2016-0007 (cit. on p. 63).

[18] M. Bessemoulin-Chatard, C. Chainais-Hillairet, and M.-H. Vignal. "Study of a Finite Volume Scheme for the Drift-Diffusion System. Asymptotic Behavior in the Quasi-Neutral Limit". *SIAM Journal on Numerical Analysis* 52.4 (2014), pp. 1666–1691. DOI: 10.1137/130913432 (cit. on pp. 30, 56, 69).

[19] M. Bessemoulin-Chatard. "A finite volume scheme for convection–diffusion equations with nonlinear diffusion derived from the Scharfetter–Gummel scheme". *Numerische Mathematik* 121.4 (2012), pp. 637–670. DOI: 10.1007/s00211-012-0448-x (cit. on pp. 6, 63, 71).

[20] J. Bezanson, A. Edelman, S. Karpinski, and V. B. Shah. "Julia: A Fresh Approach to Numerical Computing". *SIAM Review* 59.1 (2017), pp. 65–98. DOI: 10.1137/141000671 (cit. on p. 95).

[21] P. Biler and J. Dolbeault. "Long Time Behavior of Solutions to Nernst-Planck and Debye-Hückel Drift-Diffusion Systems". *Annales Henri Poincaré* 1 (2000), pp. 461–472. DOI: 10.1007/s000230050003 (cit. on p. 54).

[22] J. S. Blakemore. "The Parameters of Partially Degenerate Semiconductors". *Proceedings of the Physical Society. Section A* 65 (1952), pp. 460–461. DOI: 10.1088/0370-1298/65/6/116 (cit. on p. 16).

[23] I. Borukhov, D. Andelman, and H. Orland. "Adsorption of large ions from an electrolyte solution: a modified Poisson–Boltzmann equation". *Electrochimica Acta* 46.2 (2000), pp. 221–229. DOI: 10.1016/S0013-4686(00)00576-4 (cit. on pp. 22, 26).

[24] F. Brezzi, L. Marini, S. Micheletti, P. Pietra, R. Sacco, and S. Wang. "Discretization of Semiconductor Device Problems (I)". *Handbook of Numerical Analysis* 13 (2005), pp. 317–441. DOI: 10.1016/S1570-8659(04)13004-4 (cit. on pp. 6, 63).

[25] M. Burger, B. Schlake, and M.-T. Wolfram. "Nonlinear Poisson-Nernst-Planck equations for ion flux through confined geometries". *Nonlinearity* 25.4 (2012), p. 961. DOI: 10.1088/0951-7715/25/4/961 (cit. on pp. 10, 22, 27).

[26] M. Burger, M. Di Francesco, J.-F. Pietschmann, and B. Schlake. "Nonlinear Cross-Diffusion with Size Exclusion". *SIAM Journal on Mathematical Analysis* 42.6 (2010), pp. 2842–2871. DOI: 10.1137/100783674 (cit. on p. 22).

[27] P. Calado. "Transient optoelectronic characterisation and simulation of perovskite solar cells". PhD thesis. Imperial College London, 2018. DOI: 10.25560/66894 (cit. on p. 37).

[28] P. Calado, I. Gelmetti, B. Hilton, M. Azzouzi, J. Nelson, and P. R. F. Barnes. "Driftfusion: An open source code for simulating ordered semiconductor devices with mixed ionic-electronic conducting materials in one-dimension". *Journal of Computational Electronics* 21 (2022), pp. 960–991. DOI: 10.1007/s10825-021-01827-z (cit. on pp. 20, 21, 27, 34, 37, 39, 95, 144).

[29] P. Calado, A. Telford, D. Bryant, X. Li, J. Nelson, B. O'Regan, and P. Barnes. "Evidence for ion migration in hybrid perovskite solar cells with minimal hysteresis". *Nature Communications* 7.13831 (2016). DOI: 10.1038/ncomms13831 (cit. on pp. 3, 19, 21, 28, 34, 36, 63, 116, 117).

[30] C. Cancès, C. Chainais-Hillairet, J. Fuhrmann, and B. Gaudeul. "A numerical-analysis-focused comparison of several finite volume schemes for a unipolar degenerate drift-diffusion model". *IMA Journal of Numerical Analysis* 41.1 (2020), pp. 271–314. DOI: 10.1093/imanum/draa002 (cit. on pp. 6, 63, 71, 72, 74, 87–89, 93).

[31] C. Cancès, C. Chainais-Hillairet, B. Merlet, F. Raimondi, and J. Venel. "Mathematical analysis of a thermodynamically consistent reduced model for iron corrosion". *Zeitschrift für angewandte Mathematik und Physik* 74.96 (2023). DOI: 10.1007/s00033-023-01970-6 (cit. on pp. 10, 27, 72).

[32] C. Cancès, M. Herda, and A. Massimini. *Finite volumes for a generalized Poisson-Nernst-Planck system with cross-diffusion and size exclusion*. https://hal.science/hal-04022357. 2023 (cit. on pp. 6, 72).

[33] C. Cancès and J. Venel. "On the square-root approximation finite volume scheme for nonlinear drift-diffusion equations". *Comptes Rendus. Mathématique* 361 (2023), pp. 535–558. DOI: 10.5802/crmath.421 (cit. on p. 72).

[34] C. Chainais-Hillairet and M. Herda. "Large-time behaviour of a family of finite volume schemes for boundary-driven convection–diffusion equations". *IMA Journal of Numerical Analysis* 40.4 (2019), pp. 2473–2504. DOI: 10.1093/imanum/drz037 (cit. on pp. 63, 69, 97).

[35] C. Chainais-Hillairet, M. Herda, S. Lemaire, and J. Moatti. "Long-time behaviour of hybrid finite volume schemes for advection–diffusion equations: linear and nonlinear approaches". *Numerische Mathematik* 151 (2013), pp. 963–1016. DOI: 10.1007/s00211-022-01289-w (cit. on p. 6).

[36] C. Chainais-Hillairet. "Entropy Method and Asymptotic Behaviours of Finite Volume Schemes". *Finite Volumes for Complex Applications VII-Methods and Theoretical Aspects*. Ed. by J. Fuhrmann, M. Ohlberger, and C. Rohde. Cham: Springer International Publishing, 2014, pp. 17–35. DOI: 10.1007/978-3-319-05684-5_2 (cit. on pp. 30, 75, 93).

[37] C. Chainais-Hillairet and F. Filbet. "Asymptotic behaviour of a finite-volume scheme for the transient drift-diffusion model". *IMA Journal of Numerical Analysis* 27.4 (2007), pp. 689–716. DOI: 10.1093/imanum/drl045 (cit. on pp. 6, 71).

[38] C. Chainais-Hillairet and Y.-J. Peng. "Finite volume approximation for degenerate drift-diffusion system in several space dimensions". *Mathematical Models and Methods in Applied Sciences* 14.03 (2004), pp. 461–481. DOI: 10.1142/S0218202504003313 (cit. on pp. 6, 71).

[39] M. Chen, H. Nam, S. Wi, G. Priessnitz, I. M. Gunawan, and X. Liang. "Multibit Data Storage States Formed in Plasma-Treated MoS_2 Transistors". *ACS Nano* 8.4 (2014), pp. 4023–4032. DOI: https://doi.org/10.1021/nn501181t (cit. on p. 21).

[40] X. Y. Chin et al. "Interface passivation for 31.25%-efficient perovskite/silicon tandem solar cells". *Science* 381.6653 (2023), pp. 59–63. DOI: 10.1126/science.adg0091 (cit. on pp. 2, 34).

[41] K. Cho et al. "Electric Stress-Induced Threshold Voltage Instability of Multilayer MoS_2 Field Effect Transistors". *ACS Nano* 7.9 (2013). PMID: 23924186, pp. 7751–7758. DOI: 10.1021/nn402348r (cit. on p. 21).

[42] L. Chua. "Memristor - The missing circuit element". *IEEE Transactions on Circuit Theory* 18.5 (1971), pp. 507–519. DOI: 10.1109/TCT.1971.1083337 (cit. on p. 3).

[43] L. Chua. "If it's pinched it's a memristor". *Semiconductor Science and Technology* 29.10 (2014), p. 104001. DOI: 10.1088/0268-1242/29/10/104001 (cit. on p. 3).

[44] W. Clarke, L. Bennett, Y. Grudeva, J. Foster, G. Richardson, and N. Courtier. "IonMonger 2.0: software for free, fast and versatile simulation of current, voltage and impedance response of planar perovskite solar cells". *Journal of Computational Electronics* 22 (2022). DOI: 10.1007/s10825-022-01988-5 (cit. on pp. 21, 27, 34, 37, 41, 95, 101, 108, 110, 143).

[45] W. Clarke, M. Wolf, A. Walker, and G. Richardson. "Charge transport modelling of perovskite solar cells accounting for non-Boltzmann statistics in organic and highly-doped transport layers". *Journal of Physics: Energy* 5 (2023), p. 025007. DOI: 10.1088/2515-7655/acc4e9 (cit. on p. 18).

[46] COMSOL. *Semiconductor Module User's Guide v5.4*. Burlington, MA. 2018 (cit. on pp. 6, 27, 37, 72).

[47] N. E. Courtier. "Interpreting ideality factors for planar perovskite solar cells: Ectypal diode theory for steady-state operation". *Physical Review Applied* 14.2 (2020), p. 024031. DOI: 10.1103/PhysRevApplied.14.024031 (cit. on p. 116).

[48] N. E. Courtier, J. M. Cave, A. B. Walker, G. Richardson, and J. M. Foster. "IonMonger: a free and fast planar perovskite solar cell simulator with coupled ion vacancy and charge carrier dynamics". *Journal of Computational Electronics* 18 (2019), pp. 1435–1449. DOI: 10.1007/s10825-019-01396-2 (cit. on pp. 21, 28, 37, 39, 41, 101, 110, 143).

[49] N. E. Courtier, J. Foster, S. O'Kane, A. Walker, and G. Richardson. "Systematic derivation of a surface polarization model for planar perovskite solar cells". *European Journal of Applied Mathematics* 30 (2017). DOI: 10.1017/S0956792518000207 (cit. on p. 20).

[50] N. E. Courtier, G. Richardson, and J. M. Foster. "A fast and robust numerical scheme for solving models of charge carrier transport and ion vacancy motion in perovskite solar cells". *Applied Mathematical Modelling* 63 (2018), pp. 329–348. DOI: 10.1016/j.apm.2018.06.051 (cit. on pp. 34, 36, 40, 63, 110).

[51] N. E. Courtier. "Modelling ion migration and charge carrier transport in planar perovskite solar cells". PhD thesis. University of Southampton, 2019 (cit. on pp. 27, 34, 97, 101, 108).

[52] C. Crowell and S. Sze. "Current transport in metal-semiconductor barriers". *Solid-State Electronics* 9.11 (1966), pp. 1035–1048. DOI: 10.1016/0038-1101(66)90127-4 (cit. on pp. 45, 47).

[53] S. Das, H.-Y. Chen, A. V. Penumatcha, and J. Appenzeller. "High Performance Multilayer MoS_2 Transistors with Scandium Contacts". *Nano Letters* 13.1 (2013), pp. 100–105. DOI: 10.1021/nl303583v (cit. on p. 145).

[54] D. De G. Allen and R. Southwell. "Relaxation methods applied to determine the motion, in two dimensions, of a viscous fluid past a fixed cylinder". *The Quarterly Journal of Mechanics and Applied Mathematics* 8.2 (1955), pp. 129–145. DOI: 10.1093/qjmam/8.2.129 (cit. on p. 71).

[55] P. Dhar. "The carbon impact of artificial intelligence". *Nature Machine Intelligence* 2.8 (2020), pp. 423–425. DOI: 10.1038/s42256-020-0219-9 (cit. on p. 3).

[56] R. Dimitrov. "The Paris Agreement on Climate Change: Behind Closed Doors". *Global Environmental Politics* 16 (2016), pp. 1–11. DOI: 10.1162/GLEP_a_00361 (cit. on p. 1).

[57] G. Ding et al. "Reconfigurable 2D WSe_2-Based Memtransistor for Mimicking Homosynaptic and Heterosynaptic Plasticity". *Small* 17.41 (2021), p. 2103175. DOI: 10.1002/smll.202103175 (cit. on pp. 4, 43).

[58] P. A. M. Dirac. "On the theory of quantum mechanics". *Proceedings of the Royal Society of London. Series A, Containing Papers of a Mathematical and Physical Character* 112.762 (1926), pp. 661–677. DOI: 10.1098/rspa.1926.0133 (cit. on p. 15).

[59] S. Dirkmann, J. Kaiser, C. Wenger, and T. Mussenbrock. "Filament Growth and Resistive Switching in Hafnium Oxide Memristive Devices". *ACS applied materials & interfaces* 10.17 (2018), pp. 14857–14868. DOI: 10.1021/acsami.7b19836 (cit. on p. 145).

[60] E. A. M. van Dis, J. Bollen, W. Zuidema, R. van Rooij, and C. L. Bockting. "ChatGPT: five priorities for research". *Nature* 614 (2023), pp. 224–226. DOI: 10.1038/d41586-023-00288-7 (cit. on p. 3).

[61] D. H. Doan, A. Glitzky, and M. Liero. "Analysis of a drift–diffusion model for organic semiconductor devices". *Zeitschrift für angewandte Mathematik und Physik* 70.2 (2019), p. 55. DOI: 10.1007/s00033-019-1089-z (cit. on p. 33).

[62] W. Dreyer, C. Guhlke, and R. Müller. "Overcoming the shortcomings of the Nernst-Planck model". *Phys. Chem. Chem. Phys.* 15 (2013), pp. 7075–7086. DOI: 10.1039/C3CP44390F (cit. on p. 10).

[63] J. Droniou. "Finite volume schemes for diffusion equations: Introduction to and review of modern methods". *Mathematical Models and Methods in Applied Sciences* 24.08 (2014), pp. 1575–1619. DOI: 10.1142/S0218202514400041 (cit. on p. 6).

[64] C. Durand, X. Zhang, J. Fowlkes, S. Najmaei, J. Lou, and A.-P. Li. "Defect-mediated transport and electronic irradiation effect in individual domains of CVD-grown monolaye MoS_2". *Journal of Vacuum Science & Technology B* 33.2 (2015). DOI: 10.1116/1.4906331 (cit. on pp. 5, 128).

[65] C. Eames, J. M. Frost, P. R. F. Barnes, B. C. O'Regan, A. Walsh, and M. S. Islam. "Ionic transport in hybrid lead iodide perovskite solar cells". *Nature Communications* 6.1 (2015), p. 7497. DOI: 10.1038/ncomms8497 (cit. on pp. 20, 24, 34, 144).

[66] E. Emmrich. "Discrete versions of Gronwall's lemma and their application to the numerical analysis of parabolic problems". *Technical Report 637, Technische Universität Berlin, https://www3.math.tu-berlin.de/preprints/files/Preprint-637-1999.pdf* (1999) (cit. on p. 61).

[67] L. C. Evans. *Partial Differential Equations*. 2nd ed. Vol. 19. Graduate Studies in Mathematics. American Mathematical Society, 2010 (cit. on pp. 61, 90).

[68] R. Eymard, J. Fuhrmann, and K. Gärtner. "A finite volume scheme for nonlinear parabolic equations derived from one-dimensional local Dirichlet problems". *Numerische Mathematik* 102 (2006), pp. 463–495. DOI: 10.1007/s00211-005-0659-5 (cit. on p. 71).

[69] R. Eymard, T. Gallouët, and R. Herbin. "Discretization of heterogeneous and anisotropic diffusion problems on general nonconforming meshes SUSHI: a scheme using stabilization and hybrid interfaces". *IMA Journal of Numerical Analysis* 30.4 (2009), pp. 1009–1043. DOI: 10.1093/imanum/drn084 (cit. on p. 6).

[70] R. Eymard, T. Gallouët, and R. Herbin. "Finite volume methods". *Solution of Equation in $\mathbb{R}^n$ (Part 3), Techniques of Scientific Computing (Part 3)*. Vol. 7. Handbook of Numerical Analysis. Elsevier, 2000, pp. 713–1018. DOI: 10.1016/S1570-8659(00)07005-8 (cit. on pp. 6, 63, 64, 68, 85).

[71] P. Farrell, D. H. Doan, M. Kantner, J. Fuhrmann, T. Koprucki, and N. Rotundo. "Drift-Diffusion Models". *Handbook of Optoelectronic Device Modeling and Simulation: Lasers, Modulators, Photodetectors, Solar Cells, and Numerical Methods, Vol. 2*. CRC Press Taylor & Francis Group, 2017, pp. 733–771 (cit. on pp. 1, 6, 9, 15, 16, 27, 30, 37, 67, 71, 72).

[72] P. Farrell, T. Koprucki, and J. Fuhrmann. "Computational and analytical comparison of flux discretizations for the semiconductor device equations beyond Boltzmann statistics". *Journal of Computational Physics* 346 (2017), pp. 497–513. DOI: 10.1016/j.jcp.2017.06.023 (cit. on pp. 6, 17–19, 63, 71).

[73] P. Farrell, J. Moatti, M. O'Donovan, S. Schulz, and T. Koprucki. "Importance of satisfying thermodynamic consistency in optoelectronic device simulations for high carrier densities". *Optical and Quantum Electronics* 55.11 (2023), p. 978. DOI: 10.1007/s11082-023-05234-5 (cit. on pp. 30, 71, 128).

[74] P. Farrell, M. Patriarca, J. Fuhrmann, and T. Koprucki. "Comparison of thermodynamically consistent charge carrier flux discretizations for Fermi–Dirac and Gauss–Fermi statistics". *Optical and Quantum Electronics* 50.2 (2018), pp. 1–10. DOI: 10.1007/s11082-018-1349-8 (cit. on p. 63).

[75] P. Farrell and D. Peschka. "Nonlinear diffusion, boundary layers and non-smoothness: Analysis of challenges in drift-diffusion semiconductor simulations". *Computers & Mathematics with Applications* 78.12 (2019), pp. 3731–3747. DOI: 10.1016/j.camwa.2019.06.007 (cit. on p. 63).

[76] P. A. Farrell and E. C. Gartland Jr. "On the Scharfetter-Gummel discretization for drift-diffusion continuity equations". *Computational methods for boundary and interior layers in several dimensions* (1991), pp. 51–79 (cit. on p. 71).

[77] A. Fell, D. Walter, and S. Glunz. "A Fast and Easy Perovskite Simulation Tool Featuring Ion Migration". *33rd European Photovoltaic Solar Energy Conference and Exhibition*. 2017, pp. 1192–1195. DOI: 10.4229/EUPVSEC20172017-3DV.2.80 (cit. on pp. 20, 21, 28, 34, 37, 63, 95, 128).

[78] E. Fermi. "Zur Quantelung des idealen einatomigen Gases". *Zeitschrift für Physik* 36.11-12 (1926), pp. 902–912. DOI: 10.1007/BF01400221 (cit. on p. 15).

[79] A. Fick. "V. On liquid diffusion". *The London, Edinburgh, and Dublin Philosophical Magazine and Journal of Science* 10.63 (1855), pp. 30–39. DOI: 10.1080/14786445508641925 (cit. on p. 28).

[80] P. Fleischmann. "Mesh generation for technology CAD in three dimensions". PhD thesis. Technische Universität Wien, 1999. DOI: 10.34726/hss.1999.03012084 (cit. on p. 68).

[81] Fluxim AG, Switzerland. *Semiconducting thin film optics simulator (SETFOS)*. http://www.fluxim.com. 2020 (cit. on pp. 63, 95).

[82] J. M. Foster, H. J. Snaith, T. Leijtens, and G. Richardson. "A Model for the Operation of Perovskite Based Hybrid Solar Cells: Formulation, Analysis, and Comparison to Experiment". *SIAM Journal on Applied Mathematics* 74.6 (2014), pp. 1935–1966. DOI: 10.1137/130934258 (cit. on p. 18).

[83] S. Friedli and Y. Velenik. *Statistical Mechanics of Lattice Systems: A Concrete Mathematical Introduction*. Cambridge University Press, Cambridge, 2017. DOI: 10.1017/9781316882603 (cit. on p. 25).

[84] H. A. Friis, M. G. Edwards, and J. Mykkeltveit. "Symmetric Positive Definite Flux-Continuous Full-Tensor Finite-Volume Schemes on Unstructured Cell-Centered Triangular Grids". *SIAM Journal on Scientific Computing* 31.2 (2009), pp. 1192–1220. DOI: 10.1137/070692182 (cit. on p. 6).

[85] J. Fuhrmann. "Comparison and numerical treatment of generalised Nernst-Planck models". *Computer Physics Communications* 196 (2015), pp. 166–178. DOI: 10.1016/j.cpc.2015.06.004 (cit. on pp. 6, 10, 22, 27, 71).

[86] J. Fuhrmann and H. Langmach. "Stability and existence of solutions of time-implicit finite volume schemes for viscous nonlinear conservation laws". *Applied Numerical Mathematics* 37.1-2 (2001), pp. 201–230. DOI: 10.1016/S0168-9274(00)00039-8 (cit. on p. 63).

[87] S. Furber. "Large-scale neuromorphic computing systems". *Journal of neural engineering* 13.5 (2016), p. 051001. DOI: 10.1088/1741-2560/13/5/05100 (cit. on p. 3).

[88] H. Gajewski and K. Gärtner. "On the Discretization of van Roosbroeck's Equations with Magnetic Field". *ZAMM-Journal of Applied Mathematics and Mechanics/Zeitschrift für Angewandte Mathematik und Mechanik* 76.5 (1996), pp. 247–264. DOI: 10.1002/zamm.19960760502 (cit. on pp. 6, 63).

[89] H. Gajewski. "On Existence, Uniqueness and Asymptotic Behavior of Solutions of the Basic Equations for Carrier Transport in Semiconductors". *Z. Angew. Math. Mech.* 65 (1985), pp. 101–108. DOI: 10.1002/zamm.19850650210 (cit. on pp. 9, 53, 54, 60).

[90] H. Gajewski and K. Gröger. "On the basic equations for carrier transport in semiconductors". *J. Math. Anal. Appl.* 113 (1986), pp. 12–35. DOI: 10.1016/0022-247X(86)90330-6 (cit. on pp. 9, 53).

[91] K. Gärtner and L. Kamenski. "Why Do We Need Voronoi Cells and Delaunay Meshes? Essential Properties of the Voronoi Finite Volume Method". *Computational Mathematics and Mathematical Physics* 59 (2019), pp. 1930–1944. DOI: 10.1134/S096554251912008X (cit. on p. 68).

[92] B. Gaudeul and J. Fuhrmann. "Entropy and convergence analysis for two finite volume schemes for a Nernst-Planck-Poisson system with ion volume constraints". *Numerische Mathematik* 151 (2022), pp. 99–149. DOI: 10.1007/s00211-022-01279-y (cit. on pp. 6, 72).

[93] A. Genreith-Schriever and R. De Souza. "Field-enhanced ion transport in solids: Reexamination with molecular dynamics simulations". *Physical Review B* 94.22 (2016), p. 224304. DOI: 10.1103/PhysRevB.94.224304 (cit. on p. 145).

[94] A. Glitzky. "Uniform exponential decay of the free energy for Voronoi finite volume discretized reaction-diffusion systems". *Mathematische Nachrichten* 284.17-18 (2011), pp. 2159–2174. DOI: 10.1002/mana.200910215 (cit. on p. 63).

[95] A. Glitzky, M. Liero, and G. Nika. "Analysis of a hybrid model for the electro-thermal behavior of semiconductor heterostructures". *Journal of Mathematical Analysis and Applications* 507.2 (2022), p. 125815. DOI: 10.1016/j.jmaa.2021.125815 (cit. on p. 33).

[96] S. Göke, M. Issler, M. Patel, D. Liu, and P. Spiller. *Keeping the semiconductor industry on the path to net zero*. https://www.mckinsey.com/industries/semiconductors/our-insights/keeping-the-semiconductor-industry-on-the-path-to-net-zero (accessed 2023-10-20). 2022 (cit. on p. 5).

[97] T. Goudon, V. Miljanovic, and C. Schmeiser. "On the Shockley-Read-Hall Model: Generation-Recombination in Semiconductors". *SIAM Journal of Applied Mathematics* 67 (2007), pp. 1183–1201. DOI: 10.1137/060650751 (cit. on p. 37).

[98] I. Grant and W. Phillips. *Electromagnetism*. Manchester Physics Series. John Wiley & Sons, Chichester, 1990 (cit. on p. 48).

[99] T. Grasser, T.-W. Tang, H. Kosina, and S. Selberherr. "A review of hydrodynamic and energy-transport models for semiconductor device simulation". *Proceedings of the IEEE* 91.2 (2003), pp. 251–274. DOI: 10.1109/JPROC.2002.808150 (cit. on p. 5).

[100] T. H. Gronwall. "Note on the Derivatives with Respect to a Parameter of the Solutions of a System of Differential Equations". *Annals of Mathematics* 20.4 (1919), pp. 292–296. DOI: 10.2307/1967124 (cit. on p. 61).

[101] M. Grundmann. *The Physics of Semiconductors: An Introduction Including Nanophysics and Applications*. 3rd ed. Springer, Cham, 2016. DOI: 10.1007/978-3-319-23880-7 (cit. on pp. 1, 9, 15, 18, 19, 38).

[102] E. Hairer, S. Nørsett, and G. Wanner. *Solving Ordinary Differential Equations I: Nonstiff problems*. Second revised edition. Springer-Verlag, Berlin Heidelberg, 2008. DOI: 10.1007/978-3-540-78862-1 (cit. on p. 69).

[103] E. Hairer and G. Wanner. *Solving Ordinary Differential Equations II: Stiff and Differential-Algebraic Problems*. Springer-Verlag, Berlin Heidelberg, 1996. DOI: 10.1007/978-3-642-05221-7 (cit. on p. 69).

[104] S. W. Han et al. "Band-gap transition induced by interlayer van der Waals interaction in MoS_2". *Physical Review B* 84 (4 2011), p. 045409. DOI: 10.1103/PhysRevB.84.045409 (cit. on p. 145).

[105] M. Heida. "Convergences of the squareroot approximation scheme to the Fokker-Planck operator". *Mathematical Models and Methods in Applied Sciences* 28.13 (2018), pp. 2599–2635. DOI: 10.1142/S0218202518500562 (cit. on p. 72).

[106] J. Hong et al. "Exploring atomic defects in molybdenum disulphide monolayers". *Nature Communications* 6.1 (2015), p. 6293. DOI: 10.1038/ncomms7293 (cit. on pp. 104, 145).

[107] K. Hopf and A. Jüngel. *Convergence of a finite volume scheme and dissipative measure-valued-strong stability for a hyperbolic-parabolic cross-diffusion system*. arXiv. 2023. DOI: 10.48550/arXiv.2304.00787 (cit. on p. 63).

[108] S. Huet, C. Lavelle, H. Ranchon, P. Carrivain, J.-M. Victor, and A. Bancaud. "Chapter Thirteen - Relevance and Limitations of Crowding, Fractal, and Polymer Models to Describe Nuclear Architecture". *New Models of the Cell Nucleus: Crowding, Entropic Forces, Phase Separation, and Fractals*. Ed. by R. Hancock and K. W. Jeon. Vol. 307. International Review of Cell and Molecular Biology. Academic Press, 2014, pp. 443–479. DOI: 10.1016/B978-0-12-800046-5.00013-8 (cit. on p. 22).

[109] W. Huh, D. Lee, and C.-H. Lee. "Memristors Based on 2D Materials as an Artificial Synapse for Neuromorphic Electronics". *Advanced Materials* 32.51 (2020), p. 2002092. DOI: 10.1002/adma.202002092 (cit. on pp. 4, 21).

[110] T. Hwang, A. J. Yun, J. Kim, D. Cho, S. Kim, S. Hong, and B. Park. "Electronic Traps and Their Correlations to Perovskite Solar Cell Performance via Compositional and Thermal Annealing Controls". *ACS Applied materials & interfaces* 11.7 (2019), pp. 6907–6917. DOI: 10.1021/acsami.8b17431 (cit. on pp. 5, 128).

[111] A. M. Il'in. "Differencing scheme for a differential equation with a small parameter affecting the highest derivative". *Mathematical Notes of the Academy of Sciences of the USSR* 6 (1969), pp. 596–602. DOI: 10.1007/BF01093706 (cit. on p. 71).

[112] Y. Y. Illarionov, K. K. H. Smithe, M. Waltl, T. Knobloch, E. Pop, and T. Grasser. "Improved Hysteresis and Reliability of MoS_2 Transistors With High-Quality CVD Growth and Al_2O_3 Encapsulation". *IEEE Electron Device Letters* 38 (2017), pp. 1763–1766. DOI: 10.1109/LED.2017.2768602 (cit. on p. 21).

[113] Y. Y. Illarionov et al. "Energetic mapping of oxide traps in MoS_2 field-effect transistors". *2D Materials* 4.2 (2017), p. 025108. DOI: 10.1088/2053-1583/aa734a (cit. on p. 128).

[114] Intergovernmental Panel on Climate Change (IPCC), 2018. *Global Warming of 1.5°C: An IPCC Special Report on the impacts of global warming of 1.5°C above pre-industrial levels and related global greenhouse gas emission pathways, in the context of strengthening the global response to the threat of climate change, sustainable development, and efforts to eradicate poverty*. Cambridge University Press, Cambridge, 2022. DOI: 10.1017/9781009157940 (cit. on p. 1).

[115] A. Iserles. *A First Course in the Numerical Analysis of Differential Equations*. 2nd ed. Cambridge University Press, Cambridge, 2009. DOI: 10.1017/CBO9780511995569 (cit. on p. 69).

[116] C. Jacoboni. *Theory of Electron Transport in Semiconductors: A Pathway from Elementary Physics to Nonequilibrium Green Functions*. Springer-Verlag, Berlin Heidelberg, 2010. DOI: 10.1007/978-3-642-10586-9 (cit. on pp. 5, 9).

[117] D. A. Jacobs, H. Shen, F. Pfeffer, J. Peng, T. P. White, F. J. Beck, and K. R. Catchpole. "The two faces of capacitance: New interpretations for electrical impedance measurements of perovskite solar cells and their relation to hysteresis". *Journal of Applied Physics* 124.22 (2018). DOI: 10.1063/1.5063259 (cit. on pp. 63, 95).

[118] J. Jadwiszczak et al. "MoS_2 Memtransistors Fabricated by Localized Helium Ion Beam Irradiation". *ACS Nano* 13.12 (2019), pp. 14262–14273. DOI: 10.1021/acsnano.9b07421 (cit. on p. 126).

[119] K. Jäger, L. Korte, B. Rech, and S. Albrecht. "Numerical optical optimization of monolithic planar perovskite-silicon tandem solar cells with regular and inverted device architectures". *Optics Express* 25.12 (2017), A473–A482. DOI: 10.1364/OE.25.00A473 (cit. on p. 36).

[120] A. Jain et al. "Commentary: The Materials Project: A materials genome approach to accelerating materials innovation". *APL Materials* 1.1 (2013). DOI: 10.1063/1.4812323 (cit. on p. 22).

[121] D. Jariwala, V. K. Sangwan, D. J. Late, J. E. Johns, V. P. Dravid, T. J. Marks, L. J. Lauhon, and M. C. Hersam. "Band-like transport in high mobility unencapsulated single-layer MoS_2 transistors". *Applied Physics Letters* 102.17 (2013), p. 173107. DOI: 10.1063/1.4803920 (cit. on p. 21).

[122] J. W. Jerome. *Analysis of Charge Transport: A Mathematical Study of Semiconductor Devices*. Springer-Verlag, Berlin Heidelberg, 1996. DOI: 10.1007/978-3-642-79987-7 (cit. on p. 53).

[123] N. Jones. "How to stop data centres from gobbling up the world's electricity". *Nature* 561 (2018), pp. 163–166. DOI: 10.1038/d41586-018-06610-y (cit. on p. 3).

[124] C. Jourdana, A. Jüngel, and N. Zamponi. "Three-species drift-diffusion models for memristors". *Mathematical Models and Methods in Applied Sciences* (2023), pp. 1–44. DOI: 10.1142/S0218202523500501 (cit. on p. 53).

[125] A. Jüngel. "Numerical Approximation of a Drift-Diffusion Model for Semiconductors with Nonlinear Diffusion". *ZAMM-Journal of Applied Mathematics and Mechanics/Zeitschrift für Angewandte Mathematik und Mechanik* 75.10 (1995), pp. 783–799. DOI: 10.1002/zamm.19950751016 (cit. on p. 63).

[126] A. Jüngel and Y.-J. Peng. "A hierarchy of hydrodynamic models for plasmas. Quasi-neutral limits in the drift-diffusion equations". *Asymptotic Analysis* 28.1 (2001), pp. 49–73 (cit. on p. 56).

[127] A. Jüngel. "On the existence and uniqueness of transient solutions of a degenerate nonlinear drift-diffusion model for semiconductors". *Mathematical Models and Methods in Applied Sciences* 04.05 (1994), pp. 677–703. DOI: 10.1142/S0218202594000388 (cit. on p. 53).

[128] A. Jüngel. *Transport Equations for Semiconductors*. Vol. 773. Lecture Notes in Physics. Springer-Verlag, Berlin Heidelberg, 2009. DOI: 10.1007/978-3-540-89526-8 (cit. on pp. 5, 9).

[129] A. Jüngel. *Entropy Methods for Diffusive Partial Differential Equations*. Vol. 804. SpringerBriefs in Mathematics. Springer, Cham, 2016. DOI: 10.1007/978-3-319-34219-1 (cit. on pp. 30, 54).

[130] Y. Kang, D. Jeon, and T. Kim. "Local Mapping of the Thickness-Dependent Dielectric Constant of MoS_2". *The Journal of Physical Chemistry C* 125.6 (2021), pp. 3611–3615. DOI: 10.1021/acs.jpcc.0c11198 (cit. on p. 145).

[131] M. Kantner. "Modeling and simulation of electrically driven quantum dot based single-photon sources : From classical device physics to open quantum systems". Doctoral Thesis. Berlin: Technische Universität Berlin, 2018. DOI: 10.14279/depositonce-7516 (cit. on pp. 26, 30).

[132] M. Kantner. "Generalized Scharfetter–Gummel schemes for electro-thermal transport in degenerate semiconductors using the Kelvin formula for the Seebeck coefficient". *Journal of Computational Physics* 402 (2020), p. 109091. DOI: 10.1016/j.jcp.2019.109091 (cit. on pp. 6, 63, 72).

[133] M. S. Kilic, M. Z. Bazant, and A. Ajdari. "Steric effects in the dynamics of electrolytes at large applied voltages. II. Modified Poisson-Nernst-Planck equations". *Phys. Rev. E* 75 (2 2007), p. 021503. DOI: 10.1103/PhysRevE.75.021503 (cit. on p. 10).

[134] C. Kim, S. Issarapanacheewin, I. Moon, K. Y. Lee, C. Ra, S. Lee, Z. Yang, and W. J. Yoo. "High-Electric-Field-Induced Phase Transition and Electrical Breakdown of $MoTe_2$". *Advanced Electronic Materials* 6.3 (2020), p. 1900964. DOI: 10.1002/aelm.201900964 (cit. on p. 21).

[135] J. Y. Kim, J.-W. Lee, H. S. Jung, H. Shin, and N.-G. Park. "High-efficiency Perovskite Solar Cells". *Chemical Reviews* 120.15 (2020), pp. 7867–7918. DOI: 10.1021/acs.chemrev.0c00107 (cit. on p. 34).

[136] C. Kittel. *Introduction to Solid State Physics*. 8th ed. John Wiley & Sons, Inc., Hoboken, New Jersey, 2004 (cit. on pp. 14, 15).

[137] T.-J. Ko et al. "Two-Dimensional Near-Atom-Thickness Materials for Emerging Neuromorphic Devices and Applications". *IScience* 23.11 (2020). DOI: 10.1016/j.isci.2020.101676 (cit. on p. 4).

[138] M. Koopmans, V. M. Le Corre, and L. J. A. Koster. "SIMsalabim: An open-source drift-diffusion simulator for semiconductor devices". *Journal of Open Source Software* 7.70 (2022), p. 3727. DOI: 10.21105/joss.03727 (cit. on pp. 63, 95).

[139] T. Koprucki and K. Gärtner. "Discretization scheme for drift-diffusion equations with strong diffusion enhancement". *12th International Conference on Numerical Simulation of Optoelectronic Devices (NUSOD)*. 2012, pp. 103–104 (cit. on p. 71).

[140] T. Koprucki, N. Rotundo, P. Farrell, D. H. Doan, and J. Fuhrmann. "On thermodynamic consistency of a Scharfetter-Gummel scheme based on a modified thermal voltage for drift-diffusion equations with diffusion enhancement". *Optical and Quantum Electronics* 47.6 (2015), pp. 1327–1332. DOI: 10.1007/s11082-014-0050-9 (cit. on pp. 6, 30, 71).

[141] J. A. Kress, C. Quarti, Q. An, S. Bitton, N. Tessler, D. Beljonne, and Y. Vaynzof. "Persistent ion accumulation at interfaces improves the performance of perovskite solar cells". *ACS Energy Letters* 7.10 (2022), pp. 3302–3310. DOI: 10.1021/acsenergylett.2c01636 (cit. on p. 3).

[142] R. Krishna and J. Wesselingh. "The Maxwell-Stefan approach to mass transfer". *Chemical Engineering Science* 52.6 (1997), pp. 861–911. DOI: 10.1016/s0009-2509(96)00458-7 (cit. on pp. 13, 14, 28).

[143] M. Landstorfer, S. Funken, and T. Jacob. "An advanced model framework for solid electrolyte intercalation batteries". *Phys. Chem. Chem. Phys.* 13 (28 2011), pp. 12817–12825. DOI: 10.1039/C0CP02473B (cit. on p. 10).

[144] M. Landstorfer, M. Ohlberger, S. Rave, and M. Tacke. "A modelling framework for efficient reduced order simulations of parametrised lithium-ion battery cells". *European Journal of Applied Mathematics* 34.3 (2023), pp. 554–591. DOI: 10.1017/S0956792522000353 (cit. on p. 22).

[145] R. D. Lazarov, I. D. Mishev, and P. S. Vassilevski. "Finite Volume Methods for Convection-Diffusion Problems". *SIAM Journal on Numerical Analysis* 33.1 (1996), pp. 31–55. DOI: 10.1137/0733003 (cit. on p. 71).

[146] H.-S. Lee, V. K. Sangwan, W. A. G. Rojas, H. Bergeron, H. Y. Jeong, J. Yuan, K. Su, and M. C. Hersam. "Dual-Gated MoS_2 Memtransistor Crossbar Array". *Advanced Functional Materials* 30.45 (2020), p. 2003683. DOI: 10.1002/adfm.202003683 (cit. on pp. 4, 43).

[147] J.-W. Lee, S.-G. Kim, S.-H. Bae, D.-K. Lee, O. Lin, Y. Yang, and N.-G. Park. "The Interplay between Trap Density and Hysteresis in Planar Heterojunction Perovskite Solar Cells". *Nano letters* 17.7 (2017), pp. 4270–4276. DOI: 10.1021/acs.nanolett.7b01211 (cit. on pp. 5, 128).

[148] W. Lei, S. Piani, P. Farrell, N. Rotundo, and L. Heltai. *A weighted Hybridizable Discontinuous Galerkin method for drift-diffusion problems*. arXiv. 2023. DOI: 10.48550/arXiv.2211.02508 (cit. on p. 63).

[149] R. J. LeVeque. *Finite volume methods for hyperbolic problems*. Cambridge University Press, Cambridge, 2002. DOI: 10.1017/CBO9780511791253 (cit. on pp. 85, 96).

[150] D. Li, B. Wu, X. Zhu, J. Wang, B. Ryu, W. D. Lu, W. D. Lu, and X. Liang. "MoS_2 Memristors Exhibiting Variable Switching Characteristics toward Biorealistic Synaptic Emulation". *ACS Nano* 12.9 (2018), pp. 9240–9252. DOI: 10.1021/acsnano.8b03977 (cit. on pp. 4, 19, 22, 43, 117–119, 123, 125, 126, 145, 146).

[151] S.-L. Li et al. "Thickness-Dependent Interfacial Coulomb Scattering in Atomically Thin Field-Effect Transistors". *Nano letters* 13.8 (2013), pp. 3546–3552. DOI: 10.1021/nl4010783 (cit. on pp. 123, 145).

[152] T. Li, G. Du, B. Zhang, and Z. Zeng. "Scaling behavior of hysteresis in multilayer MoS_2 field effect transistors". *Applied Physics Letters* 105.9 (2014), p. 093107. DOI: 10.1063/1.4894865 (cit. on p. 21).

[153] Y. Liang, S. Huang, R. Soklaski, and L. Yang. "Quasiparticle band-edge energy and band offsets of monolayer of molybdenum and tungsten chalcogenides". *Applied Physics Letters* 103.4 (2013), p. 042106. DOI: 10.1063/1.4816517 (cit. on p. 145).

[154] H.-Y. Lin. "Colors of artificial intelligence". *Computer* 54.11 (2021), pp. 95–99. DOI: 10.1109/MC.2021.3102359 (cit. on p. 3).

[155] C. Liu, C. Wang, S. Wise, X. Yue, and S. Zhou. "A positivity-preserving, energy stable and convergent numerical scheme for the Poisson-Nernst-Planck system". *Mathematics of Computation* 90.331 (2021), pp. 2071–2106. DOI: 10.1090/mcom/3642 (cit. on p. 63).

[156] J.-T. Liu, T.-B. Wang, X.-J. Li, and N.-H. Liu. "Enhanced absorption of monolayer MoS_2 with resonant back reflector". *Journal of Applied Physics* 115.19 (2014), p. 193511. DOI: 10.1063/1.4878700 (cit. on p. 145).

[157] M. Kantner and T. Koprucki. "Non-isothermal Scharfetter–Gummel Scheme for Electro-Thermal Transport Simulation in Degenerate Semiconductors". *Finite Volumes for Complex Applications IX - Methods, Theoretical Aspects, Examples*. Springer International Publishing, 2020, pp. 173–182. DOI: 10.1007/978-3-030-43651-3_14 (cit. on pp. 31, 63).

[158] R. H. Macneal. "An asymmetrical finite difference network". *Quarterly of Applied Mathematics* 11.3 (1953), pp. 295–310. DOI: 10.1090/qam/99978 (cit. on p. 71).

[159] K. F. Mak, C. Lee, J. Hone, J. Shan, and T. F. Heinz. "Atomically Thin MoS_2: A New Direct-Gap Semiconductor". *Physical review letters* 105.13 (2010), p. 136805. DOI: 10.1103/PhysRevLett.105.136805 (cit. on p. 145).

[160] A. Marchewka, R. Waser, and S. Menzel. "Physical simulation of dynamic resistive switching in metal oxides using a Schottky contact barrier model". *2015 International Conference on Simulation of Semiconductor Processes and Devices (SISPAD)*. 2015, pp. 297–300. DOI: 10.1109/SISPAD.2015.7292318 (cit. on p. 10).

[161] A. Marchewka et al. "Nanoionic Resistive Switching Memories: On the Physical Nature of the Dynamic Reset Process". *Advanced Electronic Materials* 2.1 (2016), p. 1500233. DOI: 10.1002/aelm.201500233 (cit. on p. 10).

[162] S. Mariotti et al. "Interface engineering for high-performance, triple-halide perovskite–silicon tandem solar cells". *Science* 381.6653 (2023), pp. 63–69. DOI: 10.1126/science.adf5872 (cit. on pp. 2, 34).

[163] P. A. Markowich. *The Stationary Semiconductor Device Equations*. Springer-Verlag, Wien, 1985. DOI: 10.1007/978-3-7091-3678-2 (cit. on pp. 9, 40, 53).

[164] P. A. Markowich, C. A. Ringhofer, and C. Schmeiser. *Semiconductor Equations*. Springer-Verlag, Wien, 1990. DOI: 10.1007/978-3-7091-6961-2 (cit. on pp. 5, 9, 53).

[165] J. C. Maxwell. "IV. On the dynamical theory of gases". *Philosophical Transactions of the Royal Society of London* 157 (1867), pp. 49–88. DOI: 10.1098/rstl.1867.0004 (cit. on p. 13).

[166] A. Mehonic and A. J. Kenyon. "Brain-inspired computing needs a master plan". *Nature* 604 (2022), pp. 255–260. DOI: 10.1038/s41586-021-04362-w (cit. on p. 1).

[167] S. van Mensfoort and R. Coehoorn. "Effect of Gaussian disorder on the voltage dependence of the current density in sandwich-type devices based on organic semiconductors". *Physical Review B* 78 (2008). DOI: 10.1103/PhysRevB.78.085207 (cit. on p. 18).

[168] Meyer Burger, Media Release. *Meyer Burger establishes new partnerships for the development of high-performance solar modules with perovskite technology*. https://www.meyerburger.com/en/newsroom/artikel/meyer-burger-establishes-new-partnerships-for-the-development-of-high-performance-solar-modules-with-perovskite-technology (accessed 2023-10-20). 2022 (cit. on p. 1).

[169] A. Mielke. "A gradient structure for reaction–diffusion systems and for energy-drift-diffusion systems". *Nonlinearity* 24.4 (2011), p. 1329. DOI: 10.1088/0951-7715/24/4/016 (cit. on pp. 5, 33).

[170] V. Miloš, P. Vágner, D. Budáč, M. Carda, M. Paidar, J. Fuhrmann, and K. Bouzek. "Generalized Poisson-Nernst-Planck-Based Physical Model of the O_2|LSM|YSZ Electrode". *Journal of The Electrochemical Society* 169.4 (2022), p. 044505. DOI: 10.1149/1945-7111/ac4a51 (cit. on pp. 10, 24).

[171] J. Mizusaki, K. Arai, and K. Fueki. "Ionic conduction of the perovskite-type halides". *Solid State Ionics* 11.3 (1983), pp. 203–211. DOI: 10.1016/0167-2738(83)90025-5 (cit. on p. 34).

[172] J. Y. Mo. "Technological innovation and its impact on carbon emissions: Evidence from Korea manufacturing firms participating emission trading scheme". *Technology analysis & Strategic management* 34.1 (2022), pp. 47–57. DOI: 10.1080/09537325.2021.1884675 (cit. on p. 5).

[173] J. Moatti. "A structure preserving hybrid finite volume scheme for semiconductor models with magnetic field on general meshes". *ESAIM: Mathematical Modelling and Numerical Analysis* 57.4 (2023), pp. 2557–2593. DOI: 10.1051/m2an/2023041 (cit. on pp. 6, 63).

[174] M. S. Mock. *Analysis of Mathematical Models of Semiconductor Devices*. Boole Press, Dublin, 1983 (cit. on pp. 6, 9, 53, 54, 63).

[175] D. Moia et al. "Ionic-to-electronic current amplification in hybrid perovskite solar cells: ionically gated transistor-interface circuit model explains hysteresis and impedance of mixed conducting devices". *Energy Environ. Sci.* 12 (4 2019), pp. 1296–1308. DOI: 10.1039/C8EE02362J (cit. on p. 34).

[176] B. Mukherjee, F. Tseng, D. Gunlycke, K. K. Amara, G. Eda, and E. Simsek. "Complex electrical permittivity of the monolayer molybdenum disulfide (MoS_2) in near UV and visible". *Optical Materials Express* 5.2 (2015), pp. 447–455. DOI: 10.1364/OME.5.000447 (cit. on p. 145).

[177] S. Najmaei et al. "Vapour phase growth and grain boundary structure of molybdenum disulphide atomic layers". *Nature Materials* 12 (2013). DOI: 10.1038/nmat3673 (cit. on pp. 4, 22).

[178] National Renewable Energy Laboratory (NREL). *Best Research-Cell Efficiency Chart*. https://www.nrel.gov/pv/cell-efficiency.html (accessed 2023-10-20). 2023 (cit. on pp. 2, 34).

[179] J. Nelson. *The Physics of Solar Cells*. Imperial College Press, London, 2003 (cit. on p. 36).

[180] W. Nernst. "Die elektromotorische Wirksamkeit der Jonen". *Zeitschrift für physikalische Chemie* 4.1 (1889), pp. 129–181. DOI: 10.1515/zpch-1889-0412 (cit. on p. 10).

[181] M. T. Neukom. "Comprehensive Characterization and Modelling of Operation Mechanisms in Third Generation Solar Cells". PhD thesis. Universität Augsburg, 2019 (cit. on p. 18).

[182] M. T. Neukom et al. "Consistent Device Simulation Model Describing Perovskite Solar Cells in Steady-State, Transient, and Frequency Domain". *ACS Applied Materials & Interfaces* 11.26 (2019), pp. 23320–23328. DOI: 10.1021/acsami.9b04991 (cit. on pp. 20, 21, 28, 34, 37, 63, 128).

[183] T. Niu et al. "Stable High-Performance Perovskite Solar Cells via Grain Boundary Passivation". *Advanced Materials* 30.16 (2018), p. 1706576. DOI: 10.1002/adma.201706576 (cit. on p. 128).

[184] A. Nourbakhsh et al. "MoS_2 Field-Effect Transistor with Sub-10 nm Channel Length". *Nano Letters* 16.12 (2016), pp. 7798–7806. DOI: 10.1021/acs.nanolett.6b03999 (cit. on p. 145).

[185] A. Okabe, B. Boots, K. Sugihara, and S. N. Chiu. *Spatial Tessellations: Concepts and Applications of Voronoi Diagrams*. 2nd ed. John Wiley & Sons, Chichester, 2000 (cit. on p. 67).

[186] G. Paasch and S. Scheinert. "Charge carrier density of organics with Gaussian density of states: Analytical approximation for the Gauss–Fermi integral". *Journal of Applied Physics* 107 (2010). DOI: 10.1063/1.3374475 (cit. on p. 17).

[187] K. Painter and T. Hillen. "Volume-filling and quorum-sensing in models for chemosensitive movement". *Can. Appl. Math. Q.* 10 (2002), pp. 501–543 (cit. on p. 22).

[188] N.-G. Park. "Perovskite solar cells: an emerging photovoltaic technology". *Materials Today* 18.2 (2015), pp. 65–72. DOI: 10.1016/j.mattod.2014.07.007 (cit. on pp. 2, 34).

[189] R. Pathria and P. Beale. *Statistical Mechanics*. 3rd ed. Butterworth-Heinemann, Oxford, 2011 (cit. on pp. 14, 16, 25).

[190] M. Patriarca, P. Farrell, J. Fuhrmann, and T. Koprucki. "Highly accurate quadrature-based Scharfetter-Gummel schemes for charge transport in degenerate semiconductors". *Computer Physics Communications* 235 (2018), pp. 40–49. DOI: 10.1016/j.cpc.2018.10.004 (cit. on pp. 6, 71).

[191] D. A. D. Pietro, A. Ern, and S. Lemaire. "An Arbitrary-Order and Compact-Stencil Discretization of Diffusion on General Meshes Based on Local Reconstruction Operators". *Computational Methods in Applied Mathematics* 14.4 (2014), pp. 461–472. DOI: 10.1515/cmam-2014-0018 (cit. on p. 6).

[192] M. Planck. "Ueber die Erregung von Electricität und Wärme in Electrolyten". *Annalen der Physik* 275.2 (1890), pp. 161–186. DOI: 10.1002/andp.18902750202 (cit. on p. 10).

[193] M. Planck. "Ueber die Potentialdifferenz zwischen zwei verdünnten Lösungen binärer Electrolyte". *Annalen der Physik* 276.8 (1890), pp. 561–576. DOI: 10.1002/andp.18902760802 (cit. on p. 10).

[194] J. Pomplun, S. Burger, L. Zschiedrich, and F. Schmidt. "Adaptive finite element method for simulation of optical nano structures". *physica status solidi (b)* 244.10 (2007), pp. 3419–3434. DOI: 10.1002/pssb.200743192 (cit. on p. 36).

[195] H. Qiu et al. "Hopping transport through defect-induced localized states in molybdenum disulphide". *Nature Communications* 4.1 (2013), p. 2642. DOI: 10.1038/ncomms3642 (cit. on pp. 104, 145).

[196] H. J. Queisser and E. E. Haller. "Defects in Semiconductors: Some Fatal, Some Vital". *Science* 281.5379 (1998), pp. 945–950. DOI: 10.1126/science.281.5379.945 (cit. on pp. 9, 19).

[197] B. Radisavljevic, A. Radenovic, J. Brivio, V. Giacometti, and A. Kis. "Single-layer MoS_2 transistors". *Nature nanotechnology* 6.3 (2011), pp. 147–150. DOI: 10.1038/nnano.2010.279 (cit. on p. 145).

[198] M. M. Rahman and Y. Watanobe. "ChatGPT for Education and Research: Opportunities, Threats, and Strategies". *Applied Sciences* 13 (2023), p. 5783. DOI: 10.3390/app13095783 (cit. on p. 3).

[199] B. Rajendran, Y. Liu, J.-s. Seo, K. Gopalakrishnan, L. Chang, D. J. Friedman, and M. B. Ritter. "Specifications of Nanoscale Devices and Circuits for Neuromorphic Computational Systems". *IEEE Transactions on Electron Devices* 60.1 (2012), pp. 246–253. DOI: 10.1109/TED.2012.2227969 (cit. on p. 3).

[200] S. van Reenen, M. Kemerink, and H. J. Snaith. "Modeling Anomalous Hysteresis in Perovskite Solar Cells". *The Journal of Physical Chemistry Letters* 6.19 (2015), pp. 3808–3814. DOI: 10.1021/acs.jpclett.5b01645 (cit. on pp. 20, 21, 28).

[201] S. Rehfeldt. "Mehrkomponentendiffusion in Flüssigkeiten". PhD thesis. Technische Universität München, 2009 (cit. on p. 14).

[202] G. Richardson, S. E. J. O'Kane, R. G. Niemann, T. A. Peltola, J. M. Foster, P. J. Cameron, and A. B. Walker. "Can slow-moving ions explain hysteresis in the current–voltage curves of perovskite solar cells?" *Energy Environ. Sci.* 9 (4 2016), pp. 1476–1485. DOI: 10.1039/C5EE02740C (cit. on pp. 19, 23).

[203] H.-G. Roos. "Ten ways to generate the Il'in and related schemes". *Journal of Computational and Applied Mathematics* 53.1 (1994), pp. 43–59. DOI: 10.1016/0377-0427(92)00124-R (cit. on p. 71).

[204] W. van Roosbroeck. "Theory of the flow of electrons and holes in germanium and other semiconductors". *The Bell System Technical Journal* 29 (1950), pp. 560–607. DOI: 10.1002/j.1538-7305.1950.tb03653.x (cit. on pp. 4, 9, 29, 109, 117).

[205] W. Rudin. *Principles of Mathematical Analysis*. 3rd ed. McGraw-Hill, Inc., New York City, 1976 (cit. on p. 83).

[206] V. Sangwan, D. Jariwala, I. Kim, K. Chen, T. Marks, L. Lauhon, and M. Hersam. "Gate-tunable memristive phenomena mediated by grain boundaries in single-layer MoS_2". *Nature Nanotechnology* 10.5 (2015), pp. 403–406. DOI: 10.1038/nnano.2015.56 (cit. on pp. 4, 19, 22, 43, 126).

[207] V. Sangwan, H.-S. Lee, H. Bergeron, I. Balla, M. E. Beck, K.-S. Chen, and M. C. Hersam. "Multi-terminal memtransistors from polycrystalline monolayer molybdenum disulfide". *Nature* 554.7693 (2018), pp. 500–504. DOI: 10.1038/nature25747 (cit. on pp. 4, 43, 126).

[208] R. Santbergen, T. Meguro, T. Suezaki, G. Koizumi, K. Yamamoto, and M. Zeman. "GenPro4 Optical Model for Solar Cell Simulation and Its Application to Multijunction Solar Cells". *IEEE Journal of Photovoltaics* 7.3 (2017), pp. 919–926. DOI: 10.1109/JPHOTOV.2017.2669640 (cit. on p. 36).

[209] W. Schäfer and M. Wegener. *Semiconductor Optics and Transport Phenomena*. Springer-Verlag, Berlin Heidelberg, 2002. DOI: 10.1007/978-3-662-04663-0 (cit. on p. 15).

[210] D. Scharfetter and H. Gummel. "Large-signal analysis of a silicon Read diode oscillator". *IEEE Transactions on Electron Devices* 16.1 (1969), pp. 64–77. DOI: 10.1109/T-ED.1969.16566 (cit. on p. 71).

[211] A. Schlichting and C. Seis. "The Scharfetter–Gummel scheme for aggregation–diffusion equations". *IMA Journal of Numerical Analysis* 42.3 (2021), pp. 2361–2402. DOI: 10.1093/imanum/drab039 (cit. on p. 63).

[212] H. Schmidt, F. Giustiniano, and G. Eda. "Electronic transport properties of transition metal dichalcogenide field-effect devices: surface and interface effects". *Chem. Soc. Rev.* 44 (21 2015), pp. 7715–7736. DOI: 10.1039/C5CS00275C (cit. on p. 22).

[213] L. Schmidt-Mende et al. "Roadmap on organic–inorganic hybrid perovskite semiconductors and devices". *APL Materials* 9.10 (2021), p. 109202. DOI: 10.1063/5.0047616 (cit. on pp. 2, 3, 19, 20, 35).

[214] D. Schroeder / National Renewable Energy Laboratory. *Perovskite solar cell*. https://www.energy.gov/eere/solar/perovskite-solar-cells (accessed 2023-10-20). 2022 (cit. on p. 2).

[215] S. Seeger. "Herstellung und Charakterisierung der Schichtgittersulfide MoS_2 und WS_2 für photovoltaische Anwendungen". PhD thesis. Technische Universität Berlin, 2006 (cit. on pp. 22, 145).

[216] S. Selberherr. *Analysis and Simulation of Semiconductor Devices*. Springer-Verlag, Wien, 1984. DOI: 10.1007/978-3-7091-8752-4 (cit. on pp. 6, 15, 18, 63).

[217] T. S. Sherkar, C. Momblona, L. Gil-Escrig, J. Ávila, M. Sessolo, H. J. Bolink, and L. J. A. Koster. "Recombination in Perovskite Solar Cells: Significance of Grain Boundaries, Interface Traps, and Defect Ions". *ACS Energy Letters* 2.5 (2017). PMID: 28540366, pp. 1214–1222. DOI: 10.1021/acsenergylett.7b00236 (cit. on p. 34).

[218] J. R. Shewchuk. "Triangle: Engineering a 2D quality mesh generator and Delaunay triangulator". *Applied Computational Geometry Towards Geometric Engineering*. Ed. by M. C. Lin and D. Manocha. Springer-Verlag, Berlin Heidelberg, 1996, pp. 203–222. DOI: 10.1007/BFb0014497 (cit. on p. 67).

[219] S. Shi, Z. Sun, and Y. H. Hu. "Synthesis, stabilization and applications of 2-dimensional 1T metallic MoS_2". *J. Mater. Chem. A* 6 (47 2018), pp. 23932–23977. DOI: 10.1039/C8TA08152B (cit. on p. 22).

[220] H. Si. "Three dimensional boundary conforming Delaunay mesh generation". PhD thesis. Technische Universität Berlin, 2008 (cit. on p. 68).

[221] H. Si. "TetGen, a Delaunay-Based Quality Tetrahedral Mesh Generator". *ACM Trans. Math. Softw.* 41.2 (2015). DOI: 10.1145/2629697 (cit. on p. 67).

[222] H. Si, K. Gärtner, and J. Fuhrmann. "Boundary conforming Delaunay mesh generation". *Computational Mathematics and Mathematical Physics* 50 (2010), pp. 38–53. DOI: 10.1134/S0965542510010069 (cit. on p. 68).

[223] Silvaco International. *Atlas User's Manual*. Santa Clara, CA. 2016 (cit. on pp. 6, 27, 37, 72).

[224] E. C. Smith, C. L. C. Ellis, H. Javaid, L. A. Renna, Y. Liu, T. P. Russell, M. Bag, and D. Venkataraman. "Interplay between Ion Transport, Applied Bias, and Degradation under Illumination in Hybrid Perovskite p-i-n Devices". *The Journal of Physical Chemistry C* 122.25 (2018), pp. 13986–13994. DOI: 10.1021/acs.jpcc.8b01121 (cit. on pp. 3, 34).

[225] H. J. Snaith et al. "Anomalous Hysteresis in Perovskite Solar Cells". *The Journal of Physical Chemistry Letters* 5.9 (2014), pp. 1511–1515. DOI: 10.1021/jz500113x (cit. on pp. 3, 19, 34).

[226] B. Spetzler, Z. Geng, K. Rossnagel, M. Ziegler, and F. Schwierz. "Lateral 2D TMDC Memristors–Experiment and Modeling". *2022 IEEE 16th International Conference on Solid-State & Integrated Circuit Technology (ICSICT)*. IEEE. 2022, pp. 1–3. DOI: 10.1021/acs.jpcc.8b01121 (cit. on pp. 43, 123, 126).

[227] J. Stefan. "Über das Gleichgewicht und die Bewegung, insbesondere die Diffusion von Gasgemengen". *Sitzungsberichte der Mathematisch-Naturwissenschaftlichen Classe der Kaiserlichen Akademie der Wissenschaften Wien, 2te Abteilung* 63 (1871), pp. 63–124 (cit. on p. 13).

[228] D. B. Strukov, G. S. Snider, D. R. Stewart, and R. S. Williams. "The missing memristor found". *Nature* 453.7191 (2008), pp. 80–83. DOI: 10.1038/nature06932 (cit. on p. 3).

[229] D. B. Strukov, J. L. Borghetti, and R. S. Williams. "Coupled Ionic and Electronic Transport Model of Thin-Film Semiconductor Memristive Behavior". *Small* 5.9 (2009), pp. 1058–1063. DOI: 10.1002/smll.200801323 (cit. on pp. 28, 43).

[230] V. Sulzer, S. J. Chapman, C. P. Please, D. A. Howey, and C. W. Monroe. "Faster Lead-Acid Battery Simulations from Porous-Electrode Theory: Part I. Physical Model". *Journal of The Electrochemical Society* 166.12 (2019), A2363–A2371. DOI: 10.1149/2.0301910jes (cit. on p. 22).

[231] M. Sup Choi, G.-H. Lee, Y.-J. Yu, D.-Y. Lee, S. Hwan Lee, P. Kim, J. Hone, and W. Jong Yoo. "Controlled charge trapping by molybdenum disulphide and graphene in ultrathin heterostructured memory devices". *Nature Communications* 4.1 (2013), p. 1624. DOI: 10.1038/ncomms2652 (cit. on pp. 5, 128).

[232] R. H. Swendsen. *An Introduction to Statistical Mechanics and Thermodynamics*. Oxford University Press, Oxford, 2012 (cit. on pp. 25, 26).

[233] Synopsys, Inc. *Sentaurus Device UserGuide vK-2015.06*. Mountain View, CA. 2015 (cit. on pp. 6, 37, 72).

[234] S. M. Sze, C. R. Crowell, and D. Kahng. "Photoelectric Determination of the Image Force Dielectric Constant for Hot Electrons in Schottky Barriers". *Journal of Applied Physics* 35.8 (1964), pp. 2534–2536. DOI: 10.1063/1.1702894 (cit. on p. 48).

[235] S. M. Sze and K. K. Ng. *Physics of Semiconductor Devices*. 3rd ed. John Wiley & Sons, Inc., Hoboken, New Jersey, 2007 (cit. on pp. 15, 18, 47, 48).

[236] S. Tan et al. "Steric Impediment of Ion Migration Contributes to Improved Operational Stability of Perovskite Solar Cells". *Advanced Materials* 32.11 (2020), p. 1906995. DOI: 10.1002/adma.201906995 (cit. on p. 34).

[237] N. Tessler and Y. Vaynzof. "Insights from Device Modeling of Perovskite Solar Cells". *ACS Energy Letters* 5.4 (2020), pp. 1260–1270. DOI: 10.1021/acsenergylett.0c00172 (cit. on p. 34).

[238] B. Thormundsson. *Artificial Intelligence (AI) worldwide - statistics & facts*. https://www.statista.com/topics/3104/artificial-intelligence-ai-worldwide/ (accessed 2023-10-20). 2023 (cit. on p. 3).

[239] P. Tockhorn et al. "Nano-optical designs for high-efficiency monolithic perovskite–silicon tandem solar cells". *Nature Nanotechnology* 17.11 (2022), pp. 1214–1221. DOI: 10.1038/s41565-022-01228-8 (cit. on p. 36).

[240] P. Vágner, C. Guhlke, V. Miloš, R. Müller, and J. Fuhrmann. "A continuum model for yttria-stabilized zirconia incorporating triple phase boundary, lattice structure and immobile oxide ions". *Journal of Solid State Electrochemistry* 23.10 (2019), pp. 2907–2926. DOI: 10.1007/s10008-019-04356-9 (cit. on pp. 10, 27).

[241] R. S. Varga. *Matrix Iterative Analysis*. 2nd ed. Springer-Verlag, Berlin Heidelberg, 2000. DOI: 10.1007/978-3-642-05156-2 (cit. on p. 85).

[242] P. S. Vassilevski, S. I. Petrova, and R. D. Lazarov. "Finite Difference Schemes on Triangular Cell-Centered Grids with Local Refinement". *SIAM journal on scientific and statistical computing* 13.6 (1992), pp. 1287–1313. DOI: 10.1137/0913073 (cit. on pp. 6, 63).

[243] H. K. Versteeg and W. Malalasekera. *An Introduction to Computational Fluid Dynamics: The Finite Volume Method*. 2nd ed. Pearson Education Limited, Harlow, 2007 (cit. on p. 71).

[244] A. Walsh, D. O. Scanlon, S. Chen, X. G. Gong, and S.-H. Wei. "Self-Regulation Mechanism for Charged Point Defects in Hybrid Halide Perovskites". *Angewandte Chemie International Edition* 54.6 (2015), pp. 1791–1794. DOI: 10.1002/anie.201409740 (cit. on p. 20).

[245] D. Walter, A. Fell, Y. Wu, T. Duong, C. Barugkin, N. Wu, T. White, and K. Weber. "Transient Photovoltage in Perovskite Solar Cells: Interaction of Trap-Mediated Recombination and Migration of Multiple Ionic Species". *The Journal of Physical Chemistry C* 122.21 (2018), pp. 11270–11281. DOI: 10.1021/acs.jpcc.8b02529 (cit. on p. 38).

[246] J. Wesselingh and R. Krishna. *Mass transfer in multicomponent mixtures*. Delft University Press, Delft, 2000 (cit. on pp. 13, 14).

[247] World Meteorological Organization, Press Release. *Global temperatures set to reach new records in next five years*. https://public.wmo.int/en/media/press-release/global-temperatures-set-reach-new-records-next-five-years (accessed 2023-10-20). 2023 (cit. on p. 1).

[248] D. Wrzosek. "Volume Filling Effect in Modelling Chemotaxis". *Mathematical Modelling of Natural Phenomena* 5.1 (2010), pp. 123–147. DOI: 10.1051/mmnp/20105106 (cit. on p. 22).

[249] P. Würfel and U. Würfel. *Physics of Solar Cells: From Basic Principles to Advanced Concepts*. 3rd ed. Wiley-VCH Verlag GmbH & Co, Weinheim, 2016 (cit. on p. 18).

[250] J. Xiang, Y. Li, F. Huang, and D. Zhong. "Effect of interfacial recombination, bulk recombination and carrier mobility on the J–V hysteresis behaviors of perovskite solar cells: a drift-diffusion simulation study". *Phys. Chem. Chem. Phys.* 21 (32 2019), pp. 17836–17845. DOI: 10.1039/C9CP03548F (cit. on p. 63).

[251] J. Xiao, Y. Zhang, H. Chen, N. Xu, and S. Deng. "Enhanced Performance of a Monolayer MoS_2/WSe_2 Heterojunction as a Photoelectrochemical Cathode". *Nano-Micro Letters* 10 (2018), pp. 1–9. DOI: 10.1007/s40820-018-0212-6 (cit. on p. 145).

[252] X. Yan, J. H. Qian, V. K. Sangwan, and M. C. Hersam. "Progress and Challenges for Memtransistors in Neuromorphic Circuits and Systems". *Advanced Materials* 34.48 (2022), p. 2108025. DOI: 10.1002/adma.202108025 (cit. on pp. 4, 43).

[253] J. Yang, H. Kawai, C. P. Y. Wong, and K. E. J. Goh. "Electrical Doping Effect of Vacancies on Monolayer MoS_2". *The Journal of Physical Chemistry C* 123.5 (2019), pp. 2933–2939. DOI: 10.1021/acs.jpcc.8b10496 (cit. on p. 22).

[254] S. Yu. "Neuro-inspired computing with emerging nonvolatile memorys". *Proceedings of the IEEE* 106.2 (2018), pp. 260–285. DOI: 10.1109/JPROC.2018.2790840 (cit. on p. 3).

[255] Z. Yu and R. Dutton. *SEDAN III – A one-dimensional device simulator*. www-tcad.stanford.edu/tcad/programs/sedan3.html. 1988 (cit. on pp. 6, 63, 72).

[256] Z. Yu, Z.-Y. Ong, S. Li, J.-B. Xu, G. Zhang, Y.-W. Zhang, Y. Shi, and X. Wang. "Analyzing the Carrier Mobility in Transition-Metal Dichalcogenide MoS_2 Field-Effect Transistors". *Advanced Functional Materials* 27.19 (2017), p. 1604093. DOI: 10.1002/adfm.201604093 (cit. on p. 145).

[257] W. S. Yun, S. W. Han, S. C. Hong, I. G. Kim, and J. D. Lee. "Thickness and strain effects on electronic structures of transition metal dichalcogenides: 2H-MX_2 semiconductors (M = Mo, W; X = S, Se, Te)". *Phys. Rev. B* 85 (3 2012), p. 033305. DOI: 10.1103/PhysRevB.85.033305 (cit. on p. 145).

[258] A. van der Zande et al. "Grains and grain boundaries in highly crystalline monolayer molybdenum disulphide". *Nature Materials* 12.6 (2013), pp. 554–561. DOI: 10.1038/nmat3633 (cit. on pp. 4, 22).

[259] M. Zeman, J. van den Heuvel, M. Kroon, J. Willemen, B. Pieters, J. Krč, and S. Solntsev. *Advanced Semiconductor Analysis, User's Manual v6.0*. Delft University of Technology, Laboratory of Photovoltaic Materials and Devices. 2019 (cit. on p. 37).

[260] Q. Zhao et al. "Current status and prospects of memristors based on novel 2D materials". *Materials Horizons* 7.6 (2020), pp. 1495–1518. DOI: 10.1039/C9MH02033K (cit. on p. 21).

[261] Y. Zhao and G. Ouyang. "Thickness-dependent photoelectric properties of MoS_2/Si heterostructure solar cells". *Scientific Reports* 9.1 (2019), p. 17381. DOI: 10.1038/s41598-019-53936-2 (cit. on p. 145).

[262] H. Zhou, V. Sorkin, S. Chen, Z. Yu, K.-W. Ang, and Y.-W. Zhang. "Design-Dependent Switching Mechanisms of Schottky-Barrier-Modulated Memristors based on 2D Semiconductor". *Advanced Electronic Materials* (2023), p. 2201252. DOI: 10.1002/aelm.202201252 (cit. on pp. 43, 123, 126).

Acknowledgements and dedication

Completing this thesis would not have been possible without the invaluable encouragement of numerous individuals. I am deeply grateful to Patricio Farrell, whose scientific guidance, but also his optimism and way of acting have not only influenced my work but also my personal growth. Being Patricio's first PhD candidate is an honor, and it is hard to realize that we nearly completed this journey together. He has consistently supported me as my mentor and never allowed me to doubt my capabilities. Moreover, I would like to thank Nella Rotundo for her presence at the initial job interview, which marked the beginning of this PhD project and for her presence at one of the last steps, her willingness to serve as an examiner for this thesis. I also thank my collaborators, especially Claire Chainais-Hillairet, Nicola Courtier, Jürgen Fuhrmann, Maxime Herda, Benjamin Spetzler, and Petr Vágner. Learning from them, being supervised by them, and working with them has been a true privilege.

My sincere appreciation goes to my office mates Zeina Amer and Yiannis Hadjimichael, as well as my fellow PhDs Derk Frerichs-Mihov and Daniel Runge. They all have not only been great friends but also a source of constant emotional support. I would also like to extend my gratitude to our secretaries Marion Lawrenz and Imke Weitkamp for their behind-the-scenes work, which often goes unrecognized but is truly precious. I thank Benjamin, Daniel, Patricio, and Yiannis for their constructive feedback on this thesis. Thank you to the many colleagues who have contributed to the completion of this work, even though they may not have been mentioned individually.

Lastly, I am profoundly grateful for my family and my friends-who-are-family, for showering me with love and warmth. While they may not understand the details of my work, aside from it being a PhD in maths, they remain my greatest supporters. Having all of you by my side is truly all I need to find happiness.

This was not a four years project, in fact, it was a life project. Back in primary school, I dreamt of becoming a doctor, even though I had a different one in mind. This thesis is dedicated to all those young minds who may not yet fully grasp what a doctor looks like or what they can do, but who recognize that they do not look like them nor their family members. Despite this, they still hold onto the dream of those two letters added up to their name. It is dedicated to those who long for recognition, believing that the world will finally appreciate them and their family when they participate in the illusion that a persons' worth can be measured by (scientific) achievements.

I tried to deconstruct this illusion, still I find myself struggling.
As so many others.

Zusammenfassung

Angesichts der Klimakrise ist es entscheidend, verstärkt auf technologischen Fortschritt zu setzen, um den steigenden CO_2-Ausstoß zu reduzieren. Zwei vielversprechende Halbleitertechnologien, die in diesem Kontext hervorstechen, sind Perowskit-basierte Solarzellen und auf Übergangsmetall-Dichalkogenide (TMDC) basierende memristive Bauteile. Diese Technologien könnten eine Schlüsselrolle beim Ausbau erneuerbarer Energien oder bei der Entwicklung energieeffizienterer Hardware spielen. In beiden Materialien, Perowskit und TMDC, belegen experimentelle Studien die Existenz und Akkumulation von Vakanzen, Leerstellen in der Kristallstruktur, die in den Halbleitermaterialien migrieren können. Dieser zusätzliche Effekt und sein Einfluss auf das Verhalten der Bauteile sind bislang nicht hinreichend erforscht worden.

Deswegen hat sich die vorliegende Dissertation als Ziel gesetzt, auf umfängliche theoretische Art den Effekt des zusätzlichen Vakanzentransports in Halbleitern zu untersuchen. Dabei setzen wir uns mit der Herleitung, der Modellierung, der numerischen Diskretisierung und schlussendlich mit der numerischen Simulation auseinander. Im ersten Schritt leiten wir Drift-Diffusions Gleichungen her, um den Ladungstransport in Materialien mit zusätzlicher Vakanzenbewegung zu beschreiben. Die Herleitung basiert auf thermodynamischen Konzepten wie dem Maxwell-Stefan-Diffusionsmodell und dem großkanonischen Ensemble. Besonderes Augenmerk legen wir darauf, die vakanzenbasierte Migration und Akkumulation physikalisch korrekt darzustellen. Anschließend formulieren wir gekoppelte Systeme partieller Differentialgleichungen, die den Ladungstransport in Perowskit-Solarzellen und TMDC-Memristoren modellieren. Aufbauend auf diesen kontinuierlichen Gleichungen diskretisieren wir die Transportgleichungen mithilfe des Finite-Volumen-Verfahrens. Durch das Anwenden der Entropie-Methode können wir die Existenz von diskreten Lösungen für unsere zugrundeliegenden diskreten Modelle nachweisen. Diese Dissertation schließt mit Simulationen ab, die wir mithilfe von `ChargeTransport.jl` durchführen, einer von uns entwickelten Software, die in der Programmiersprache Julia verfasst wurde. Dabei untersuchen wir das Langzeitverhalten der diskreten Lösungen für das Perowskit-Solarzellen und das TMDC-Memristor Transportmodell. Zusätzlich diskutieren wir den Einfluss zweier unterschiedlicher Modellierungsansätze der Vakanzenstromdichte auf den Ladungstransport in Perowskit-Solarzellen. Des Weiteren vergleichen wir unsere Simulationsergebnisse zum vakanzenbasierten Ladungstransport in TMDC-basierten memristiven Bauteilen mit experimentellen Messungen aus der Literatur.

Selbstständigkeitserklärung

Ich, Dilara Abdel, erkläre gegenüber der Freien Universität Berlin, dass ich die vorliegende Dissertation selbstständig und ohne Benutzung anderer als der angegebenen Quellen und Hilfsmittel angefertigt habe. Die vorliegende Arbeit ist frei von Plagiaten. Alle Ausführungen, die wörtlich oder inhaltlich aus anderen Schriften entnommen sind, habe ich als solche kenntlich gemacht. Diese Dissertation wurde in gleicher oder ähnlicher Form noch in keinem früheren Promotionsverfahren eingereicht.

Mit einer Prüfung meiner Arbeit durch ein Plagiatsprüfungsprogramm erkläre ich mich einverstanden.

Berlin, den 25. Oktober 2023 .....
(Unterschrift)